Alma Mater Studiorum - Università di Bologna

DOTTORATO DI RICERCA IN

SCIENZE DELLA TERRA, DELLA VITA E DELL'AMBIENTE

Ciclo 36

Settore Concorsuale: 04/A3 - GEOLOGIA APPLICATA, GEOGRAFIA FISICA E GEOMORFOLOGIA

Settore Scientifico Disciplinare: GEO/05 - GEOLOGIA APPLICATA

ANALYSIS OF THE LONG-TERM SUBSIDENCE IN THE URBAN AREA OF BOLOGNA

Presentata da: Alessandro Zuccarini

Coordinatore Dottorato

Maria Giovanna Belcastro

Supervisore

Matteo Berti

Esame finale anno 2024

Abstract

Land subsidence in urban areas due to excessive groundwater withdrawals represents a dangerous and widespread geological hazard that, in the context of climate change, constitutes a pressing challenge for modern society. Despite the general knowledge about the triggering and deformation mechanisms, as well as the availability of reliable monitoring techniques, conducting a comprehensive study of ongoing ground deformation in an urban environment often entails significant challenges.

In the present PhD project, the complex subsidence process affecting the city of Bologna (Italy) is thoroughly analysed. Since the 1960s the urban area of Bologna has experienced a severe ground deformation process due to aquifers overexploitation that peaked during the 1970s with maximum displacement rates exceeding 10 cm/year, leading to manifest structural and infrastructural damage. Despite a general lowering of these rates observed over the subsequent decades, thanks to regional groundwater regulations policies, recent data clearly underscore a subsidence resurgence in a prominent portion of the study area.

To reconstruct the subsurface stratigraphic architecture of the urban area of Bologna and generate a reliable 3D geological model, serving as a basis for future subsidence analyses, a multidisciplinary approach was defined and adopted. This approach was primarily centred on a detailed stratigraphic analysis relying on the lithofacies criterion. The convergence of these analyses within the multidisciplinary framework resulted in the partitioning of the study area into three distinct geological domains. Despite sharing a common alluvial context, these domains consistently exhibit unique morphological features and depositional stacking patterns.

Subsequently, since long-term data are crucial for a comprehensive understanding of the ongoing subsidence, a methodology was developed to integrate ground-based and remotely sensed ground displacement data. This processing chain enabled the generation of cumulative subsidence time series and maps describing the long-term temporal evolution and spatial distribution of the ground deformation process, respectively. The reconstructed long-term subsidence field consistently aligns with the primary stratigraphic features and geological variations summarised in the 3D model. Concurrently, the generated cumulative displacement curves systematically match the pluriannual trends observed in groundwater level and pumping monitoring time series.

Lastly, to evaluate the expression of the observed relationships from a geotechnical perspective, a series of one-dimensional subsidence calculations were conducted considering the mechanical properties of the investigated deposits and piezometric data. The analyses performed provided valuable insight into the overall mechanical behaviour of the existing soils, as well as the post-pumping groundwater level and pore pressure distributions, consistent with field data.

The methodological approach employed in this PhD enables the comprehensive analysis of land subsidence in urban areas. It allows the detailed exploration of the individual factors governing the ongoing deformation process and their interactions, even within complex stratigraphic and hydrogeological environments, as exemplified in the urban area of Bologna.

Contents

1. Introduction **1**

1.1 Preface 1

1.2 Theory and background 2

1.2.1 Subsidence mechanisms 2

1.2.2 Terzaghi's consolidation theory 7

1.2.3 Subsidence monitoring techniques 19

1.2.3.1 Deformation monitoring 19

1.2.3.2 Ground surface displacement monitoring 21

1.3 Impact on society 25

1.3.1 Subsidence in developing countries and rapidly growing cities 26

1.3.2 Subsidence and climate change 28

1.4 Research questions and outline 29

1.5 References 31

2. Introduction **37**

2.1 Preface 37

2.2 Abstract 38

2.3 Introduction 38

2.4 Study Area 40

2.5 Methodology 42

2.5.1 Surface morphology 42

2.5.2 Urban river network 42

2.5.3 Geophysical surveys 42

2.5.4 Boreholes and wells 43

2.5.5 Lithofacies analysis 44

2.5.6 Two-dimensional stratigraphic cross-sections 46

2.5.7 Simplified geological model 47

2.5.8 3D geological model 47

2.6 Results 48

2.6.1 Surface morphology 48

2.6.2 Urban river network 49

2.6.3 Geophysical surveys 50

2.6.4 Lithofacies analysis 52

2.6.5 Two-dimensional stratigraphic cross-sections 53
2.6.5.1 Transversal stratigraphic sections 53
2.6.5.2 Longitudinal stratigraphic sections 54
2.6.6 Simplified geological model 57
2.6.7 3D geological model 59
2.6.8 Geological interpretation 61
2.7 Discussion 61
2.7.1 General remarks on the lithofacies approach 61
2.7.2 3D modelling or rendering? 61
2.7.3 Geotechnical implications 62
2.8 Conclusions 65
2.9 Supplementary Material 66
2.10 References 68

3. Long-term spatiotemporal evolution of land subsidence in the urban area of Bologna, Italy **73**
3.1 Preface 73
3.2 Abstract 74
3.3 Introduction 74
3.4 Study Area 75
3.5 Methodology 78
3.5.1 Input data 78
3.5.2 Data integration 80
3.5.2.1 Time series 80
3.5.2.2 Raster maps 83
3.5.3 Comparison with groundwater data 85
3.6 Results 86
3.6.1 Long-term evolution 86
3.6.1.1 Time series 86
3.6.1.2 Subsidence maps 91
3.6.1.3 Groundwater map 93
3.6.2 Recent subsidence evolution 95
3.6.2.1 Time series (2008 – 2020) 95
3.6.2.2 Comparison with EGMS data 98
3.7 Discussion 99
3.7.1 Comparison between subsidence pattern and 3D geology 99

3.7.2 Impact of subsidence on structures 100
3.8 Conclusions 103
3.9 Supplementary Material 104
3.9.1 Long-term cumulative ground displacement time series (1970 – 2020) 104
3.9.2 Recent subsidence and groundwater withdrawals time series comparison (2008 – 2020) 106
3.10 References 110

4. Introduction 114
4.1 Preface 114
4.2 Methodology 115
4.2.1 Input stratigraphies 115
4.2.2 Mechanical characterisation 116
4.2.2.1 Fine-grained deposits 116
4.2.2.1.1 Available data 116
4.2.2.1.2 Lithological classification 118
4.2.2.1.3 Fine-grained intervals parametrisation 122
4.2.2.1 Coarse-grained deposits 126
4.2.3 Groundwater 126
4.2.4 One-dimensional subsidence calculation 127
4.3 Results 129
4.3.1 Fine-grained to coarse-grained soil percentage distribution 129
4.3.2 Parametrisation of fine-grained soils 131
4.3.3 One-dimensional subsidence calculation 135
4.4 Discussion and conclusive remarks 142
4.5 Supplementary Material 144
4.6 References 150

5. General conclusions 152
5.1 References 155

General references 156

Chapter 1 – Introduction

1.1 Preface

The present chapter provides an introduction to the primary subjects addressed during the course of this PhD project. Firstly, an overview of the different mechanisms responsible for natural and anthropogenic subsidence will be presented, with particular emphasis on deformations resulting from excessive subsurface fluid withdrawal (section 1.2.1). Next, section 1.2.2 will provide theoretical insights into the consolidation process, focusing on Terzaghi's one-dimensional theory (1925; 1943), accompanied by examples of analytical and numerical solutions to the governing differential equation. Subsequently, the main ground-based and remotely sensed monitoring techniques typically used to measure subsurface layer deformations and ground surface sinking will be reviewed, highlighting their primary capabilities and limitations (section 1.2.3).
In section 1.3, the global diffusion and impact of subsidence processes on society in urban areas are examined, with a focus on their occurrence in rapidly urbanising environments and developing countries (section 1.3.1). Finally, the implications of subsidence processes within a broader context of global climate change are discussed in section 1.3.2.
Lastly, section 1.4 illustrates the fundamental scientific questions underlying the present PhD project, followed by an outline of the thesis structure serving as a brief guide to the subsequent chapters.

1.2 Theory and background

1.2.1 Subsidence mechanisms

Land subsidence is a globally widespread and dangerous geological hazard which can manifest as both the sudden sinking and the gradual downward movement of the Earth's surface (Marker 2013), resulting in a lowering of the ground level. Ground displacements are predominantly vertical, with a generally limited horizontal component. However, horizontal deformations induced by the main vertical movement are often not negligible and can also have significant damaging effects (Galloway & Burbey 2011).
Land subsidence can be attributed to various natural processes, human activities and their interaction. Natural processes generally occur at larger regional scales and exhibit a more uniform and regular distribution. On the other hand, anthropogenic subsidence is frequently superimposed on natural ground deformation processes (Galloway & Burbey 2011) but is typically more localised, unevenly distributed, and distinguished by higher sinking rates. Moreover, natural and anthropogenic subsidence occurs at sensibly different time scales ranging from 10^6 to 10^3 years to hundreds or tens of years, respectively (Holzer 1984, Pirazzoli 1996, Borchers 1998, Carminati & Di Donato 1999, Carminati & Martinelli 2002).

The natural causes of land subsidence encompass numerous mechanisms, such as the gradual compaction of sedimentary deposits (Zhang et al. 2018). This process involves the long-term compaction and consolidation of sequences of loose sedimentary bodies of varying thickness under their own weight. The driving mechanisms can be found in the progressive accumulation of younger sediments, leading to increased overburden load and a decrease in the void ratio (e) of the materials involved. Factors such as erosion and sedimentation rates in the basin, as well as the textural, compositional, and mechanical properties of the sediments, can influence the evolution of this process (Meade 1968).

Subsidence can also be related to tectonic processes acting at different scales (Ma et al. 2018), ranging from regional scales of the sedimentary basin to more localised areas. In these instances, ground displacements are progressively accommodated by the present structures and faults, moving the existing geological units. Tectonics can play a significant role in sedimentation (Amorosi et al. 1996; Carminati & Martinelli 2002), influencing erosion and deposition rates within sedimentary basins and potentially affecting other subsidence mechanisms, such as the already mentioned natural sediment compaction. The presence of tectonic structures can also influence the regional-scale subsidence spatial distribution pattern. For example, this was observed in the northeastern portion of the Po Plain (Italy), where varying long-term (10^3-10^6 years) subsidence rates were associated with different tectonic structures (Bruno et al. 2020). For instance, while anticlines displayed lower rates, syncline areas demonstrated higher subsidence values that may have been enhanced by high sedimentation rates and the preferential accumulation of compressible sedimentary bodies (Bruno et al. 2020).

Rock dissolution processes mainly involving evaporites such as limestones and gypsum, represent another widespread natural cause of land subsidence (Laouafa et al. 2023). This phenomenon is driven by the effect of water circulation in the presence of soluble rocks. The progressive transformation of rock solid into flowing fluid may trigger the creation of cavities (Laouafa et al. 2021) and cave systems, typical of karst environments, in the subsurface (Cooper 1988). Subsequently, roof cave instabilities may lead to either smooth subsidence or sudden collapses of the ground surface (Laouafa et al. 2021), typically known as *sinkholes* (Fig. 1.1).

Other natural subsidence mechanisms can be attributed to volcanic and seismic activity. In the case of volcanic activity, ground displacement may occur due to magma migration from shallow chambers and outgassing processes (Hamlyn et al. 2018; Battaglia et al. 2021) or changes in pore-fluid pressures within shallow confined hydrothermal systems (Lu et al. 2002).
As regards seismic activity, subsidence can result from sudden coseismic displacements accommodated by the involved seismogenic faults (Leeper et al. 2017). In this scenario, the mechanism resembles that observed in the previously described tectonically driven subsidence, but the displacement occurs abruptly and is

concentrated within a short time interval during the seismic event. Additionally, subsidence may be linked to ground instabilities caused by the dynamic solicitation generated by earthquakes. An example of this is the earthquake-induced softening process that can lead to ground or foundation sinking in soft soil areas (Wood et al. 1908; Seed 1990; Mendoza & Romo 1989; Li et al. 2022).

Fig. 1.1 Aerial photograph of a large sinkhole which formed in Winter Park, Florida (USA), in May 1981. (Retrieved from Hammett et al. 2001)

As regards anthropogenic subsidence, the most common and globally significant cause coincides with the extraction and the mobilisation of fluids in the subsurface (Barends et al. 1995; Ma et al. 2018). This process involves both excessive groundwater withdrawals from aquifer systems and the exploitation of underground gas and oil reservoirs. In each case, subsidence results from the progressive sediment compaction process caused by stress balance changes induced by the extraction of underground fluids.
Groundwater withdrawals usually take place from unconsolidated geological basins of alluvial, lacustrine or shallow marine deposits, which typically formed during the Quaternary period (Gambolati & Teatini 2015). In these contexts, especially in the alluvial one, the depositional architecture is defined by an intricate vertical succession of coarse-grained and fine-grained sedimentary bodies, characterised by a certain lateral variability, depending on the depositional environment. From a hydrogeological perspective, the coarse-grained gravel and sand deposits, generally characterised by high values of hydraulic conductivity (k), can be defined as aquifers. On the other hand, silty and clayey deposits exhibit a hydraulic conductivity several orders of magnitude lower than aquifers and are defined as aquitards. Typical hydraulic conductivity values for different geological mediums are reported in Table 1.1, after Domenico & Schwartz (1990).

Unconsolidated Sedimentary Materials	**Hydraulic conductivity (k) [m/s]**
Gravel	$3\times10^{-4} – 3\times10^{-2}$
Coarse sand	$9\times10^{-7} – 6\times10^{-3}$
Medium sand	$9\times10^{-7} – 5\times10^{-4}$
Fine sand	$2\times10^{-7} – 2\times10^{-4}$
Silt, loess	$1\times10^{-9} – 2\times10^{-5}$
Till	$1\times10^{-12} – 2\times10^{-6}$
Clay	$1\times10^{-11} – 4.7\times10^{-9}$
Unweathered marine clay	$8\times10^{-13} – 2\times10^{-9}$

Table 1.1 Typical hydraulic conductivity values for unconsolidated sedimentary deposits (Domenico & Schwartz 1990)

Depending on the depositional architecture, the aquifer systems can have different structures, and geometries that range between two well-defined end-members. On the one hand, unconfined aquifers, also known as phreatic aquifers, are only limited at the bottom by a low-permeability layer, and the groundwater level in natural conditions depends on atmospheric pressure. The piezometric level in unconfined aquifers coincides with the water table. On the other hand, confined aquifers are sealed at the top and the bottom by laterally continuous low-permeability deposits, and the water level measured at their top does not necessarily match their associated piezometric level. Additionally, while recharge in phreatic aquifers directly depends on water infiltration from the ground surface, confined aquifers only receive recharge from precipitation and infiltration where the water-bearing formations outcrop at the land surface (Jalota et al. 2018), as conceptually represented in Figure 1.2.

Unconfined aquifers may either constitute a single one-layer aquifer system or represent the shallowest layer of a more complex multi-layer aquifer system configuration, with underlying layers consisting of confined aquifers sealed by aquitards (Fig. 1.2). When the piezometric level associated with a confined aquifer differs from that of the underlying or overlying ones, including the shallower phreatic aquifer, upward or downward flows may generate within the separating aquitard. These vertical flows are slow due to the low hydraulic conductivity of the aquitard, and their direction follows the hydraulic gradient from the layer with a higher piezometric level to the one with a lower level. Consequently, while the groundwater flow in the aquifers is predominantly horizontal, the flow within aquitards is mainly monodimensional and vertical.

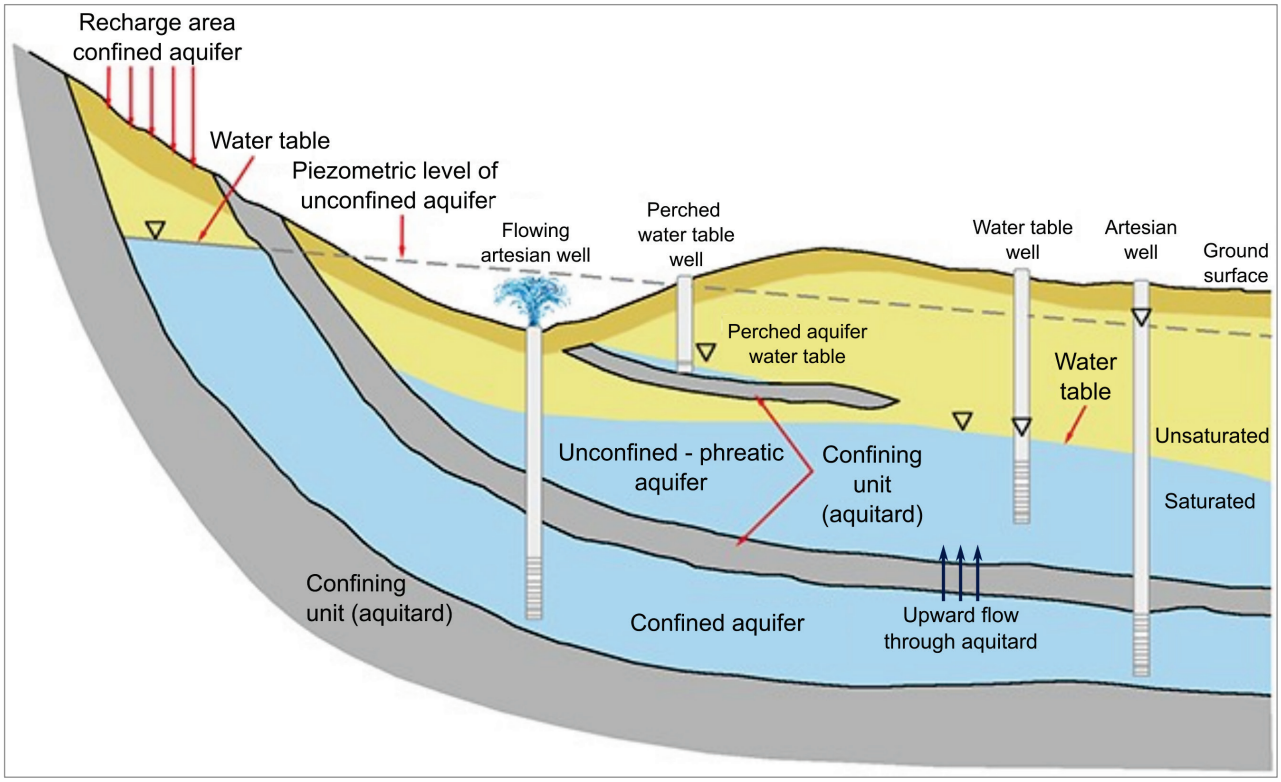

Fig. 1.2 Conceptual representation of the main elements and the different types of aquifers and wells in a multi-layer groundwater aquifer system. The blue arrows highlight the occurrence of a slow upward flow within the aquitard separating a phreatic aquifer at the top and a confined one, exhibiting a higher piezometric level. (Retrieved and modified from Wyoming State Geological Survey archive: https://www.wsgs.wyo.gov).

The introduction of a production well into a natural aquifer system, as described in Gambolati et al. (2005), induces modifications in the stress and the fluid-dynamic fields, generating a disturbance that propagates its effects in space and time through the existing geological media. This phenomenon is manifested by the

formation of a cone of depression in the water table for phreatic aquifers or in the piezometric surface if the pumping is limited to a confined aquifer (Fig. 1.3). The shape, propagation over time and the radius of influence (I_R) of the cone of depression, under identical pumping conditions, are contingent on the geometry and the structure of the aquifer system, as well as the hydromechanical properties of both the fluid and the porous medium involved (Fileccia 2015; Zhai et al. 2021). Typically, the lateral expansion of the cone of depression is sensibly larger than its vertical development (Gambolati & Teatini 2015). The ultimate size of the cone of depression and the associated groundwater level drop also depends on the mass balance between pumping rates and groundwater inflow from the aquifer system (Zhai et al. 2021).
The region within the depression cone experiences a groundwater level drawdown which translates into a pore water pressure drop, triggering the consolidation process of the existing deposits. The induced settlements involve both coarse-grained and fine-grained sedimentary bodies but with differences depending on the type of deposits and their hydromechanical properties. Generally, the deformation is primarily accommodated by the more compressible fine-grained aquitard lenses and layers interbedded with the coarse-grained ones. The overall compression of the sequence of subsurface deposits involved then translates into the subsidence of the ground surface. The mechanism at the base of this process will be separately addressed and described in the following section (1.2.2), considering a simplified monodimensional approach.

Similarly, the extraction of hydrocarbons from deep reservoirs generates a loss of pressure in the gas/oil-bearing strata, determining their progressive compaction (Severi et al. 2021). This compression propagates upward eventually causing the sinking of the ground surface (Fig. 1.3).

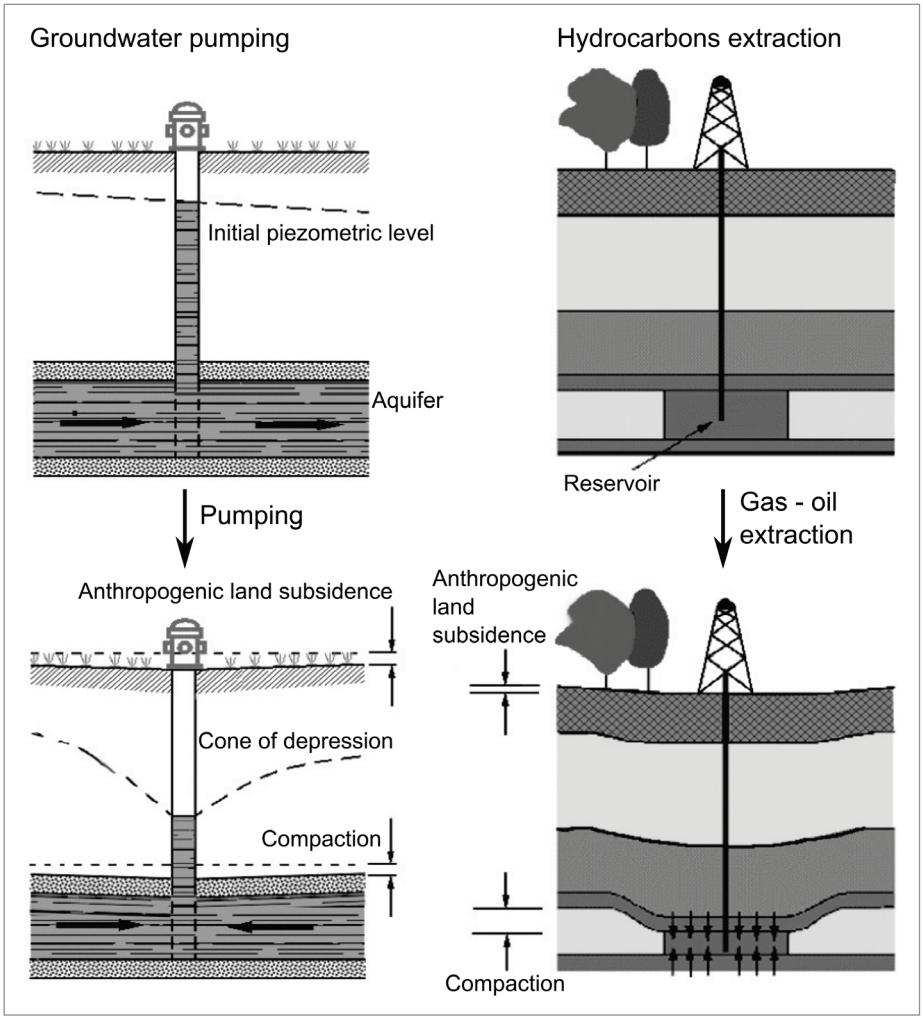

Fig. 1.3 Conceptual representation of anthropogenic subsidence mechanism due to excessive groundwater withdrawals and hydrocarbon reservoir exploitation (Gambolati et al. 2005, modified).

As highlighted in Gambolati et al. (2005), although there are overall similarities, the surface expression of subsurface deposits compression in groundwater withdrawal and hydrocarbon extraction processes can exhibit significant differences (Fig. 1.3). In the case of hydrocarbon extractions, the reservoirs are typically located at considerable depth within the basin, and when their compaction occurs, a portion of the deformation tends to be absorbed by the surrounding geological units. Consequently, the final ground surface sinking represents only a portion of the original reservoir compaction, depending on factors such as its depth, volume and mechanical properties, along with those of the surrounding deposits. Despite being less than the reservoir's actual compaction, the ground surface subsidence generally affects a larger area than the extraction field, generating a vertical bowl-shaped distribution pattern (Doornhof et al. 2006), as displayed in the bottom-right corner of Figure 1.3.
Differently, groundwater is usually withdrawn from shallower aquifer systems, and due to the extensive lateral propagation of the cone of depression, the associated ground subsidence interests sensibly larger areas compared to hydrocarbon extractions. The extent of subsiding regions typically exhibits in fact a good consistency with the distribution of groundwater depression cones (Ma et al. 2018). In these systems, the compaction and consolidation processes of the involved deposits are generally not counteracted by the surrounding sedimentary bodies, leading to a direct upward propagation of the deformation with a spreading factor of one. As a result, the displacement observed at the ground surface reflects the cumulative compression of the subsurface deposits, as illustrated in the bottom-left corner of Figure 1.3.

Moreover, groundwater extraction processes can influence and accelerate other ongoing natural subsidence mechanisms, such as ground deformation and collapse due to limestones and gypsum dissolution (Cooper 1988). As previously mentioned, the activation of a production well in an aquifer system profoundly alters the natural three-dimensional flow path, imposing steeper hydraulic gradients and encouraging the mobilisation of groundwater from distant or less affected subsurface regions. The induced flow through soluble geological units may trigger or exacerbate rock dissolution processes that would normally occur at much lower rates under natural flow conditions. This is particularly evident when well-defined and developed joints and rock mass discontinuity sets are present (Cooper 1988), as they exhibit extremely high hydraulic conductivity, facilitating the generation of rapid groundwater flows. Flow velocity, in fact, significantly influences the dissolution rate of soluble rocks such as gypsum, in addition to the chemical properties of the circulating groundwater (Rahimi et al. 2022).

Another widespread anthropogenic subsidence cause is related to underground mining. The excavation of tunnels and cavities, depending on the mining activity and the corresponding excavation technique, leads to the creation of voids in the subsurface, producing a redistribution of the stress field. The excavation and eventual collapse of these cavities, due to insufficient or aged roof support, can result in either the sudden sinking or gradual and relatively continuous deformations of the ground surface (Maaß & Schüttrumpf 2018). As stated by the authors, the onset of subsidence may vary from several weeks to decades after the beginning of mining activities. The intensity and spatial distribution of ground deformations are influenced by multiple factors such as extraction depth, excavation method, the geometry of the depleted seam and the geomechanical properties of the overlying rock mass (Guzy & Witkowski 2021). Typically the overall cumulative displacements recorded at the ground surface represent approximately 90-95% of the removed seam thickness (Szelag & Weber, 1993; Harnischmacher & Zepp, 2016; Maaß & Schüttrumpf 2018).
Ground deformations predominantly occur during the life and production cycle of a mine. However, numerous field studies have reported the occurrence of residual subsidence after mine closure, which generally accounts for approximately 6% of the overall long-term displacements (Bräuner 1973; Maaß & Schüttrumpf 2018).
Besides tunnel and cavity instability, ground subsidence can also result from other ancillary activities related to underground mining. For instance, as described in Guzy & Witkowski 2021, extensive and continuous groundwater pumping is required since the early stages of construction to prevent flooding in mining tunnels and facilitate excavation procedures. Prolonged aquifer drainage, spanning several decades throughout the

mine's life cycle, results in the extraction of substantial volumes of groundwater, often exceeding billions of m^3 (Guzy & Malinowska 2020), leading to permanent changes in the aquifer system's hydraulic properties. This sustained groundwater withdrawal can generate a depression cone of the piezometric level, triggering consolidation and compaction processes in the involved geological units. The ground surface subsidence resulting from this process, due to the extent of the depression cone, is generally much larger than the direct impact of underground mining and extends beyond the mining boundaries.
Additionally, the anthropic alteration of the natural groundwater flow path through mine drainage pumping may also trigger or accelerate rock dissolution processes, especially when mining activities involve soluble rocks such as gypsum (Whittaker & Raddish 1989).

More localised anthropogenic land subsidence can arise from the construction of buildings and structures that exert concentrated loads on the ground surface, triggering the consolidation process of the underlying deposits (Abidin et al. 2015). Similarly, the realisation of shallow underground excavations and infrastructures may lead to surface deformation, along with modifications to the natural groundwater flow (De Caro et al. 2020).

1.2.2 Terzaghi's consolidation theory

Surface ground deformation due to excessive groundwater withdrawals and aquifers overexploitation is the most widespread anthropogenic subsidence mechanism with the greatest impact on modern society. As previously described, the ground-sinking process is the expression of the cumulative deformation of the subsurface deposits, which can be described and schematised through the effective stress and one-dimensional consolidation principles formulated by Terzaghi (1925, 1943).

From a mechanical perspective, each sedimentary deposit, or more generally, a three-dimensional element of soil can be described as a porous medium, comprising a solid skeleton formed by the material's particles and grains, along with voids that can be filled by fluids (water or air). Thus, soils can be classified as multiphase media, consisting of a solid, a liquid and possibly an air fraction. When all the voids within the soil are filled with water, the soil is considered saturated.
For a fully saturated element of soil, excluding the negligible effects of electrostatic attraction and repulsion between the solid particles, the mechanical behaviour depends on the definition and the balance of three main stresses, represented by the following equation:

$$\sigma = \sigma' + u \qquad [1.1]$$

where:

- σ = total normal stress [kPa], representing the total vertical stress acting on a finite three-dimensional element of soil
- u = pore water pressure [kPa], being the pressure of the water filling the pores between the solid particles
- σ' = effective normal stress [kPa], consisting of the stress transmitted through the solid skeleton only, due to intergranular forces (Knappett & Craig 2019).

In natural conditions, a saturated element of soil is characterised by a geostatic stress field depending solely on its depth, weight (Wang et al. 2021) and the static position of the water table. Any natural or anthropogenic disturbance to this condition of equilibrium results in a redistribution of the stress field.
For instance, external forces such as the application of a load on the ground surface (e.g., constructing buildings and structures) or lowering of the water table due to excessive groundwater withdrawals can act as perturbations. When a load or surcharge pressure ($\Delta\sigma$) is applied to the ground surface, a fully saturated soil element at a certain depth experiences an increase in total normal stresses equal to the applied load ($\Delta\sigma$). Since both the pore-filling water and the solid skeleton are incompressible, and the considered soil element is laterally

confined, no grain rearrangement can occur until some water is expelled from the voids. Consequently, immediately after the load application ($\Delta\sigma$), the pore water pressure increases by the same amount, resulting in excess pore water pressure (Δu). This pore pressure increase generates a hydraulic gradient, leading to the development of seepage flow toward a free-draining boundary (Knappett & Craig 2019) of the soil element, governed by Darcy's empirical law:

$$q = v_d A = Aki \quad [1.2]$$

in which:

- q = total discharge or flow rate, representing the volume of water flowing per unit of time [m³/s]
- v_d = discharge velocity [m/s]
- A = cross-sectional area of soil interested by the flow [m²]
- k is the permeability coefficient or hydraulic conductivity of the soil [m/s]
- i is the hydraulic gradient.

Hydraulic conductivity strongly depends on the average pore size, which reflects the size distribution and shape of soil particles, as well as the soil structure (Knappett & Craig 2019). This parameter can vary significantly between coarse and fine-grained deposits, exhibiting differences spanning several orders of magnitude (see Table 1.1).
The seepage process occurs at different rates depending on the coefficient of permeability of the soil and continues until the hydraulic gradient responsible for the flow is zero, and the excess pore water pressure (Δu) is completely dissipated. Throughout this process, which transitions the soil element from *undrained* to equilibrium *drained* conditions, the soil is always at full saturation. As Δu gradually dissipates and decreases, the effective stress (σ') increases by the same amount, in accordance with equation [1.1]. This process is reflected by the rearrangement of the soil's particles with a reduction in the void ratio (e) and volume, leading to the progressive settlement of the soil element's surface, and is referred to as consolidation.
Similarly, the drawdown of the water table produces a reduction in pore water pressure and an increase in the effective stress, triggering the consolidation process of the involved soil element.

The total settlement (s_t) measured on the considered element of soil results from the sum of three different components:

$$s_t = s_i + s_c + s_s \quad [1.3]$$

where:

- s_i = immediate settlement (elastic) that manifests immediately after the load application in undrained conditions
- s_c = consolidation settlement (time-dependent) that progressively occurs as the applied load transfers to the solid skeleton and the pore pressure excess dissipates, while the water is expelled from the pores
- s_s = secondary settlement (time-dependent) that occurs in the long-term, after the excess pore pressure and consolidation processes are complete, and involves further viscous deformation of the soil's solid skeleton under the action of constant effective stress.

This is true for fine-grained soils which are typically characterised by low hydraulic conductivity values and can experience prolonged excess pore pressure dissipation processes, spanning months to decades.
In contrast, coarse-grained soils and deposits, due to their sensibly higher hydraulic conductivity, exhibit instantaneous dissipation of pore water pressure and are considered to be always in drained conditions. In such cases, the total settlement results from an immediate (elastoplastic) settlement due to the rearrangement of the soil's particles triggered by the increased effective stress, along with a minor secondary settlement due to long-term viscous processes.

The time-dependent consolidation process, which greatly accounts for the settlement of fine-grained soils, can be visualised through the oedometric laboratory test. This test involves measuring the monodimensional vertical displacement over time of a soil specimen of known geometry, within an oedometric cell (Fig. 1.4) as the consolidation process occurs following the controlled application of a load. The soil deformation is exclusively vertical due to the lateral confinement imposed by the metallic ring containing the soil sample (zero lateral strain condition).

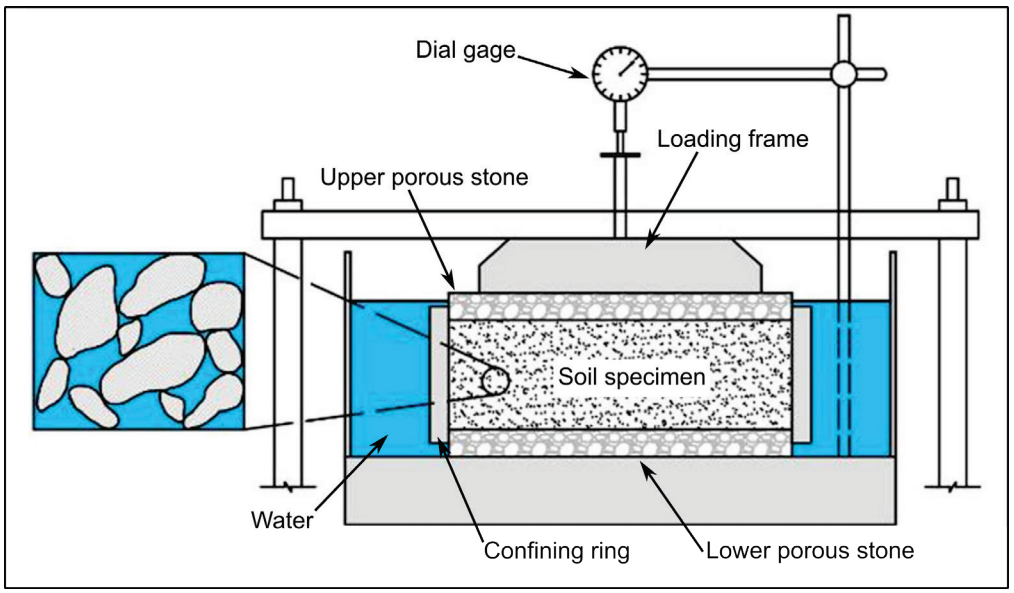

Fig. 1.4 Schematic representation of an oedometric cell and test arrangement (Giomi & Francisca 2022, modified)

After the application of a load, the vertical displacement is continuously recorded for the subsequent 24 hours, as the pore water is expelled through a flow through the porous stones and the Δu progressively dissipates while the consolidation occurs. At the end of this process, the soil sample reaches equilibrium with the new load, and the applied total stress equals the effective stress in the specimen (Knappett & Craig 2019). The recorded displacement can be plotted against time as displayed in Figure 1.5.

At the end, and during each loading step the vertical deformation (ε_z) of the specimen can be calculated and the evolution of its void ratio (e) can be determined through the following equations:

$$\varepsilon_z = \frac{\Delta H}{H_0} \qquad [1.4]$$

and

$$e = e_0 - (1 + e_0)\varepsilon_z \qquad [1.5]$$

where:

- ΔH = change in thickness during the test [mm]
- H_0 = initial specimen thickness before load application [mm]
- e_0 = initial void ratio of the specimen before load application

Knowing the void ratio before, during, and at the end of the consolidation process it is possible to calculate the degree of consolidation (U_v), labelled as U in Figure 1.5, and defined as:

$$U_v = \frac{e_0 - e_t}{e_0 - e_1} \qquad [1.6]$$

where:

- e_t = void ratio at a certain time t during the consolidation process
- e_1 = void ratio of the specimen at the end of the consolidation process ($t = t_{100}$)

U_v is null before the beginning of the load step, reaches a value of 1 at the end of the consolidation phase, and assumes a value in between as the excess pore water pressure gradually dissipates.

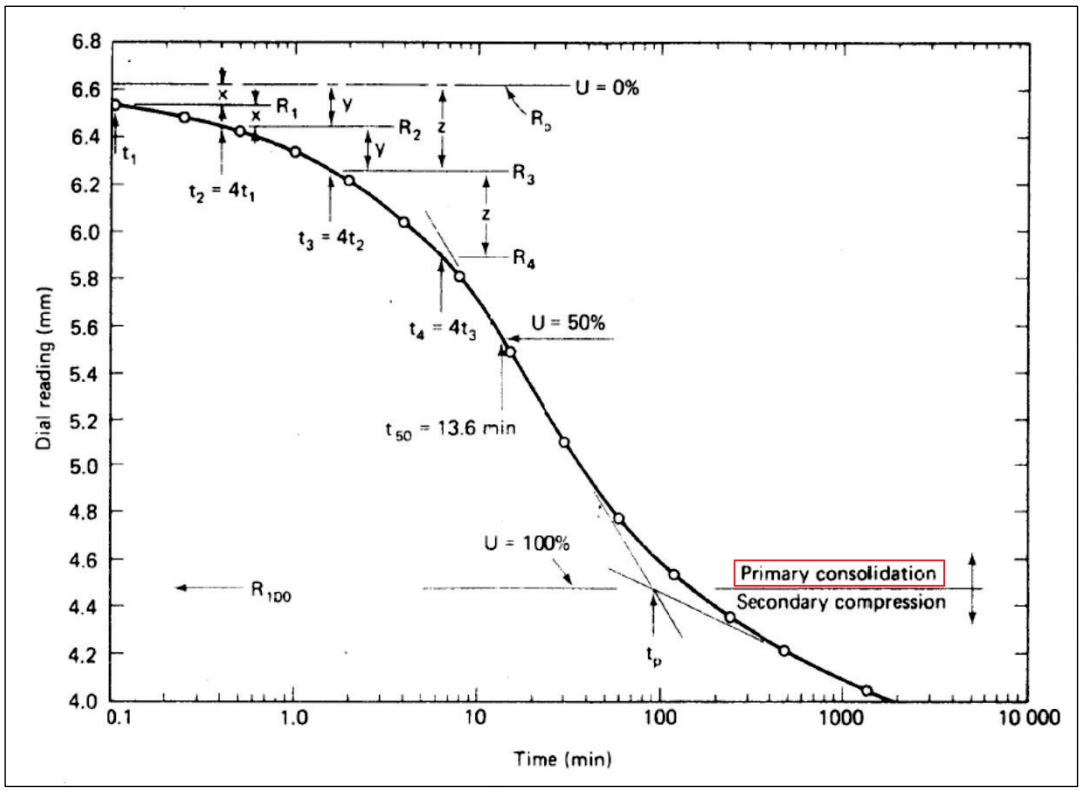

Fig. 1.5 Primary and secondary (viscous) consolidation phases measured during an oedometric test load step lasting 24 hours. The time at which the consolidation process terminates and the secondary settlement begins is labelled as t_p. This time is graphically determined by the intersection of the tangents to the preceding and following segments of the consolidation curve (Holtz & Kovacs 1981).

Conducting multiple consecutive load steps enables the assessment of the vertical deformation and the void ratio evolution of the specimen at different stress states. Particularly significant is the representation of the void ratio against the logarithm of the effective stress, known as oedometric curve (Fig. 1.6).

The relationship between void ratio and effective stress for a specific soil element at a depth z below the ground level is summarised in the oedometric curve, reflecting its stress and geological history. If the current effective stress is the highest the soil specimen has ever experienced, it can be classified as normally consolidated (NC). Conversely, if the effective stress at some time in the past had been greater than the present value (Knappett & Craig 2019), the soil is categorised as overconsolidated (OC). Overconsolidation could result from either a past greater overburden or surcharge load that has been eroded or removed over time after the soil reached equilibrium, or from a past prolonged drawdown of the water table, followed by a subsequent rise after the completion of the consolidation process of the underlying layers. The maximum vertical effective stress that the soil has ever experienced is known as preconsolidation stress (σ'_p). The ratio between preconsolidation pressure (σ'_p) and the current in situ effective vertical stress (σ'_{v0}), measured at the depth at which the soil sample was taken gives the overconsolidation ratio (OCR):

$$OCR = \frac{\sigma'_p}{\sigma'_{v0}} \qquad [1.7]$$

OCR is equal to one for normally consolidated soils, while exceeds the unity for overconsolidated deposits.

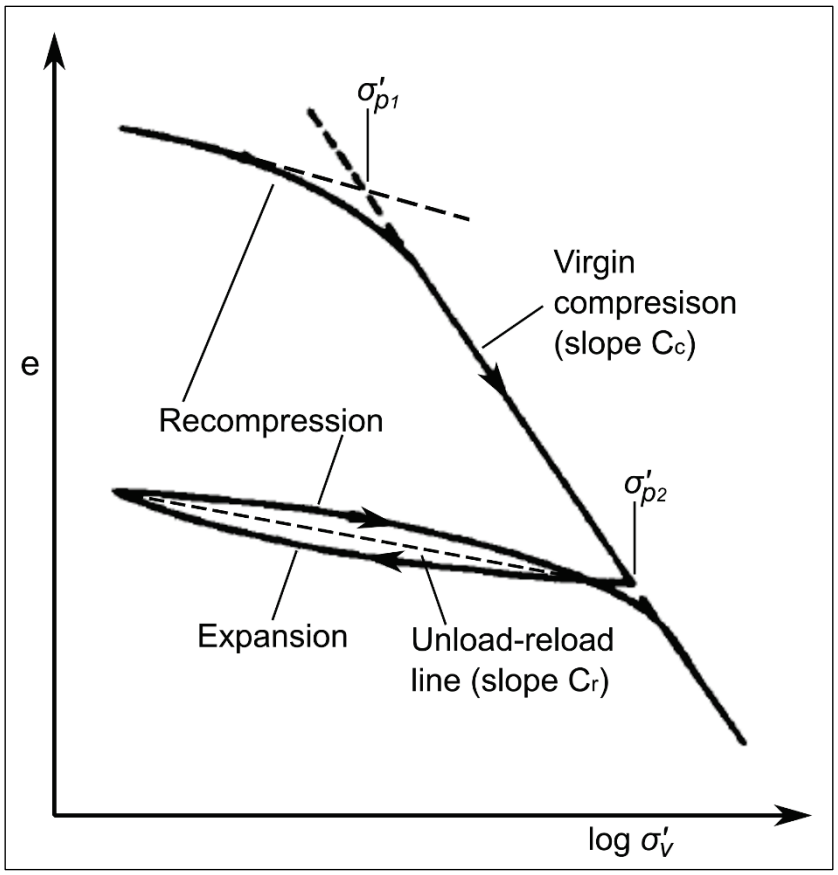

Fig. 1.6 Oedometric curve, depicting the relationship between void ratio and vertical effective stress for a soil specimen sampled at a certain depth (Craig 1974, modified).

For NC soils, the relationship between void ratio and the logarithm of the effective stress (*e-logσ'_v*) can be considered linear and is referred to as *virgin (one-dimensional) compression line* (Knappett & Craig 2019), as displayed in Figure 1.6. In contrast, for overconsolidated soils, the *e-logσ'_v* relationship is non-linear and corresponds to the recompression or recompression-expansion portions of the oedometric curve (Fig. 1.6). In these segments, compression is mostly recoverable as long as the effective stress remains below the preconsolidation pressure. However, once σ'_p is exceeded, the soil undergoes an abrupt mechanical behaviour change and transitions to an elastoplastic regime, following the virgin compression line (Lancellotta 1987). Along this line compression results in permanent deformations associated with the rearrangement of the solid skeleton particles during consolidation. When the vertical effective stress decreases, the soil that was previously in equilibrium with a higher stress state becomes overconsolidated and re-enters the non-linear elastic regime. During the expansion phase, only the elastic deformations are fully recoverable, representing a small fraction of the total deformation (Fig. 1.6). With a subsequent increment in the effective stress the soil deforms elastically, erasing the void ratio increase from the expansion phase, until it rejoins the virgin compression line again (Fig. 1.6).

As illustrated in Figure 1.6, soils in the overconsolidated state would be much less compressible than that in a normally consolidated state (Craig 1974). The compressibility of soils can be expressed and quantified using different coefficients derived from experimental oedometric curves. For NC soils, the compression index C_c represents the slope of the virgin compression line of the curve:

$$C_c = \frac{\Delta e}{\Delta log\sigma'_v} \qquad [1.8]$$

On the other hand, for OC soils, the recompression or expansion index C_r is obtained from the slope of the unload-reload line. Typically the range of C_r is approximately from one-tenth to one-fifth of C_c (Das 1983).

Alternatively, the soil compressibility can be described using the *coefficient of volume compressibility* (m_v), which represents the ratio of volumetric strain to applied stress (Knappett & Craig 2019):

$$m_v = \frac{1}{1 + e_0}\left(\frac{\Delta e}{\Delta \sigma'_v}\right) \quad [1.9]$$

or:

$$m_v = \frac{1}{H_0}\left(\frac{\Delta H}{\Delta \sigma'_v}\right) \quad [1.10]$$

where the volume change, occurring solely in the vertical direction, is expressed by the decrease in the void ratio [1.9] or in the soil sample's thickness [1.10]. Being defined as the ratio between deformation and stress the units of m_v are [kPa^{-1}].

Another parameter used to define soil compressibility is the *constrained modulus* (E_m), also referred to as *oedometric modulus* or *one-dimensional elastic modulus* (Knappett & Craig 2019), and corresponds to the reciprocal of m_v:

$$E_m = \frac{1}{m_v} = H_0\left(\frac{\Delta \sigma'_v}{\Delta H}\right) \quad [1.11]$$

Being defined as the ratio between applied stress and resulting deformation the units of E_m are [kPa].

Considering a natural aquifer system constituted by the vertical alternation of coarse-grained (aquifers) and fine-grained (aquitards) deposits, as depicted in Figure 1.7, the anthropogenic lowering of the water table leads to a stress field redistribution, resulting in an increase in effective stress. This, in turn, induces primarily vertical deformations that mainly affect the existing aquitards.

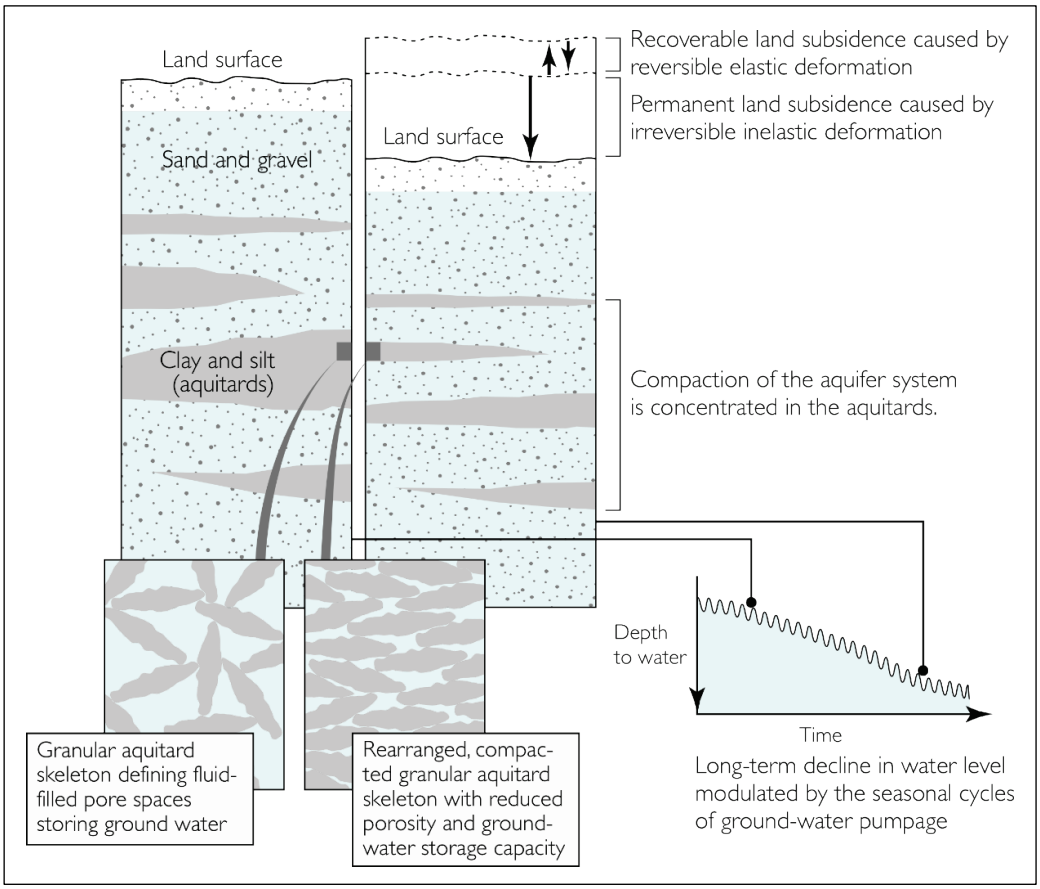

Fig. 1.7 Recoverable and irreversible ground subsidence in an aquifer system caused by seasonal and long-term excessive groundwater pumping, respectively (Galloway et al. 1999).

As described in Galloway et al. (1999), seasonal groundwater fluctuations, governed by the balance between anthropogenic pumping during the summer and the recharge during normally wetter winter months, mainly induce elastic recoverable deformations. These deformations involve the compression and the expansion of the solid skeleton as the pore pressure fluctuates during relatively small discharge and recharge cycles of the aquifer system. However, when a significant long-term lowering of the water table induces an effective stress increase exceeding the preconsolidation pressure, significant inelastic deformations occur in the aquitards that enter a normally consolidated state, exhibiting much higher compressibility. Moreover, especially in multilayer aquifer systems affected by large-scale pumping, the volume of water derived from the irreversible consolidation of the aquitards is practically equivalent to the volume of subsidence and ranges from 10-30% of the total volume of groundwater withdrawn. This, in particular, represents a one-time mining resource, as the overdraft induces a small permanent reduction in the storage capacity of the aquifer system.

Mathematical formulation of Terzaghi's theory of one-dimensional consolidation

The present section presents the mathematical formulation of Terzaghi's one-dimensional consolidation theory (1925; 1943) as described in Craig (1974) and Knappett & Craig (2019).

Terzaghi's theory relies firstly on the following fundamental assumptions:

1. The soil is homogeneous and isotropic
2. The soil is fully saturated
3. The solid particles and the pore fluid (water) are incompressible
4. Compression and flow are monodimensional and occur in the vertical direction
5. The applied loads produce only small strains in the soil (small strain conditions, Holtz & Kovacs 1981)
6. Darcy's law governs the pore water drainage process and is valid at all hydraulic gradients
7. The coefficient of permeability (k), or hydraulic conductivity, and the coefficient of volume compressibility (m_v) remain constant throughout the consolidation process
8. There is a unique relationship, independent of time, between void ratio (e) and effective stress (σ').

These assumptions, however, have a few limitations:

- Darcy's law may not be valid at low gradients (point 6)
- As the material consolidates and permanently reduces its void index, k also decreases (point 7)
- m_v decreases as well during the consolidation process as the relationship between e and σ' is non-linear. The assumption can however be reasonable for small stress increments (point 7)
- The e-σ' relationship, in reality, is not unique and independent of time (point 8). This assumption excludes secondary settlements in which e decreases at constant σ' (Holtz & Kovacs 1981).

Terzaghi's theory involves three main quantities:

- The excess of pore water pressure (u_e, previously indicated as Δu)
- The depth (z) below the top of the considered soil layer
- The time (t) measured from the instantaneous application of the total stress increment, responsible for the consolidation process.

Initially, an element of dimensions dx, dy, and dz within a compressible layer of soil of thickness $2d$ is considered, as displayed in Figure 1.8.

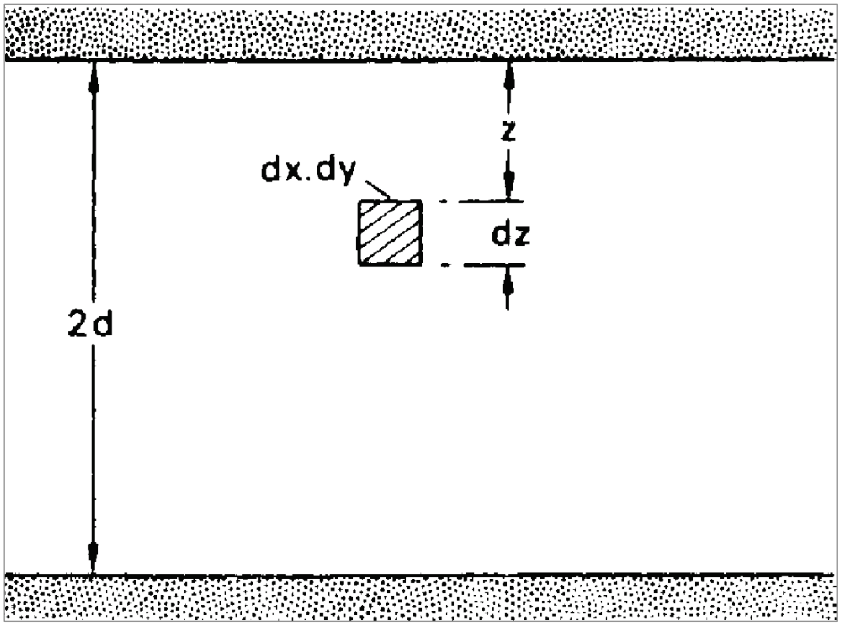

Fig. 1.8 Considered soil element of dimensions *dx*, *dy*, and *dz* within a compressible layer of thickness *2d* (Craig 1974).

When an increment of total vertical stress ($\Delta\sigma$) is instantaneously applied to the element, the associated vertical drainage pore water flow is governed by Darcy's law [1.2] that can be rewritten in the following general form:

$$v_z = ki_z = -k\frac{\partial h}{\partial z} \qquad [1.12]$$

The subscript *z* indicates that the flow associated with the change in total head (h) is vertical. Considering that for any fixed position *z* any variation in *h* can solely be ascribed to a change in pore water pressure, and that:

$$h = \frac{u}{\gamma_w} \qquad [1.13]$$

one can write:

$$v_z = -\frac{k}{\gamma_w}\frac{\partial u_e}{\partial z} \qquad [1.14]$$

where γ_w represents the unit weight of water equal to 9.81 kN/m³.

The condition of continuity in case of incompressible fluid (water) and volume (V) changes over time in the considered soil element can be written as:

$$\left(\frac{\partial v_z}{\partial z}\right)dxdydz = \frac{dV}{dt} \qquad [1.15]$$

that based on [1.14] can be formulated as:

$$-\frac{k}{\gamma_w}\frac{\partial^2 u_e}{\partial z^2}dxdydz = = \frac{dV}{dt} \qquad [1.16]$$

The rate of volume change can be expressed in terms of m_v:

$$\frac{dV}{dt} = m_v\frac{\partial \sigma'}{\partial t}dxdydz \qquad [1.17]$$

As $\Delta\sigma$ is gradually transferred to the soil particles, σ' increases and u_e decreases, the rate of volume change could be written as:

$$\frac{dV}{dt} = -m_v \frac{\partial u_e}{\partial t} dxdydz \qquad [1.18]$$

Lastly, by combining equations [1.16] and [1.18], the differential equation of monodimensional consolidation is obtained:

$$m_v \frac{\partial u_e}{\partial t} = \frac{k}{\gamma_w} \frac{\partial^2 u_e}{\partial z^2} \qquad [1.19]$$

or alternatively:

$$\frac{\partial u_e}{\partial t} = c_v \frac{\partial^2 u_e}{\partial z^2} \qquad [1.20]$$

where c_v represents the *coefficient of consolidation* defined as:

$$c_v = \frac{k}{m_v \gamma_w} \qquad [1.21]$$

c_v units are [m²/s], and, since k and m_v are assumed to be constant, it is considered constant as well.

The obtained differential equation [1.20] describes the evolution of the excess pore water pressure (u_e) as a function of depth (z) and time (t). This equation can be solved through either analytical or numerical methods through the application of appropriate initial and boundary conditions.

Analytical solution

As the load increment application is assumed to be instantaneous, at zero time ($t = 0$), $\Delta\sigma$ will be entirely carried by the water pressure. Therefore the initial value of excess pore water pressure (u_i) is equal to $\Delta\sigma$ and the initial condition can be written as: $u_e = u_i = \Delta\sigma$ for each depth within the considered layer ($0 \leq z \leq 2d$). The upper and lower boundaries of the layer displayed in Figure 1.8, are considered to be *free-draining* and represent a sharp transition with deposits characterised by sensibly higher k values. In this scenario, the longest drainage path length is equal to d for a considered layer thickness of $2d$. This boundary condition at any time after the application of $\Delta\sigma$ can be written as: $u_e = 0$ (for $z = 0$) and $z = 2d$ (when $t > 0$).
The solution for the excess pore water pressure (u_e) at depth (z) and after time (t) assumes the form of a Taylor sine series (Taylor 1948) that in the specific case of u_i constant throughout the considered layer, can be expressed as:

$$u_e(z,t) = \sum_{m=0}^{m=\infty} \frac{2u_i}{M} \left(sin \frac{Mz}{d} \right) exp(-M^2 T_v) \qquad [1.22]$$

where:

$$M = \frac{\pi}{2}(2m+1) \qquad [1.23]$$

and T_v is a dimensionless number, referred to as *time factor*, defined as:

$$T_v = \frac{c_v t}{d^2} \qquad [1.24]$$

The solution and hence the progress of the consolidation process can be visualised by plotting a series of curves depicting the variation of u_e with depth at different time periods (t) following the load application. These curves are known as *isochrones*, and their shape and evolution over time are controlled by the specified initial and

boundary conditions. For instance, the considered scenario, where both the lower and upper boundaries of the layer are free draining (*open layer*) and the value of u_i is constant with depth, resembles the conditions of a specimen during a traditional oedometric test (Lancellotta 1979), as shown in Figure 1.9a. Figure 1.9b illustrates that soon after the load application, u_e rapidly dissipates in the regions closer to the draining boundaries, while it takes much longer to have the same effect in the middle of the layer where the drainage path is maximum (d). Furthermore, the slope of the isochrones at any depth represents the hydraulic gradient and indicates the flow direction. It can be noted that as the hydraulic gradient is always null at the midpoint of the layer, this portion could be considered impermeable and the problem could be also split considering only half layer of thickness d with only one draining boundary (*half-closed layer*), as displayed in Figure 1.9c.

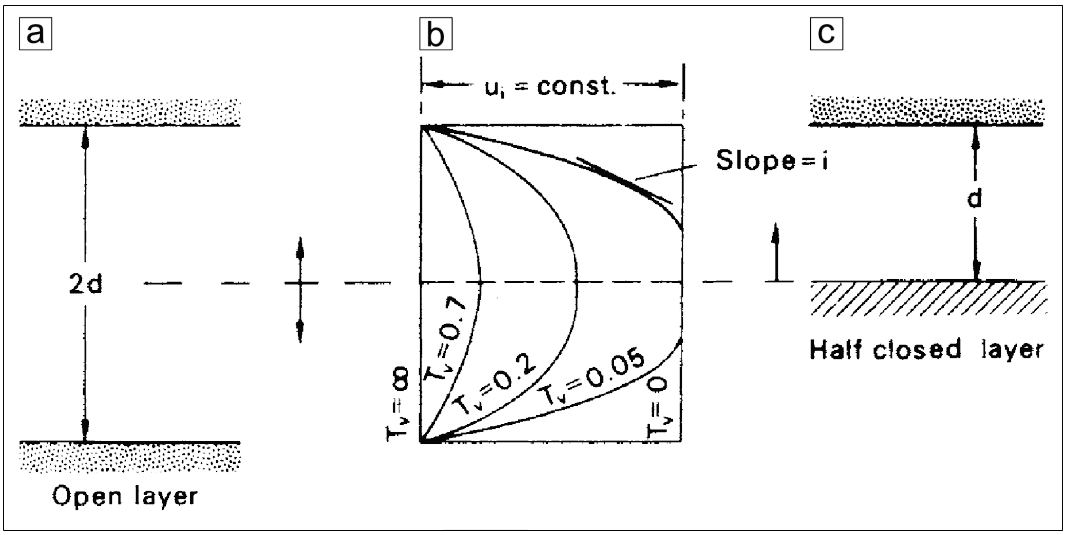

Fig. 1.9 (a) Considered open layer of thickness $2d$ bounded by draining surfaces; (b) isochrone evolution with time starting from the initial condition u_i constant with depth; (c) Half-closed layer of thickness d representing the upper portion of the original deposit (Craig 1974, modified).

As reported in Lancellotta (1979), the considerations made so far regard the progressive dissipation of u_e, but they can also be extended to evaluate the settlement process evolution. Under this perspective, the average degree of consolidation (U_m) could be defined as the ratio between the settlements recorded after time t and at the end of consolidation, indicated respectively as $S(t)$ and S_C:

$$U_m = \frac{S(t)}{S_C} \qquad [1.25]$$

Considering that the degree of consolidation U_v previously defined through equation [1.6] can be expressed also as:

$$U_v = \frac{u_i - u_e}{u_i} = 1 - \frac{u_e}{u_i} \qquad [1.26]$$

U_m could be written in the following form:

$$U_m = 1 - \frac{\left(\frac{1}{2d}\right)\int_0^{2d} u_e dz}{u_i} = 1 - \sum_{m=0}^{m=\infty} \frac{2}{M^2}\exp(M^2 T_v) \qquad [1.27]$$

This equation enables the determination of the average degree of consolidation at any time t during consolidation.

However, when u_i is not constant and the initial isochrone assumes a different, non-symmetrical shape and the average degree of consolidation can be expressed through a more general form:

$$U_m = 1 - \frac{\int_0^{2d} u_e dz}{\int_0^{2d} u_i dz} \qquad [1.28]$$

The solution of the consolidation equation depends on the initial and boundary conditions and is represented by the different curves reported in Figure 1.10 developed by Janbu et al. (1956):

- Curve 1 is always valid as long as the considered layer is not half-closed and the initial isochrone is asymmetrical
- Curve 2 represents virgin consolidation
- Curve 3 approximately represents the field conditions where a surcharge load is applied on the ground surface or when the piezometric level is significantly lowered in the case of anthropogenic subsidence.

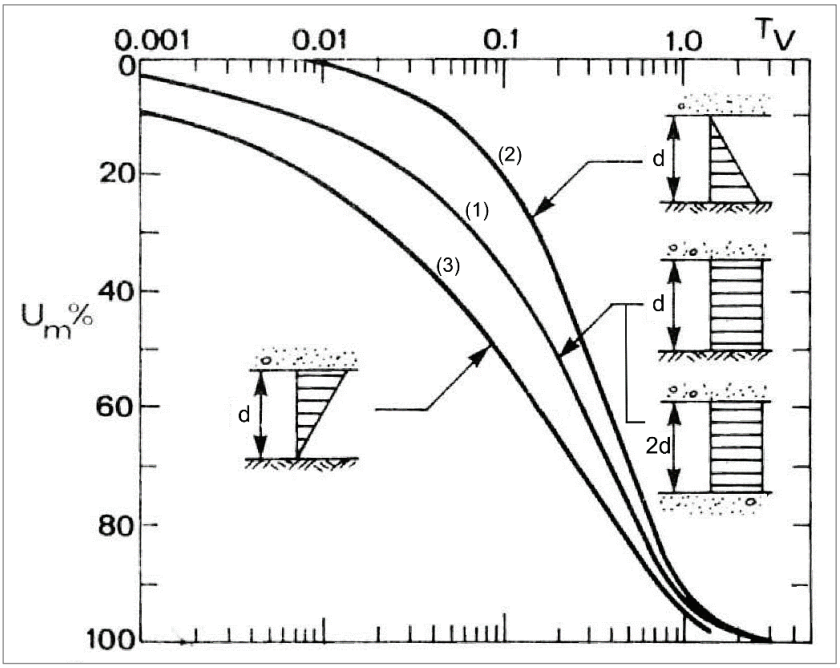

Fig. 1.10 Solutions of the consolidation equation for different initial and boundary conditions after Janbu et al. 1956 (Lancellotta 1979, modified).

In order to solve the consolidation equation through the illustrated solutions, the coefficient of consolidation (c_v) needs to be determined for a stress interval representative of the case study. This can be accomplished through an oedometric test, analysing for example the consolidation curve under the desired stress field (Fig. 1.5), as suggested in Casagrande (1936). This method involves comparing the time required to obtain a deformation of the soil specimen equal to 50% of the total consolidation settlement (Fig. 1.5) with the corresponding theoretical value of T_v when U_m is 0.5 (Fig. 1.10). Based on curve 1 of Figure 1.10 and equation [1.27], the value of T_v when $U_m = 0.5$ is 0.196, for the considered scenario. Therefore the value of c_v needed to solve the consolidation equation is given by:

$$c_v = \frac{0.196 d^2}{t_{50}} \qquad [1.29]$$

Numerical solution

The parabolic partial differential equation [1.20], which describes the consolidation process, can be effectively solved numerically through the application of the finite differences method. Unlike analytical solutions which rely on specific assumptions, numerical modelling enables considering more complex and representative scenarios of the *in situ* conditions. For instance, this approach allows adopting any initial distribution pattern (isochrone) of excess pore pressure, accounting for heterogeneous geological media with varying mechanical properties during consolidation, or investigating cases where the load is applied gradually and not exclusively instantaneously.

In numerical modelling the first step involves defining the calculation grid and establishing appropriate initial and boundary conditions. Since the Terzaghi's consolidation equation is monodimensional, the second dimension of the modelling grid can be utilised to calculate the evolution of the pore water pressure with time, as displayed in Figure.1.11.

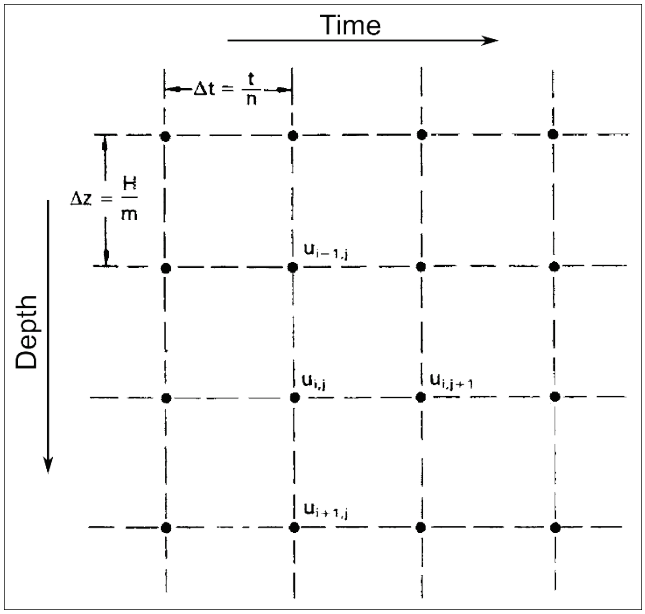

Fig. 1.11 One-dimensional depth (*z*) – time (*t*) finite difference grid (Craig 1974, modified)

Following Taylor's series expansion method, the approximation at the finite differences of the two members of the consolidation equation [1.20] can be written as:

$$\frac{\partial u}{\partial t} = \frac{1}{\Delta t}\left(u_{i,j+1} - u_{i,j}\right) \qquad [1.30]$$

and:

$$\frac{\partial^2 u}{\partial z^2} = \frac{1}{(\Delta z)^2}\left(u_{i-1,j} + u_{i+1,j} - 2u_{i,j}\right) \qquad [1.31]$$

where: u represents the excess pore water pressure, previously denoted as u_e or Δu.

By substituting [1.30] and [1.31] into [1.20], the finite difference s approximation of Terzaghi's one-dimensional consolidation equation is obtained:

$$u_{i,j+1} = u_{i,j} + \beta\left(u_{i-1,j} + u_{i+1,j} - 2u_{i,j}\right) \qquad [1.32]$$

where the operator β is:

$$\beta = \frac{c_v \Delta t}{(\Delta z)^2} \qquad [1.33]$$

This equation enables the evaluation of the excess pore pressure in point *i* at time *j+1*, based on the values relative to the previous instant *j* measured in the same point and in the adjacent *i-1* and *i+1*. This method can be referred to as *explicit scheme*, and its convergence is ensured as long as β is lower than 0.5. Therefore, special attention should be given to discretising the modelling grid in *m* depth intervals (Δz) and *n* time steps (Δt) to ensure stability, as:

$$T_v = \frac{c_v(n\Delta t)}{\left(\frac{1}{2}m\Delta z\right)^2} = 4\frac{n}{m^2}\beta \qquad \text{(for } \textit{open} \text{ layers)} \qquad [1.34]$$

or:

$$T_v = \frac{c_v(n\Delta t)}{(m\Delta z)^2} = \frac{n}{m^2}\beta \qquad \text{(for } \textit{half-closed} \text{ layers)} \qquad [1.35]$$

Furthermore, discretisation errors that may derive by neglecting higher-order derivatives in Taylor's series expansion theorem are typically minimised when the operator β is equal to 1/6 (Scott 1963).

1.2.3 Subsidence monitoring techniques

As discussed in the previous sections, the land subsidence process can arise from several natural and anthropic mechanisms, operating at various spatial and temporal scales, each with distinct effects and distribution patterns on the ground surface. Ground deformations are predominantly vertical and necessitate continuous monitoring to thoroughly comprehend the ongoing subsidence process extent and evolution with respect to its triggering mechanisms and the local geological setting. Reliable and extensive monitoring data are fundamental to train and calibrate stochastic and numerical models to predict future subsidence evolution and potential impacts on society. Over the decades, several types of monitoring equipment, sensors and techniques have been developed and implemented worldwide to investigate subsidence phenomena. Depending on the type of instrumentation, monitoring can target two interconnected primary aspects of subsidence (Gambolati & Teatini 2015). The first regards the deformation due to the compaction and consolidation processes that interest, for instance, the single overexploited aquifers and interbedded aquitards within an aquifer system. On the other hand, different ground-based or remotely sensed techniques may be employed to analyse ground surface sinking, representing the cumulative deformation of the subsurface deposits.

1.2.3.1 Deformation monitoring

The deformation of subsurface deposits, for example within exploited aquifer systems, can be continuously monitored by employing borehole extensometers. These instruments measure vertical variations in the distance between the ground surface and a subsurface reference benchmark placed at the bottom or at a certain depth within a deep borehole. Depending on the geological setting and the configuration of the aquifer system, the subsurface benchmark, when fixed in the bedrock or below the compacting layers, can serve as a stable reference for local geodetic surveys (Gambolati & Teatini 2021).

Borehole extensometers have been in use since the early 1930s (Wang et al. 2014), and over the decades, various equipment and designs have been developed and employed (Poland et al. 1984). A typical extensometer setup consists of a counterweighted balance beam carrying a steel cable or pipe, tensioned and fastened to an anchor weight fixed at the bottom of the aquifer system (Gambolati et al. 2005), as shown in Figure 1.11a. When subsidence occurs, the cable would lose tension if it were not for the counterweight applied to the beam on the surface, causing it to move downward. This movement or the corresponding reading on a potentiometer linked to a pulley system is appropriately converted to represent the vertical compaction of the involved deposits. These measurements are continuously executed and stored in a data logger.

Other systems, as reported in (Gambolati & Teatini 2015), involve wider boreholes in which a steel casing with slip-joints is inserted to prevent crumpling as subsidence occurs, enabling investigation at greater depths. A steel bar is fixed to the bedrock through a concrete plug and linked to a chart recorder at the ground surface (Figure 1.12b). The accuracy of these systems can be significantly influenced by installation and *in situ* conditions, but a nominal sub-millimetre resolution approximately spanning 0.01-0.1 mm can be obtained over a depth range of 200-1000 m (Riley 1986).

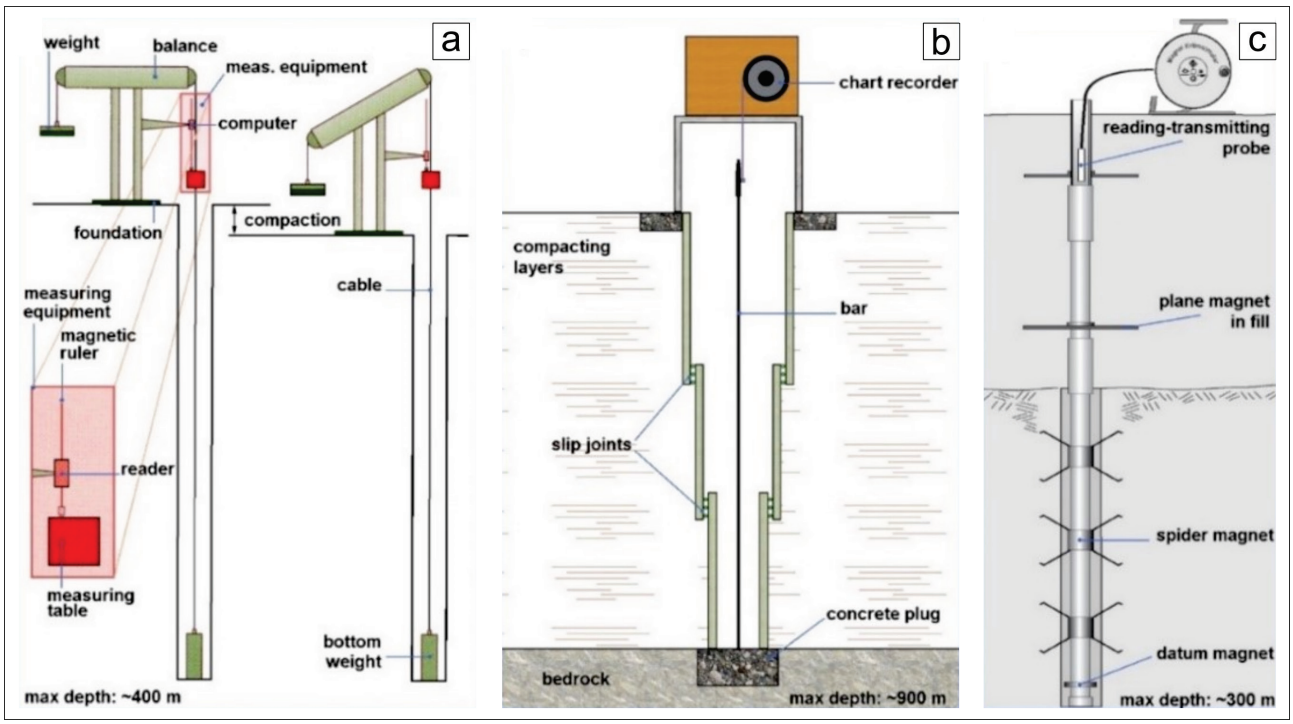

Fig. 1.12 Schematic representation of single-layer cable (a), slip-joint casing (b) and multi-layer magnetic (c) borehole extensometers (Gambolati & Teatini 2015, modified).

The described configurations offer precise punctual measurements of the vertical cumulative deformation of the entire aquifer system. To differentiate the contribution of each deposit to the overall settlement within multi-layer systems, a series of closely spaced extensometers can be installed at different depths to measure the compaction of each unit. Alternatively, multiple-position borehole extensometers may be employed (Fig. 1.12c). These systems rely on repeated measurement over time of the distance between marker positions employing a magnetic sensor. The accuracy of these measurements, which involve tens of sensors along the borehole, is approximately 1-2 mm over several hundred meters.

Frequently borehole extensometers are combined with piezometers measuring the hydraulic head in the same units. This approach allows for investigating the vertical strain of the deposits in relation to the corresponding pore pressure values, providing an *in situ* estimate of soil compressibility and the vertical hydraulic conductivity of aquitards based on the time-response characteristics of the system (Gambolati & Teatini 2015). Borehole extensometers offer the advantage of yielding extremely accurate deformation measurements and the capability to filter out subsidence contributions from other mechanisms acting at scales larger than the aquifer system in which they are installed, such as regional tectonics. Nonetheless, these monitoring instruments have a few limitations, mainly related to their high cost and the fact that they only represent point measurements (Burbey 2020).

1.2.3.2 Ground surface displacement monitoring

Ground surface displacements can be measured and monitored through various ground-based or remotely sensed geodetic techniques. Among ground-based methods, differential topographic levelling also referred to as geometric or spirit levelling, has been widely used since its introduction in the 19th Century. This technique relies on measuring height differences with the help of a precisely levelled telescope and a pair of graduated vertical rods, enabling the transfer of elevation data from a known reference point to other geodetic marks, known as *levelling benchmarks* (Gambolati et al. 2005), as displayed in Figure 1.13. The elevation difference between the two benchmarks results from the cumulative height differences measured at a series of temporary turning points obtained by moving the rods at fixed distances between them. Typically, benchmarks are evenly spaced along monitoring levelling lines at distances of about 1 km, while intermediate turning points are placed at fixed intervals ranging from 20 to 100 m, depending on the equipment used and the morphological characteristics of the surveyed area.

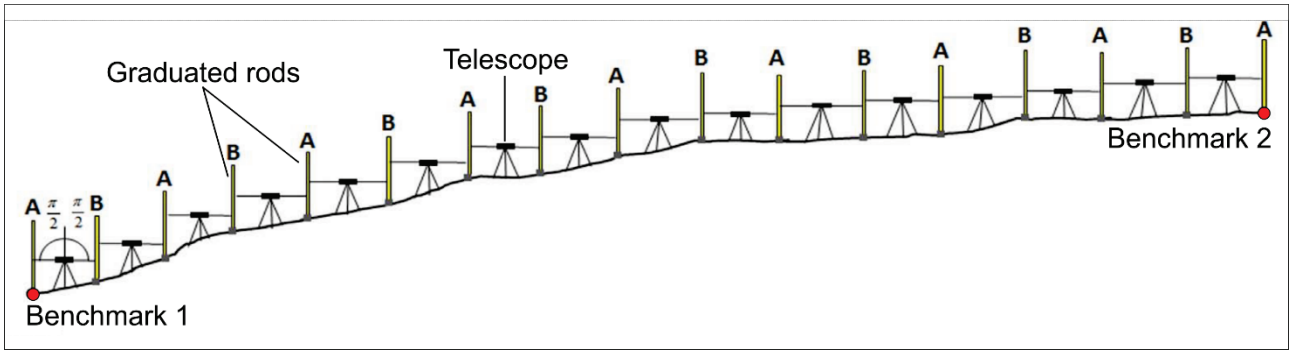

Fig. 1.13 Operating scheme for the differential topographic levelling technique for measuring the height difference between two benchmarks (Bitelli et al. 2018, modified).

Measurements are conducted along the same levelling ling line twice, reasonably close in time, with a *forward* and a *backward* run. The discrepancies in elevation measured in both directions determine the survey's accuracy. For instance, in first-order levelling networks, as described in Bitelli et al. (2018), the height difference between the forward and backward measurements in a section between two consecutive benchmarks of known length S must fall within a tolerance of $\pm 2\sqrt{S[km]}$ [mm], equivalent to three times the standard deviation. Typically, these high-precision systems yield sub-millimetre height accuracies over benchmark distances of approximately 1 km (Vanicek & Krakiwsky 1982). On the other hand, for second-order and third-order networks, the tolerance thresholds are generally set to $\pm 3\sqrt{S[km]}$ [mm] and $\pm 5\sqrt{S[km]}$ [mm], respectively.

A subsequent survey, performed after a certain time interval using the same methods on the same levelling lines, reveals the eventual vertical displacements of the benchmarks. To ensure reliable and long-term time series, levelling benchmarks, consisting of a brass cup or headed bolted, are typically secured and embedded into stable structures, buildings, or bedrock outcrops. Alternatively, they can be fixed at the top 5 to 10-meter-long bars driven into the ground and protected by a sleeve (Gambolati & Teatini 2021).

Levelling networks are established by defining a series of stable reference points outside the subsiding area, whose elevation is assumed to remain constant over time. As this technique provides geoidal height differences relative to the sea level "zero" (Bitelli et al. 2018), the differential ground displacements obtained by comparing two consecutive levelling surveys are integrated into an absolute reference system (Roque et al. 2014).

In addition to its capability of providing high-precision absolute measurements, topographic levelling exhibits a few drawbacks. The procedures involved are generally costly and time-consuming, and they are highly influenced by the morphological characteristics of the study area (Bitelli et al. 2018). Moreover, since the obtained ground surface displacement data is condensed to a limited number of points (benchmarks) and results from the comparison of successive surveys, topographic levelling monitoring records are typically

characterised by limited spatial and temporal resolutions. Consequently, this technique may not enable the identification of complex subsidence spatial distribution patterns, linked to the local geological setting, or short-term ground deformation trends, such as those linked to pumping and groundwater level seasonal fluctuations (Galloway & Burbey 2011).

Another ground-based method for land surface displacement monitoring involves the use of GNSS (Global Navigation Satellite Systems) stations. These systems have been fully operational and consistently used for subsidence monitoring since the mid-1990s. This technique relies on evaluating the time travel of radio signals emitted by a series of earth-orbiting artificial satellites, which move on defined quasi-circular orbits, to accurately retrieve positions on the ground surface. These satellite constellations include the United States Global Positioning System (GPS), the European Galileo global navigation system, as well as Russian GLONASS and Chinese BeiDou systems. For example, the GPS constellation comprises 24 satellites arranged along 6 orbital planes with a 55° inclination with respect to the Earth's equator, spaced at intervals of 60° right ascension of the ascending node (RAAN).
Radio signals from a minimum of four satellites are necessary to determine the approximate absolute (non-differential) position of an autonomous receiver, representing a single point on the Earth's surface (Galloway & Burbey 2011). However, this technique is usually not sufficiently accurate for precise surveying due to factors such as satellite ephemeris, clock errors and signal path delays through the atmosphere (Gambolati et al. 2005). On the other hand, differential GNSS surveys can be employed to measure the relative displacement between two receivers with high precision. As described in Galloway & Burbey (2011), GNSS signals acquired simultaneously at two receivers, one of which can be a continuously station recording (C-GNSS), establish a precise baseline between them. Based on the location of the C-GNSS, referred to as the *base* or *master* station, the 3D position of the roving receiver can be determined by adding the calculated baseline vector to its known position. A subsequent measurement at the same stations conducted after a period of time reveals the eventual relative motion that occurred between them. This technique takes advantage of the fact that reasonably close receivers simultaneously experience common errors, which can be at least partially removed through observation data post-processing (Gambolati et al. 2005).
The accuracy of GNSS measurements primarily depends on the baseline between the stations and the duration of data acquisition by the roving receiver. Typically, accuracies in the order of ± 3 mm can be achieved when estimating height differences over short distances, spanning 1-2 km (Vittuari et al. 2016, Bitelli et al. 2018).
GNSS monitoring networks generally consist of a series of expensive stations in permanent acquisition (Fig. 1.14), with an extensive baseline, as well as a series of closer reference marks periodically surveyed employing portable receivers. Similar to topographic levelling, GNSS monitoring networks require at least one fundamental station located in a stable reference area (Fig. 1.14). Frequently, these two geodetic techniques have been integrated and used in combination within comprehensive surface ground displacement monitoring networks, as displayed in Figure 1.14 showing the Emilia-Romagna Region (Italy) subsidence geodetic monitoring network.
While the GNSS technique offers several operational benefits over topographic levelling, including its efficiency and reduced error propagation with respect to point distances (Bitelli et al. 2018), it still faces the limitation of providing displacement data for a restricted number of reference points on the ground surface (Roque et al. 2014). On the other hand, GNSS data provide the 3D position of the reference points over time, enabling the additional investigation of the horizontal components of displacement, usually expressed with respect to the North-South and East-West main directions. As mentioned earlier, although land subsidence is primarily associated with vertical displacements, the horizontal component is often not negligible and can contribute to surface deformations and structural damage. For instance, points located on the margin of a subsidence (or uplift) feature may exhibit nearly a 1:1 ratio of vertical and horizontal displacements (Bawden et al. 2001, Galloway & Burbey 2011).

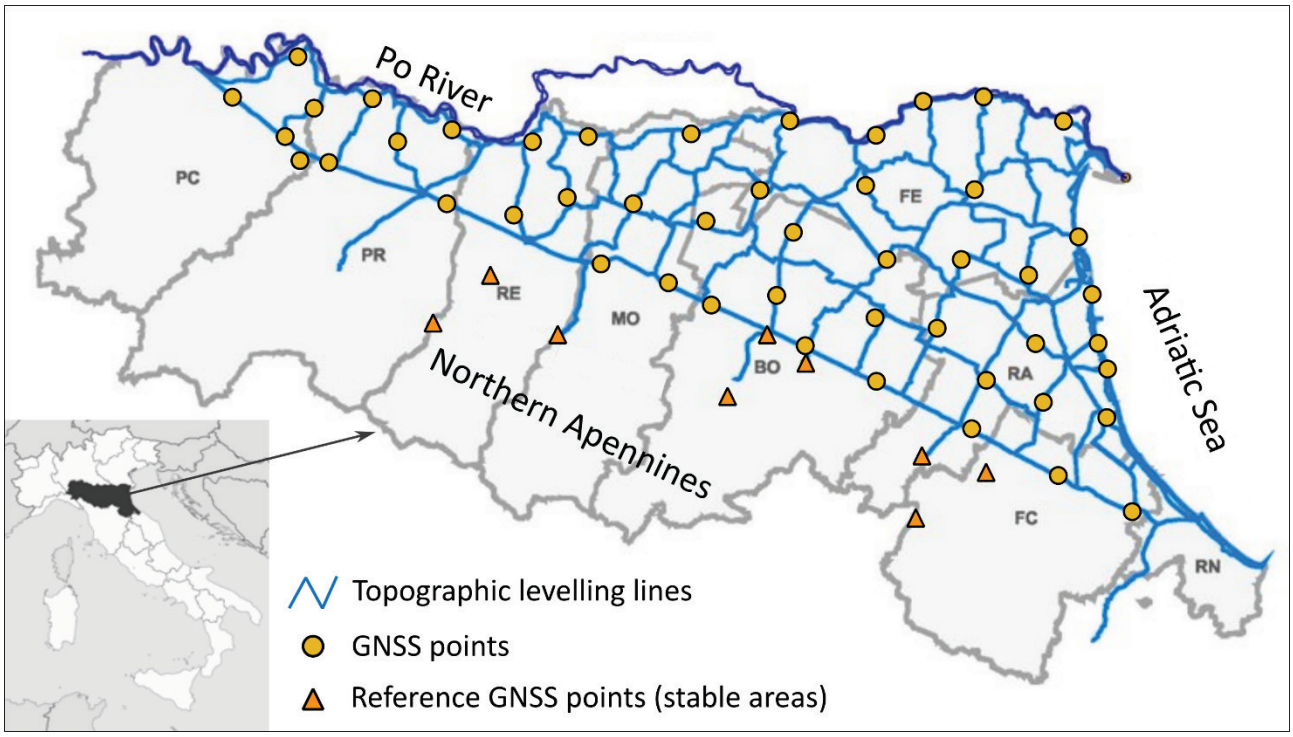

Fig. 1.14 Emilia-Romagna Region (Italy) topographic levelling and GNSS points subsidence monitoring network (Retrieved and modified from Arpae website, https://www.arpae.it/it/temi-ambientali/suolo/subsidenza/la-rete-regionale-di-monitoraggio-della-subsidenza/rilievo-subsidenza-1999-2002).

The most widespread and extensively employed remotely sensed geodetic technique for evaluating ground surface displacements coincides with satellite radar interferometry. Spaceborne Synthetic Aperture Radar Interferometry (InSAR) technique relies on measuring the phase difference of radar signals between subsequent acquisitions over the same area to determine eventual land surface deformations (Gabriel et al. 1989). In particular, as described in Franceschetti et al. (1992) and Gambolati et al. (2005), the electromagnetic microwaves emitted by the radar sensor, and reflected on the ground, are received back by the satellite antenna, forming a digital image of the scanned region on the earth's surface. Each pixel of this image contains information regarding the amplitude and phase of the radar wave backscattered by existing reflectors on the examined ground portion such as buildings, structures and rocks, also referred to as *scatterers*. In differential InSAR methods, a minimum of two radar images, taken from reasonably close orbital positions at different times over the same area, are appropriately subtracted or *interfered* (Galloway & Burbey 2011) to retrieve an interferogram, displaying the signal phase shift for each pixel during the time interval between the acquisitions (Fig. 1.15). The measured radar wave phase difference is strongly related to scatterers displacements and, consequently, deformations of the ground surface, once the atmospheric and topographic phase shift contributions are identified and appropriately filtered out.

InSAR measurements provide monodimensional records along the satellite's line-of-sight (LOS) between the sensor and the ground surface, of the actual three-dimensional displacement of the scatterer. Due to the radar's view angle being less than 45° from the vertical, InSAR measurements are most sensitive to vertical motions (Galloway & Burbey 2011). As mentioned in Gambolati & Teatini (2021), the combination of Earth's rotation and satellite's motion along its orbit results in the radar sensor illuminating any area of the Earth's surface in two different geometries. When the satellite moves from south to north with the radar sensor pointing eastward, the orbit is defined as *ascending*. Conversely, if the satellite's motion follows the north-south direction with a west viewing angle, the geometry is referred to as *descending*. Starting from two InSAR LOS acquisitions over the same area performed in ascending (d_{asc}) and descending (d_{desc}) geometries during the same time interval,

the vertical (d_v) and the horizontal (d_h) components of the local displacement can be determined. This can be achieved by solving the following system of equations (Pepe & Calò 2017):

$$\begin{bmatrix} d_v \\ d_h \end{bmatrix} = \begin{bmatrix} \dfrac{d_{asc} - d_{desc}}{2sin\theta} \\ \dfrac{d_{asce} + d_{desc}}{2cos\theta} \end{bmatrix} \qquad [1.36]$$

where θ [°] represents the LOS view angle with respect to the vertical.

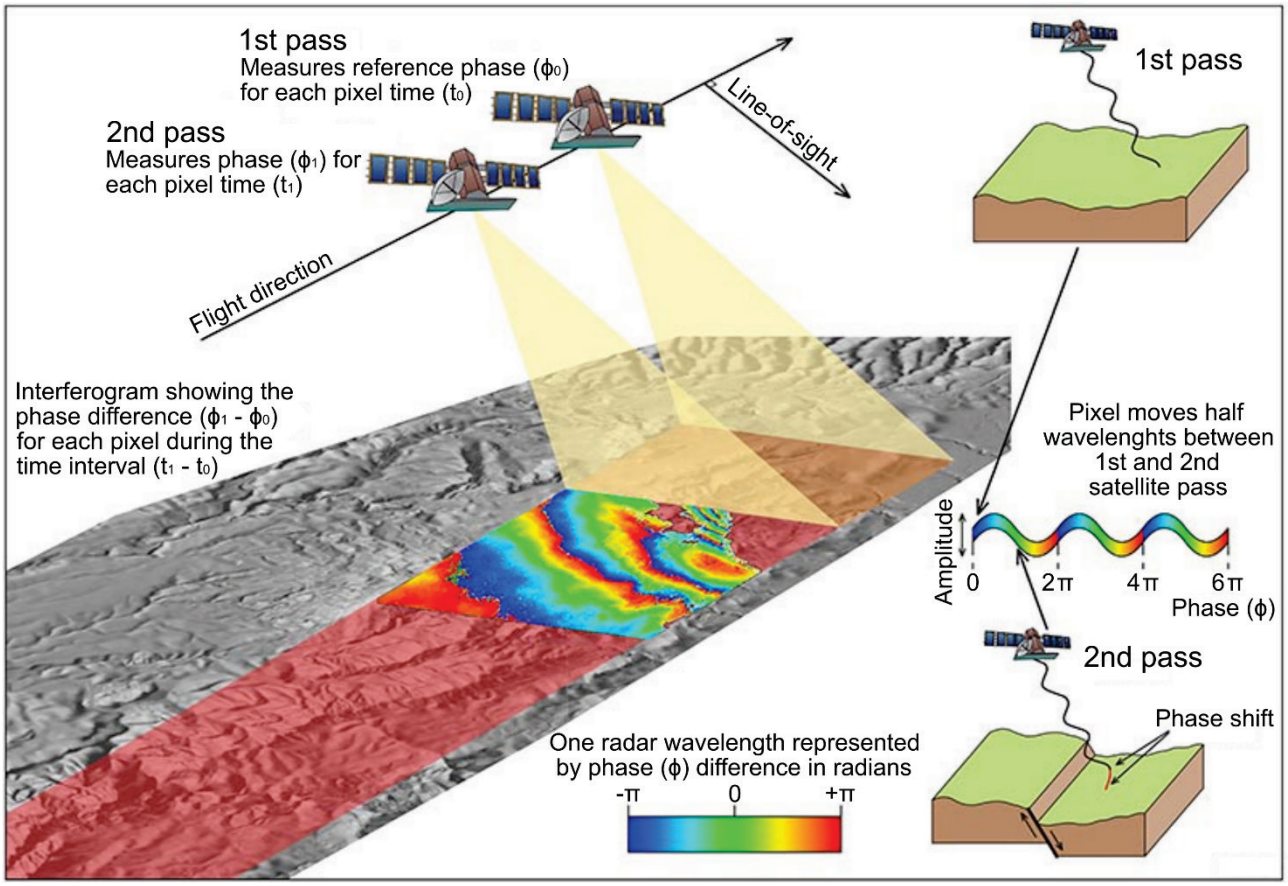

Fig. 1.15 Schematic representation of InSAR acquisitions over the same area at different times. If the surface moves between the two surveys a phase difference is recorded. The derived interferogram maps this phase shift spatially (retrieved from the following website: https://www.ga.gov.au/scientific-topics/positioning-navigation/geodesy/geodetic-techniques/interferometric-synthetic-aperture-radar).

Similar to topographic levelling, InSAR displacement data are the outcome of differential measurements, representing the relative motion of the scatterers. Without an absolute reference in both time and space, these measurements require to be calibrated using existing ground-based data, obtained either from previous topographic levelling surveys or GNSS permanent station acquisitions (Farolfi et al. 2019). As regards smaller to medium-scale acquisitions (in the order of 10 x 10 km²), a single reference point is usually enough for calibration. However, larger-scale surveys may necessitate multiple, evenly distributed benchmarks to achieve accurate calibration (Gambolati & Teatini 2015).

Typically, InSAR techniques can achieve sub-centimetre ground displacement measurements with high spatial resolution, down to a few meters, with data point densities ranging from 10^4 to 10^5 per km² (Gambolati & Teatini 2021). The spatial resolution of InSAR data not only depends on the satellite's sensor type and specifics, but also by the processing chain adopted for the analysis. Meanwhile, the temporal coverage reflects the revisiting time of the satellite or constellation under consideration. For example, temporal resolution can range

from 35 days for ERS-1, ERS-2 and Envisat, to 24 days for RADARSAT-1 and RADARSAT-2, or to 6 days for the Sentinel-1A and Sentinel-1B satellite constellation. Compared to other geodetic ground displacement measurement techniques, InSAR provides monitoring data with much more denser and continuous spatial and temporal coverage over large areas, generally at lower costs and with more expeditious procedures (Raspini et al. 2022). As a result, InSAR data can effectively detect complex and variable ground deformation spatial distribution patterns that might be indiscernible by other techniques. This capability enables the analysis of the recorded surface deformation field in relation to the localisation of anthropic subsidence sources such as pumping wells, shallow underground excavations and constructions, as well as the local geological setting.
However, the effectiveness of the InSAR technique relies on the presence of reflectors on the ground surface. In areas with bare natural terrain or in densely vegetated areas, where the signal loses coherence and decorrelates, monitoring data from other geodetic methods become crucial. Therefore, adopting a comprehensive monitoring approach that integrates various ground displacement and deformation measurements could be of fundamental importance for achieving a thorough understanding of the ongoing subsidence process. Such an approach also allows for calibration, cross-validation and improvement of the accuracy of different independent acquisitions (Gambolati et al. 2005).

1.3 Impact on society

Land subsidence represents a significant global environmental, socio-economic and dangerous geological hazard of topical interest. Its most significant impact is typically observed in the proximities of human-influenced regions, such as urban settlements and areas devoted to productive activities. In these contexts, depending on the local geological setting, external anthropogenic influences can either trigger land subsidence or superimpose and exacerbate pre-existing natural ground deformation processes. In a recent study, Bagheri-Gavosh et al. (2021) conducted a comprehensive review of 290 subsidence case studies mostly situated in large metropolitan areas across 41 different countries. According to the authors' findings, natural and anthropogenic subsidence mechanisms account for approximately 23% and 77% of the documented land subsidence occurrences, respectively. Among anthropogenic factors, over-abstraction of groundwater stands out as the leading cause, being responsible for approximately 60% of the studied cases, followed by land use changes, including urbanisation and development of industrial and agricultural activities, exhibiting a contribution of around 9%. Additionally, other mechanisms, such as hydrocarbon extraction and underground excavation for mining activities, each represent approximately 4% of the recorded subsidence cases.
Unlike other widespread and hazardous geological and hydraulic processes that can impact urban environments, such as earthquakes, volcanic activity, landslides and floods, which often occur over relatively short periods, subsidence, intended as the gradual deformation of the ground surface, can inflict continuous and prolonged damage to existing structures and infrastructures. Recent studies report that the economic damage associated with subsidence in urban environments amounts to billions of dollars annually around the globe (Erkens et al. 2015). However, due to its gradual nature, subsidence and its continuous and prolonged effects over time are often overlooked and receive relatively less attention by the authorities, compared to other processes that are overall equally hazardous and damaging, but condensed in a shorter time interval and consequently more evident (Lixin et al. 2010; Kok & Costa 2021). This could also depend on the fact that frequently subsidence is not the direct or sole cause of damage, but rather one of multiple drivers affecting the stability of buildings and structures, therefore complicating the effective recognition of its contribution (Kok & Costa 2021).
In a recent study, Herrera-García et al. (2021) performed an extensive review of 200 case studies across 34 countries of anthropogenic subsidence due to excessive groundwater withdrawals documented during the past century. According to the authors, the spatial analysis of the considered subsidence occurrences revealed a predisposition for overall flat regions where the subsurface mainly consists of unconsolidated sedimentary bodies, within alluvial or coastal environments, particularly in the vicinity of urban and agricultural areas

developed in temperate to arid climates. Based on statistical analyses that combined the main observed subsidence predisposing geological, environmental, and anthropogenic factors, the authors developed a global-scale subsidence susceptibility model (Fig.1.16) with a spatial resolution of 1km² (at the equator).

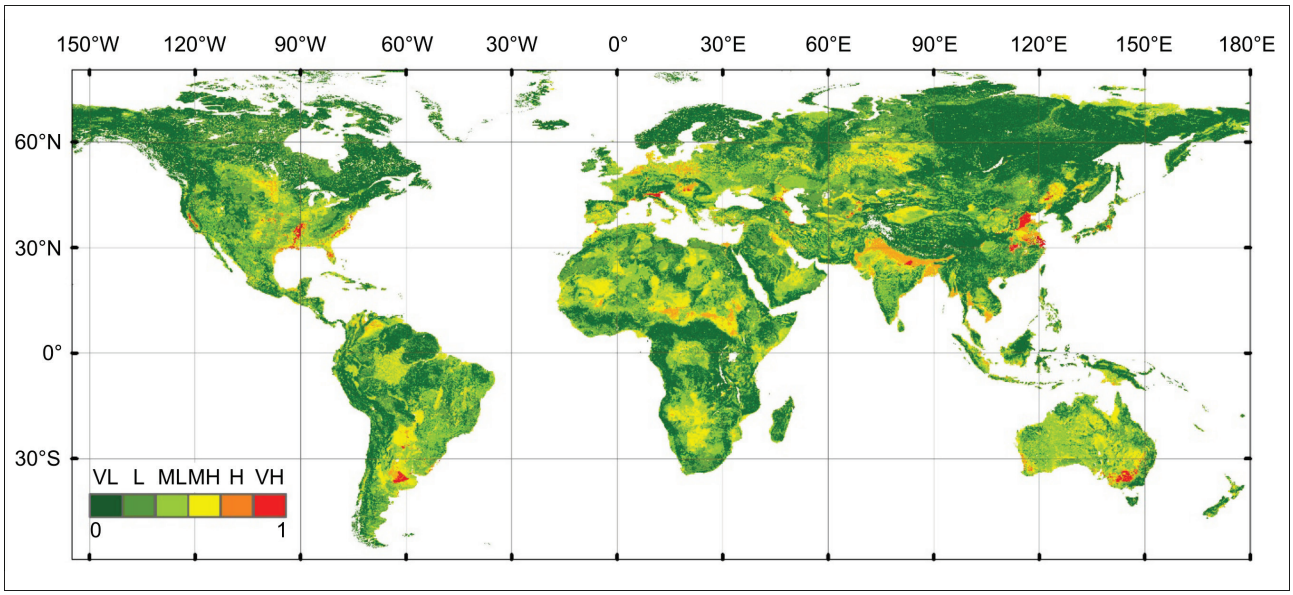

Fig. 1.16 Potential global subsidence map. The colour scale represents the probability intervals classified from *Very Low* (*VL*) to *Very High* (*VH*), calculated for every 30" resolution pixel, equal to 1 km² at the equator (Herrera-García et al. 2021).

This large-scale susceptibility analysis suggests that subsidence resulting from aquifer overdraft could potentially impact approximately 12 million km² (8%) of the global ground surface with a probability exceeding 50%. These areas fall between the *Medium-high* (*MH*) and the *Very High* (*VH*) fields indicated in Figure 1.16.

1.3.1 Subsidence in developing countries and rapidly growing cities

As mentioned earlier, the most significant impacts of the subsidence phenomenon on society are concentrated in the proximity of heavily anthropised areas and urban settlements. In such contexts, subsidence can lead to serious structural, infrastructural, environmental, economic and social consequences (Abidin et al. 2015). Ground deformation directly threatens the stability of buildings and structures and may disrupt infrastructure efficiency including roads, railways, subway networks, and underground drainage and sewerage systems. These damages have evident practical socio-economic implications, encompassing maintenance and reconstruction costs, prolonged unserviceability of the affected elements, and potential losses of historical and cultural heritage (Kok & Costa 2021). Moreover, subsidence often indirectly aggravates the potential impact of other geohazards, such as riverine or coastal flooding. This increased potential arises from the progressive sinking of the ground level, leading to changes in canal gradients and surface morphology, distortion of the natural surface water drainage capacity and infiltration mechanisms (Bagheri-Gavosh et al. 2021), and reduced efficiency of the existing flood mitigation systems (Chang et al. 2019).

These issues are particularly evident and pressing in regions characterised by rapid urbanisation, which is often observed in developing countries, where the expansion of urban and manufacturing centres frequently occurs without adequate land-use planning and resource management regulations.

Over the past two centuries, the proportion of the world's population residing in urban centres has grown significantly, from 2% to 50%, and is projected to further increase in the coming years, surpassing 60% by the 2030s (United Nations 2004). Intense migration fluxes from rural areas can lead to rapid and sometimes

uncontrolled urban growth, with several potential environmental repercussions including air and water pollution, as well as the formation of urban heat islands (Aljammaz et al. 2021). The concentration of a rapidly increasing population and production centres in urban areas and metropolises escalates the demand for resources, particularly water, for both domestic and industrial use. In regions where surface water availability from streams and reservoirs is insufficient, groundwater often represents the sole source of water supply. Extensive groundwater pumping, conducted without appropriate withdrawal rationalisation policies, can then lead to exceeding the natural recharge capacity of the subsurface aquifer system, resulting in the inelastic consolidation of the existing deposits and subsequent ground surface subsidence. Additionally, the natural recharge capacity, especially in phreatic aquifers, may be severely impacted by land use change and extensive surface impermeabilisation caused by urbanisation, which reduces the potential of effective precipitation and infiltration mechanisms (Foster et al. 1999). In addition to the overall stress field redistribution induced by pumping, more localised surcharges are exerted by the rapid construction of buildings and structures. These local loads contribute to the general ground deformation process, operating at a smaller scale, and trigger the consolidation processes in the existing deposits down to the influence depth of each structure.

Apart from external anthropogenic forcing agents, the extent and magnitude of land subsidence are influenced by the local geological setting. The rapidly growing metropolises are frequently located in overall flat regions, such as alluvial, delta, or coastal plains, characterised by thick sequences of interbedded coarse-grained and fine-grained unconsolidated deposits, which are particularly susceptible to deformation processes (Zeitoun & Wakshal 2013).

In China, for instance, subsidence due to aquifer overdraft has been documented in approximately 40 cities and metropolises, primarily situated in floodplains, coastal, and delta regions (Hu et al. 2004). For example, in Shanghai, ground displacements have been extensively monitored since the first occurrence in the 1920s, revealing cumulative sinking peaks exceeding 2.6 m in certain portions of the city centre over the past century (Lyu et al. 2019). In Iran, uncontrolled groundwater extractions during the last decades have produced a severe drawdown of the piezometric level, leading to extensive subsidence processes in large portions of the country. In the capital, Tehran, displacement rates reached peaks up to 25 cm/year (Haghshenas Haghighi & Motagh 2021). Similarly, Indonesia has been experiencing severe ground deformations, mainly concentrated near major cities like Bandung, Semarang and the capital, Jakarta. Here, subsidence has reached values up to 4 m over the past two decades, significantly exacerbating coastal flooding potential. The situation in Jakarta is so severe that government authorities are considering relocating the capital to the island of Borneo (Herrera-García et al. 2021). Lastly, in Mexico City, a recent analysis of 115 years of ground sinking monitoring data has revealed substantial inelastic deformations associated with the progressive compaction of a thick aquitard unit beneath the capital. The documented subsidence rates have remained nearly constant since the 1950s, with peaks spanning approximately 40 to 50 cm/year in specific sectors of the city (Chaussard et al. 2021).

In multiple cases, within contexts of extensive land anthropisation and rapid urban growth, especially in coastal metropolises, a substantial portion of the observed subsidence may be ascribed to the implementation of practices commonly known as *land reclamation*, also referred to as *land fill* or *land reengineering*. In coastal areas, land reclamation involves the creation of new land from the sea through a series of processes, including constructing seawalls, draining seawater and infilling the enclosed space with various materials (Chapman 1984; Sengupta et al. 2023). These infilling materials typically consist of boulders, gravel and sand, sometimes mixed with cement, overlain by shallower clayey soil layers, added until the required height is achieved (Stauber et al. 2016). The rapid urbanisation of the reclaimed land results in the application of extensive surcharge loads. These loads, based on the influence depth of the structures and buildings involved, trigger widespread compaction and consolidation processes in both the uncompacted infill materials and the underlying unconsolidated natural marine sediments (Yang et al. 2018). As a consequence, urbanised reclaimed lands often experience severe and pervasive subsidence, posing a threat to newly constructed structures and infrastructures, leading to potential economic losses and high maintenance costs (Li et al. 2022).

For instance, in China, the city of Macao has experienced extensive land reclamation expansion phases over the last decades, resulting in a cumulative reclaimed surface greater than 20 km². Since the 1990s, in conjunction with rapid urban expansion, subsidence rates attained peak values ranging from 0.1 to 1 m/year during the initial stages after land reclamation, reflecting the severe compaction of the infill material and the underlying silty and clayey natural deposits (Jiang et al. 2011).

1.3.2 Subsidence and climate change

One of the most complex and pressing challenges encumbering modern society, but at the same time intrinsically linked and interconnected to it, lies in climate change. Climate change refers to the long-term trends in climate occurring over several decades, centuries or longer, distinct from climate variability which involves short-term yearly fluctuations (Stauber et al. 2016). This long-term process is primarily driven by human activities that have progressively altered the composition and balance of the natural atmospheric system, both physically and chemically. Industrial activities and burning of fossil fuels, aggravated by widespread deforestation practices, resulted in the release and concentration increase of heat-trapping greenhouse gases in the atmosphere over the last centuries, particularly in recent decades (Gurjar et al. 2013). Climate change has a broad impact on society, encompassing various ecological and environmental risks that could potentially lead to severe socio-economic repercussions. The foremost environmental consequence of the substantial increase in greenhouse gas concentration in the atmosphere pertains to the progressive elevation of the global mean temperature. Since the advent of the Industrial Revolution, the global mean temperature has already risen by approximately 1°C and is projected to increase further in the coming years (Fletcher & Smith 2020). This temperature increase directly contributes to sea level rise, driven by the progressive melting of land-based ice, including glaciers and ice sheets, as well as the thermal expansion of ocean waters (Gehrels & Garrett 2021). Another major environmental consequence of climate change involves the alteration of the natural hydrological cycle. The rising temperatures and the more frequent occurrence of prolonged and severe draughts, along with overall drier seasons, intensify the evapotranspiration potential, leading to significant shifts in rainfall patterns and increasing the likelihood of extreme precipitation events (Herrera-García et al. 2021). These events, in turn, may have severe implications for society, exacerbating the occurrence and the magnitude of catastrophic events, such as floods and landslides (Stauber et al. 2016).

The primary environmental factors associated with climate change can indirectly but significantly impact both natural and anthropogenic subsidence trends. For instance, as regards natural ground deformation processes, changes in climate patterns, such as increased frequency of droughts and higher evapotranspiration rates, can profoundly alter soil moisture conditions. Prolonged dry periods may lead to an extensive reduction in soil moisture, potentially triggering significant shrinkage processes in shallow clayey soils, which can result in damage to buildings and structures (Harrison et al. 2012; Charpentier et al. 2021). Moreover, the overall global temperature rise, particularly pronounced at high latitudes, may exacerbate natural ground deformations associated with thawing permafrost processes. Thawing permafrost reduces pore pressure and void ratio of the soil, as the ice gradually melts and is replaced by water, leading to ground subsidence. While this process typically occurs due to seasonal temperature fluctuations, climate change is causing these short-term variations to progressively shift to permanent thawing and deformations (Kok & Costa 2021). The effects can range from localised ground sinking, threatening individual structures, to deep and extensive depressions and vast irregular *thermokarst* terrain in response to long-term climate change, with potential settlements of several meters depending on the ice content (Nelson et al. 2001).

As regards anthropogenic subsidence, deformation processes induced by groundwater pumping can be further exacerbated by climate change. The increased frequency and duration of dry periods, along with higher evapotranspiration, heavily reduce infiltration and aquifer recharge processes. Concurrently, draughts negatively impact surface water supply, driving higher demand for groundwater and increased pumping rates

to compensate. The persistent occurrence and combination of these conditions result in extensive and significant groundwater level drawdown, leading to increased subsidence rates over time (Guo et al. 2022).
In urban coastal areas, subsidence associated with rapid urbanisation, land reclamation procedures, and predominantly groundwater pumping, which can be potentially aggravated by climate change, causes pronounced downward ground displacements. Additionally, climate change leads to a progressive relative sea level rise and increase in the frequency of intense precipitation events and storm surges, further exacerbating the flooding potential already heightened by subsidence. The interaction of these two mechanisms, schematised in Figure 1.17 and projected to continue and worsen over time (Sweet et al. 2022), poses a significant threat to the future of several coastal and delta urban areas and metropolises, often referred to as *sinking cities* (Erkens et al 2015).

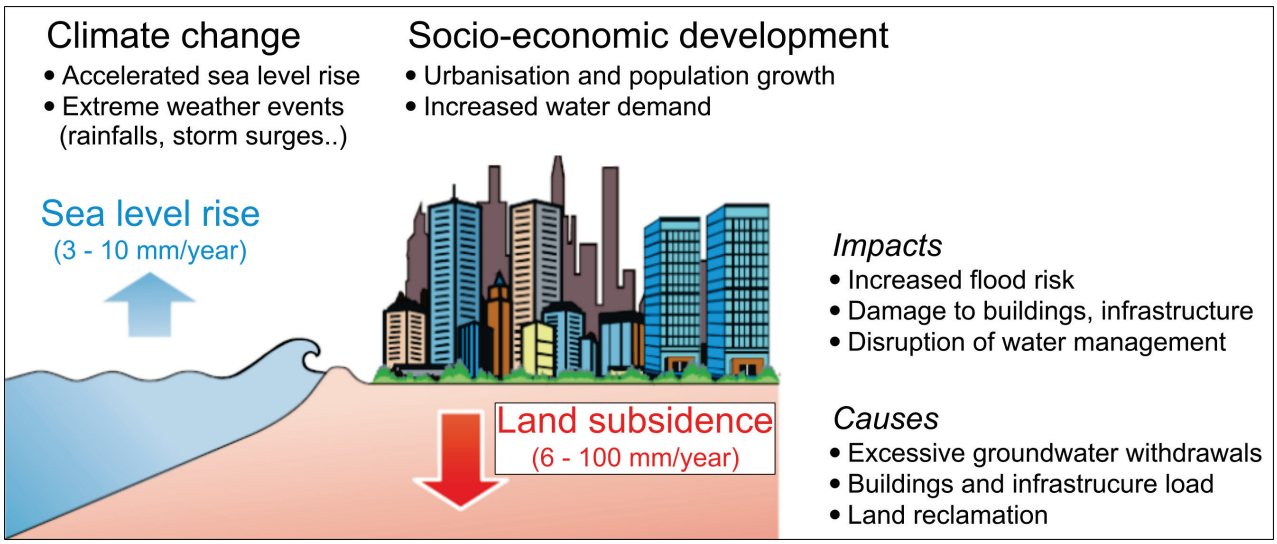

Fig. 1.17 Illustration of the primary drivers, processes and impacts of land subsidence in coastal cities. The average subsidence rates observed in coastal metropolises can exceed global absolute sea level rise by a factor of 10 (Erkens et al. 2015, modified).

1.4 Research questions and outline

In the previous sections, subsidence in urban areas has been discussed as a complex and significant challenge for modern society. Despite the general knowledge about the triggering and deformation mechanisms, as well as the widespread occurrence and the availability of sophisticated and reliable monitoring techniques, effectively reconstructing the evolutive dynamics of subsidence in a specific area of interest, in relation to its anthropogenic forcing and local geological setting, can still pose considerable challenges. The primary issues typically involve defining a representative geological model of the subsurface, reconstructing the long-term evolution of the ground deformation process, and the mechanical characterisation of the involved deposits. These challenges cover some of the main aspects and the fundamental research questions addressed in this PhD project, which will be briefly introduced in this section and explored in detail in the subsequent chapters, considering the case study of the ongoing subsidence process in the urban area of Bologna (Italy).
The city of Bologna has suffered severe ground deformations since the beginning of the 1960s, primarily attributed to excessive groundwater extractions for domestic use. The sinking process peaked at the turn of the 1970s and the 1980s when displacement rates exceeding 10 cm/year were recorded and significant damage to structures and infrastructures occurred. The implementation of regional groundwater management regulations subsequently led to a substantial reduction in these rates. However, recent data indicate a notable upsurge in the subsidence process due to increased pumping aimed at counteracting the impact of reduced precipitation, highlighting the potential influence of climate change on the ongoing deformation process.

The identification of the subsidence process in the urban area of Bologna as the primary subject of this PhD project is grounded in several factors. In addition to its historical significance and recent resurgence, the deformation process has been intensively monitored over the decades, resulting in the availability of extensive ground displacement and groundwater pumping data, as well as, comprehensive geognostic survey archives.

Question 1 – *What is the 3D depositional architecture of the subsurface in the urban area of Bologna and can it be reconstructed through a stratigraphic approach based on lithofacies?*

Question 2 – *What is the long-term spatiotemporal evolution of the subsidence process in Bologna, and how is it influenced by the local geological setting and groundwater pumping trends?*

Question 3 – *How can the observed relationships between geological setting and subsidence evolution be interpreted from a geotechnical perspective, considering the mechanical characteristics of the deposits and piezometric data?*

The first research question will be addressed in chapter 2, focusing on the generation of a 3D geological model of the subsurface of the urban area of Bologna. The second thematic question will be explored in chapter 3, regarding the integration of various sources of monitoring data to reconstruct the long-term spatial and temporal evolution of the subsidence process in Bologna. Subsequently, the third research question will be investigated in chapter 4, by conducting a series of one-dimensional subsidence calculations employing an analytical solution of Terzaghi's consolidation equation (1925; 1943). Lastly, chapter 5 will provide a summary of the main results and briefly outline future perspectives.

1.5 References

Abidin HZ, Andreas H, Gumilar I, Sidiq T, Gamal M, 2015. Environmental Impacts of Land Subsidence in Urban Areas of Indonesia, in: Proceedings of the FIG Working Week 2015, TS 3– Positioning and Measurement, Sofia, Bulgaria, Paper no. 7568, 17–21 May 2015.

Aljammaz A, Sultan M, Izadi M, Abotalib AZ, Elhebiry MS, Emil MK, Abdelmohsen K, Saleh M, Becker R, 2021. Land Subsidence Induced by Rapid Urbanization in Arid Environments: A Remote Sensing-Based Investigation. Remote Sensing, 13, 1109. https:// doi.org/10.3390/rs13061109.

Amorosi A, Farina M, Severi P, Preti D, Caporale L, Di Dio G, 1996. Genetically related alluvial deposits across active fault zones: an example of alluvial fan-terrace correlation from the upper Quaternary of the southern Po Basin, Italy, Sedimentary Geology, 102, 275-295. ISSN 0037-0738. https://doi.org/10.1016/0037-0738(95)00074-7.

Barends FBJ, Brouwer FJJ, Schroder FH, 1995. Land subsidence: natural causes; measuring techniques; the Groningen Gasfields. IAHS Publ 234, IAHS, Wallingford, UK, pp. 409.

Battaglia M, Pagli C, Meuti S, 2021. The 2008–2010 Subsidence of Dallol Volcano on the Spreading Erta Ale Ridge: InSAR Observations and Source Models. Remote Sensing 2021, 13, 1991. https://doi.org/10.3390/rs13101991.

Bawden GW, Thatcher W, Stein RS, Hudnut KW, Peltzer G, 2001. Tectonic contraction across Los Angeles after removal of groundwater pumping effects, Nature, 412, 812–815.

Bitelli G, Roncari G, Tini MA, Vittuari L, 2018. High-precision topographical methodology for determining height differences when crossing impassable areas, Measurement, 118, 147-155, ISSN 0263-2241, https://doi.org/10.1016/j.measurement.2018.01.013.

Borchers JW, 1998. Land subsidence case studies and current research. Proceedings of the Dr. J.F. Poland Symposium, Association of Engineering Geologists, Star Publishing, Belmont, California.

Bräuner G, 1973. Subsidence due to underground mining (in Two Parts): 1. Theory and Practices in Predicting Surface Deformation, US Department of the Interior, Bureau of Mines, Denver.

Bruno L, Campo B, Costagli B, Stouthamer E, Teatini P, Zoccarato C, Amorosi A, 2020. Factors controlling natural subsidence in the Po Plain, Proceedings of IAHS, 382, 285–290. https://doi.org/10.5194/piahs-382-285-2020.

Burbey TJ, 2020. Extensometer forensics: what can the data really tell us?, Hydrogeology Journal, 28 (2), 637–655. https://doi.org/10.1007/s10040-019-02060-6.

Carminati E, Di Donato G, 1999. Separating natural and anthropogenic vertical movements in fast subsiding areas: the Po plain (N Italy) case. Geophys. Res. Lett., 26, 2291-2294.

Carminati E, Martinelli G, 2002. Subsidence rates in the Po Plain, northern Italy: the relative impact of natural and anthropogenic causation. Engineering Geology, 66, 241-255.

Casagrande A, 1936. The Determination of the Pre-Consolidation Load and its Practical Significance, Proceedings of the 1st International Conference on Soil Mechanics, Harvard University Cambridge, Mass., 3, D-34, p. 60-64.

Chang YL, Tsai TL, Yang JC, 2019. Flood hazard mitigation in land subsidence prone coastal areas by optimal groundwater pumping, Journal of Flood Risk Management, 12(2). https://doi.org/10.1111/jfr3.12517.

Chapman DM, 1984. The edge of the sea, In M. Schwartz (Ed.), Beaches and coastal Geology. Springer US.

Charpentier A, James M, Ali H, 2022. Predicting drought and subsidence risks in France, Natural Hazards and Earth System Sciences, 22, 2401–2418. https://doi.org/10.5194/nhess-22-2401-2022.

Chaussard E, Havazli E, Fattahi H, Cabral-Cano E, Solano-Rojas D, 2021. Over a century of sinking in Mexico City: No hope for significant elevation and storage capacity recovery. Journal of Geophysical Research: Solid Earth, 126, e2020JB020648. https://doi.org/10.1029/2020JB020648.

Cooper AH, 1988. Subsidence resulting from the dissolution of Permian gypsum in the Ripon area; its relevance to mining and water abstraction, Published in Bell FG, Culshaw MG, Cripps JC, Lovell MA (eds), 1988. Engineering Geology of Underground Movements, Geological Society Engineering Geology Special Publication No. 5, pp. 387-390.

Craig RF, 1974. Craig's Soil Mechanics (7th edition), CRC Press, London. https://doi.org/10.4324/9780203494103.

Das BM, 1983. Advanced soil mechanics, Hemisphere Publishing Corporation and McGraw-Hill, New York, p.1-511, ISBN 0-07-015416-3.

De Caro M, Crosta GB, Previati A, 1985. Modelling the interference of underground structures with groundwater flow and remedial solutions in Milan, Engineering Geology, 272, 105652. 0013-7952, https://doi.org/10.1016/j.enggeo.2020.105652.

Domenico PA, Schwartz FW, 1990. Physical and Chemical Hydrogeology, John Wiley & Sons, New York, p. 824.

Doornhof D, Kristiansen TG, Nagel NB, Pattillo PD, Sayers C, 2006. Compaction and Subsidence. Oilfield Review, Autum, 50-67.

Erkens G, Bucx T, Dam R, de Lange G, Lambert J, 2015. Sinking coastal cities, Proceedings of IAHS, 372, 189-198, https://doi.org/10.5194/piahs-372-189-2015.

Fileccia A, 2015. Some simple procedures for the calculation of the influence radius and well head protection areas (theoretical approach and a field case for a water table aquifer in an alluvial plain), Italian Journal of Groundwater (2015). DOI 10.7343/AS-117-15-0144.

Fletcher WD, Smith CB, 2020. Chapter 1 – Introduction, Eds: Fletcher WD, Smith CB, Reaching Net Zero, Elsevier, p.1-8. ISBN 9780128233665, https://doi.org/10.1016/B978-0-12-823366-5.00001-4.

Foster SSD, Morris BL, Chilton PJ, 1999. Groundwater in urban development: a review of linkages and concerns. IAHS-AISH publication, 259, 3-12.

Franceschetti G, Migliaccio M, Riccio D, Schirinzi G, 1992. SARAS: a synthetic aperture radar (SAR) raw signal simulator, in IEEE Transactions on Geoscience and Remote Sensing, 30(1), p. 110-123, doi: 10.1109/36.124221.

Gabriel AK, Goldstein RM, Zebker HA, 1989. Mapping small elevation changes over large areas: Differential radar interferometry, J. Geophys. Res., 94(B7), 9183–9191, doi:10.1029/JB094iB07p09183.

Galloway DL, Jones D, Ingebritsen SE, 1999. Land subsidence in the United States, U.S. Geological Survey, Circular 1182, 185 pp., doi: 10.3133/cir1182.

Galloway DL, Burbey TJ, 2011. Regional land subsidence accompanying groundwater extraction. Hydrogeology Journal 19(8): 1459-1486. Galloway, D.L., Burbey, T. J., 2011. Review: Regional land subsidence accompanying groundwater extraction, Hydrogeology J., 19(8), 1459-1486.

Gambolati G, Teatini P, Ferronato M, 2005. Anthropogenic Land Subsidence, Encyclopedia of Hydrological Sciences. John Wiley & Sons, Ltd. doi:10.1002/0470848944.hsa164b.

Gambolati G, Teatini P, 2015. Geomechanics of subsurface water withdrawal and injection, Water Resources Research, 51(6), 3922-3955. https://doi.org/10.1002/2014WR016841.

Gambolati G, Teatini P, 2021. Land Subsidence and its Mitigation, Guelph, Ontario, Canada, pp. 92, ISBN: 978-1-77470-001-3, https://gw-project.org/books/land-subsidence-and-its-mitigation.

Gehrels R, Garrett E, 2021. Chapter 11 - Rising sea levels as an indicator of global change, Ed(s): Letcher TM, Climate Change (Third Edition), Elsevier, p.205-217. ISBN 9780128215753, https://doi.org/10.1016/B978-0-12-821575-3.00011-6.

Giomi I, Francisca FM, 2022. Numerical Modeling of the Oedometrical Behavior of Collapsible Loess, Geotechnical and Geological Engineering, 40(5), 2501-2512. https://doi.org/10.1007/s10706-021-02042-0.

Guo H, Hao A, Li W, Zang X, Wang Y, Zhu J, Wang L, Chen Y, 2022. Land subsidence and its affecting factors in Cangzhou, North China Plain, Front. Environ. Sci. 10:1053362. doi: 10.3389/fenvs.2022.1053362.

Gurjar BR, Ojha CSP, Surampalli RY, Walvekar PP, Tyagi V, 2013. Greenhouse Gas Emissions and Climate Change: An Overview, in: Climate Change Modeling, Mitigation, and Adaptation (Chapter 2), 9-25, American Society of Civil Engineers, USA. doi: 10.1061/9780784412718.ch02.

Guzy A, Malinowska AAA, 2020. Assessment of the Impact of the Spatial Extent of Land Subsidence and Aquifer System Drainage Induced by Underground Mining. Sustainability, 12, 7871.

Guzy A, Witkowski WT, 2021. Land subsidence estimation for aquifer drainage induced by underground mining. Energies 14. doi:10.3390/en14154658.

Haghshenas Haghighi M, Motagh M, 2021. Land subsidence hazard in Iran revealed by country-scale analysis of Sentinel-1 InSAR, Int. Arch. Photogramm. Remote Sens. Spatial Inf. Sci., XLIII-B3-2021, 155–161, https://doi.org/10.5194/isprs-archives-XLIII-B3-2021-155-2021.

Hamlyn J, Wright T, Walters R, Pagli C, Sansosti E, Casu F, Pepe S, Edmonds M, McCormick Kilbride B, Keir D, Neuberg J, Oppenheimer C, 2018. What causes subsidence following the 2011 eruption at Nabro (Eritrea)?, Prog Earth Planet Sci 5, 31. https://doi.org/10.1186/s40645-018-0186-5.

Hammett KM, Katz BG, McPherson BF, Patiño E, Schiffer DM, Wedderburn L, Yobbi DK, 2001. Science Plan U.S. Geological Survey Florida District. 37, Open-File Report 01-180, Tallahassee, Florida.

Harnischmacher S, Zepp H, 2010. Bergbaubedingte Höhenänderungen im Ruhrgebiet – Eine Analyse auf Basis digitalisierter historischer Karten, zfv:386–397.

Harrison AM, Plim JFM, Harrison M, Jones LD, Culshaw MG, 2012. The relationship between shrink–swell occurrence and climate in south-east England, Proceedings of the Geologists' Association, 123(4), p.556-575. ISSN 0016-7878, https://doi.org/10.1016/j.pgeola.2012.05.002.

Holtz RD, Kovacs WD, 1981. An Introduction to Geotechnical Engineering. Prentice-Hall Inc., New Jersey.

Holzer TL, 1984. Man-Induced Land Subsidence, Reviews in Engineering Geology, vol. VI, Geological Society of America, Boulder, CO, 221.

Hu RL, Yue ZQ, Wang LC, Wang SJ, 2004. Review on current status and challenging issues of land subsidence in China, Engineering Geology, 76, 65-77, ISSN 0013-7952. https://doi.org/10.1016/j.enggeo.2004.06.006.

Jalota SK, Vashisht BB, Sharma S, Kaur S, 2018. Chapter 4 - Climate Change and Groundwater, Eds. Jalota SK, Vashisht BB, Sharma S, Kaur S, Understanding Climate Change Impacts on Crop Productivity and Water Balance, Academic Press, 2018, 149-181, ISBN 9780128095201, https://doi.org/10.1016/B978-0-12-809520-1.00004-5.

Janbu N, Bjerrum L, Kjaernsli B, 1956. Soil Mechanics Applied to some Engineering Problems, Norwegian Geotechnical Institute Publication, 16, Oslo, Norway.

Jiang L, Lin H, Cheng S, 2011. Monitoring and assessing reclamation settlement in coastal areas with advanced InSAR techniques: Macao city (China) case study, International Journal of Remote Sensing, 32(13), 3565-3588. DOI:10.1080/01431161003752448.

Knappett J, Craig RF, 2019. Craig's Soil Mechanics (9th edition), CRC Press, London. https://doi.org/10.1201/9781351052740.

Kok S, Costa AL, 2021. Framework for economic cost assessment of land subsidence, Natural Hazards, 106, 1931–1949. https://doi.org/10.1007/s11069-021-04520-3.

Lancellotta R, 1987. Geotecnica, Zanichelli, Bologna, p.1-531, ISBN 88-08-04362-2.

Laouafa F, Guo J, Quintard M, 2021. Underground Rock Dissolution and Geomechanical Issues. Rock Mech Rock Eng 54, 3423–3445. https://doi.org/10.1007/s00603-020-02320-y.

Laouafa F, Guo J, Quintard M, 2023. Modelling and applications of dissolution of rocks in geoengineering. J. Zhejiang Univ. Sci. A 24, 20–36. https://doi.org/10.1631/jzus.A2200169.

Leeper R, Rhodes B, Kirby M, Scharer K, Carlin J, Hemphill-Haley E, Avnaim-Katav S, MacDonald G, Starratt S, Aranda A, 2017. Evidence for coseismic subsidence events in a southern California coastal saltmarsh. Sci Rep 7, 44615. https://doi.org/10.1038/srep44615.

Li G, Zhao C, Wang B, Liu X, Chen H, 2022. Land Subsidence Monitoring and Dynamic Prediction of Reclaimed Islands with Multi-Temporal InSAR Techniques in Xiamen and Zhangzhou Cities, China. Remote Sensing, 14(12), 2930. https://doi.org/10.3390/rs14122930.

Li P, Gu J, Liu Y, Li Y, 2022. The study of soft soil seismic subsidence based on the 3D OpenSees model. Geoenviron Disasters 9, 10. https://doi.org/10.1186/s40677-022-00212-7.

Lixin Y, Jie W, Chuanqing S, Guo J, Yanxiang J, Liu B, 2010. Land subsidence disaster survey and its economic loss assessment in Tianjin, China, Natural Hazards Review, 11(1), 35-41. https://doi.org/10.1061/(ASCE)1527-6988(2010)11:1(35).

Lu Z, Masterlark T, Power J, Dzurisin D, Wicks C, 2002. Subsidence at Kiska volcano, western Aleutians, detected by satellite radar interferometry. Geophysical research letters, 29(18). http://dx.doi.org/10.1029/2002GL014948 (2-1-2-4).

Lyu HM, Shen SL, Zhou A, Yang J, 2020. Risk assessment of mega-city infrastructures related to land subsidence using improved trapezoidal FAHP. Science of The Total Environment, 717, 135310. ISSN 0048-9697, doi: 10.1016/j.scitotenv.2019.135310.

Ma T, Du Y, Ma R, Xiao C, Liu Y, 2018. Review: Water–rock interactions and related eco-environmental effects in typical land subsidence zones of China, Hydrogeology Journal, 26, 1339–1349. https://doi.org/10.1007/s10040-017-1708-8.

Maaß AL, Schüttrumpf H, 2018. Long-term effects of mining-induced subsidence on the trapping efficiency of floodplains. Anthropocene 24, 1–13. doi:10.1016/j.ancene.2018.10.001.

Marker BR 2013. Land Subsidence. In: Bobrowsky, P.T. (eds) Encyclopedia of Natural Hazards. Encyclopedia of Earth Sciences Series. Springer, Dordrecht. https://doi.org/10.1007/978-1-4020-4399-4_208.

Meade RH, 1968. Compaction of sediments underlying areas of land subsidence in central California, Geological Survey Professional Paper, 497 (D), 10.3133/pp497D.

Mendoza M, Romo M, 1989. Behavior of building foundations in Mexico City during the 1985 Earthquake: second stage. In: Proc., Lessons Learned from the 1985 Mexico Earthquake, pp 66–70.

Nelson FE, Anisimov OA, Shiklomanov NI, 2001. Subsidence risk from thawing permafrost, Nature 410 (6831), 889–890. https://doi.org/10.1038/35073746.

Pirazzoli PA, 1996. Sea level changes, The Last 20000 Years, Wiley, Chichester, 211.

Poland JF, Yamamoto S, et al., 1984. Field measurement of deformation, Guidebook to studies of land subsidence due to groundwater withdrawal, Poland JF, ed., United Nations Educational Scientific and Cultural Organization (UNESCO), Paris, 17–35.

Rahimi MR, Mohammadi SD, Taleb Beydokhti A, 2022. Laboratory simulation of gypsum rock dissolution at different pressures, water-flow velocities and pH ranges, Quarterly Journal of Engineering Geology and Hydrogeology, 56(1), doi: https://doi.org/10.1144/qjegh2021-120.

Raspini F, Caleca F, Del Soldato M, Festa D, Confuorto P, Bianchini S, 2022. Review of satellite radar interferometry for subsidence analysis, Earth-Science Reviews, doi:10.1016/j.earscirev.2022.104239.

Riley FS, 1984. Developments in borehole extensometry, Proceedings of the 3rd International. Symposium on Land Subsidence, International Association of Hydro-logical Sciences, London, 169–186.

Roque D, Fonseca AM, Henriques MJ, Falcão AP, 2014. A First Approach for Displacement Analysis in Lisbon Downtown Using PS-InSAR, Procedia Technology, 16, 288-293. https://doi.org/10.1016/j.protcy.2014.10.094.

Scott RF, 1963. Principles of Soil Mechanics, Addison-Wesley Publishing Co., Boston.

Seed RB, 1990. Preliminary report on the principal geotechnical aspects of the October 17, 1989, Loma Prieta Earthquake Report No. UCB/EERC-90/05.

Sengupta D, Choi YR, Tian B, Brown S, Meadows M, Hackney CR, Banerjee A, Li Y, Chen R, Zhou Y, 2023. Mapping 21st century global coastal land reclamation, Earth's Future, 11(2), e2022EF002927. https://doi.org/10.1029/2022EF002927.

Severi P, 2021. Soil uplift in the Emilia-Romagna plain (Italy) by satellite radar interferometry. 527-542. 10.4430/bgta0349.

Stauber JL, Chariton A, Apte S, 2016. Global Change, in: Marine Ecotoxicology: Current Knowledge and Future Issues, Elsevier, p. 273–313. doi:10.1016/B978-0-12-803371-5.00010-2.

Sweet WV, Hamlington BD, Kopp RE, Weaver CP, Barnard PL, Bekaert D, Brooks W, Craghan M, Dusek G, Frederikse T, Garner G, Genz AS, Krasting JP, Larour E, Marcy D, Marra JJ, Obeysekera J, Osler M, Pendleton M, Roman D, Schmied L, Veatch W, White KD, Zuzak C, 2022. Global and Regional Sea Level Rise Scenarios for the United States: Updated Mean Projections and Extreme Water Level Probabilities Along U.S. Coastlines, NOAA Technical Report NOS 01, National Oceanic and Atmospheric Administration, National Ocean Service, Silver Spring, Maryland, MD, pp. 111.

https://oceanservice.noaa.gov/hazards/sealevelrise/noaa-nostechrpt01-global-regional-SLR-scenarios-US.pdf.

Szelag S, Weber U, 1993. Bergsenkung. In: Wiggering, H. (Ed.), Steinkohlebergbau: Steinkohle als Grundstoff. Energieträger und Umweltfaktor, Ernst & Sohn, Essen.

Taylor DW, 1948. Fundamentals of Soil Mechanics, John Wiley and Sons, New York.

Terzaghi K, 1925. Erdbaumechanik auf Bodenphysikalisher Grundlage, Deuticke, Vienna.

Terzaghi K, 1943. Theoretical soil mechanic. Wiley, New York.

United Nations, 2004. World Economic and Social Survey, UN, New York.

Vanicek E, Krakiwsky P, 1982. Geodesy: the concepts, North-Holland Publishing Co., Netherlands, 1982.

Vittuari L, Tini MA, Sarti P, Serantoni E, Borghi A, Negusini M, Guillaume S, 2016. A comparative study of the applied methods for estimating deflection of the vertical in terrestrial geodetic measurements, Sensors (Switzerland), 16. http://dx.doi. org/10.3390/s16040565.

Wang G, Yu J, Kearns TJ, Ortega J, 2014. Assessing the Accuracy of Long-Term Subsidence Derived from Borehole Extensometer Data Using GPS Observations: Case Study in Houston, Texas, Journal of Surveying Engineering, 140 (3), doi:10.1061/(ASCE)SU.1943-5428.0000133.

Wang X, Yuan Y, Hu C, Mei Y, 2021. Research on the Geostatic Stress Field Procedure under Complex Conditions, Advances in Civil Engineering, https://doi.org/10.1155/2021/6674369.

Whittaker BN, Reddish DJ, 1989. Subsidence: Occurrence, Prediction, and Control; Elsevier: Amsterdam, The Netherlands.

Wood HO, 1908. Distribution of apparent intensity in San Francisco. The California Earthquake of April, 18(1906), pp 220–227.

Yang M, Yang T, Zhang L, Lin J, Qin X, Liao M, 2018. Spatio-Temporal Characterization of a Reclamation Settlement in the Shanghai Coastal Area with Time Series Analyses of X-, C-, and L-Band SAR Datasets, Remote Sensing, 10(2), 329. https://doi.org/10.3390/rs10020329.

Zeitoun DG, Wakshal E, 2013. Land Subsidence Analysis in Urban Areas - The Bangkok Metropolitan Area Case Study, Springer Dordrech. https://doi.org/10.1007/978-94-007-5506-2.

Zhai Y, Cao X, Jiang Y, Sun K, Hu L, Teng Y, Wang J, Li J, 2021. Further Discussion on the Influence Radius of a Pumping Well: A Parameter with Little Scientific and Practical Significance That Can Easily Be Misleading. Water. 13(15):2050. https://doi.org/10.3390/w13152050.

Zhang Y, Huang H, Liu Y, Liu Y, 2018. Self-weight consolidation and compaction of sediment in the Yellow River Delta, China. Physical Geography, 39(1), 84–98. https://doi.org/10.1080/02723646.2017.1347420.

Chapter 2 - 3D geological modelling of the Bologna urban area (Italy)

2.1 Preface

The initial step in this PhD project, which ultimately aims at the comprehensive analysis of the ongoing subsidence process in Bologna, regards the development of a reliable 3D geological model of the subsurface serving as a basis for subsequent one-dimensional subsidence calculations. The Emilia-Romagna Region (RER) granted access to extensive geognostic survey archives, regional-scale stratigraphic sections and geological maps. Although the high level of detail and abundance of the basic geological data might create the impression of the development of the 3D geological model as an established and guaranteed process, the complex alluvial context of the study area demanded an extensive stratigraphic analysis that took over a year to be completed.

The 3D geological model is the outcome of a multidisciplinary analysis undertaken in collaboration with the research fellow Serena Giacomelli, who directly oversaw the stratigraphic aspect of the work, Professor Alessandro Amorosi and the Geologic, Soil, and Seismic Survey of the Emilia-Romagna Region.

This chapter summarises and presents the multidisciplinary analysis approach that led to the development of the 3D geological model of the subsurface of Bologna. The chapter consists of a paper edited in the journal *Engineering Geology*: Giacomelli S[1], Zuccarini A[2], Amorosi A[2], Bruno L[3], Di Paola G[4], Severi P[5], Martini A[5], Berti M[2], 2023. 3D geological modelling of the Bologna urban area (Italy), Engineering Geology, 324, 107242, ISSN 0013-7952, https://doi.org/10.1016/j.enggeo.2023.107242.

[1] ISPRA, Institute for Environmental Protection and Research, via Vitaliano Brancati 48, Rome, Italy

[2] Department of Biological, Geological, and Environmental Sciences (BiGeA), University of Bologna, via Zamboni 67, Bologna, Italy

[3] Department of Chemical and Geological Sciences, University of Modena and Reggio Emilia, Via Giuseppe Campi 103, Modena, Italy

[4] Department of Biosciences and Territory, University of Molise, Pesche, Italy

[5] Geologic, Soil, and Seismic Survey – Emilia-Romagna Region, Viale Aldo Moro 30, Bologna, Italy

2.2 Abstract

Urban geological modelling plays a crucial role in facilitating the sustainable utilization of the urban subsurface and the development of effective strategies for geohazard mitigation. Traditionally, geological models of urban areas rely on lithological correlations of boreholes and well data. However, in complex depositional settings such as alluvial environments, where the standard concepts of superposition and lateral continuity of strata are often violated, lithostratigraphic correlation can be challenging even over short distances, leading to considerable uncertainty in the final geological model. Therefore, in such cases, lithofacies analysis can provide a more robust categorisation of subsurface geological units as lithofacies mainly reflect the depositional process, while their associations provide a reliable picture of sedimentary bodies and their geometries. In this work, we used the lithofacies correlation approach to develop a 3D geological model of the urban area of Bologna (Italy) where a complex, thick alluvial succession makes lithological correlations very difficult. To minimize subjectivity, we re-interpreted 940 existing borehole logs in terms of depositional facies and combined stratigraphic data with geophysical HSVR (Horizontal to Vertical Spectral Ratio) measurements and surface analysis (morphology and river network) based on a DTM (Digital Terrain Model). This led to the detailed reconstruction of the subsurface depositional architecture, forming the basis for the 3D geological model. The model revealed the presence of three distinct depositional domains with different stratigraphic architectures. From west to east: Domain A (Reno River) corresponds to the gravel-dominated fill of a river valley abruptly passing to Domain B (Bologna urban area) that represents a morphological and stratigraphical divide, topographically elevated with respect to the surrounding areas and characterised by fine-grained deposits with frequent paleosols. Lastly, Domain C (Savena River) exhibits the typical alluvial fan pattern, marked by a gentle convex-up surface morphology with gravelly-sandy deposits with a low degree of lateral amalgamation. The geological model effectively explains the distribution of ground subsidence in Bologna since the 1960s, which is attributable to significant groundwater pumping. This is evident from the comparison of the model with both the ground displacement contours resulting from the 1983 – 1987 topographic levelling campaign and the subsidence rate map derived from the 2006 – 2011 Radarsat interferometric survey. Subsidence shows strong variations at the domains' boundaries, especially at the limit between Domain A (Reno River) where high values prevail, and Domain B (Bologna city centre) characterised by the lowest values.

2.3 Introduction

Underground space has become increasingly important for the sustainable development of urban areas (Hooimeijer & Maring 2018; Von der Tann et al. 2019) since it provides new construction space, saves land resources, alleviates the pressure on the surface, preserves cultural heritage, and absorbs in part environmental pollution (He et al. 2020; Volchko et al. 2020). The subsurface is also rich in geothermal resources that offer great potential for decarbonisation and is a major source of drinking water (Huggenberger & Epting 2011; Hemmerle et al. 2022). Moreover, subsurface areas are less susceptible to natural disasters and can increase the resilience of future cities (Price et al. 2016). For these reasons, underground development is nowadays seen as the main path towards modern sustainable cities.

The key requirement for subsurface planning is a superior understanding of local geological conditions. A well-developed geological model is a prerequisite for obtaining reliable geotechnical, geomechanical, and hydrogeological models, as well as for assessing and mitigating natural hazards (El May et al. 2010; Culshaw & Price 2012; Lapenna et al. 2020). Typically, urban subsurface models are built by combining different types of data (boreholes, wells, geological maps, stratigraphic cross-sections, geophysical surveys) in order to understand the 3D distribution of geological units. Modelling strategies depend on the specific aims of the study, and different approaches have been used to balance user requirements with geological complexity and

data availability (e.g., Thierry et al. 2009; Stafleu et al. 2011; Mathers et al. 2014; Fordyce & Campbell 2017; Kokkala & Marinos 2022). Regardless of the modelling procedure, the first and most important step is the subdivision of sedimentary sequences into homogeneous geological units. Different criteria can be used for this purpose, such as lithostratigraphy, chronostratigraphy, or biostratigraphy (Miall 2016). Urban geological models are primarily based on lithostratigraphy. Lithostratigraphic units are differentiated based on the type of rock or soil, namely its composition and texture. Lithology is an objective parameter that can be easily derived from borehole descriptions and that is closely related to the mechanical, physical, and hydrological properties of the material. For this reason, most published models employ this criterion to represent the urban subsurface.

However, in complex depositional environments, lithology-based stratigraphic correlation can be challenging. Alluvial deposits, in particular, consist of stacked sequences of coarse-grained sediments that commonly violate the standard concepts of superposition and lateral continuity of strata (Miall 1985). In such cases, the sequence stratigraphic approach has the potential to overcome the limitations of lithostratigraphy. Sequence stratigraphy combines lithofacies analysis, biostratigraphy, and chronostratigraphy to subdivide sedimentary deposits into time-coherent packages (Van Wagoner et al. 1990; Posamentier & Allen 1999; Catuneanu 2006; Miall 2016). The fundamental point of this approach is the recognition of stratigraphic surfaces that bound sedimentary facies (i.e., lithostratigraphic bodies) formed in specific depositional environments (e.g., floodplain, active channel, crevasse splay, etc.). Since depositional systems include facies tracts where the spatial distribution of lithostratigraphic units can be predicted, lithofacies provide a powerful framework for stratigraphic correlation beyond the simple lithologic approach and are widely employed in oil and gas exploration (Vail et al. 1977; Wornardt 1993; Miall 1996). Despite its potential, sequence stratigraphy received little attention in urban geology. This is probably attributed to the challenges in reconstructing lithofacies associations from borehole logs, which requires specific sedimentological expertise. Only a few studies used such a multidisciplinary approach to reconstruct urban subsurface (Velasco et al. 2012; Salvany & Aguirre 2020).

In this work, we combine morphological, geophysical, and stratigraphic analyses to develop a 3D geological model of the city of Bologna, in northern Italy. Bologna is settled upon a hundred-metres thick alluvial succession with a complex internal architecture that makes traditional lithological correlation very difficult. A Digital Terrain Model (DTM) based analysis, combined with a detailed reconstruction of the stratigraphic architecture relying on lithofacies correlations of more than 900 boreholes and wells, and integrated with a geophysical survey based on the HVSR technique (Horizontal to Vertical Spectral Ratio) enables the identification of three depositional domains within the study area. Despite their common alluvial origin, the three domains exhibit distinct surface morphology and subsurface deposits stacking patterns, implying different geotechnical behaviours, as revealed by the comparison between the obtained subsurface geological model and the ground-subsidence maps derived from InSAR (Interferometric Synthetic Aperture Radar) data. The subsidence values, in fact, display a spatial distribution within the study area that allows the distinction of three different areas, well overlapping the three identified geological domains.

The present study emphasizes the effectiveness of the lithofacies approach in constructing a reliable geological model within complex alluvial settings, as the subsurface units are correlated considering the depositional environment they belong to and the inferred geometry, thus reducing the subjectivity of interpretation and providing useful information on potential geotechnical implications.

2.4 Study Area

The city of Bologna (Italy) is located at the southern margin of the Po Plain (Fig. 2.1). The Po Plain represents the surface of a subsiding foreland basin, bounded by two fold-and-thrust belts: the Alps to the north and the Northern Apennines to the south (Pieri & Groppi 1981). This foreland basin is filled by a Pliocene–Quaternary sedimentary succession characterised by shallowing-upward sequences (Castellarin et al. 1985; Ricci Lucchi 1986). Most of the Northern Apennines, including the areas south of Bologna, has undergone a general uplift since the early Pleistocene (Argnani et al. 2003). The Po Plain, instead, including the area of Bologna, subsided at rates of 1–2 mm/year during the last 1.43 million years (Carminati & Di Donato, 1999).

The study area is about 88 km2 and extends west to east from the Reno River to the Savena River, and south to north from the Apennine foothills to the northern suburbs of Bologna (Fig. 2.1). Elevation ranges from about 80 m a.s.l. at the Apennine foothill to about 30 m above sea level (a.s.l.) in the northwest corner. Surface deposits mostly consist of gravels, sands, and fine-grained soils related to the fluvial activity of the Reno and Savena rivers.

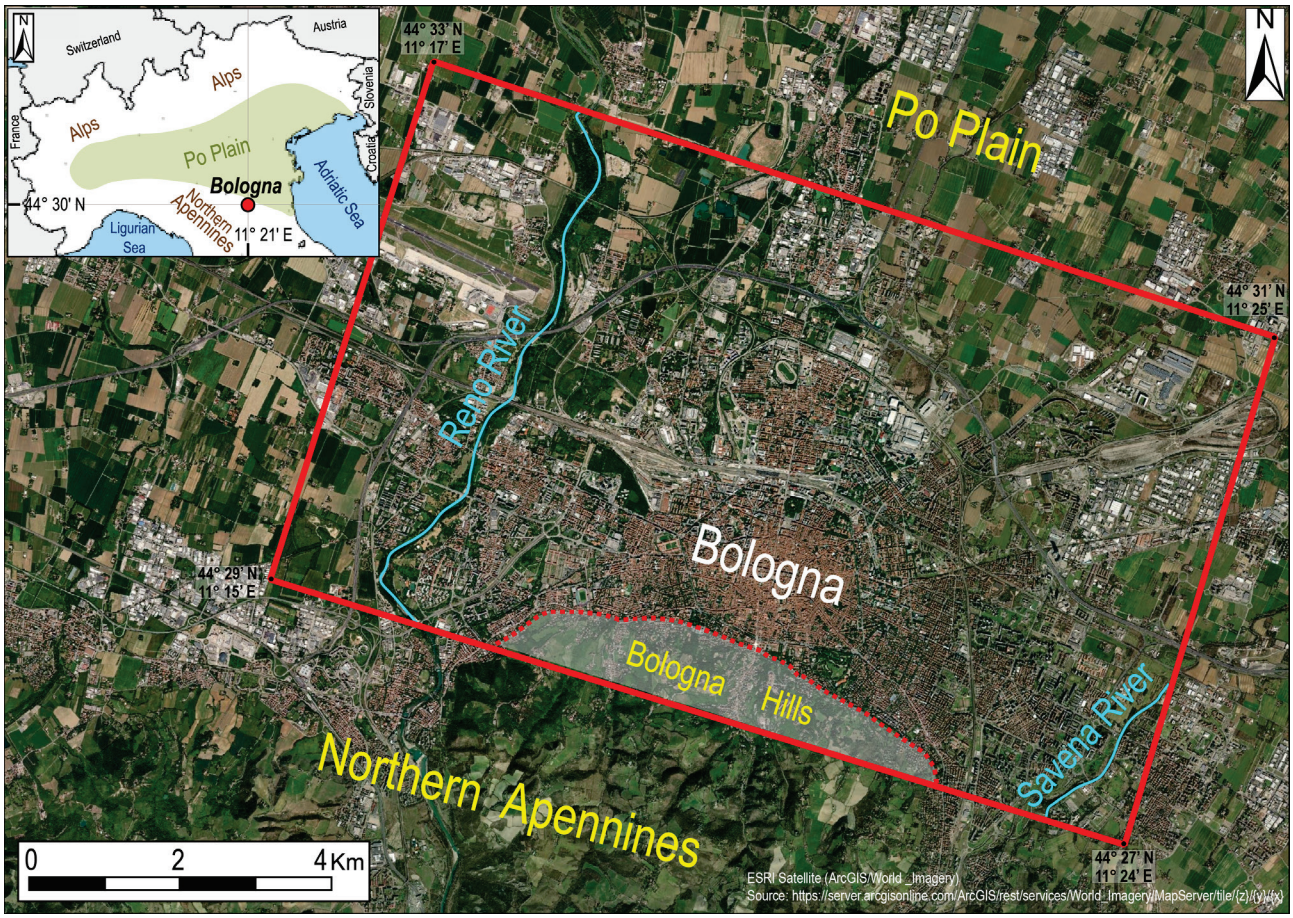

Fig. 2.1 Study area (red rectangle). The city of Bologna (northern Italy) is located at the southern edge of the Po Valley, at the foot of the Northern Apennines, in an area between the two main rivers crossing this sector of the plain: the Reno River to the west and the Savena River to the east.

According to the Geological Map of Italy 1:50000 (Sheet 220 "Casalecchio di Reno" and Sheet 221 "Bologna") by ISPRA , Istituto Superiore per la Protezione e la Ricerca Ambientale (2009), thick gravel bodies are present at the outlets of the Reno and Savena rivers, that grade into alternations of sands with mud-prone strata in their distal part (section AA', Fig. 2.2). Underneath the Bologna historical centre (see Fig. 2.2, section BB') coarse-grained fluvial deposits are rare and occur only at depths greater than 100 m. The centre of

Bologna, indeed, acted as an interfluve during the Holocene, the Late Pleistocene, and part of the Middle Pleistocene (Amorosi et al. 1996, 1997; Bruno et al. 2013). Here, a stacked succession of paleosols dating from the Middle Pleistocene onwards suggests prolonged periods of subaerial exposure (Amorosi et al. 2014; Bruno et al. 2020).

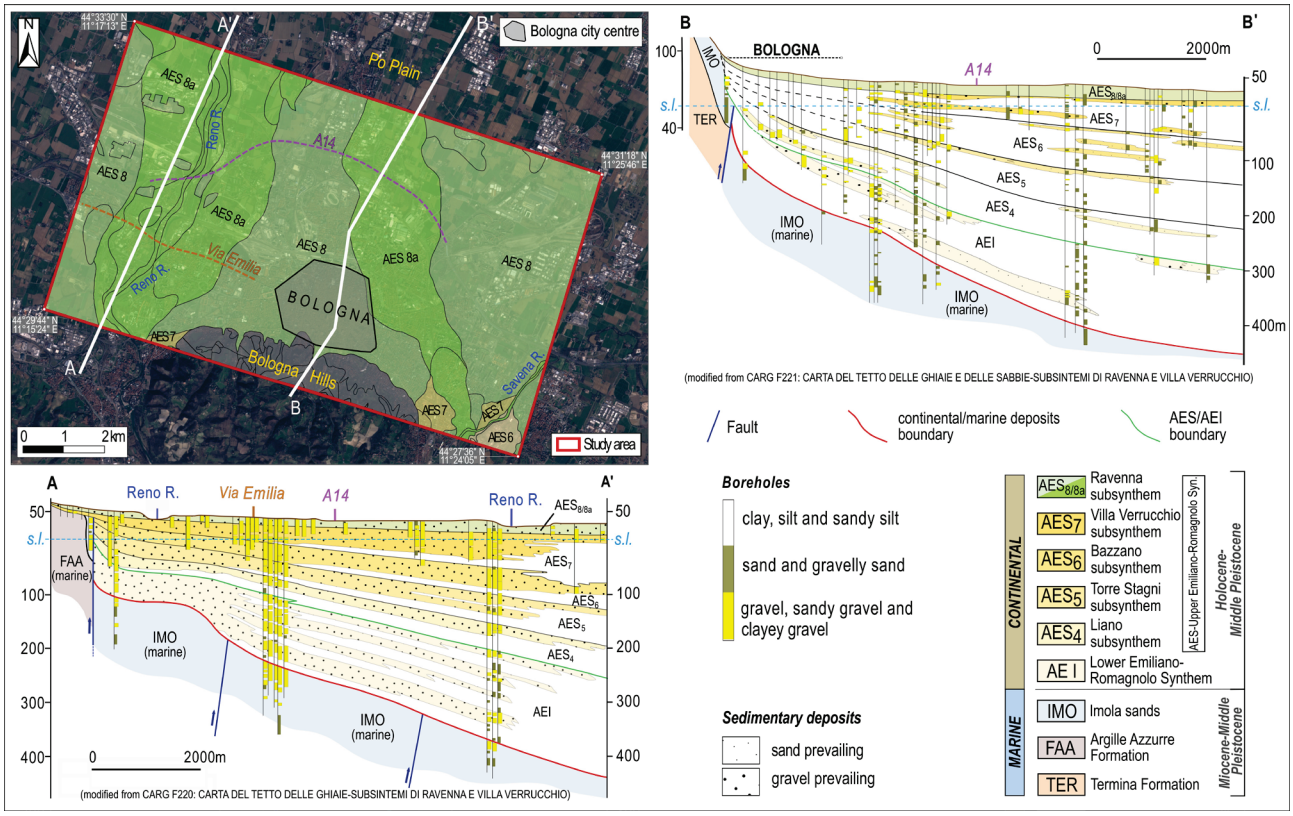

Fig. 2.2 Geological setting of the study area. Geological map of Bologna and stratigraphic cross-sections showing the late Quaternary stratigraphy beneath the Reno River (AA') and the urban area of Bologna (BB'). In the Geological Map of Italy 1:50000 (Sheets 220-221 and related notes), alluvial deposits are subdivided into two synthems, the Lower and the Upper Emilia-Romagna Synthems (AEI and AES, respectively), separated by a regional unconformity dated to 450 ky BP (Martelli et al. 2017). The base of AEI is marked by the unconformity separating marine-coastal sediments (TER, FAA, and IMO) from continental deposits, dated to ca. 800 ky BP (Gunderson et al. 2014). The internal architecture of AEI and AES is characterized by the cyclic alternation of coarse-grained deposits with fine-grained strata (Amorosi et al. 1996; 2008), reflecting Milankovitch-scale (100 kyrs) climate oscillations. This cyclic structure of lithofacies permitted the subdivision of AES into five lower-rank units (subsynthems): AES4, AES5, AES6, AES7, and AES8. Sediments belonging to AES8 (dated to the Holocene) and its sub-unit AES8a, corresponding to post-Roman deposits, are largely exposed in the study area.

2.5 Methodology

The 3D geological model of Bologna was developed by integrating surface and subsurface data as shown in Figure 2.3.

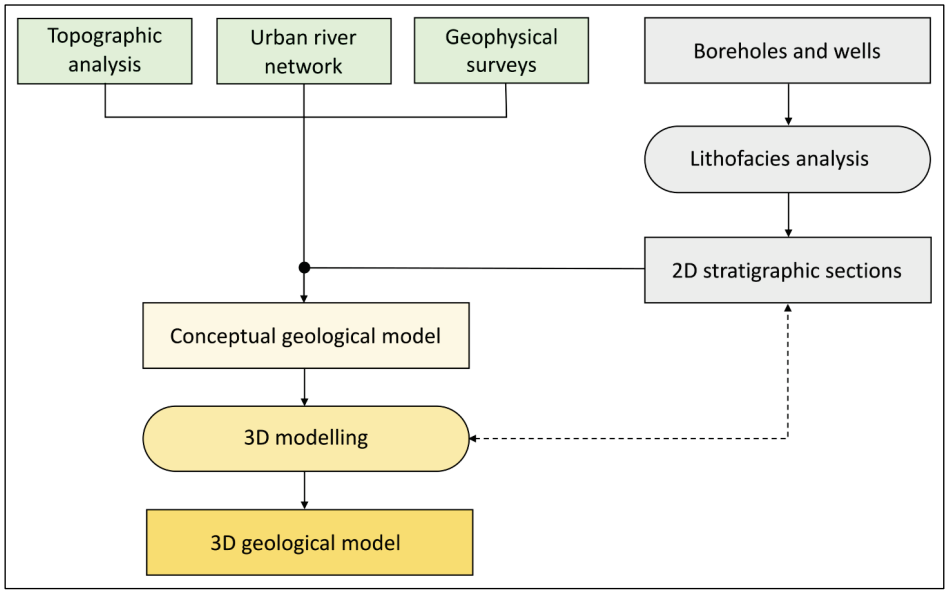

Fig. 2.3 Flowchart illustrating the methodology employed to develop the 3D geological model of the study area. Rounded boxes highlight activities driven by expert judgment.

2.5.1 Surface morphology

Surface morphology was analysed using a 10 m resolution Digital Terrain Model (DTM) obtained by digitizing the contour lines from the 1:5000 topographic map. The DTM has a planimetric accuracy (Root Mean Square - RMS) of 4 m, and although small-scale fluvial landforms such as levees, terraces, or depositional lobes may not be discernible, the DTM effectively captures the overall topography of the area. To enhance the visibility of the main topographic features associated with fluvial activity, we employed a custom colourmap consisting of a repeated sequence of rainbow colours (see section 2.6.6). Additionally, a set of topographic profiles with varying orientations was extracted to highlight the main topographic changes.

2.5.2 Urban river network

The urban area of Bologna is fed by several small watercourses that flow down the hills and cross the city through a network of canals and sewage. These streams are characterised by small watersheds (a few square kilometres) with very limited sediment transport capacity. However, during the Holocene, they delivered large amounts of sediment to the area between the Reno and Savena rivers playing a significant role in land building. The stream network of the urban area was reconstructed by integrating recent literature (Cremonini 1980; 1992; Elmi et al. 1984) with historical maps (Chiesa 1742).

2.5.3 Geophysical surveys

A geophysical campaign based on the HVSR technique (Horizontal to Vertical Spectral Ratio, Nakamura 1989) was carried out to detect the boundary between marine and continental deposits (IMO-AEI limit in Fig. 2.2)

and support the stratigraphic analysis. HVSR measurements provide an estimate of site resonant frequencies that are a function of subsurface geology (Castellaro & Mulargia 2009; Choobbasti et al. 2013; Moisidi et al. 2015, Martona et al. 2016; Akkaya & Özvan 2019). Forty-five HVSRs tests were performed in the central and southern parts of the city (Fig. 2.4) using a three-component sensor-velocimeter (Tromino™ from Micromed). To achieve adequate statistical sampling for the frequency range used in this study (0.1 to 64 Hz), ground vibrations were sampled at 128 Hz for 16 minutes at each measurement station (SESAME 2004). HVSR data were then combined with the results of MASW (Multichannel Analysis of Surface Waves) and ESAC (Extended Spatial Autocorrelation) surveys carried out by the Geological, Soil and Seismic Survey of Emilia-Romagna (RER) as part of the seismic microzonation of Bologna, to assess the shear-wave velocity profile at each measurement station. Post-processing was undertaken using the Grilla software (Micromed).

2.5.4 Boreholes and wells

Subsurface stratigraphic data were extracted from the open-access RER geognostic database. The RER database returned 940 stratigraphic data consisting of 312 water wells and 628 continuous-core boreholes. The overall data density is about 10 points for km^2, with a mostly clustered spatial distribution. The highest density is around railway lines and pumping well fields while the lower density is in the northern part of the area (Fig. 2.4). The major differences between wells and continuous cores are the quality of log descriptions and the investigation depths. Continuous cores are generally shorter but contain accurate lithological descriptions that are useful for facies interpretation. Water wells are typically deeper (down to 480 m, Fig. 2.4), but often subsurface stratigraphy is poorly described. The wide time span of the dataset (from 1900 to 2021) is a further element of complexity since the terminology and detail used for the stratigraphic description varied through time.

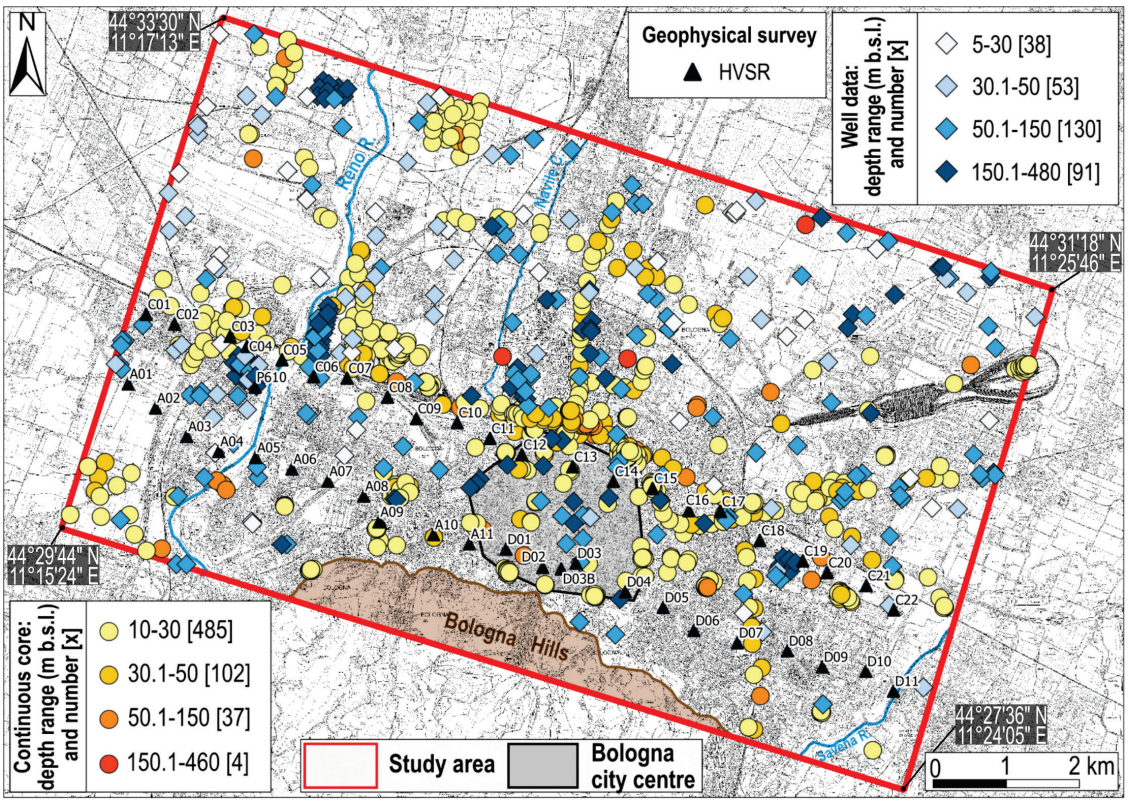

Fig. 2.4 Subsurface data and geophysical investigations. Location of boreholes and wells extracted from the RER geognostic database (circles and diamonds) and HVSR measurements (triangles).

2.5.5 Lithofacies analysis

All the boreholes and wells were re-interpreted in terms of lithofacies. Lithofacies are stratigraphic intervals based on lithology and a set of accessory components (fossils, vegetal remains, carbonate nodules etc.) that bear a direct relationship to the depositional process. Lithofacies are the key component of facies associations, which are usually defined by the study of outcrops (where two- or three-dimension geometry and lateral extent of sediment bodies can be observed) and by analogy with modern depositional environments (Allen 1963; Bridge et al. 2000). Stratigraphic correlations guided by lithofacies and their lateral relationships (facies tracts) allow a plausible reconstruction of subsurface stratigraphy, as they offer a reliable picture of sediment bodies and their geometry. In complex alluvial environments, such as the subsurface of Bologna, lithofacies analysis requires integrating basic geological information (grain size, texture, and thickness) with additional data, such as the type (abrupt vs gradual) of stratigraphic contact. Based on the existing literature on lithofacies of alluvial systems, both from worldwide outcrops (e.g., Miall 1977, 1978, 1985) and exposures near Bologna (Ori 1982; Bruno et al. 2015), nine different lithofacies, listed and described in Table 2.1, were considered. The lithofacies and their reciprocal spatial relationships are graphically depicted in Figure 2.5, where the two depositional environments that typically host such lithofacies, i.e., the alluvial fan and the alluvial plain, are schematically represented. As it can be seen, gravelly lithofacies characterise both alluvial fan and floodplain environments with different plan distribution and vertical stacking pattern due to the different sedimentation processes. Amalgamated successions of gravels with radial arrangements on plan dominate the proximal and medial portions of the alluvial fan (A-B, B-C, Fig. 2.5). These deposits result from the loss of flow capacity of a fluvial channel emerging from a mountain catchment onto the plain. In proximal locations gravels are typically very thick, massive and poorly sorted (lithofacies PC, Table 2.1). Moving towards the plain, these deposits (lithofacies DC, Fig. 2.5) may vertically alternate with fining-upwards sequences of gravelly and sandy deposits (lithofacies Ch1, Fig. 2.5). These alternations result from the irregular and intermittent activity of multiple channels characterising the medial portion of the alluvial fan. In distal portions (C-D, Fig. 2.5), where the channels activity become prevalent, lithofacies similar to those characterising the alluvial plain can be found. Fluvial channels are responsible for the alluvial plain formation. Fining upwards gravelly-to-sandy/silty deposits (lithofacies Ch, Table 2.1) typically mark the depocentral area of the river. In the adjacent areas, such as levees (lithofacies Lv, Table 2.1) and overbanks (lithofacies O, Table 2.1), increasing amount of silty, silty-clayey, and clayey deposits, with latero-vertical heteropy typically occur. Within these areas, sandy-to-silty layers (lithofacies Cr, Table 2.1) may also be present, whereas the floodplain (PF/WF) is dominated by clayey deposits.

Code	Lithofacies	Main sedimentological features
A/S	Anthropogenic/Soil	Surficial deposits made of heterogeneous filling material, such as brick fragments, pebbles, and asphalt often included within a matrix of variable grain size (*A*) or vegetal terrains frequently containing roots and organic matter (*S*)
PC/ DC	Proximal alluvial fan channel/ Distal alluvial fan channel	Very thick hetero-granular and heterogeneous gravel deposits, from matrix-supported to grain-supported, with frequent amalgamation and usually abundant sandy/clayey matrix (*PC*) or very thick gravel deposits typically characterised by a clast-supported texture with a subordinate sandy/clayey matrix (*DC*).
Ch	Fluvial channel	Thick gravel-to-sand and coarse sand-to-silty sand deposits, typically forming fining-upward sequences, corresponding to the equivalent at distal location, i.e., towards the plain, of the gravel-rich facies identified at the river outlet (*PC* and *DC*) and mostly characterising the middle-distal portion of the plain.
ChA/Dv	Channel abandonment/ Deactivation	Clay, less frequently silt, with a very low average thickness, sharply lying on thick gravel deposits. At distal locations (*ChA*), clays may include organic matter, while at more proximal locations clays are associated with thin pebble or sand layers (*Dv*). *ChA* is interpreted as the abrupt abandonment of the fluvial channel, such as in the case of an avulsion event, and may pass upwards to the floodplain facies (e.g., *O*, *WF*, and *PF*). *Dv* represents, instead, the sudden deactivation of a stream. It can be followed by reactivation, testified by the superposition of thick gravel deposits, corresponding to lithofacies *PC* and/or *DC*.
Lv	Levee	Alternating cm-thick to dm-thick silt/clay and sand deposits. This lithofacies usually characterises the upper part of a fluvial channel sequence, although it may be also found within a thick floodplain succession.
Cr	Crevasse	Thin fine sand to sandy silt deposits usually associated with flood layers formed when riverbanks break up, with the spilling of sandy and silty deposits on the floodplain. Crevasse deposits can interrupt floodplain sequences abruptly, at distinct stratigraphic levels.
O	Floodplain with overbank	Clay deposits of variable consistency and thickness, marked by the recurrence of thin silty, sandy silt, and silty sand layers. They represent the over-bank deposits, related to flood events affecting floodplain areas nearby the fluvial channel.
WF	Well-drained floodplain	Usually thick, yellowish to brownish, mostly stiff, clay deposits. The occurrence within clayey deposits of calcareous nodules is very common. This lithofacies represents undisturbed floodplain deposits, usually undergoing subaerial exposure
PF	Poorly-drained floodplain	Light to dark grey, generally soft clay, usually thick, occasionally including organic material. This lithofacies corresponds to undisturbed floodplain deposits, commonly undergoing stagnant conditions.

Table 2.1 Lithofacies used to characterize the alluvial deposits under the city of Bologna.

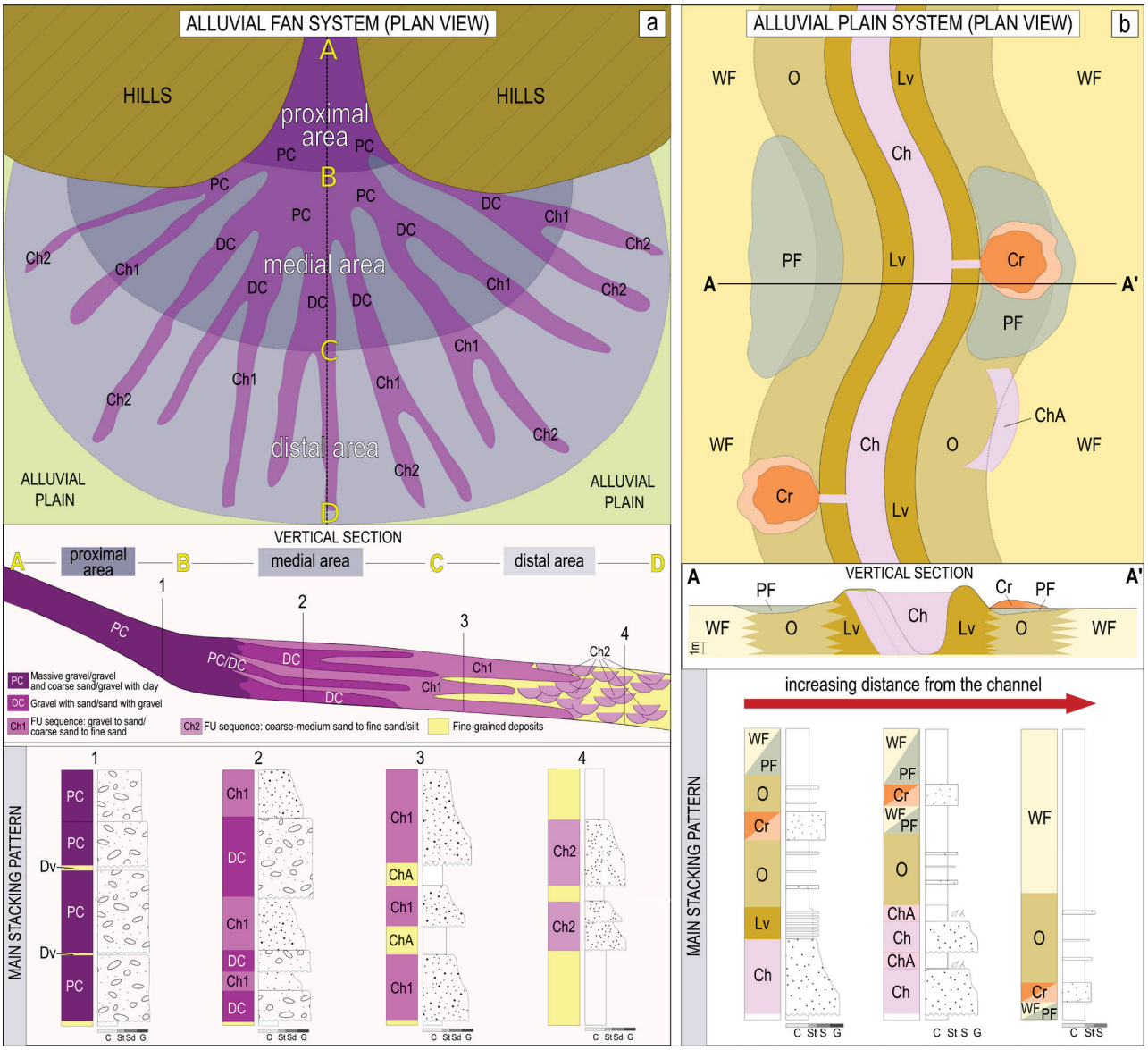

Fig. 2.5 Depositional environments and lithofacies distribution. Schematic representation of an alluvial fan (a) and alluvial plain (b) depositional systems with the spatial locations of the corresponding different lithofacies.

2.5.6 Two-dimensional stratigraphic cross-sections

Thirteen stratigraphic cross-sections were drawn parallel and perpendicular to the general depositional strike to identify the main sedimentary bodies (Fig. 2.6). Eight cross-sections were traced NW-SE and five SSW-NNE, covering the whole study area. All transects were drawn to intercept the most significant boreholes, with a resulting average spacing of 1 borehole every 400 m. Along each section, stratigraphic correlations were carried out based on the lithofacies criterion illustrated in the previous section, overcoming the limitations arising from the oversimplified correlation of strata on a lithological basis. Considering the expected geometry of each deposit type, similar lithofacies were correlated based on their stratigraphic position, essentially allowing the lateral and vertical distribution of fluvial deposits to be traced, as opposed to floodplain deposits (see sub-section 2.6.5.1 and 2.6.5.2). A denser grid of differently oriented straight-lined sections including projected boreholes data was then carried out within a 3D modelling software, Leapfrog Works (Seequent Limited) to validate the stratigraphic framework derived from the 13 main cross-sections shown in Figure 2.6.

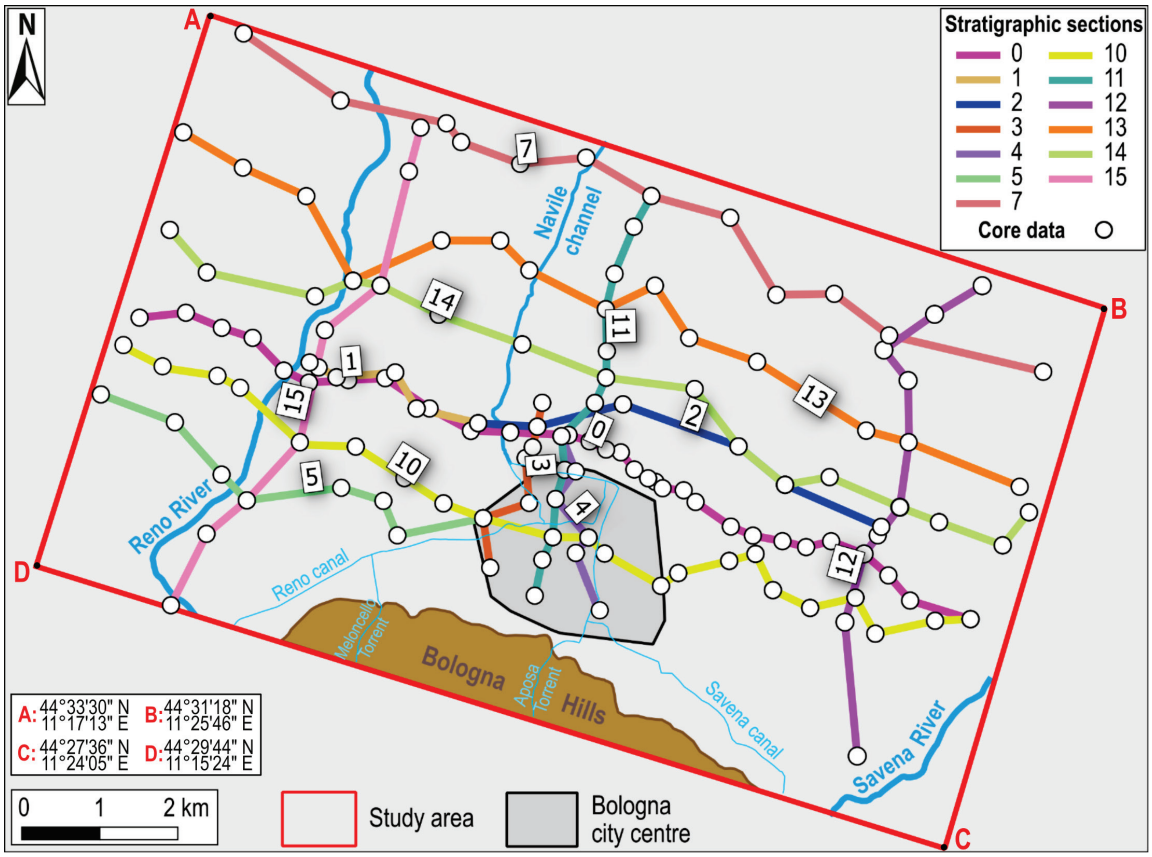

Fig. 2.6 Location of the stratigraphic cross-sections.

2.5.7 Simplified geological model

The combination of surface morphology, drainage network, geophysical surveys, and 2D stratigraphic cross-sections lead to the development of a simplified geological model. In particular: i) surface morphology supported facies interpretation in the shallow subsurface based on core descriptions; ii) river network analysis guided the correlation of coarse fluvial deposits and possible subsurface distribution of ancient alluvial fan complexes (lithofacies Ch, PC, and DC); iii) geophysical surveys were used to model the boundary between continental and marine deposits detected in deep boreholes; iv) 2D stratigraphic sections provided the geometry of the main sedimentary bodies. The simplified geological model provided a basic understanding of the main geological domains and guided 3D modelling in our complex case.

2.5.8 3D geological model

3D geological modelling was carried out using the Leapfrog Works 3.1 software. This software allows to visualise and manage spatial data and can model underground infrastructures like tunnels or pipelines, which are important in urban areas. The 940 boreholes selected from the RER database, reinterpreted in terms of lithofacies, were uploaded to the Leapfrog environment and the modelling domain volume was created. To outline the model within the three dimensions, the perimeter of the study area was used to define its lateral extent, whereas the DTM and the continental/marine boundary were chosen as its top and bottom, respectively. Then, alluvial bodies were modelled according to the thirteen 2D stratigraphic cross-sections.

The 3D modelling was performed using two different interpolating tools, called “Intrusion” and “Deposit”. The two interpolators utilize distinct logic, algorithms, and different operational procedures, producing alternative graphical outputs. The “Intrusion” tool generates a 3D surface that tightly encloses manually selected lithofacies intervals from a restricted group of boreholes, resulting in a limited extension sedimentary body. This 3D surface interpolation is based on a linear semi-variogram model, which assigns weight to the surrounding stratigraphic data based on their distance from the considered deposit (Seequent 2019). The “Deposit” tool interpolates a sheet-like surface that passes through the contact points between two distinct units, based on their stratigraphic relationships, in terms of “younger/older” deposits. This surface considers/include all the available boreholes, extending to the whole modelling domain, and represents the top/bottom of a certain unit with respect to a confining one. Thus, two surfaces (i.e., top and bottom) are needed to /define each single tabular sedimentary body. In both scenarios, the modelling procedure for each element is manually controlled and based on the attribution of user-defined parameters describing its spatial orientation and shape. 3D modelling of our complex lithostratigraphic setting required a simplified operational approach. The logic was to merge lithofacies belonging to the same depositional environment: lithofacies Ch, PC, DC, Lv, Cr, ChA/Dv, and O, which refer to the fluvial environment in which traction processes prevail, were grouped and attributed to a single class named “granular deposits”; whereas WF and PF, related to the fluvial environment dominated by the settling of clay particles, were grouped in a single class named “fine-grained deposits”. Thin (<5 m) granular bodies embedded within thick fine-grained successions with low correlation potential were individually shaped with the “Intrusion” tool, but finally merged with the hosting fine-grained deposits and attributed to a third class named "fine-prevailing deposits". Although the final model contains only three units (granular deposits, fine-grained deposits, and fine-prevailing deposits), all nine lithofacies were used to guide the correlation process.

2.6 Results

2.6.1 Surface morphology

The visual analysis of the DTM reveals a particular morphology for the study area. Although the topography is almost flat (Fig. 2.7a), three distinct zones were recognized (Fig. 2.7b):

- zone A is crossed by the Reno River and is characterised by an overall flat morphology, with relatively low ground elevation ranging between 30 and 50 m;
- zone B covers the urban area of Bologna and it is characterised by a slightly convex-up morphology, with a higher elevation of about 60 m;
- zone C is crossed by the Savena River and shows a marked convex-up morphology, with an average elevation of about 50-60 m.

Zone B, therefore, stands as a “relative high” between the Reno and Savena rivers. The transition from the Reno River (zone A) to the “relative high” is quite abrupt (see Fig. 2.7, topographic profile T1), while the western limit of the Savena River (zone C) is marked by a narrow incision. The “relative high” of the Bologna urban area is no longer present at a distal location (see topographic profile T2, Fig. 2.7) where areas A and C merge.

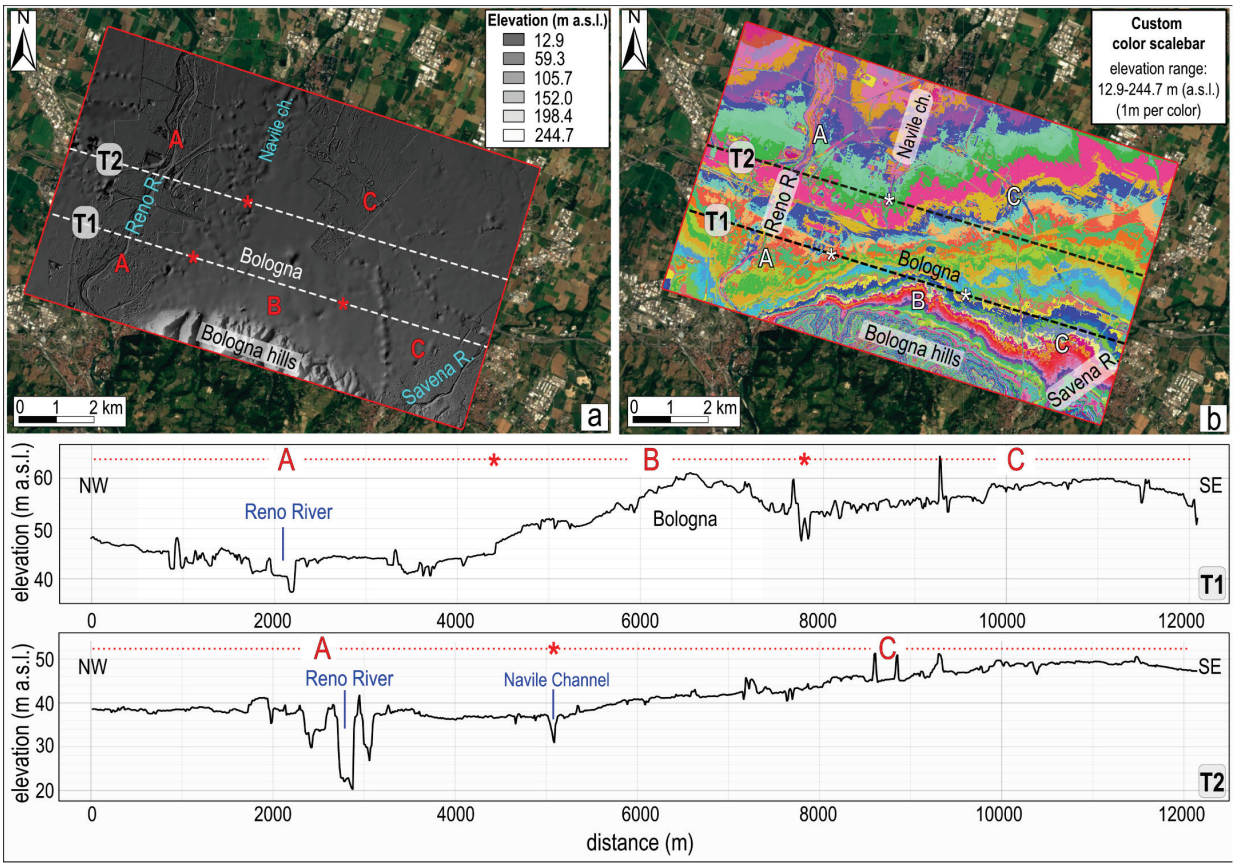

Fig. 2.7 Shaded relief (a) and Digital Terrain Model (b) of the study area. T1 and T2 are topographic profiles showing the overall surface morphology perpendicular to the main depositional strike. The occurrence of local spikes along the two topographic profiles can be attributed to anthropic features (e.g., highways, overpasses…) and to artifacts depending on the quality of the DTM.

2.6.2 Urban river network

Figure 2.8 shows the river network of the Bologna urban area. The streams flow in the south-north direction and cross the historical city centre merging with an artificial channel network dating back to the Middle Ages and Renaissance. Within the perimeter of the historical centre, these artificial watercourses have a total length of about 6.6 km and nowadays, after centuries of human intervention, are buried for about 95% of their cumulative course. The sections that have not been filled mostly belong to the Reno and Moline channels (Fig. 2.8b). The anthropic channel network in the historical centre is fed by two artificial canals that depart from the Reno and Savena rivers. The first one, called Reno Canal, has a length of about 4.3 km and WSW-ENE orientation; the Savena Canal, is about 3.7 km long and ESE-WNW oriented. The other main artificial canal is the Navile, which flows for 4.6 km within the study area in a depressed reach elongated in SSW-NNE direction (possibly corresponding to a former Aposa riverbed, Elmi et al., 1984), located north of the city centre and about 3 km east of the Reno River. This zone and its prosecution northwards have been occupied during Roman times by a Reno River paleochannel, known as “Ancient Reno”. The Savena River historic course observed in historical maps (“Abandoned Savena” in Fig. 2.8a; Chiesa 1742) was active until 1776, before diversion by anthropic activities (Cremonini 1980; Elmi et al. 1984). Nowadays, the Abandoned Savena is fed by the anthropic channel network and is pensile in its northernmost section.

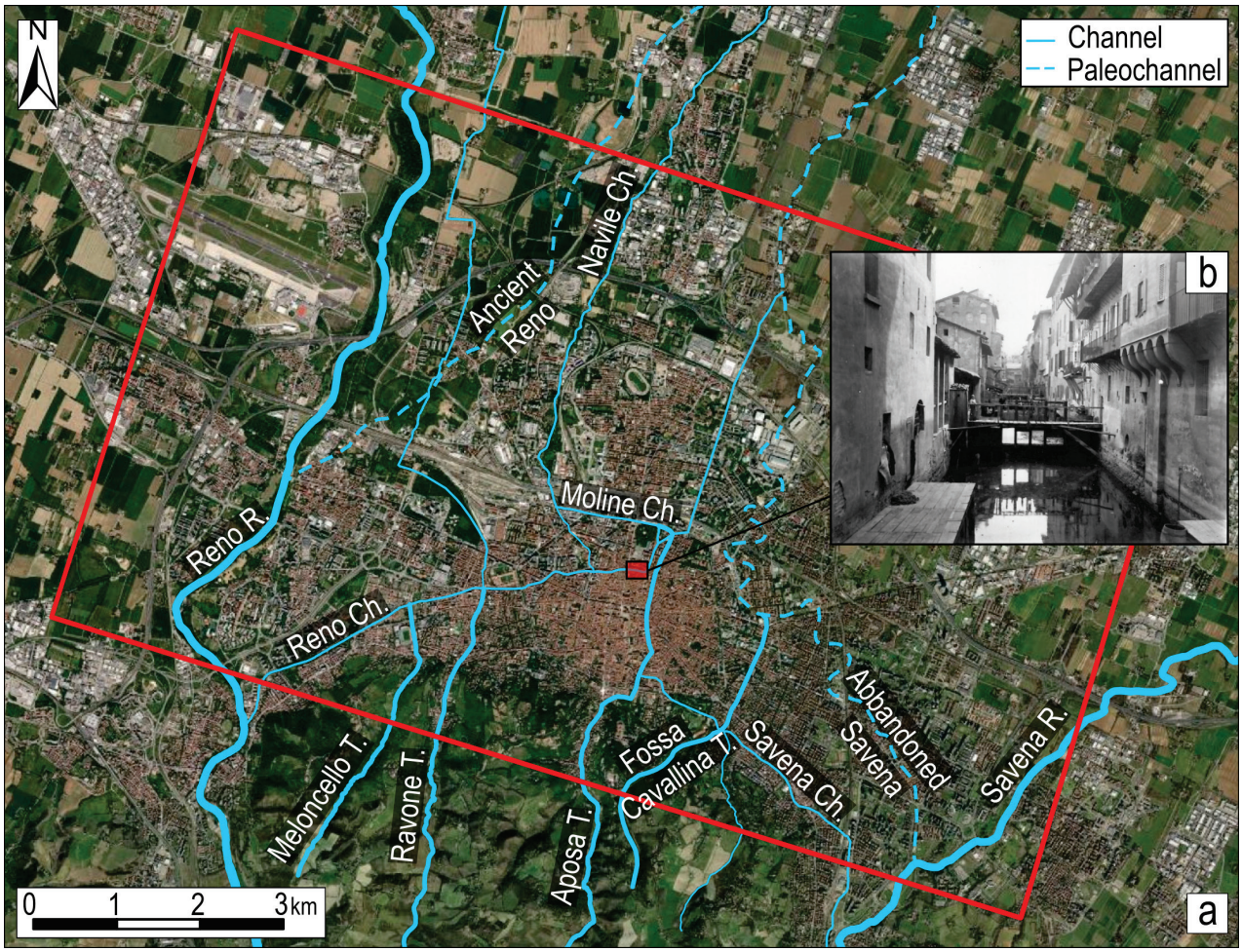

Fig. 2.8 a) Hydrographic network of the study area. The thickness of the light-blue lines represents the type of channel: maximum for rivers, medium for torrents, and minimum for artificial canals. Dashed lines indicate paleochannels; b) the red square marks the location of the provided picture, showing a detailed view of the Moline channel ("Bologna, Moline Channel, Anonymous [1900-1920], Fondo Gonni").

2.6.3 Geophysical surveys

The seismic stratigraphy obtained by HVSR measurements showed a good correlation with the 3 zones detected by surface morphology (A, B, C in Fig. 2.7). In zones A and C, several H/V peaks are present at shallow depth (see peaks identified by black arrows in Fig. 2.9 with values of approximately 10 Hz, likely related to the occurrence of gravel bodies interbedded with finer material), and shear waves velocity reach 600 m/s within the uppermost 50 m of depth (Fig. 2.9). Instead, in the Bologna urban area (zone B), a substantial homogeneity in the H/V trend is observed, and shear wave velocities reach 600 m/s only at depths greater than 150 m (Fig. 2.9).

The boundary between Quaternary continental and marine deposits was clearly detected only in 11 of the 35 HVSR measurements (Table 2.2). Here, an abrupt change in shear wave velocity was observed at a depth consistent with the continental/marine transition reported in the literature (RER & ENI-AGIP 1998). In all other instances, the increase in shear wave velocity is considered as small or uncertain, likely because of the small difference in seismic impedance between the two sequences of deposits.

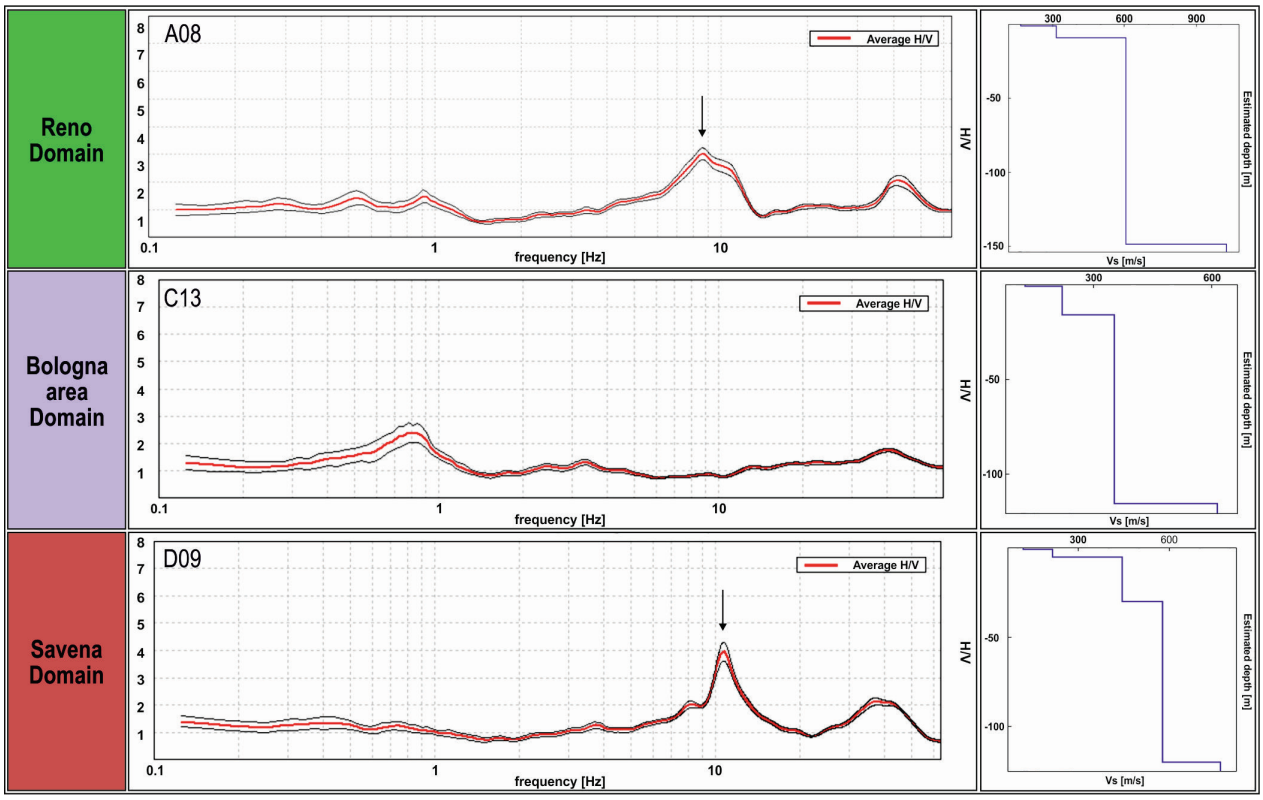

Fig. 2.9 HVSR (Horizontal to Vertical Spectral Ratio) patterns. Comparison of HVSR measured in the three different domains. The figure includes H/V graphs and Vs models resulting from the processed measurements. The H/V graphs and Vs variations with depth show similar patterns for the Reno and Savena areas (zones A and C, sub-section 2.6.1) significantly different from the pattern characterising the Bologna urban area (zone B, sub-section 2.6.1). Black arrows highlight H/V peaks likely related to gravel bodies interbedded with finer material.

HVSR measurement	Domain	Elevation (m a.s.l.)	Continental/marine boundary		Vs (m/s)
			Depth (m)	Elevation (m a.s.l.)	
A04	A	42.6	244.6	-202	955
A08	A	47.2	149	-101.8	606
A09	A	53.3	145.5	-92.2	535
A10	A	56	161.5	-105.5	603
A11	A	61.9	158.5	-96.6	542
C09	A	47.7	218.2	-170.5	683
C20	C	57.3	223	-165.7	541
C21	C	57.4	221.5	-164.1	530
C22	C	58.7	168	-109.3	508
D05	C	67	216	-149	655
D11	C	63.6	235.5	-171.9	590

Table 2.2 HVSR measurements. Vs (shear wave velocity) of the continental/marine boundary in the subsurface characterising zones A (Reno area) and C (Savena area) distinguished within the study area according to surface morphology.

2.6.4 Lithofacies analysis

The analysis of subsurface data in terms of lithofacies produced 940 tables, where distinctive lithofacies were assigned to each stratigraphic layer described in the borehole logs. Table 2.3 (Supplementary Material) shows, as an example, the lithofacies interpretation of the boreholes used in cross-section 10, which intersects the three morphological zones parallel to the foothills (Fig. 2.6). The lithofacies can be correlated both in the vertical (depth) and in the horizontal (planimetric) direction. An example of the planimetric lithofacies distribution for the shallow subsurface is shown in Figure 2.10. For each borehole, the prevailing lithofacies within the stratigraphic interval of 0-30 m is depicted in different colours. The resulting lithofacies pattern highlights a clear variation in the southern portion of the study area, from NW to SE, with proximal/distal alluvial fan channels in the Reno River area that pass to floodplains nearby the city of Bologna, and again to proximal/distal alluvial fan channels towards the Savena River. A change in lithofacies can be also observed in the NW-SE direction along the Navile Channel, from proximal/distal alluvial fan channels to fluvial channels and floodplain deposits.

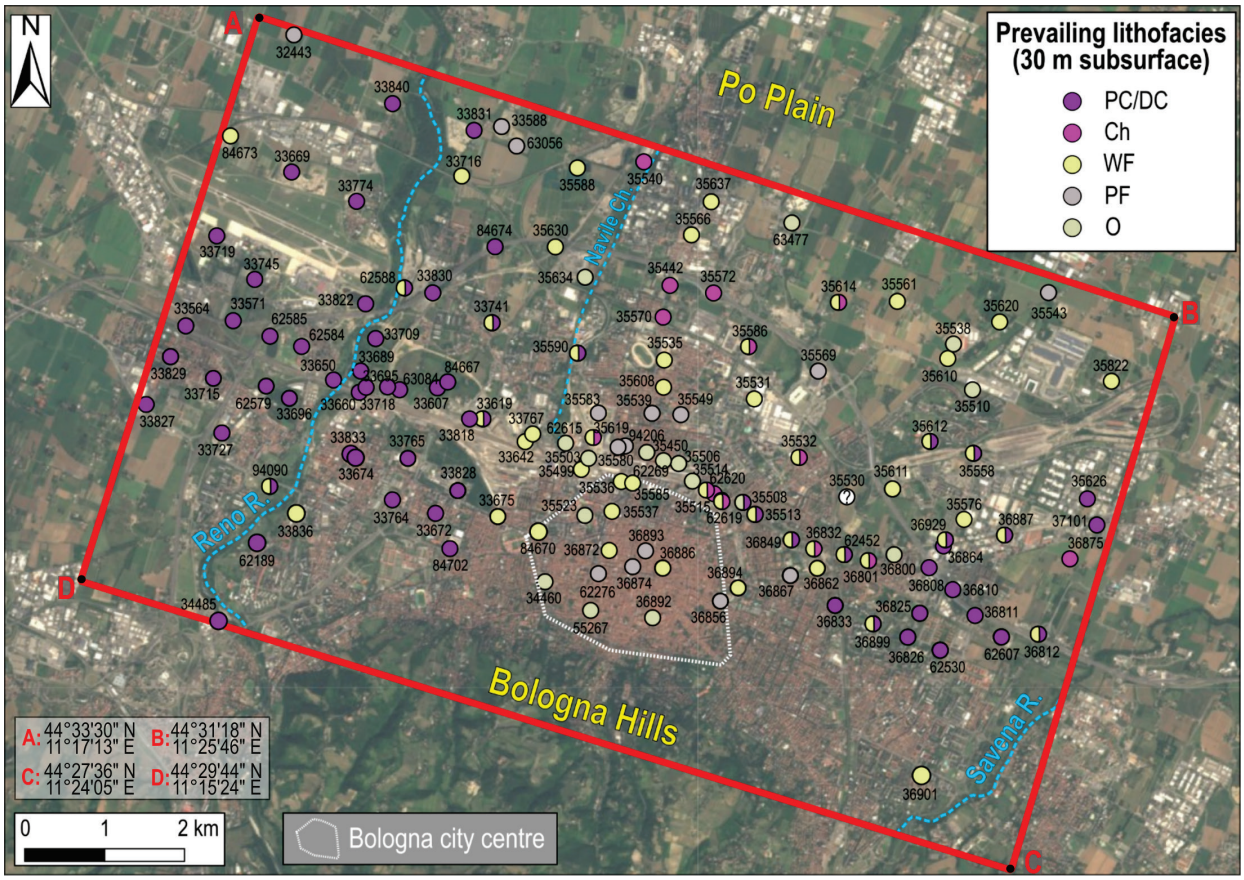

Fig. 2.10 Example of subsurface data interpretation. Boreholes intercepted by the 13 main stratigraphic cross-sections, illustrating the different prevailing lithofacies characterizing the shallow subsurface (30 m). PC= proximal channel; DC= distal channel; Ch= fluvial channel; WF= well-drained floodplain; PF= poorly-drained floodplain; O= overbank.

Figure 2.11 provides a detailed depiction of the Savena River (zone C). Here, the lithofacies distribution is particularly complex and more data (detailed lithostratigraphic descriptions and surface hydrographic network) must be used to reduce subjectivity. As can be seen, a general S-N trend can be recognised, with lithofacies passing from proximal-to-distal alluvial fan channels to fluvial channels and floodplains. In the southern-central part, the planimetric lithofacies distribution is then combined with (*i*) information on the thickness and degree of amalgamation of coarse-grained deposits, and (*ii*) the main recent drainage axes, to reconstruct the

different sedimentary bodies, highlighting the approximately radial trend consistent with an alluvial fan environment.

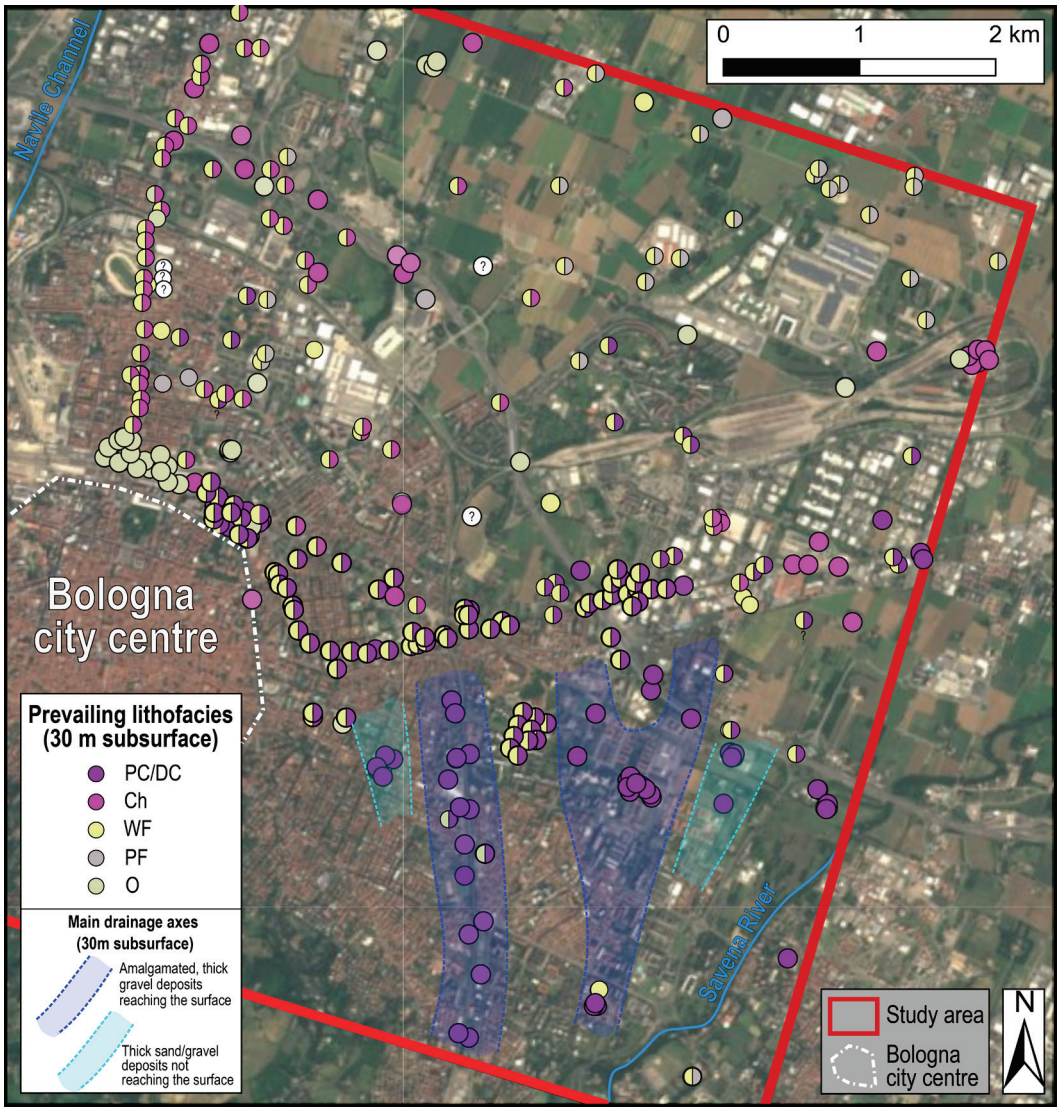

Fig.11 Detail of the Savena River area and plan lithofacies distribution. This zoomed-in view of the Savena River area illustrates the prevailing lithofacies within the shallow subsurface (0-30m) from the boreholes database. PC= proximal channel; DC= distal channel; Ch= fluvial channel; WF= well-drained floodplain; PF= poorly-drained floodplain; O= overbank.

2.6.5 Two-dimensional stratigraphic cross-sections

Lithofacies were correlated in the subsurface across the thirteen 2D stratigraphic cross-sections shown in Fig. 2.6. Due to the varying depths of the boreholes and their uneven spatial distribution, the correlation is quite robust in the uppermost 100 – 150 m and more uncertain at depths exceeding 150 m. Despite these limitations and the inherent complexity of the alluvial environment, the stratigraphic sections revealed a well-defined stratigraphic framework.

2.6.5.1 Transversal stratigraphic sections

Figure 2.12 shows the two most significant sections drawn perpendicular to the main depositional strike. Section PP' crosses the proximal area parallel to the foothills and exhibits, from west to east, three distinct

depositional domains characterised by different fluvial-channel stacking patterns. The western part, corresponding to the Reno River domain, is characterised by two gravel-dominated stratigraphic intervals (PC/DC) 100 – 150 m thick (from the surface to about -80 m, and from about -110 m to -260 m respectively) separated by 20 – 30 m of fine-grained deposits (WF). The central part of the cross-section, which corresponds to the Bologna city centre, is marked by a 100 – 150 m thick mud-prone succession (WF/PF), with isolated gravel or sand bodies (a few m thick) mainly found at depths greater than 100 m (Ch). The eastern part of the cross-section corresponds to the Savena River domain and shows, again, the predominance of sand and gravel deposits (PC/DC) down to a depth of about 100 m. Gravel bodies are here thinner, less continuous and amalgamated than in the Reno domain.

In a more distal position (section DD', Fig. 2.12), clay soils (WF/PF) are more abundant and two different stacking patterns of fluvial-channel deposits (Ch) can be observed: the western part is marked by alternating thick coarse-grained bodies with silt and clay, whereas the eastern sector is dominated by fine-grained deposits, with scattered sand or gravel bodies, a few metres thick.

2.6.5.2 Longitudinal stratigraphic sections

Figure 2.13 shows three cross-sections drawn along the main depositional strike. Section RR' is along the Reno River and shows two massive gravel layers (PC/DC), 100-150 m thick, separated by a layer of fine-grained material about 20 m thick (WF). The vertical amalgamation of gravel bodies slightly decreases with depth (i.e., beyond about 100 m depth), with a parallel increase in the thickness of fine-grained deposits and the local occurrence of sand bodies a few metres thick. The central cross-section through the Bologna city centre (section MM') is dominated to the south by clay soils (WF/PF) with the occurrence, below about 100 m depth, of scattered, thin sand and gravel bodies (Ch). Northwards, the frequency of coarse deposits increases. The easternmost cross-section, drawn approximately along the Savena River (section SS', Fig. 2.13) shows a 50 m-thick succession of gravel bodies in the uppermost portion of the proximal area (DC/PC), which grades downsection into a clay-dominated succession (WF/PF) with sparse gravel and sand bodies (Ch), generally less than 10 m thick.

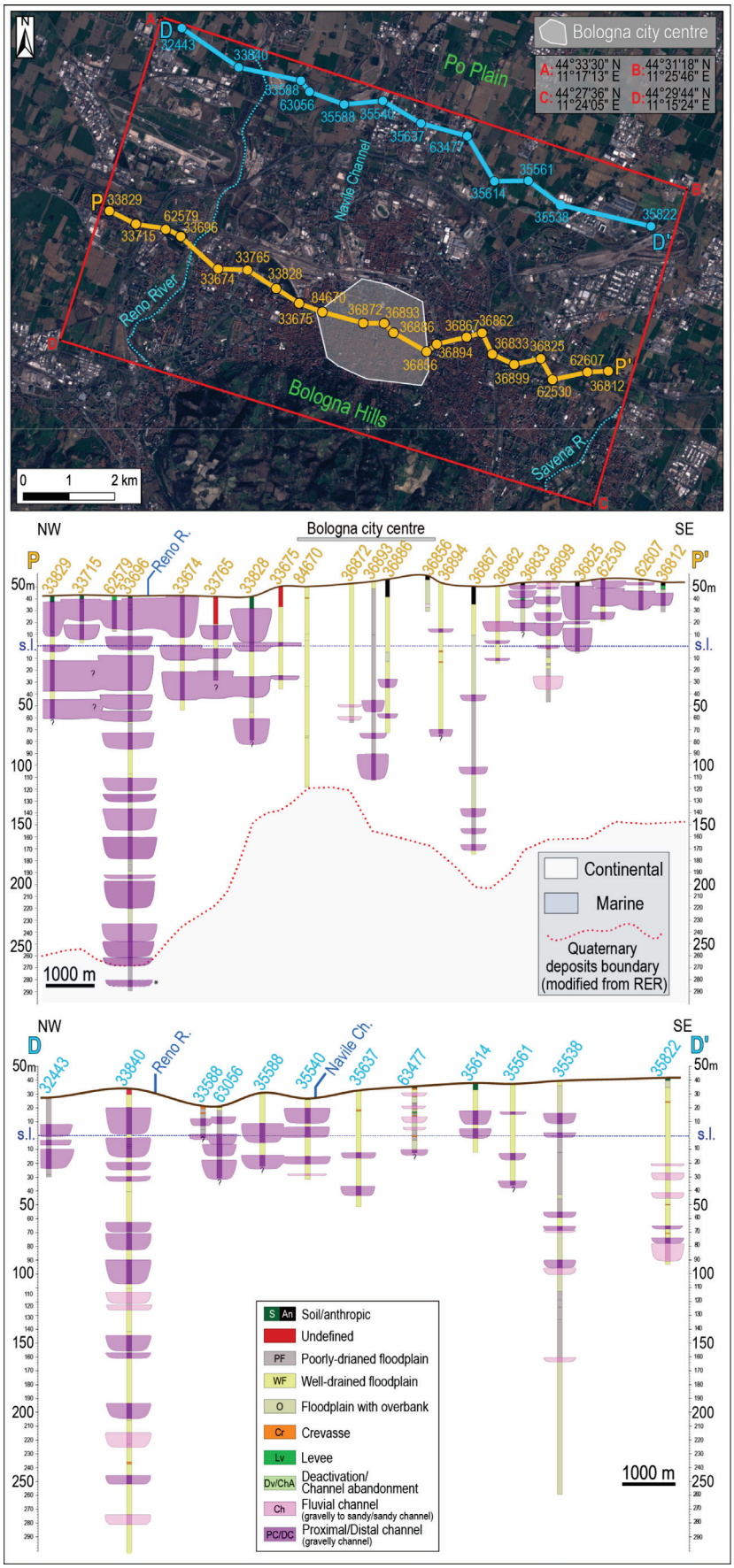

Fig. 12 Transversal stratigraphic cross-sections: Proximal (PP') and distal (DD') intersecting the study area perpendicular to the main depositional strike. *The deepest layer from the 33696 well stratigraphic log was interpreted as a channel deposit on the basis of a description that did not allow its attribution to a marine environment.

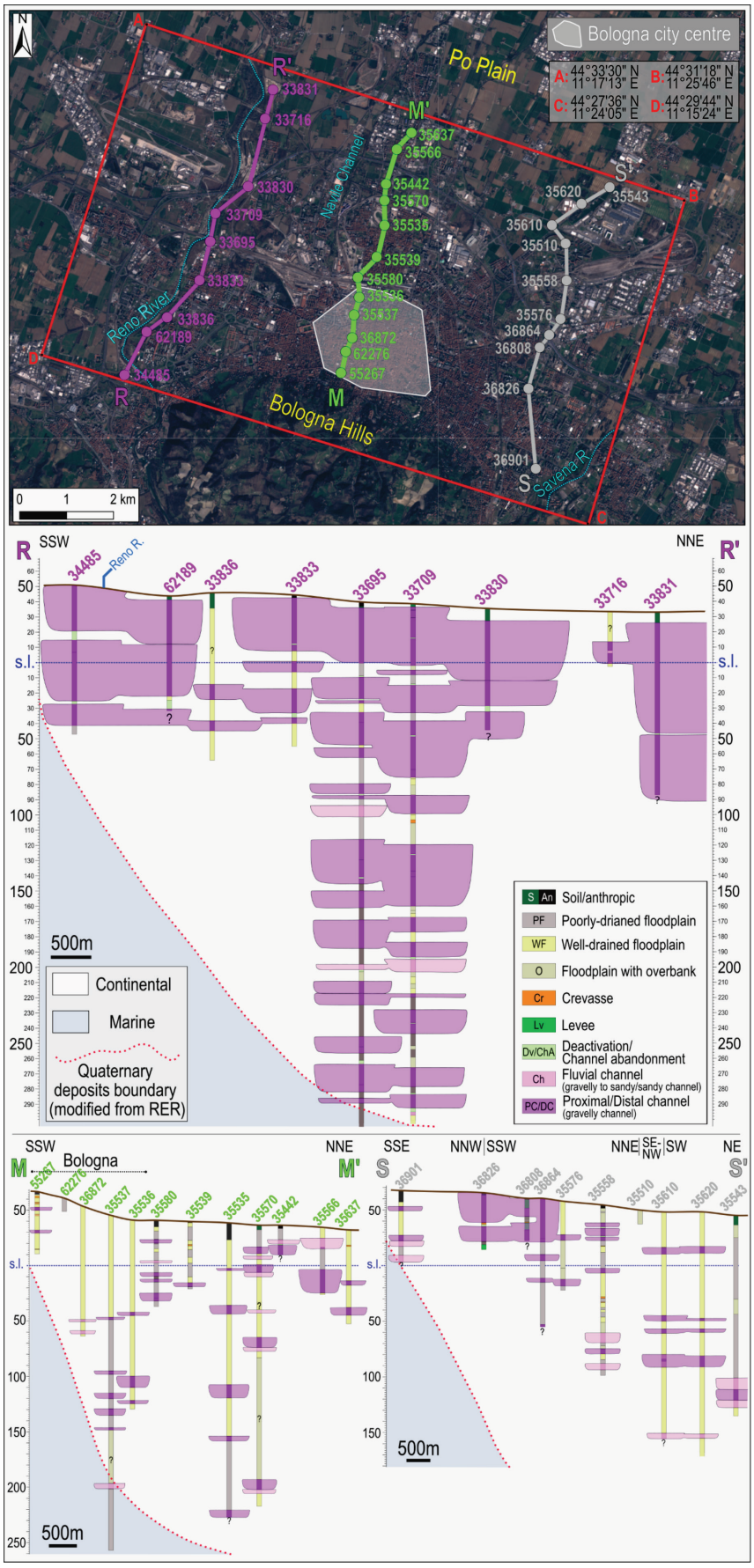

Fig. 13 Longitudinal stratigraphic cross-sections Aligned parallel to the main depositional strike, intersecting the western (RR'), central (MM'), and eastern (SS') part of the study area.

2.6.6 Simplified geological model

Morphological, hydrological, geophysical, and stratigraphic data were combined to obtain a simplified geological model of the study area. The first and most important outcome of data integration is the general agreement between surface morphology and subsurface depositional patterns. The three morphological domains identified through surface analysis (i.e., Domain A- Reno River; Domain B- Bologna historical centre; Domain C- Savena River) align with the three stratigraphic domains highlighted in cross-sections (Fig. 2.14). These domains also showed slight differences in the HVSR patterns detected during the geophysical survey (see Fig. 2.9, section 2.6.3). Domain A (Reno River) is the gravel-dominated filling of a river valley. The high degree of amalgamation of the channel bodies, as well as the abrupt transition with Domain B, suggest that the valley was partially confined to the east. Domain B (Bologna urban area) represents a morphological and stratigraphical divide, topographically elevated compared to the surrounding areas. This area is characterised by fine-grained deposits with frequent paleosols (Amorosi et al 2014; Bruno et al. 2020). Domain C (Savena River) corresponds to a typical alluvial fan marked by a gentle convex-up surface morphology. The lower degree of lateral amalgamation of fluvial channel bodies reflects multiple events of nodal avulsion in the fan apex.

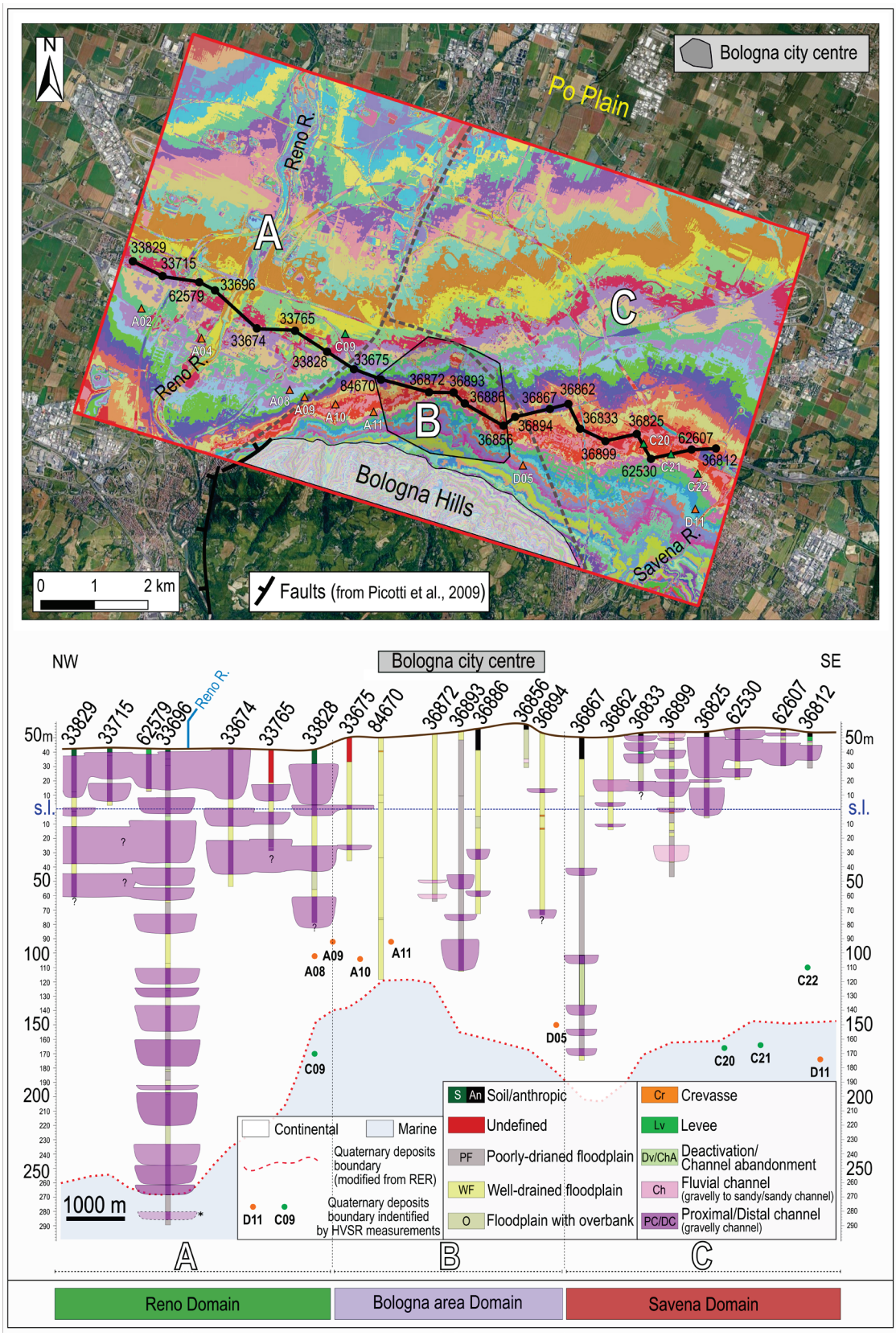

Fig. 2.14 Simplified geological model of the study area. Upper) DTM plan view showing the three domains with distinct morphological characteristics (A, B, and C). Lower) Transversal stratigraphic cross-section highlighting the different stacking patterns observed in the three domains. HVSR measurements detecting the Quaternary continental/marine deposits boundary are also included. *The deepest layer from the 33696 well stratigraphic log was interpreted as a channel deposit based on a description that did not allow its attribution to a marine environment.

2.6.7 3D geological model

The 3D geological model covers an area of 88 km^2 and extends to a maximum depth of about 400 m. According to the simplified geological model, the model bounding volume was subdivided into three sub-volumes corresponding to Domains A, B, and C (Fig. 2.15), bounded by two curvilinear surfaces. In section 2.6.5, it was observed that these surfaces denote transitional areas between distinct depositional domains rather than abrupt geological boundaries. Thus, they were positioned based on significant shifts in subsurface depositional patterns and surface topography.

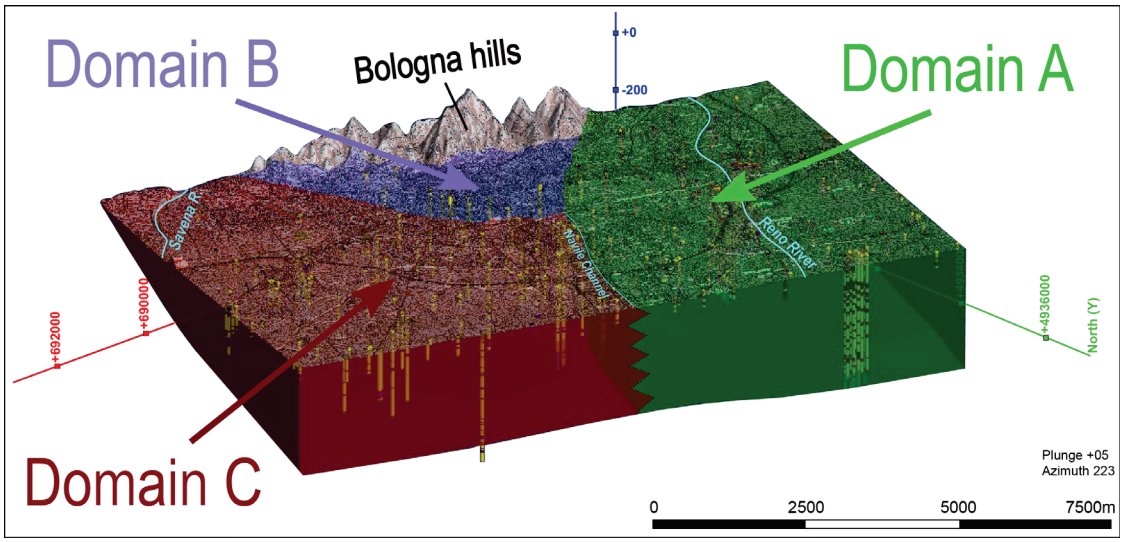

Fig. 2.15 3D view of the study area, displaying the distinction of the three geological domains. From east to west: the Savena alluvial fan (red block-Domain C), the Bologna relief (purple block-Domain B), and the Reno River (green block-Domain A).

A sub-vertical surface, dipping northwest, separates Domains A from B and A from C. This surface extends in a SW-NE direction west of the city centre (A – B boundary), and N-S along the Navile Channel (A – C boundary) (see Fig. 2.15). A second surface, dipping towards the plain with a slightly lower angle with respect to the previous one, separates domains B and C in the eastern part of Bologna. An additional, high-angle surface was added to exclude the Apennines from the model (Bologna hills in Fig. 2.15). Both coarse and fine-grained deposits were modelled in Domains A and C (Reno and Savena rivers), whereas in Domain B (Bologna city centre) only fine-grained deposits were considered.

In Domain C, granular soils were modelled following a conservative approach using the "Intrusions" tool (see section 2.5.8), because of the poor correlation potential of gravel and sand bodies supplied by the Savena River. The “Intrusion” tool proved to be particularly effective in such an unpredictable context, where granular bodies show a spatial distribution and lithostratigraphic patterns consistent with the characteristics of an alluvial fan. In the proximal portion, in fact, the granular deposits are closely stacked and locally amalgamated, resulting in an almost single thick body, while in the middle-distal portion they are separated by fine-grained intervals and tend to be elongated on the horizontal plane following different orientations (Fig. 2.16a, b). The distal part of this domain is highly uncertain due to the uneven data distribution and the difficulty of carrying out lithostratigraphic correlations among scattered granular bodies. Here, a further sub-volume was used to indicate a thick sequence of predominant fine-grained deposits with dispersed granular layers (see Fig. 2.16a, b, “C fine-grained prevailing”).

In Domain A, the high lateral continuity of the granular bodies and the large number of boreholes allowed considering a double approach to model granular bodies, using both the “Intrusion” and “Deposit” interpolation

tools, and thus obtaining two alternative geological models (Fig. 2.16a, b). Regardless of the interpolator used, the modelled granular bodies show a large areal extent at all stratigraphic levels and a high degree of amalgamation close to the mouth of the Reno River, where they tend to form a single thick body (from 100 m to more than 200 m depth). Towards the plain, the degree of amalgamation gradually decreases, and the granular layers (around 100 – 150 m thick) are separated by comparatively thinner layers of fine-grained deposits. Here, the different interpolation techniques provide quite different results: the "Intrusion" tool limits the extent of the granular bodies to a small volume around the stratigraphic data (Fig. 2.16a); the "Deposit" tool extends the interpolated volume to almost the entire domain (Fig. 2.16b). The NE part in the "Intrusion" model (Fig. 2.16a) is indicated as a "no-data" volume because this algorithm gives unrealistic results without stratigraphic data. Domain B (Bologna city) is characterised by the prevalence of fine-grained deposits. The occurrence of scattered granular bodies at great depth is maintained within the different stratigraphic logs, but not modelled as 3D volumes.

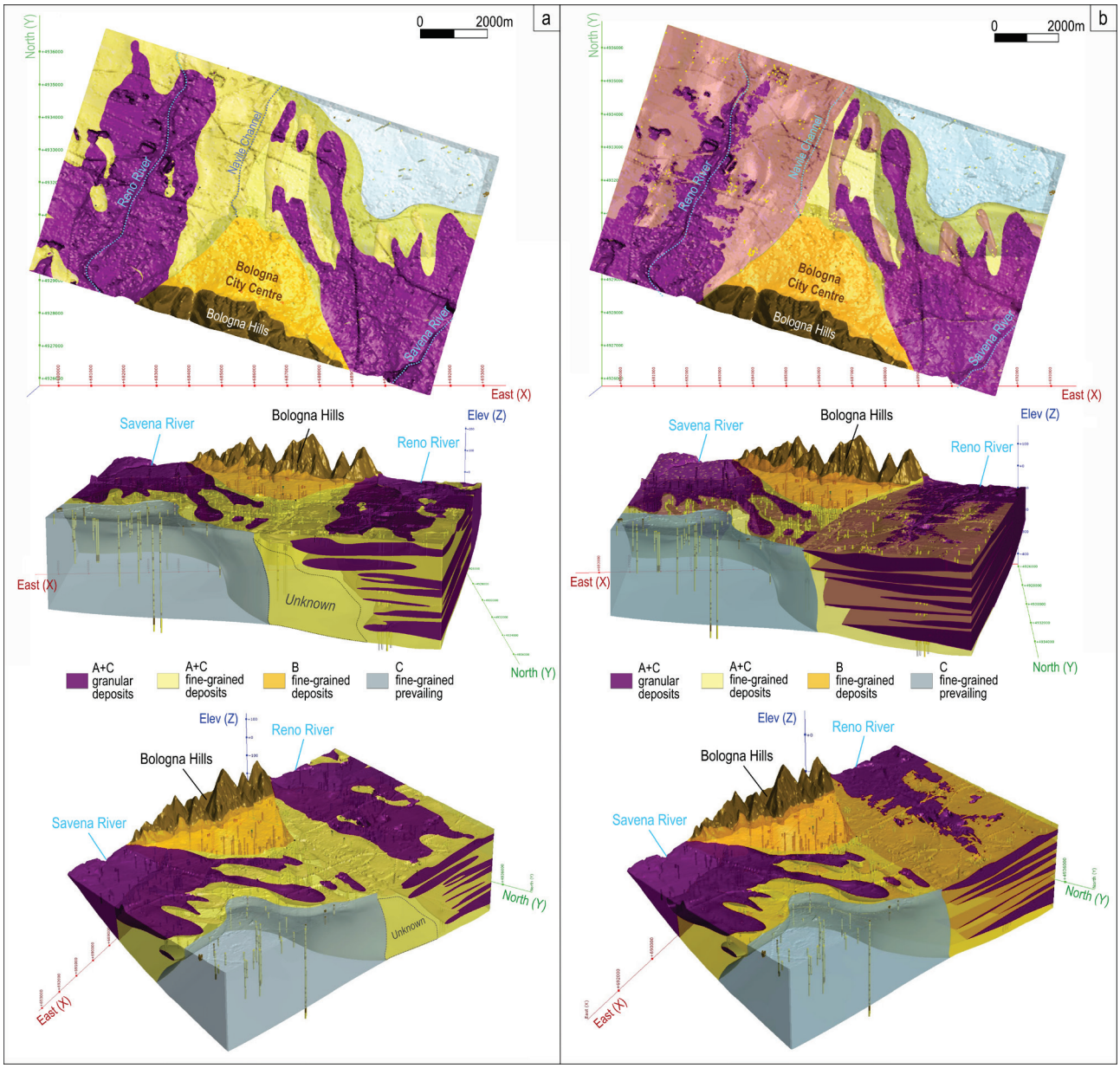

Fig. 2.16 The 3D geological model of the Bologna urban area. In the Reno River domain (Domain A) the granular deposits were modelled within Leapfrog Works using both the "Intrusion" (a) and the "Deposit" tools (b).

2.6.8 Geological interpretation

The different characteristics of Domains A, B, and C are likely related to the combined effect of fluvial and tectonic activity. The Reno River has a drainage basement about ten times larger than the Savena River (1060 km2 vs 107 km2 respectively) and it is mostly composed of clayey erodible rocks. A large catchment is expected to have a high capacity for sediment transport; therefore, the Reno River could have easily compensated for the uplift of the Apennine margin by cutting its deposits at the valley mouth. Moreover, the Reno River lies on the prolongation of a normal fault that flanks the lower reach of the valley (Picotti et al. 2009, see Fig. 2.14). The possible presence of an extensional tectonic structure in the subsurface of the alluvial plain (Martelli et al. 2017) could explain the vertical amalgamation and confinement of the gravel bodies deposited by the Reno River, as well as the multi-stage sedimentation in a partially confined alluvial plain which finally resulted in the absence of a real fan. On the contrary, the limited transport capacity of the Savena River (possibly combined with the absence of active tectonic structures) could explain the convex fan morphology, the higher elevation of the apex, and the different internal architecture of the deposits. The prevalence of fine-grained soils beneath the historical centre of Bologna reflects instead the poor transport capacity of minor rivers draining the Apennine foothills. Here, the occurrence of vertically stacked paleosols indicates that Domain B was not involved in the fluvial dynamics of the Reno and Savena rivers, leaving this area essentially undisturbed.

2.7 Discussion

2.7.1 General remarks on the lithofacies approach

Geological modelling of urban areas is typically based on stratigraphic correlation of borehole data. Although data density and quality are critical aspects for obtaining a reliable model, geological complexity is probably the most important issue. Cities built upon alluvial deposits, which are characterised by a high degree of heterogeneity and lateral facies changes, are much more complicated to model than cities settled, for example, upon coastal deposits where strata have greater areal continuity. In complex depositional environments, data is never enough, and the geological model may be uncertain even if the borehole density is very high.

The lithofacies approach, though time-consuming, was particularly effective in the subsurface of Bologna, where lithological correlation is difficult even over short distances, despite an average data density of 10 boreholes/km2. Here, stratigraphic analysis was combined with other types of data, including surface morphology, river network, and geophysical surveys. The lithofacies approach reduced the risk of correlating logs belonging to different depositional environments and led to the identification of three distinct depositional domains not recognized before (see Figs. 2.14, 2.16).

2.7.2 3D modelling or rendering?

In general, volume shaping within 3D modellers is based on the use of mathematical interpolators that spatially correlate stratigraphic data. We investigated the performance of automatic interpolation by comparing the two interpolators provided by Leapfrog Works named “Intrusion” and “Deposit” (see section 2.5.8). Despite the software offers a high degree of customization on these algorithms, neither was found fully suitable for our case. The “Intrusion” algorithm allows for a flexible shaping of the deposits that closely follows the stratigraphic data, but leaves uncovered large areas where data are absent (see Fig. 2.16 “Unknown” portion). The “Deposit” algorithm creates sheet-like volumes which extend far beyond the data, but over whose geometry the user has little control. In both cases, interpolation is by no means automatic and, at least in our complex geological setting, the 3D model cannot be totally entrusted to the software. That is why we first

defined the geometry of sedimentary bodies using a dense grid of 2D stratigraphic sections, then we reproduced the inferred geometry by employing the most appropriate interpolator. As a matter of fact, in our complex case, the software was essentially used as a powerful 3D rendering tool rather than a real 3D modeller.

2.7.3 Geotechnical implications

3D geological models are essential tools, particularly in complex contexts with high latero-vertical lithostratigraphic variability such as the study area. These models not only condense and effectively display the general depositional architecture of the study area but also decisively support the analysis and interpretation of processes closely related to the geological setting. The 3D geological model, obtained exclusively through the stratigraphic analysis and the methodology described herein, has been, in fact, crucial in understanding the ongoing subsidence process evolution in the study area. Bologna experienced strong subsidence since the 1960s, due to groundwater pumping into the aquifers of the Reno and Savena rivers (Pieri & Russo 1980; Brighenti et al. 1995; Bitelli et al. 2015). The subsidence reached in the early 1980s a peak of about 100 mm/year, then gradually decreased following the introduction of more restrictive regional pumping regulations (ARPAE, 2018). The geological model, however, which was developed independently from subsidence data, highlights a significant correspondence between the three identified depositional domains (i.e., A, B, and C) and the spatial distribution of the ground deformation field (Fig. 2.17). In the figure, the three identified domains are compared with the ground displacement maps obtained by topographic levelling (period 1983-1987, Barbarella et al. 1990) and by satellite interferometry from ascending orbit RADARSAT data (period 2006-2011, ARPAE 2012, Bitelli et al. 2014, 2015). Both the subsidence contour map (Fig. 2.17a) and the spatial distribution of punctual values obtained from radar interferometry (Fig. 2.17b) exhibit abrupt changes at the domains' boundary, especially at the limit between Domains A (Reno River) and B (Bologna city centre). Moreover, the settlement field varies inside each domain according to their different stratigraphy. In Domain A (Reno River), the ground subsidence is relatively small in the proximal portion, where thick gravel bodies are amalgamated and fine-grained layers are almost absent, and it increases downstream following the higher abundance of clayey deposits. The distal portion of this domain, characterised mostly by silty and clayey deposits, shows the highest subsidence rate. Similarly, within Domain C (Savena River) subsidence values are relatively small close to the fan apex and increase northward approaching the "fine-prevailing" area of the model. Interestingly, although composed mainly of fine-grained deposits, Domain B is characterised by small subsidence rates (see Fig. 2.16a). This apparent discrepancy is likely related to the peculiar features of Domain B, that according to the lithofacies analysis consists of stiff clay deposits (well-drained floodplain, WF) hosting frequent paleosols (Amorosi et al. 2017; Bruno et al. 2020). Aging in secondary compression and periods of subaerial exposure may have resulted in the overconsolidation of the fine-grained deposits with a consequent increase in soil stiffness.

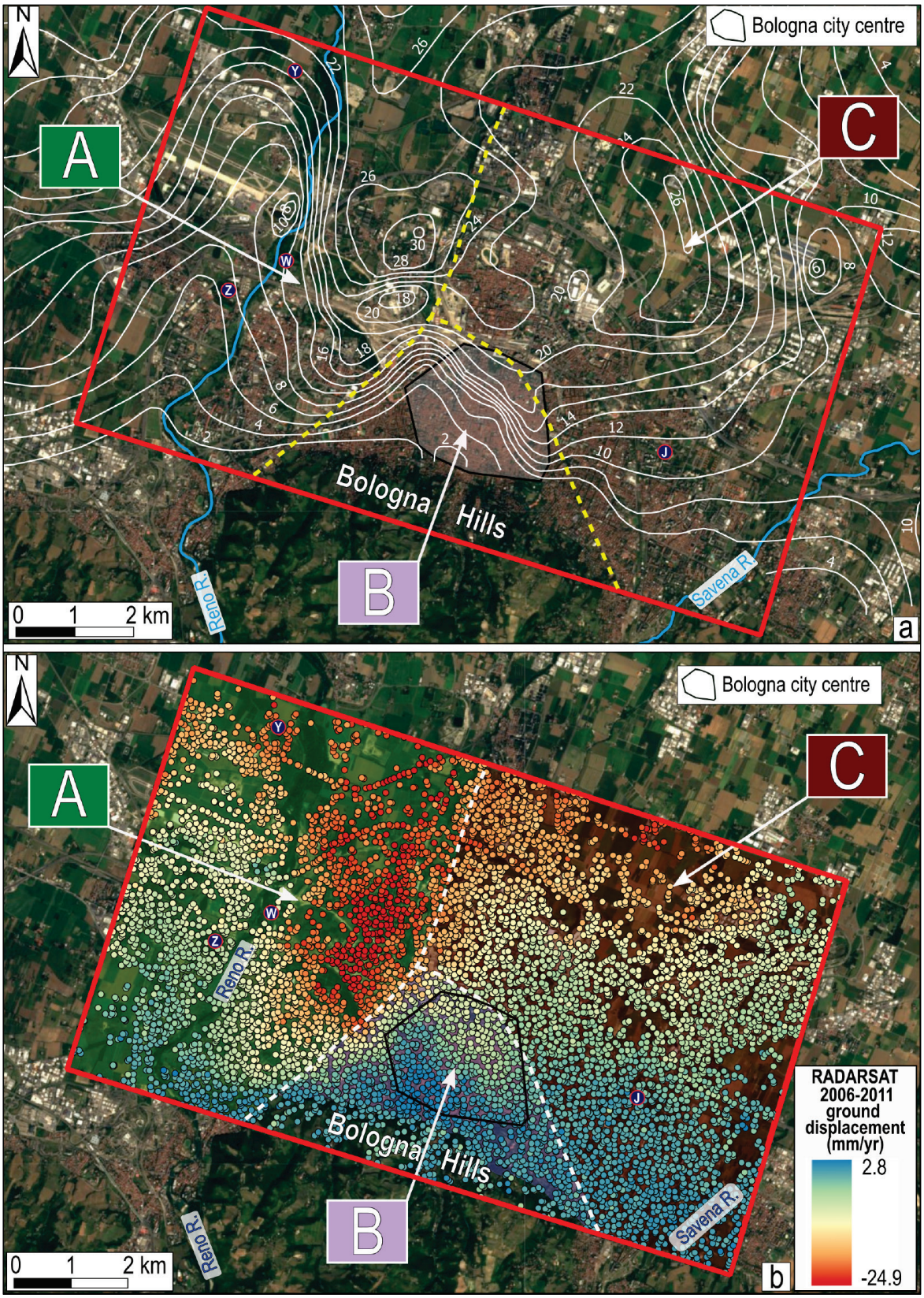

Fig. 2.17 Comparison between the three domains identified in the geological model (A, B, and C) and ground displacement data: (a) the ground displacement map, measured in millimetres and reported as white contours, resulting from the 1983–1987 topographic levelling campaign (Barbarella et al. 1990); (b) the subsidence rate map, expressed in mm/year, from 2006–2011 Radarsat interferometric survey, displayed as coloured dots. The figure also includes the locations of the main wells stations: J- Fossolo; Y-San Vitale; W-Tiro a segno; Z-Borgo Panigale.

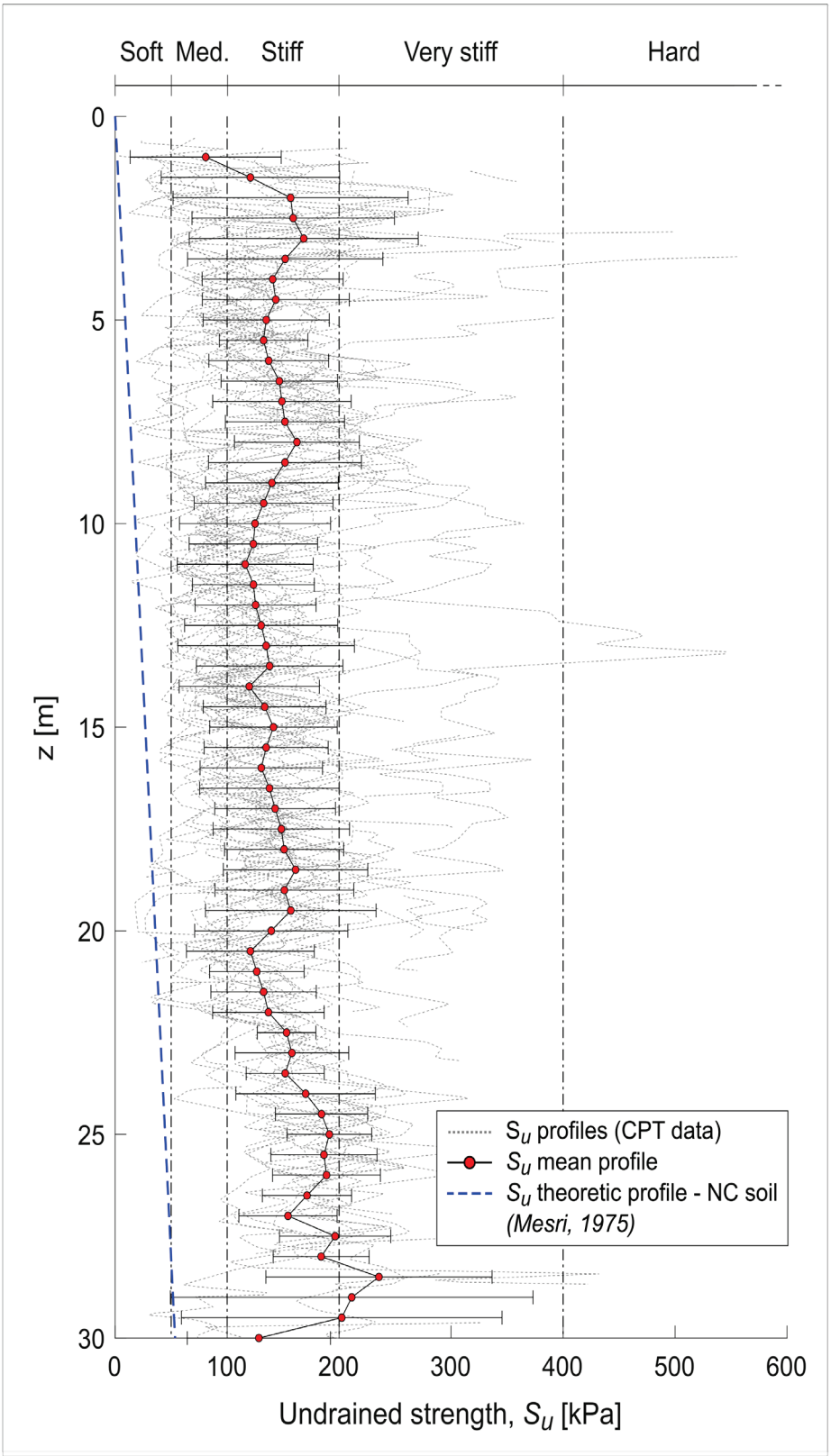

Fig. 2.18 Comparison of undrained shear strength (Su) profiles in Domain B derived from CPT data. The S_u profiles were determined through the equation proposed by Robertson (2009): $S_u = (q_t - \sigma_{v0})/N_{kt}$, where q_t is the corrected cone resistance, σ_{v0} is the total overburden stress and N_{kt} is the cone factor, set to an average value of 14 after Robertson & Cabal (2015). The mean S_u profile (red dots) along with the corresponding standard deviation values is compared with the typical consistency values chart for fine-grained soils developed by Terzaghi & Peck (1967) and the theoretical trend for normally consolidated (NC) soils proposed by Mesri (1975): $S_u = 0.22\sigma'_{vo}$, where σ'_{vo} is the effective vertical stress.

Beside the lithostratigraphic analysis, a survey was conducted to gather information on available Cone Penetration Tests (CPTs) within the study area. A total of 589 CPTs were available, out of which 143 were digitised. The selection prioritised surveys deeper than 15 m and those located in areas with limited stratigraphic data coverage. Lithological data from these tests were systematically derived using either the Schmertmann (1970) or Robertson et al. (1986) classification methods, depending on the type of survey. Literature empirical relations were then employed to determine the main geotechnical parameters of the identified coarse and fine-grained layers. CPT surveys in Domains A and C, situated along the course of the Reno River and the alluvial fan apex of the Savena River, are often shallow due to the presence of gravel. Consequently, the geotechnical characteristics of these sedimentary bodies, including both gravel deposits and the deeper clayey intervals between them, are generally unknown. On the contrary, the geotechnical characteristics of Domain B were investigated through several relatively deep penetration tests. Geotechnical data for Domain B were obtained from 31 digitised CPTs with depths ranging from 15 to 30 m. The undrained shear strength (Su) profiles (Fig. 2.18) systematically exhibit relatively high values, ranging from 81 to 235 kPa on average, falling between the "Stiff" and "Very Stiff" fields of the soil consistency classification proposed by Terzaghi & Peck (1967). Moreover, these high undrained strength values do not increase with depth and significantly diverge from the theoretical profile expected for normally consolidated (NC) soils, reported in Figure 2.18.
The 3D geological model effectively accounts for the existence of firm, overconsolidated clays beneath Bologna city. As mentioned earlier, Domain B seems to have remained unaffected by the fluvial dynamics of the Reno and Savena rivers, resulting in an undisturbed area where the material has become overconsolidated due to the combined effects of aging and drying. This is also evident from the abundance of paleosols found in this domain.
The simplification, for geotechnical purposes, of the obtained 3D geological model led to grouping different layers into two main types of deposits, that are coarse-grained and fine-grained deposits (see Fig. 2.16). However, the simplification process within a complex alluvial environment such as that of the study area, when guided by the lithofacies and their correlations, results in a more coherent and conscious approach. In fact, based on lithofacies correlations, it was possible to distinguish, as discussed above, three main domains with different depositional characteristics, underlying different ground surface behaviour, as also evidenced by subsidence data.

Further in-depth analysis of the geotechnical properties of the sedimentary bodies reconstructed in the 3D model and their relation to subsidence evolution, in view of a detailed numerical modelling analysis of the ground deformation process, is currently underway and will be deepened in future work.

2.8 Conclusions

In this work, we present a 3D geological model of the Bologna urban area developed through a detailed surface (DTM, hydrography) and subsurface (geophysical surveys, boreholes) data analysis. A simplified geological model was built integrating surface morphology and subsurface stratigraphy, based on lithofacies correlation criterion, that guided the final 3D modelling.

Based on the findings of this study, the following conclusions can be drawn:

1) The lithofacies criterion proved to be an effective approach for reconstructing the urban subsurface in a complex alluvial setting; stratigraphic correlation guided by lithofacies provides a reliable representation of sediment bodies and their geometry, overcoming the limitations of the lithologic approach commonly used in engineering geology.

2) The main difficulty of the lithofacies approach is the identification of the depositional facies based uniquely on log descriptions; re-interpreting borehole data, from lithology to lithofacies, requires time and specific sedimentological expertise.

3) The analysis allowed the definition of three different depositional domains with a common alluvial origin, but distinct morphological characteristics and depositional stacking patterns: the western part of the city (Domain A) lies over massive, thick gravel deposits that filled a subsiding alluvial valley; the central part (Domain B) is an interfluve area dominated by stiff fine-grained soils that were essentially unaffected by the activity of the main rivers; the eastern part (Domain C) corresponds to a typical alluvial fan with gravel-dominated proximal deposits.

4) The three depositional domains guided the development of the 3D geological model and imposed to divide the bounding volume into three independently modelled sub-volumes; within each sub-volume, the geometry of sedimentary bodies was defined based on a dense grid of 2D stratigraphic cross-sections; no automatic algorithm proved to be really suitable to interpolate stratigraphic data in our complex case.

5) The 3D geological model showed a good agreement with the spatial distribution of the ground subsidence observed in Bologna since the 1960s, providing independent confirmation of the model itself.

Acknowledgements

This study was supported by the research grant URGENT - Urban Geology and Geohazards: Engineering geology for safer, resilieNt and smart ciTies funded by the Italian Government (Progetti di Ricerca di Rilevante Interesse Nazionale, PRIN2017, Prot. 2017HPJLPW). We thank Stefano Cremonini very much for his helpfulness and support.

2.9 Supplementary Material

This section presents an example of the procedure adopted for reclassifying borehole and well logs in terms of lithofacies. The classification was performed by analysing the available descriptions of the encountered deposits, coupled with their vertical sequence and mutual position along the borehole log.

GISID	TOP [m]	BOTTOM [m]	RER LITHOLOGY	SYNTHETIC DESCRIPTION (LOG)	ASSIGNED LITHOFACIES
33696	0,0	1,8	Z	soil	S
33696	1,8	7,2	GS	gravel with little sand and pebbles	PC/DC
33696	7,2	11,5	GA	gravel and sandy clay	PC/DC
33696	11,5	28,6	GS	gravel and sand with pebbles/cobbles	PC/DC
33696	28,6	34,0	A	dark grey firm clay	PF
33696	34,0	45,4	GS	gravel and sand with pebbles/cobbles	PC/DC
33696	45,4	46,9	A	dark grey clay	PF
33696	46,9	50,0	AG	yellowish clay with gravel	Dv
33696	50,0	79,3	GS	gravel and sand with pebbles/cobbles	PC/DC
33696	79,3	83,0	A	dark ash-grey clay	PF
33696	83,0	95,0	GS	gravel and sand	PC/DC
33696	95,0	96,6	AG	yellowish clay with gravel	Dv
33696	96,6	105,2	GS	gravel and sand with pebbles/cobbles	PC/DC
33696	105,2	106,7	A	yellowish clay	WF
33696	106,7	114,5	A	ash-grey clay	PF
33696	114,5	128,3	GS	gravel and cemented sand	PC/DC
33696	128,3	148,5	A	yellowish and ash-grey clay	WF
33696	148,5	152,0	AG	grey clay; downward, yellowish clay with gravel	WF
33696	152,0	163,0	GS	gravel with little sand and pebbles	PC/DC
33696	163,0	165,5	SA	clayey sand	Dv
33696	165,5	167,5	SG	sand with sandstone and little gravel	PC/DC
33696	167,5	172,0	GS	conglomerated gravel with sand	PC/DC
33696	172,0	177,7	AS	yellowish sandy clay	O
33696	177,7	178,9	G	conglomerate	PC/DC
33696	178,9	195,3	GS	conglomerated gravel with sand and pebbles	PC/DC
33696	195,3	201,3	A	light blue firm clay	PF
33696	201,3	219,5	GS	light blue gravel with little sand	PC/DC
33696	219,5	222,0	A	ash-grey firm clay	PF
33696	222,0	223,5	AS	ash-grey sandy clay	O
33696	223,5	229,5	A	light blue firm clay	PF
33696	229,5	233,0	///	ash-grey sandy clay	O
33696	233,0	236,1	GS	gravel and sand, with clay	PC/DC
33696	236,1	238,0	AS	grey sandy clay	Dv
33696	238,0	239,5	GS	light blue gravel with sand	PC/DC
33696	239,5	242,5	AG	conglomerated clay and light blue gravel	PC/DC
33696	242,5	262,0	GS	gravel with little cemented sand	PC/DC
33696	262,0	274,8	AS	greyish-green lightly sandy clay	O
33696	274,8	289,5	GS	cemented gravel with little yellowish sand	PC/DC
33696	289,5	303,0	GS	cemented gravel with little sand	PC/DC
33696	303,0	310,0	GS	gravel with little sand	PC/DC
33696	310,0	321,5	A	grey hard clay	PF
33696	321,5	323,5	GS	light blue gravel with little sand	PC/DC
33696	323,5	327,0	SG	loose sand and gravel	PC/DC
33696	327,0	330,8	A	grey firm clay	PF
33696	0,0	1,8	Z	soil	S
33696	1,8	7,2	GS	gravel with little sand and pebbles	PC/DC
33696	7,2	11,5	GA	gravel and sandy clay	PC/DC
33696	11,5	28,6	GS	gravel and sand with pebbles/cobbles	PC/DC
33696	28,6	34,0	A	dark grey firm clay	PF

RER-LITHOLOGY (CODE)			
A	clay	GS	gravel with sand
AS	clay with sand	Z	unknown
L	silt	X	unknown
LS	silt with sand	AT	clay
S	sand	ZS	soil
SL	sand with silt	LZ	silt

Table. 2.3 Example of the lithofacies criterion employed for borehole and well logs reinterpretation. While the assigned lithofacies codes are reported in Table 1, the lithology codes used by RER Geological survey are presented here.

2.10 References

Allen JRL, 1963. The classification of cross-stratified units with notes on their origin. Sedimentology, 2, 93-114.

Amorosi A, Farina M, Severi P, Preti D, Caporale L, Di Dio G, 1996. Genetically related alluvial deposits across active fault zones: an example of alluvial fan-terrace correlation from the upper Quaternary of the southern Po Basin, Italy. Sediment. Geol., 10 ’2, 275–295.

Amorosi A, Caporale L, Farina M, Preti D, Severi P, 1997. Late Quaternary sedimentation at the southern margin of the Po Basin (Northern Italy). Geologia Insubrica 2, 149–159.

Amorosi A, Pavesi M, Ricci Lucchi M, Sarti G, Piccin A, 2008. Climatic signature of cyclic fluvial architecture from the Quaternary of the central Po Plain, Italy. Sediment. Geol. 209, 58–68.

Amorosi A, Bruno L, Rossi V, Severi P, Hajdas I, 2014. Paleosol architecture of a late Quaternary basin-margin sequence and its implications for high-resolution, nonmarine sequence stratigraphy. Glob. Planet. Chang. 112, 12–25.

Amorosi A, Bruno L, Cleveland DM, Morelli A, Hong W, 2017. Paleosols and associated channel-belt sand bodies from a continuously subsiding late Quaternary system (Po Basin, Italy): new insights into continental sequence stratigraphy. Geol. Soc. Am. Bull, 129, 449–463.

Argnani A, Barbacini G, Bernini M, Camurri F, Ghielmi M, Papani G, Rizzini F, Rogledi S, Torelli L, 2003. Gravity tectonics driven by Quaternary uplift in the Northern Apennines: insights from the La Spezia-Reggio Emilia geo-transect. In Uplift and Erosion; Driving Processes and Resulting Landforms; Dynamic Relations Between Crustal and Surficial Processes, Bartolini C, Piccini L, Catto NR (eds). Quatern. Int., 13–26.

ARPAE (Agenzia Prevenzione Ambientale Energia Emilia-Romagna), 2012. Rilievo della subsidenza nella pianura emiliano-romagnola - seconda fase, Bologna, 2018.

ARPAE (Agenzia Prevenzione Ambientale Energia Emilia-Romagna), 2018. Rilievo della subsidenza nella pianura emiliano-romagnola - seconda fase, Bologna, 2018.

Akkaya İ, & Özvan A, 2019. Site characterization in the Van settlement (Eastern Turkey) using surface waves and HVSR microtremor methods. J. Appl. Geophys., 160, 157-170.

Barbarella M, Pieri L, Russo P, 1990. Studio dell’abbassamento del suolo nel territorio bolognese mediante livellazioni ripetute: Analisi dei movimenti e considerazioni statistiche. Inarcos, 506, 1-19.

Bitelli G, Bonsignore F, Del Conte S, Novali F, Pellegrino I, Vittuari L, 2014. Integrated use of advanced InSAR and GPS data for subsidence monitoring. In: Lollino G, Manconi A, Guzzetti F, Culshaw M, Bobrowsky PT and Luino F (eds), Engineering Geology for Society and Territory, Springer, Berlin, Germany, Vol. 5, pp. 147-150, doi: 10.1007/978-3-319-09048-1_29.

Bitelli G, Bonsignore F, Pellegrino I, Vittuari L, 2015. Evolution of the techniques for subsidence monitoring at regional scale: the case of Emilia-Romagna region (Italy), Proc. IAHS, 372, 315–321, https://doi.org/10.5194/piahs-372-315-2015.

Bridge JS, Jalfin GA, Georgieff SM, 2000. Geometry, Lithofacies, and Spatial Distribution of Cretaceous Fluvial Sandstone Bodies, San Jorge Basin, Argentina: Outcrop Analog for the Hydrocarbon-Bearing Chubut Group. J. Sed. Res., 70 (2): 341–359. https://doi.org/10.1306/2DC40915-0E47-11D7-8643000102C1865D.

Brighenti G, Borgia GC, Mesini E, 1995. Chapter 5 Subsidence studies in Italy, Editor(s): Chilingarian G.V., Donaldson E.C., Yen T.F., Developments in Petroleum Science, Elsevier, Volume 41, 1995, Pages 215-283, ISSN 0376-7361, ISBN 9780444818201, https://doi.org/10.1016/S0376-7361(06)80052-X.

Bruno L, Marchi M, Bertolini I, Gottardi G, Amorosi A, 2020. Climate control on stacked paleosols in the Pleistocene of the Po Basin (northern Italy). J. Quaternary Sci, 35, 559–571.https://doi.org/10.1002/jqs.3199.

Bruno L, Amorosi A, Severi P, Bartolomei P, 2015. High-frequency depositional cycles within the late Quaternary alluvial succession of Reno River (northern Italy). Ital. J. Geosci., 134(2), 339–354. https://doi.org/10.3301/IJG.2014.4

Bruno L, Amorosi A, Curina R, Severi P, Bitelli R, 2013. Human–landscape interactions in the Bologna area (northern Italy) during the mid–late Holocene, with focus on the Roman period. Holocene, 23, 1560– 1571.

Carminati E, & Di Donato G, 1999. Separating natural and anthropogenic vertical movements in fast subsiding areas: the Po Plain (N. Italy) case. Geophys. Res. Lett., 26: 2291–2294.

Castellarin A, Eva C, Giglia G, Vai GB, Rabbi E, Pini GA, Crestana G, 1985. Analisi strutturale del Fronte Appenninico Padano. Giorn. Geol. 47, 47–75.

Castellaro S, & Mulargia F, 2009. Vs_{30} estimates using constrained H/V measurements. Bull. Seismol. Soc. Am., 99:761–773.

Catuneanu O, 2006. Principles of Sequence Stratigraphy, Elsevier, Amsterdam, 375 pp.

Choobbasti AJ, Rezaei S, Farrokhzad F, 2013. Evaluation of site response characteristics using microtremors. Gradevinar, 65: 731–741.

Chiesa A, 1742. Carta topografica di tutta la pianura del Bolognese, scala in miglia italiane.

Cremonini S, 1980. Evoluzione morfologica della pianura bolognese tra Reno e Idice. Tesi di laurea, Università di Bologna, inedita.

Cremonini S, 1992. Il torrente Savena oltre i limiti dell'analisi storica. Un esempio di "archeologia fluviale". Atti e Memorie della Deputazione di Storia Patria per le province di Romagna, 12:159-205.

Culshaw MG, & Price SJ, 2012. The contribution of urban geology to the development, regeneration and conservation of cities. The 2010 Hans Cloos lecture. Bull. Eng. Geol. Environ, Volume 70, No 3, pp 333-376. doi 10.1007/s10064-011-0377-4.

El May M, Dlala M, Chenini I, 2010. Urban geological mapping: Geotechnical data analysis for rational development planning. Eng. Geol., 116 (1-2), 129-138, https://doi.org/10.1016/j.enggeo.2010.08.002

Elmi C, Bergonzoni A, Massa T, Montaletti V, 1984. Il territorio di pianura del Comune di Bologna: aspetti geologici e geotecnici. Giornale di Geologia, Rivista di Geologia Sedimentaria e Geologia Marina, 46, n. 2. ISSN 0017-0291.

Fordyce FM, Campbell SDG, 2017. The Geosciences in Europe's Urban Sustainability: Lessons from Glasgow and Beyond (CUSP). Earth and Environmental Science Transactions of the Royal Society of Edinburgh Special Issue, 108 (2–3).

He HH, He J, Xiao JZ, Zhou YX, Liu Y, Li C, 2020. 3D geological modeling and engineering properties of shallow superficial deposits: a case study in Beijing, China. Tunn Undergr Sp Tech.;100:103390, https://doi.org/10.1016/j.tust.2020.103390.

Geological Map of Italy 1:50.000 by the Geological Survey of Italy-ISPRA –Sheets: 220 Casalecchio di Reno-221 Bologna and Geological notes.

Gunderson K, Pazzaglia FJ, Picotti V, Anastasio DA, Kodama KP, Rittenour T, Frankel KF, Ponza A, Berti C, Negri A, Sabbatini A, 2014. Unraveling tectonic and climatic controls on synorogenic growth strata (Northern Appennines, Italy). Geol. Soc. Am. Bull., 126, 3/4: 532-552.

Hemmerle H, Ferguson G, Blum P, Bayer P, 2022. The evolution of the geothermal potential of a subsurface urban heat island. Environ. Res. Lett., 17 (8).

Hooimeijer FL, Maring L, 2018. The significance of the subsurface in urban renewal. Journal of Urbanism: International Research on Placemaking and Urban Sustainability, 11:3, 303-328, DOI: 10.1080/17549175.2017.1422532.

Huggenberger P, Epting J, 2011. Urban Geology. Process-Oriented Concepts for Adaptive and Integrated Resource Management. Springer, Basel, https://doi.org/10.1007/978-3-0348-0185-0.

NotesISPRA (Istituto Superiore per la Protezione e la Ricerca Ambientale), 20232009. Geological Map of Italy 1:50000: Sheet 220 “Casalecchio di Reno”, Sheet 221 “Bologna”, and Geological Notes. https://www.isprambiente.gov.it/Media/carg/220_CASALECCHIO_DI_RENO/Foglio.html; https://www.isprambiente.gov.it/Media/carg/220_CASALECCHIO_SOTTO/Foglio.html; https://www.isprambiente.gov.it/Media/carg/221_BOLOGNA/Foglio.html; https://www.isprambiente.gov.it/Media/carg/221_BOLOGNA_SOTTO/Foglio.html.

Kokkala A, Marinos V, 2022. An engineering geological database for managing, planning and protecting intelligent cities: The case of Thessaloniki city in Northern Greece. Eng. Geol., 301, https://doi.org/10.1016/j.enggeo.2022.106617.

Lapenna V, Chambers J, Shi B, Lienhart W, Zhu H, 2020. Frontiers and applications of geological engineering and geophysical monitoring technologies in urban areas. Eng. Geol., Special Issue, 268, https://doi.org/10.1016/j.enggeo.2020.105508.

Martelli L, Bonini M, Calabrese L, Corti G, Ercolessi G, Molinari FC, Piccardi L, Pondrelli S, Sani F, Severi P, 2017. Seismotectonic map of the Emilia-Romagna Region and surrounding areas, Scale 1:250,000, nd edn. D.R.E.AM, Firenze.

Martorana R, Capizzi P, Avellone G, D’Alessandro A, Siragusa R, Luzio D, 2017. Assessment of a geological model by surface wave analyses, J. Geophys. Eng., 14, 1, 159–172. https://doi.org/10.1088/1742-2140/14/1/159.

Mathers S, Burke H, Terrington R, Thor S, Dearden R, Williamson J, Ford J, 2014. A geological model of London and the Thames Valley, southeast England. Proceedings of the Geologists' Association, 125(4): 373-382.

Mesri G, 1975. New design procedure for stability of soft clays. Discussion, J. of the Geotech. Eng. Div., ASCE, 101(4), 409-412.

Miall AD, 1977. A review of the braided river depositional environment. Earth Sci. Rev., 13 (1), 1-62.

Miall AD, 1978. Lithofacies types and vertical profile models in braided river deposits: a summary Canadian Society of Petroleum Geologists, 52 (5), 597-604.

Miall AD, 1985. Architectural-element analysis: A new method of facies analysis applied to fluvial deposits, Earth-Science Reviews, 22, Issue 4, 261-308. https://doi.org/10.1016/0012-8252(85)90001-7.

Miall AD, 1996. The geology of fluvial deposits: sedimentary facies, basin analysis and petroleum geology. Berlin, Springer International, 582 p. https://doi.org/10.1007/978-3-662-03237-4.

Miall AD, 2016. Stratigraphy: A Modern Synthesis. Switzerland, Springer International, 454 p.

Moisidi M, Vallianatos F, Kershaw S, Collins P, 2015. Seismic site characterization of the Kastelli (Kissamos) basin in northwest Crete (Greece): assessments using ambient noise recordings. Bull. Earthq. Eng., 13, 725–753.

Nakamura Y, 1989. A method for dynamic characteristics estimation of subsurface using microtremor on the ground surface. Q. Rep. Railw. Tech. Res. Inst. 30:25–33.

Ori GG, 1982. Braided to meandering channel patterns in humid-region alluvial fan deposits, River Reno, Po Plain (northern Italy). Sediment. Geol. 31, 231–248.

Picotti V, Ponza A, Pazzaglia FJ, 2009. Topographic expression of active faults in the foothills of the Northern Apennines. Tectonophysics, 474, 285–294.

Pieri M, Groppi G, 1981. Subsurface geological structure of the Po Plain, Italy. P.F. Geodin. Publ., 414. C.N.R., Roma 1–23.

Pieri L, Russo P, 1980. Abbassamento del suolo della zona di Bologna: considerazioni sulle probabili cause e sulla metodologia per lo studio del fenomeno. Collana di orientamenti geomorfologici ed agronomico-forestali. Pitagora Editrice, Bologna, 1980.

Posamentier HW, Allen GP, 1999. Siliciclastic sequence stratigraphy— concepts and applications. Concepts in sedimentology and paleontology, SEPM Society for Sedimentary Geology, Tulsa, 7, 210 p. https://doi.org/10.2110/csp.99.07.

Price SJ, Ford JR, Campbell SDG, Jefferson I, 2016. Urban Futures: the sustainable management of the ground beneath cities. In: Developments in Engineering Geology (Eggers et al., eds.), https://doi.org/10.1144/EGSP27.2.

RER & ENI-AGIP, 1998. Riserve idriche sotterranee della Regione Emilia-Romagna. Bologna. A cura di G.M: DI Dio. S.EL.CA, Firenze, 120 pp.

Ricci Lucchi F, 1986. Oligocene to Recent foreland basins of Northern Apennines. In Foreland Basins, Allen P, Homewood P (eds). International Association of Sedimentologists, Special Publications, 105–139.

Robertson P K, Campanella RG, Gillespie D, Greig J, 1986. Use of Piezometer Cone Data. Proceedings of the ASCE Specialty Conference on In Situ'86: Use of In Situ Tests in Geotechnical Engineering, Blacksburg, Virginia, 151–158.

Robertson PK, 2009. Interpretation of cone penetration tests – a unified approach. Can. Geotech. J. 49 (11), 1337–1355.

Robertson PK, Cabal KL, 2015. Guide to Cone Penetration Testing for Geotechnical Engineering. Gregg Drilling & Testing, Inc. 6th Edition.

Salvany JM, Aguirre J, 2020. The Neogene and Quaternary deposits of the Barcelona city through the high-speed train line. Geologica Acta, 18. [DOI: 10.1344/GeologicaActa2020.18.10].

Schmertmann JH, 1970. Static cone to compute static settlement over sand. JSMF Div. ASCE, Vol.96 (3), 1011–1043.

Seequent, 2019. User Manual for Leapfrog Works version 3.0.

SESAME, 2004. Guidelines for the implementation of the H/V spectral ratio technique on ambient vibrations measurements, processing, and interpretation. In: SESAME European Research Project Wp12 – Deliverable d23.12, European Commission – Research General Directorate, Project No. EVG1-CT-2000-00026, http://sesame.geopsy.org/Papers/HV_User_Guidelines.pdf Accessed 21 Jun 2022.

Stafleu J, Maljers D, Gunnink JL, Busschers FS, 2011. 3D modelling of the shallow subsurface of Zeeland, the Netherlands, Netherlands. J. Geosc., 16(1), 5647. https://doi.org/10.5242/iamg.2011.0076.

Terzaghi K, Peck RB, 1967. Soil mechanics in engineering practice, John Wiley, New York, NY, USA, p. 729.

Thierry P, Prunier-Leparmentier A, Lembezat C, Vanoudheusden E, Vernoux J, 2009. 3D geological modelling at urban scale and mapping of ground movement susceptibility from gypsum dissolution: The Paris example (France). Eng. Geol., 105 (1–2), https://doi.org/10.1016/j.enggeo.2008.12.010.

Vail PR, Mitchum Jr RM, Thompson III S, 1977. Seismic Stratigraphy and Global Changes of Sea Level, Part 4: Global Cycles of Relative Changes of Sea Level. In: Payton C.E. (Ed.). Seismic Stratigraphy — Applications to Hydrocarbon Exploration. AAPG Memoir, 26, 83-97.

Van Wagoner JC, Mitchum RM, Campion KM, Rahmanian VD, 1990. Siliciclastic Sequence Stratigraphy in Well Logs, Cores, and Outcrops: Concepts for High-Resolution Correlation of Time and Facies. Mem. Am. Assoc. Pet. Geol. Memoir, 55 p. https://doi.org/10.1306/Mth7510 Van Wagoner J.C.

Velasco V, Cabello P, Vázquez-Suñé E, López-Blanco M, Ramos E, Tubau I, 2012. A sequence stratigraphic based geological model in the urbanized area of the Quaternary Besòs delta (NW Mediterranean coast, Spain). Geologica Acta, 10, 373-393.

Volchko Y, Norrman J, Ericsson LO, Nilsson KL, Markstedt A, Öberg M, Mossmark F, Bobylev N, Tengborg P, 2020. Subsurface planning: Towards a common understanding of the subsurface as a multifunctional resource. Land Use Policy, 90, 104316, https://doi.org/10.1016/j.landusepol.2019.104316.

Von der Tann L, Sterling RL, Zhou Y, Metje N, 2019. Systems approaches to urban underground space planning and management – A review. Underground Space 5(2), DOI: 10.1016/j.undsp.2019.03.003.

Wornardt WW, 1993. Application Of Sequence Stratigraphy To Hydrocarbon Exploration. Paper presented at the Offshore Technology Conference, Houston, Texas, May 1993. doi: https://doi.org/10.4043/7084-MS.

Chapter 3 - Long-term spatiotemporal evolution of land subsidence in the urban area of Bologna, Italy

3.1 Preface

The analysis summarised in the preceding chapter enabled the exploration of the initial scientific question of this PhD project, which pertains to the complexities of reconstructing the 3D depositional architecture, and hence a reliable 3D geological model, in an urban environment within an intricate alluvial context. The subsequent crucial step involves the comprehensive investigation of the long-term historical evolution of the ongoing subsidence process with respect to the geological setting, reconstructed by the 3D model, as well as groundwater withdrawals.

The present work involved an extensive phase of literature research and harmonisation of fragmented historical and recent subsidence and groundwater pumping monitoring data, collected over the years by various local institutions. A vast portion of ground displacement data was provided by the Geologic, Soil, and Seismic Survey of the Emilia-Romagna Region, while groundwater level and pumping data were collected and analysed in collaboration with Professor Alessandro Gargini and Dr Maria Filippini of the hydrogeology research group at the University of Bologna.

This chapter provides a summary of the analyses that resulted in the reconstruction of the long-term spatiotemporal evolution of the ongoing subsidence by integrating different sources of monitoring data, which required more than a year to be completed. The chapter consists of a paper submitted to the journal *Bulletin of Engineering Geology and the Environment*, and currently under review: Zuccarini A[1], Giacomelli S[2], Severi P[3], Berti M[1], IN REVIEW. Long-term spatiotemporal evolution of land subsidence in the urban area of Bologna, Italy.

[1] Department of Biological, Geological, and Environmental Sciences (BiGeA), University of Bologna, via Zamboni 67, Bologna, Italy

[2] ISPRA, Institute for Environmental Protection and Research, via Vitaliano Brancati 48, Rome, Italy

[3] Geologic, Soil, and Seismic Survey – Emilia-Romagna Region, Viale Aldo Moro 30, Bologna, Italy

3.2 Abstract

Land subsidence in urban areas is a highly significant and globally widespread issue of topical interest. This type of ground deformation process commonly occurs in rapidly expanding cities due to the combined effects of structural loading from built infrastructures and excessive groundwater withdrawals due to the increasing water demand of growing populations and industries. In this study, we perform a detailed analysis of the ongoing subsidence process in Bologna (Italy) with respect to historical pumping trends and the 3D geological model of the subsurface. Since the 1960s, the city of Bologna has experienced severe subsidence attributed to the overexploitation of aquifers for civil water use. Ground deformation peaked in the 1970s, with documented maximum rates of approximately 10 cm/year, causing structural and infrastructural damages. Over the years, the subsidence process has been intensively monitored by local authorities, collecting extensive ground displacement measurements employing different and increasingly sophisticated techniques, including topographic levelling and satellite interferometry. Long-term data are essential for a comprehensive understanding of the subsidence process evolution and for calibrating numerical or statistical predictive models. Therefore, we developed a methodology to integrate ground-based and remotely sensed monitoring data and produce cumulative ground displacement time series and maps, capturing the long-term temporal evolution and spatial distribution of the subsidence process, respectively. The long-term deformation field reconstructed aligns well with the 3D geological model of the area, and the produced cumulative displacement curves consistently match the pluriannual trends observed in groundwater level and pumping monitoring time series.

3.3 Introduction

Land subsidence in urban environments represents a serious and globally widespread geological hazard (Hu et al. 2004), that includes both the sudden sinking and the progressive down-warping of the ground surface (Galloway & Burbey 2011; Bagheri-Gavkosh et al. 2021). This type of ground deformation process can result from a combination of natural causes, such as local tectonics (Dehghani et al. 2009, Yousefi & Talebbeydokhti 2021) or the self-weight consolidation of the existing sedimentary deposits (Zhang et al., 2018), as well as anthropogenic factors. Frequently anthropogenic influences are superimposed on regional-scale natural processes (Galloway & Burbey 2011), yet they are typically more localised and result in higher vertical deformation rates. Common sources of external anthropogenic forcing may be found in underground construction and mining (Ng et al. 2015; Zhao et al. 2019), and in fluid mobilisation in the subsurface (Herrera-García et al., 2021), such as water, crude oil and natural gas (Mahmoudpour et al. 2015). Excessive groundwater withdrawals, triggering the consolidation of compressible layers in susceptible aquifer systems are frequently identified as the primary cause of subsidence in large and rapidly expanding cities, due to the escalating demands for industrial and civil water use (Mahmoudpour et al. 2015).

The reconstruction of the geological setting in highly anthropized contexts, and the development of 3D geological models fundamental for obtaining reliable geotechnical and hydrogeological models, can pose significant challenges. These difficulties typically stem from the absence of outcrops due to extensive urbanisation and the complexities associated with performing lithostratigraphic correlations in intricate depositional environments (Velasco et al. 2012; Luberti et al. 2015; He et al. 2023). Major cities frequently rise in flat regions within coastal or alluvial plain contexts, where the subsurface comprises stacked sequences of coarse-grained and fine-grained sedimentary bodies exhibiting frequent lateral variability, thereby deviating from the fundamental principles of stratigraphic superposition and lateral continuity of strata (Miall 1985). In this particular context, also the hydrogeological characterisation of the subsurface implies notable challenges, including the definition of homogeneous hydrogeological units within the complex architecture of the existing deposits and the reconstruction of groundwater flow, which may be altered by the presence of underground structures and infrastructures (Vázquez-Suñé et al. 2005; Attard et al. 2016; De Caro et al. 2020). Additional

complexities may arise from the existence and the irregular distribution of multiple groundwater withdrawals for both industrial and domestic purposes, which often can prove difficult to thoroughly assess and quantify (ARPAE 2008; Foster 2022).

In this study, we perform a detailed analysis of the ongoing subsidence process in the city of Bologna (Italy) investigating its long-term temporal and spatial evolution with respect to historical pumping trends and the 3D geological model of the subsurface. Since the 1960s, the urban area of Bologna experienced severe land subsidence due to excessive groundwater withdrawals. Local authorities have regularly monitored the sinking process over the years through a series of measurement campaigns, employing progressively advanced methods including topographic levelling and, since 1992, satellite interferometry. InSAR (Interferometric Synthetic Aperture Radar) data, in particular, has given a substantial contribution to the reconstruction of the ongoing subsidence process in recent times, with increasingly higher temporal and spatial resolution towards the newer surveys. Long-term data are crucial to comprehensively understand the subsidence process evolution as well as to calibrate numerical and statistical models that can be employed for the prediction of future sinking trends based on anticipated pumping rates. To this end, a processing chain has been devised to combine ground-based and remotely sensed data, resulting in long-term time series and spatial subsidence maps. Long-term data reveal a consistent response of the subsidence process to significant pumping and groundwater level fluctuations, and a strong correlation between the ground deformation field and the 3D geological model of the study area. Moreover, recent data indicate a subsidence upsurge due to increased pumping to offset reduced precipitation, underscoring the potential impact of climate change on the ground deformation process.

3.4 Study Area

The city of Bologna (Italy) rises in the southern portion of the Po Plain (Northern Italy) in a peculiar transition zone with the Northern Apennines front (Fig. 3.1). The Po Plain, which extends north of the study area, represents the surface of an active foredeep basin bounded by two mountain belts still in formation: the Alps to the north and the Apennines to the south (Ori 1993; Severi 2021). The uppermost portion of the local stratigraphic succession is mainly characterised by Quaternary recent alluvial deposits that, in the context of a shallowing upward sequence (Castellarin et al. 1985; Ricci Lucchi 1986), lie upon Quaternary marine deposits. The study area, centred on the historical city centre, covers a surface of approximately 88 km² and stretches south to north from the Northern Apennines foothills to the northern suburbs of Bologna. The region is bounded at the west and the east by the Reno and Savena rivers, respectively (Fig. 3.1). Elevation ranges from about 80 to 30 m above sea level (a.s.l.), moving from the Apennines foothills, at the south, to the northernmost portions of the area.

The morphological and geological setting of the study area is dominated by the presence of the Reno and Savena rivers' alluvial fans (Bergonzoni & Elmi 1985) that mainly consist of stacked coarse-grained deposits, which grade into less amalgamated and finer bodies towards their distal portions. These two main morphological elements bound the west and the east sides of the area where the city centre rises. The subsurface of this region exhibits a depositional architecture with predominant silty-clayey deposits (Amorosi et al. 1997) and rare coarse-grained bodies occurring at depths greater than 100 m (Giacomelli et al. in review). The sedimentation of these finer deposits is associated with the activity of multiple minor streams that flow from the hills towards the city, forming a complex network of canals in the city centre. Despite having small catchment areas and limited transport capacity, these watercourses played a significant role in land building during the Holocene, especially in the area between the Reno and Savena outlets (Giacomelli et al. in review). This region has been acting as an interfluve since the Middle Pleistocene (Amorosi et al. 1996, 1997; Bruno et al. 2013, Giacomelli et al. in review) and is characterised by a stacked paleosols succession suggesting prolonged periods of subaerial exposure (Amorosi et al. 2014, Bruno et al. 2020; Giacomelli et al. in review). Recently, a detailed analysis of the available geognostic surveys archives (312 water wells and 628 continuous-core boreholes) based on the systematic reinterpretation of the stratigraphic data in terms of *lithofacies*, and

the correlations performed on variously oriented cross-sections, was carried out as described in Giacomelli et al. (in review). This analysis, aimed at understanding the general subsurface depositional architecture of the study area, allowed its subdivision into three geological domains, namely A, B and C (Fig. 3.1). These regions, despite their common alluvial origin, exhibit different morphological features and depositional staking patterns. Domain A, located in the western portion of the study area, displays an overall flat morphology and is marked by the course of the Reno River which deposited heavily-stacked gravelly bodies. The high degree of amalgamation of these sedimentary bodies gradually decreases towards the northeast, moving farther from the river's outlet. Domain B occupies the central-southern portion of the study area and it is characterised by a slightly convex morphology, topographically elevated compared to the surrounding areas, and by the presence of the historical city centre. Differently from the others, the subsurface in Domain B is marked by thick and rather continuous sequences (about 100 m) of fine-grained overconsolidated stiff deposits. The occurrence of several orders of paleosols suggests the prolonged exclusion of this "relative high" from the main rivers' dynamics. Domain C is located in the eastern sector of the area and exhibits a clear convex morphology that corresponds to the Savena alluvial fan. Here, although the subsurface is defined by the frequent occurrence of gravelly deposits associated with the river activity, the coarse-grained bodies are generally thinner, significantly more dispersed and laterally discontinuous than in Domain A. The amalgamation of the gravel deposits is limited to the fan apex and progressively decreases northward grading to more scattered and finer sandy bodies in the distal portions. While the transition between Domain B and the adjacent ones (A to the west and B to the east) is rather sharp, the passage from Domain A to C in the northern portion of the study area is less abrupt, albeit evident.

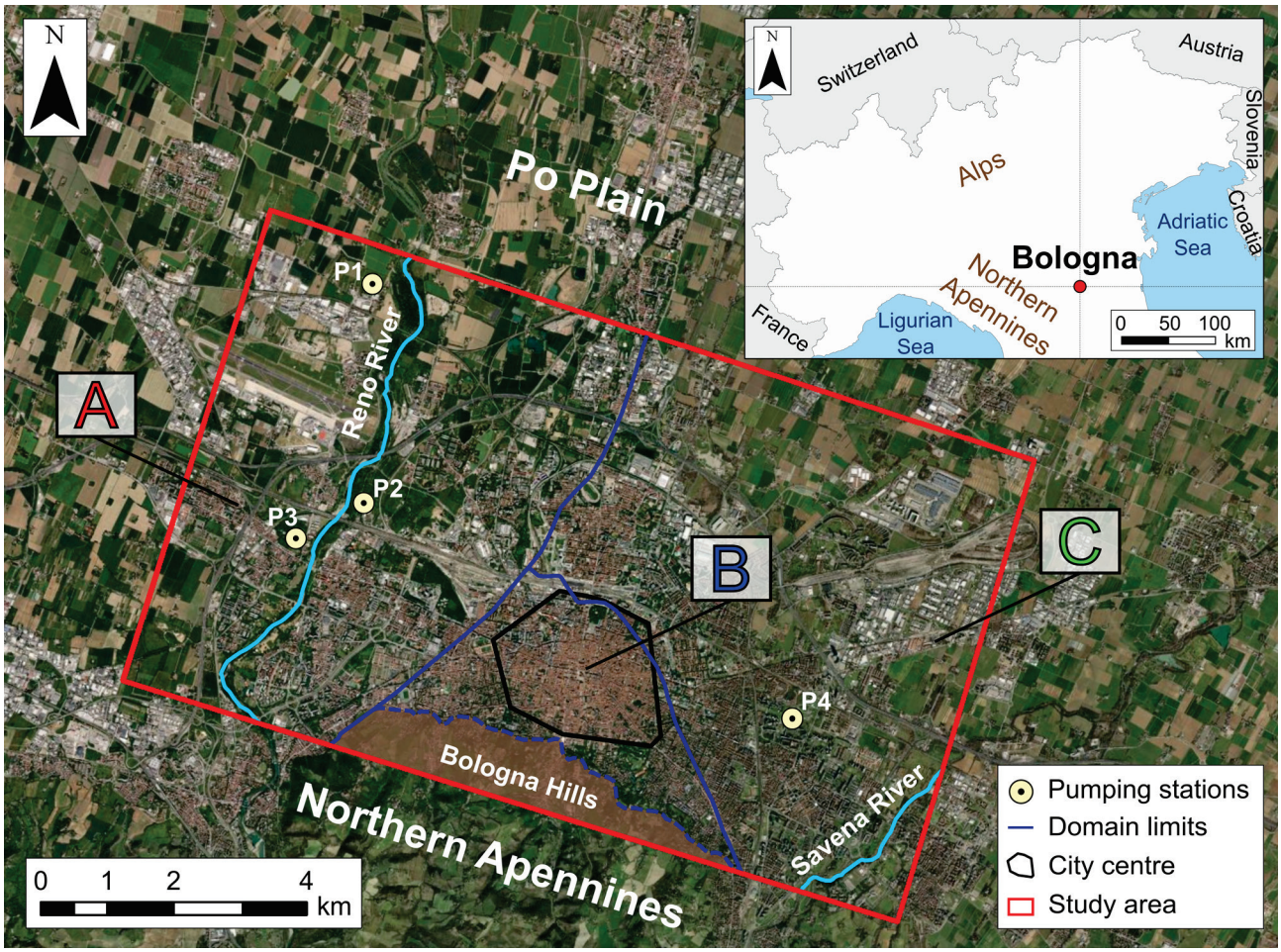

Fig. 3.1 Study area. The dark blue lines represent the boundaries of the three different geological domains identified after the stratigraphic analysis performed and described in Giacomelli et al. (in review). The light yellow circles mark the centroids of the four main groundwater pumping stations for civil water supply (*P1-P4*).

These stratigraphic observations guided the construction of a 3D geological model of the study area subsurface in the Leapfrog Works environment (Fig. 3.2). Firstly, a simplified model showing the three different domains was generated (Fig. 3.2a). Then, their internal characterisation was performed by transposing the 2D stratigraphic correlations made on vertical cross-sections into the three dimensions (Fig. 3.2b-d), as described in Giacomelli et al. (in review).

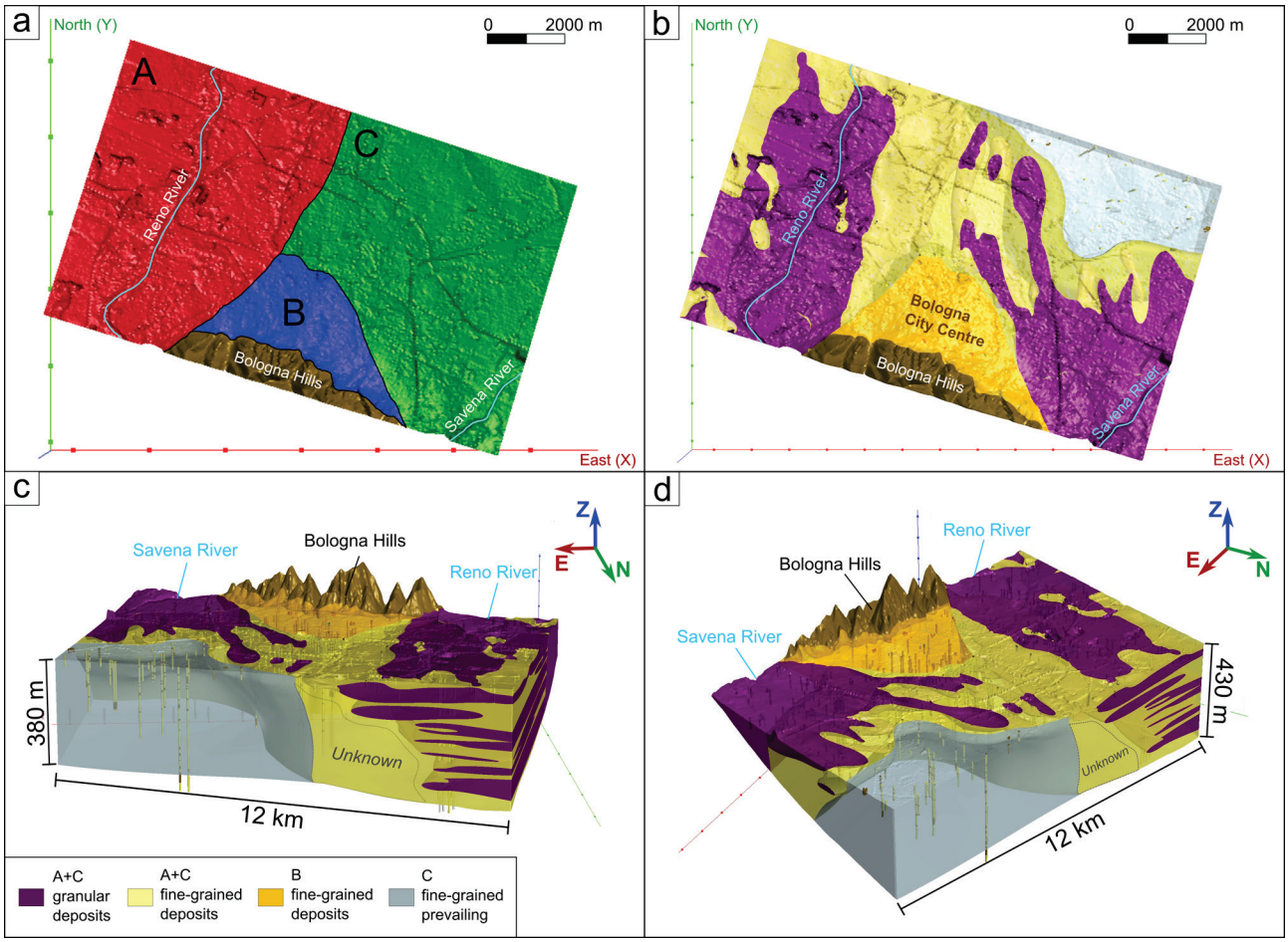

Fig. 3.2 3D geological model of the study area (*Giacomelli et al., in review*). (a) presents a plan view of the simplified geological model with the subdivision of the study area into three different geological domains; (b) and (c, d) provide a plan view and two 3D views, respectively, of the final geological model, showing the internal characterisation of the three domains. The reconstructed coarse-grained sedimentary bodies are indicated in purple, while the fine-grained deposits are shown in light yellow. The overconsolidated stiff clayey deposits in Domain B are distinguished from the fine-grained bodies reported in Domains A and C and are displayed in light orange. The northeastern region of Domain C is characterised by a "fine-grained prevailing" portion, shown in grey. Due to the low thickness and scattered distribution of coarse-grained deposits, as well as the poor availability of geognostic surveys, 3D correlations were not performed in this area. Similarly, the deeper portion of the northeastern corner of Domain A is labelled as "*unknown*" due to the lack of stratigraphic data.

While the sectors at the south of Bologna, as most of the Northern Apennines, have experienced a general uplift since the early Pleistocene (Argnani et al. 2003), the Po Plain, including the study area, has undergone land subsidence, during the last 1.43 million years at rates of 1-2.5 mm/year (Carminati & Di Donato 1999; Carminati & Martinelli 2002; Stramondo et al. 2007). Tectonic loading (Sclater & Christie 1980; Carminati & Martinelli 2002) and the self-weight consolidation of thick alluvial sediment sequences (Modoni et al. 2013) have been identified as the main components contributing to the documented natural ground sinking. Alongside this phenomenon, since the beginning of the 1960s, the area of Bologna has experienced severe anthropogenic

subsidence. This process differs from the uniform natural component, showing a significantly higher intensity and more localised and uneven spatial distribution. Excessive groundwater withdrawals to meet the increasing water demand of a rapidly growing city like Bologna have been identified as the major external anthropic forcing responsible for the ground deformation process (Pieri & Russo 1980; Brighenti et al. 1995; Bitelli et al. 2015). The main pumping stations in the study area were built during the 1970s on the stacked coarse-grained deposits of the Reno River and the Savena alluvial fan apex (Fig. 3.1), extracting water at rates of about $4x10^7$ and $5x10^6$ m^3/year, respectively (Viel et al. 2005). Shortly after, subsidence peaks of about 100-110 mm/year were recorded. Ground displacements gradually decreased since the mid-1980s following the introduction of more restrictive groundwater pumping regional regulations (ARPAE 2018). Nowadays, although the subsidence process persists to a lesser extent, ground sinking is still relevant and therefore deserves further in-depth analysis.

3.5 Methodology

3.5.1 Input data

The ongoing subsidence process in Bologna has been intensively monitored over the last 40 years, and extensive ground displacement measurements were collected by local authorities employing different and increasingly sophisticated techniques. In this work, three main sources of subsidence data were considered (Table 3.1). Dataset *D1* represents the oldest monitoring data, dating back to the first half of the last century onward. These data are available as cumulative sinking or subsidence rate contour maps (Fig. 3.3a), as the original topographic levelling measurements are nowadays no longer accessible. Dataset *D2* consists of periodic topographic surveys conducted at reference levelling benchmarks from 1950 to 2005 (Fig. 3.3b). Dataset *D3* consists of the most recent ground displacement measurements derived by satellite interferometry (Fig. 3.3c).

Historical contour maps (*D1*) offer valuable perspectives on how land subsidence was spatially distributed in the initial phase of the phenomenon. The accuracy of these data is unknown because neither the spatial distribution of measurement points nor the interpolation technique are known. However, the maps were derived from topographic levelling and should provide a reasonably accurate representation of land subsidence pattern. The more recent topographic data (*D2*) consists of ground elevation measurements conducted on 53 points spaced approximately 600 m apart and aligned along two primary directions. The first line runs from NW to SE, while the second one is oriented SW-NE, crossing the study area transversally and longitudinally, respectively. The general accuracy of these data is estimated to be approximately 1 mm for benchmark distances on the order of 1 km (Vanicek & Krakiwsky 1982; Bitelli et al. 2017). Satellite data (*D3*) were obtained using the Permanent Scatterers (PS) technique (Ferretti et al. 2001) across five distinct satellite acquisitions (See Table 3.1).

PS data are characterised by a wide and dense distribution, providing information on a more continuous spatial domain and with greater temporal resolution (6-35 days depending on the revisiting time of the satellite). However, as these data are derived from relative measurements along the sensor line of sight (LOS) and referred to a stable motionless reference point, they lack absolute reference in time and space (Farolfi et al. 2019) and should be referred to conventional geodetic reference systems (Farolfi et al. 2019) using ground-based monitoring data such as topographic levelling (Bitelli et al. 2015, 2020) or GNSS (Global Navigation Satellite System) permanent stations measurements (Bitelli et al. 2015, 2020; ARPAE 2018; Farolfi et al. 2019). InSAR data acquired in the study area have an accuracy in the range of 1-2 mm/year, determined from the standard deviation of the PS mean velocity with respect to the local reference point (ARPAE 2018).

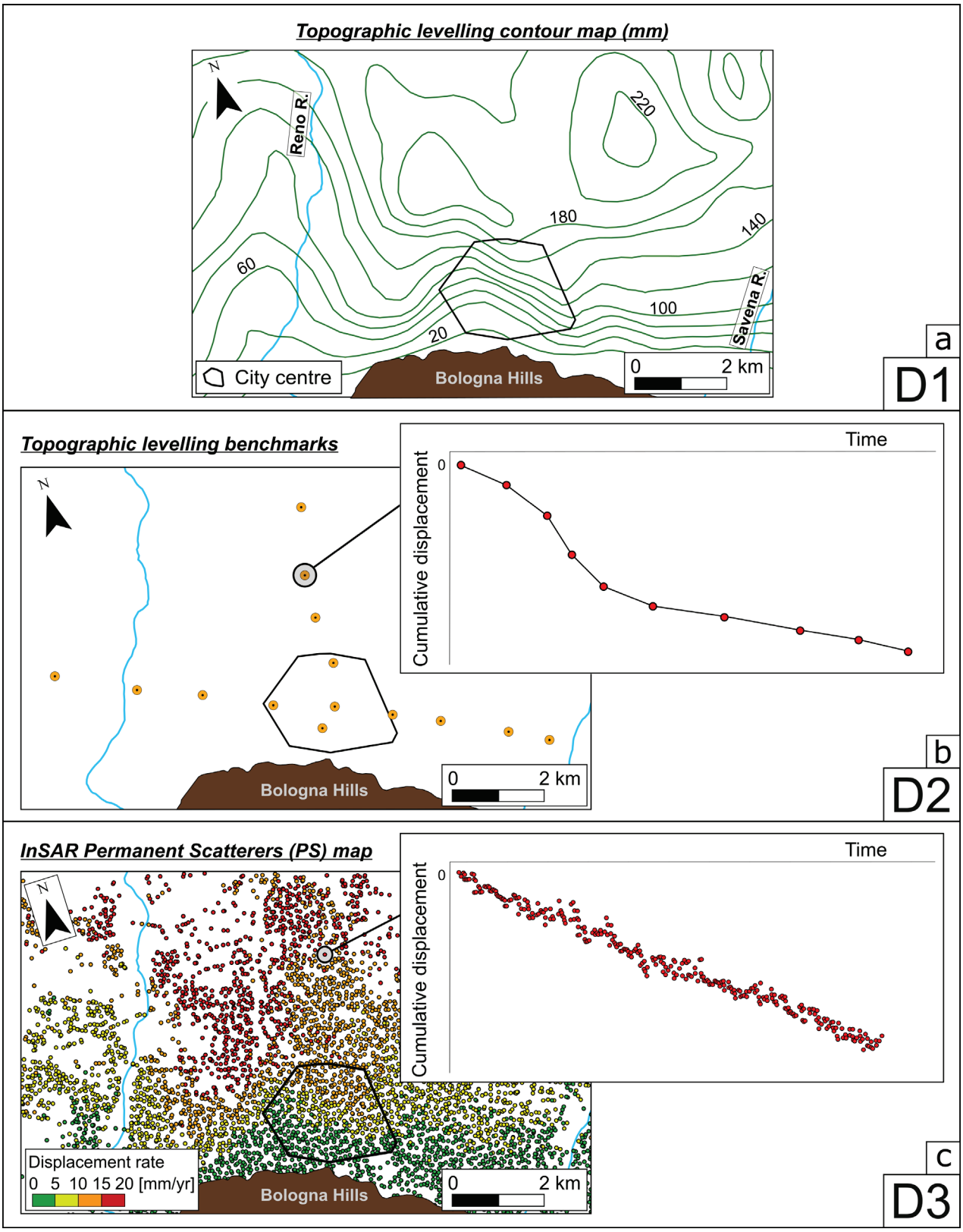

Fig. 3.3 Conceptual representation of the three different available sources of ground displacement monitoring data.

ID	Data type	Years	Source	Survey details	N° benchmarks - PS (study area)
D1	Historical subsidence map	1900 – 1950	Salvioni (1953), Pieri & Russo (1985)	/	/
D1	Historical subsidence map	1950 – 1972	Pieri & Russo (1984, 1985)	/	/
D1	Historical subsidence map	1973 – 1983	Barbarella et al. (1990)	/	/
D1	Historical subsidence map	1983 – 1987	Barbarella et al. (1990)	/	/
D1	Historical subsidence map	1987 – 1992	Folloni et al. (1996)	/	/
D2	Topographic levelling	1950 – 1992	UniBo archive	/	18
D2	Topographic levelling	1983 – 2005	Bologna Municipality archive – Arpae	/	35
D3	InSAR	1992 – 2001	Arpae – TRE Altamira	ERS1 + ERS2 (desc.)	3711
D3	InSAR	2002 – 2006	Arpae – TRE Altamira	ENVISAT (asc. and desc.)	2764
D3	InSAR	2006 – 2011	Arpae – TRE Altamira	RADARSAT1 (asc.)	6720
D3	InSAR	2011 – 2016	Arpae – TRE Altamira	RADARSAT2 + COSMO-SkyMed (asc.)	18800
D3	InSAR	2015 – 2020	UniBo (*Fragile*)	SENTINEL1 (asc.)	145956

Table 3.1 Details of the available topographic levelling (*D1*, *D2*) and InSAR (*D3*) datasets used in this work.

3.5.2 Data integration

Long-term data are crucial for a comprehensive understanding of the ongoing subsidence process evolution. To this end, two main long-term types of products (time series and raster maps) have been generated by integrating the available ground-based and remotely sensed monitoring data. Time series depict the temporal evolution of the ground-sinking process in specific points of the study area, while raster maps illustrate its overall spatial distribution.

3.5.2.1 Time series

The available punctual measurements were homogenised into a series of tables containing the measured displacements over time of all the levelling benchmarks (*D2*) and *PS* from each InSAR survey (*D3*) within the study area. The construction of long-term subsidence continuous time series is strongly influenced by the distribution of the existing levelling benchmarks, in which the topographic survey data are condensed. Therefore, a set of control points (C_p) were defined on their exact location. In case of benchmarks closer than 100 m, they were assigned to the same C_p, fixed at their midpoint. A series of circles of constant size was then traced around the control points to isolate and extract all the PS, of each InSAR survey, in their proximity (Fig. 3.4a). The radius of these interrogation circles (200 m) was defined in such a way as to consider a significant number of PS and avoid enclosing adjacent control points. The following procedure was systematically reiterated for each interrogation circle to integrate the extracted topographic and satellite data and generate continuous time series.

Firstly, topographic levelling data (*D2*) were considered. Due to inconsistencies in the starting dates of the available measurements, the lack of information on the referencing system of the recorded displacements, and the fact that these measurements were collected after the onset of the subsidence process, displacement rate time series were initially used instead of cumulative sinking ones. Once extracted, the subsidence rate curve of the selected control point was resampled every two years and subsequently converted into the corresponding cumulative displacement one (Fig. 3.4b). Where two close levelling benchmarks had been assigned to the same C_p, their resampled subsidence rate time series were averaged before extracting the corresponding displacement curve.

Considering satellite data (*D3*), one InSAR survey at a time, the PS enclosed by the interrogation circle in question were isolated, and the corresponding monitoring displacement curves were retrieved. To reduce noise in each extracted time series, the best-fitting second-order polynomial curve was computed and then resampled to obtain a more regular subsidence evolution trend, with only one measurement per year. These curves were then averaged to get a single reference time series for the extracted PS set (Fig. 3.4c). In this phase, the mean displacement computed for each year was verified to significantly represent the distribution of sinking values from which it was derived and it was paired with its corresponding standard deviation. By reiterating these steps for all the InSAR surveys, a fragmented set of time series was obtained, describing successive short intervals of the subsidence process evolution, within the same interrogation circle (Fig. 3.4d).
The derived displacement time series were finally integrated starting from the concatenation of the older topographic levelling curve (*D2*) and the first InSAR one (*D3*). When two curves share at least one year of measurements the latter (*D3*) was shifted by a value equal to the distance between the two series, measured at its first point (Fig. 3.4d). Otherwise, the more recent series was shifted and connected to the continuation of the older one, provided that the two surveys are reasonably close in time. In case of a narrow time gap (one or two years at maximum), the first curve was extended by determining the equation of the line between its final two known points and estimating the cumulative displacement value for the required year, corresponding to the first measurement of the second survey. Conversely, in the event of larger time gaps, the concatenation was not performed and the control point (C_p) fixed on the benchmark in question was discarded.
Following this procedure, each successive fragmented time series was shifted and attached to the previous one, progressively generating a continuous cumulative displacement curve covering the entire available monitoring period (Fig. 3.4d). Overlapping segments between consecutive survey series were averaged and the respective standard deviation values were updated accordingly (Fig. 3.4e).
In order to account for the variability in the starting date of subsidence measurements, the cumulative displacement time series were homogenised and defined on a common reference interval. Consistently with the availability of monitoring data from water pumping stations, which ranges from 1970 to 2020 (see sub-section 3.5.3), the starting year for subsidence records was set at 1970 (Fig. 3.4e). Displacement curves starting earlier were clipped over the new interval, whereas the others were reset to the new baseline and shifted accordingly. The estimation of displacement value between 1970 and the first actual recorded measurement was achieved by extending the time series backwards, calculating the equation of the line between its first two points, and extracting the displacement value for 1970. The maximum backward extension applied to the time series was 18 years for the most recent ones starting in 1988. It should be noted that this method assumes a constant rate for the estimated displacement, as it is defined on the slope of the first segment of the curve.
The reconstructed cumulative sinking time series were then used to derive the subsidence rate time series through the following procedure. Firstly, each ground displacement curve was regularised by employing the Savitzky-Golay smoothing algorithm (Savitzky & Golay 1964), considering a 1^{st}-order regression polynomial and a moving window length of three measurements, on which the least-squares fitting was computed. The best-fitting polynomial of the n^{th} order was then calculated to closely reproduce the smoothed time series trend. In this specific case, the 6^{th}-order fitting polynomial provided the most representative results for all the analysed time series. Finally, by calculating the first derivative at each point of these curves, representing the smoothed cumulative displacement ones, the corresponding subsidence rate time series were obtained.

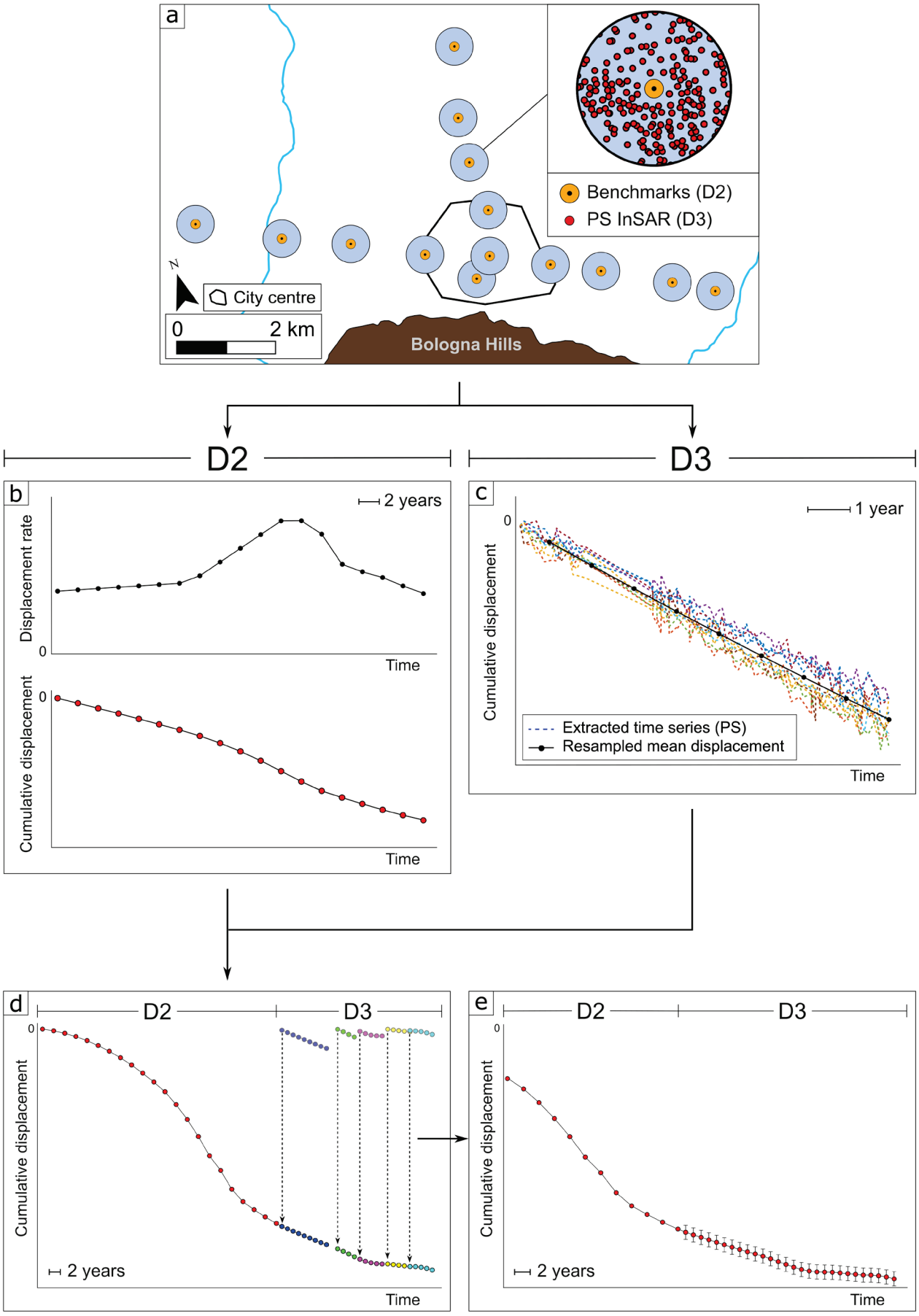

Fig. 3.4 Flow chart summarising the processing chain employed to integrate topographic levelling and InSAR monitoring time series, and generate continuous long-term cumulative displacement curves.

Alongside the long-term time series, detailed short-term curves were generated using a similar methodology to investigate the more recent evolution of the ground deformation process within the reference period 2008-2020 with a higher temporal resolution. The PS cumulative displacement time series (*D3*) previously extracted at each control point (C_p) were clipped over the new interval and averaged considering a 3-month moving window with a 1-month shift. The resulting mean displacement series were then paired with the corresponding standard deviation values and concatenated using the same procedure as the long-term curves to create continuous ones.
The obtained cumulative displacement time series were initially smoothed similarly to the long-term ones, and their first derivative was computed to generate short-term subsidence rate curves. Concurrently, a new set of long-term displacement rate time series was created using the same methodology as the original ones, but with 4^{th} and 5^{th}-order regression polynomials which provided, in this case, the most representative results.

3.5.2.2 Raster maps

The available historical subsidence maps (*D1*) were first digitised in the ArcMap environment and converted into mean displacement rate contours (Fig. 3.5a). In parallel, mean subsidence rate maps were generated from the well-distributed PS data from the available InSAR surveys (*D3*), employing the *kriging* interpolation method in the Surfer environment (Fig. 3.5b). The obtained contour maps were homogenised and transformed into a series of perfectly overlapping rasters using ArcMap's *topo to raster* interpolation method (Fig. 3.5c). The displacement rate value stored in each (5x5 m) cell was then converted into the respective cumulative displacement one by multiplying it by the survey duration. Time overlaps and gaps between consecutive campaigns were taken into account. While overlaps were resolved by considering only the data from the more recent survey, short gaps were filled by assuming the subsidence rate from the older campaign for the missing years. Lastly, the obtained rasters were orderly summed to produce a cumulative subsidence map describing the long-term ground displacement distribution in the study area over the entire monitoring period (Fig. 3.5d).

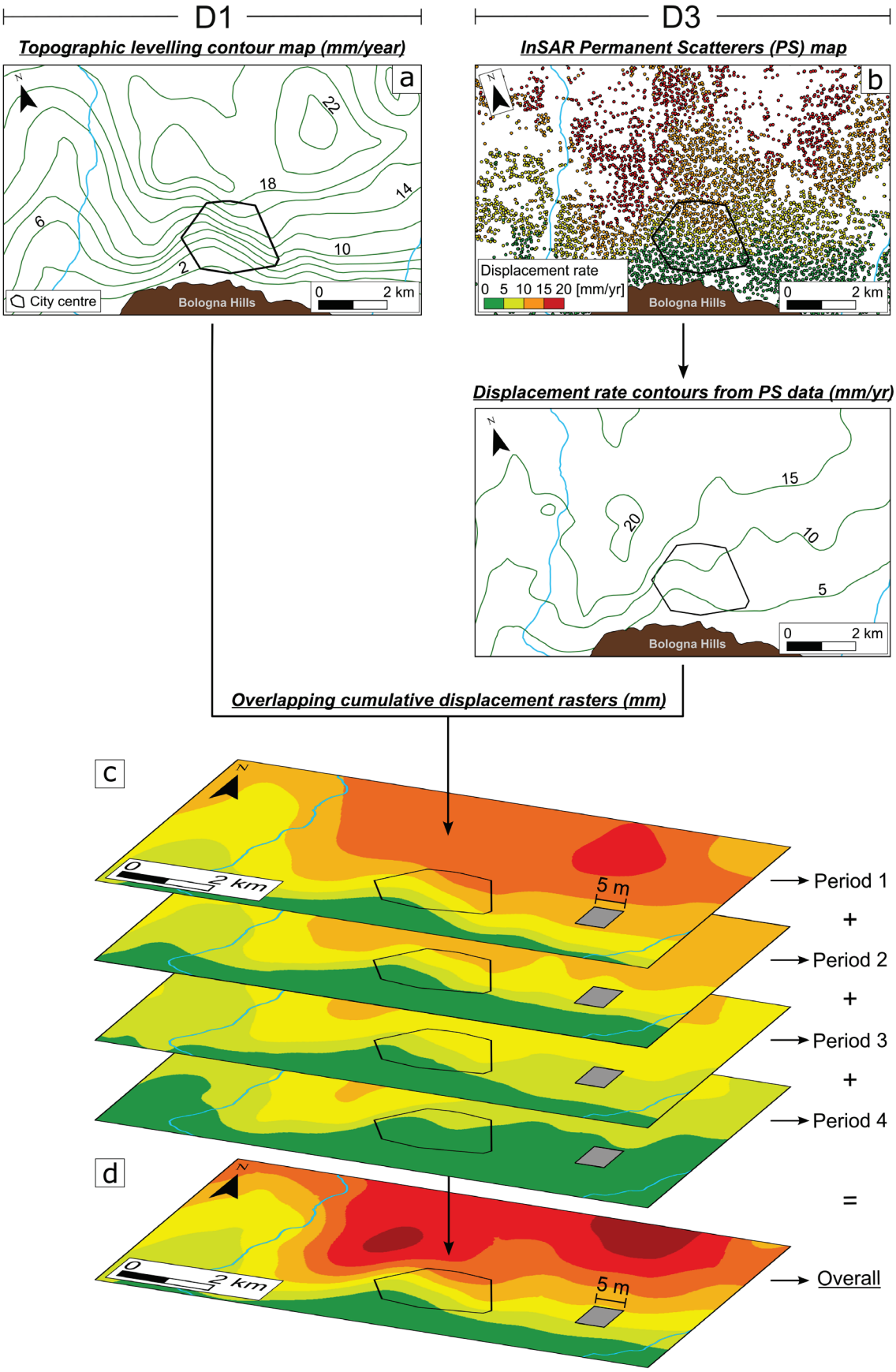

Fig. 3.5 Flow chart summarising the processing chain followed to integrate topographic levelling and InSAR-derived subsidence contours, and generate a long-term cumulative ground displacement map.

3.5.3 Comparison with groundwater data

The long-term subsidence time series were compared with groundwater level and pumping data to investigate their relationship. The available piezometric data archives were categorised into two major groups concerning the more heterogeneous monitoring wells database (*W1*) and the detailed water pumping stations records (*W2*), respectively (Table 3.2). While the former is generally characterised by scattered piezometric level measurements with a low temporal resolution, the latter includes long and continuous groundwater level and pumping time series, updated monthly between 1970 and 2020, and referred to the geometric centroids of the four water pumping stations within the study area (see Fig. 3.1). The three main groundwater extraction and purification centres are situated along the course of the Reno River (Domain A). The *P1* station is located in the distal region of the Reno River deposits and comprises 10 deep wells filtered between 100 and 420 m b.g.l. Differently, the *P2* and *P3* centres rise in a more proximal portion of the Reno River deposits and consist of 13 and 17 deep wells, respectively, with filtration depths ranging from 145 and 350 m b.g.l. Lastly, the *P4* water purification centre is situated in the apical region of the Savena alluvial fan (Domain C) and includes 6 deep wells filtered between 80 and 260 m b.g.l.

ID	Database	Data type	Years	N° wells (study area)
W1	Bologna Municipality – RER	Piezometric level (static)	1900 - 2003	593
W1	Arpae	Piezometric level (static)	1976 - 2020	24
W2	Hera pumping stations (centroids)	Piezometric level (static and dynamic) Pumping	1970 - 2020	4

Table 3.2 Details of the available monitoring wells (*W1*) and pumping stations (*W2*) datasets used in this work.

Drawdown data show both long-term (pluriannual) and short-term (monthly to annual) fluctuations. Since our goal is to investigate the long-term evolution of the subsidence process, the short-term signal was removed using a moving average convolution algorithm with a 5-year moving window. The resulting smoothed time series were compared qualitatively with the long-term subsidence trend. A quantitative analysis based on statistical methods was not performed because of the different temporal resolution of groundwater and ground displacement data.

Short-term groundwater level and pumping curves with higher temporal resolution were extracted over the period of 2008-2020 and compared qualitatively with the recent evolution of the ground sinking process, following the same methodology employed to retrieve the pluriannual trend from *W2* data. However, to match the resolution of the short-term subsidence curves, a 3-month moving average window was used instead of the previous 5-year one.

Concurrently, through the integration of *W1* and *W2* monitoring datasets, a mean groundwater depth map was generated over a reference period, enabling the comparison between the obtained groundwater level distribution with the subsidence deformation field. To account for the heterogeneity of the piezometric level time series included in the *W1* database, a reference time interval from 1995 to 2005 was identified based on the continuous records of the water pumping stations, as it exhibits a degree of stationarity in both groundwater level and pumping smoothed trends (see sub-section 3.6.1.3). To develop the groundwater map, all the monitoring (*W1*) and pumping (*W2*) wells with at least one measurement within the selected interval were initially isolated. The corresponding time series were then extracted, clipped, and averaged to generate a distribution of mean groundwater depth values at discrete points in the study area over the reference period. The resulting values were classified based on the depth of the corresponding wells to identify any potential measurement of a more superficial perched water table in the shallower ones. To ensure higher consistency,

only wells with a minimum of two records between 1995 and 2005 were considered for the interpolation. Groundwater depth contours were finally generated in the Surfer environment employing the *kriging* gridding method and converted into a map using ArcMap's *topo to raster* interpolation function.

The analysis specifically focused on pumping and groundwater level time series, as the investigation of the historical yearly cumulated rainfall time series did not indicate any significant pluriannual trend that could be correlated with the observed groundwater level and the resulting subsidence long-term evolution.

3.6 Results

3.6.1 Long-term evolution

3.6.1.1 Time series

In this section, the monitoring data is utilised to present the reconstructed long-term time series of ground subsidence, groundwater level, and pumping evolution curves. The subsidence data are associated with 37 control points (C_p) distributed across various geological domains (Fig. 3.6), whereas the groundwater data corresponds to the four water pumping stations. The cumulative displacement curves reconstructed at each control point are categorised by domain and presented comprehensively in Fig. 3.17-3.19, provided in the Supplementary Material.

Hereafter, the focus will be placed on the most representative control points, highlighted in Fig.3. 6. The selected points offer extensive datasets and are evenly distributed along the two levelling lines in the study area.

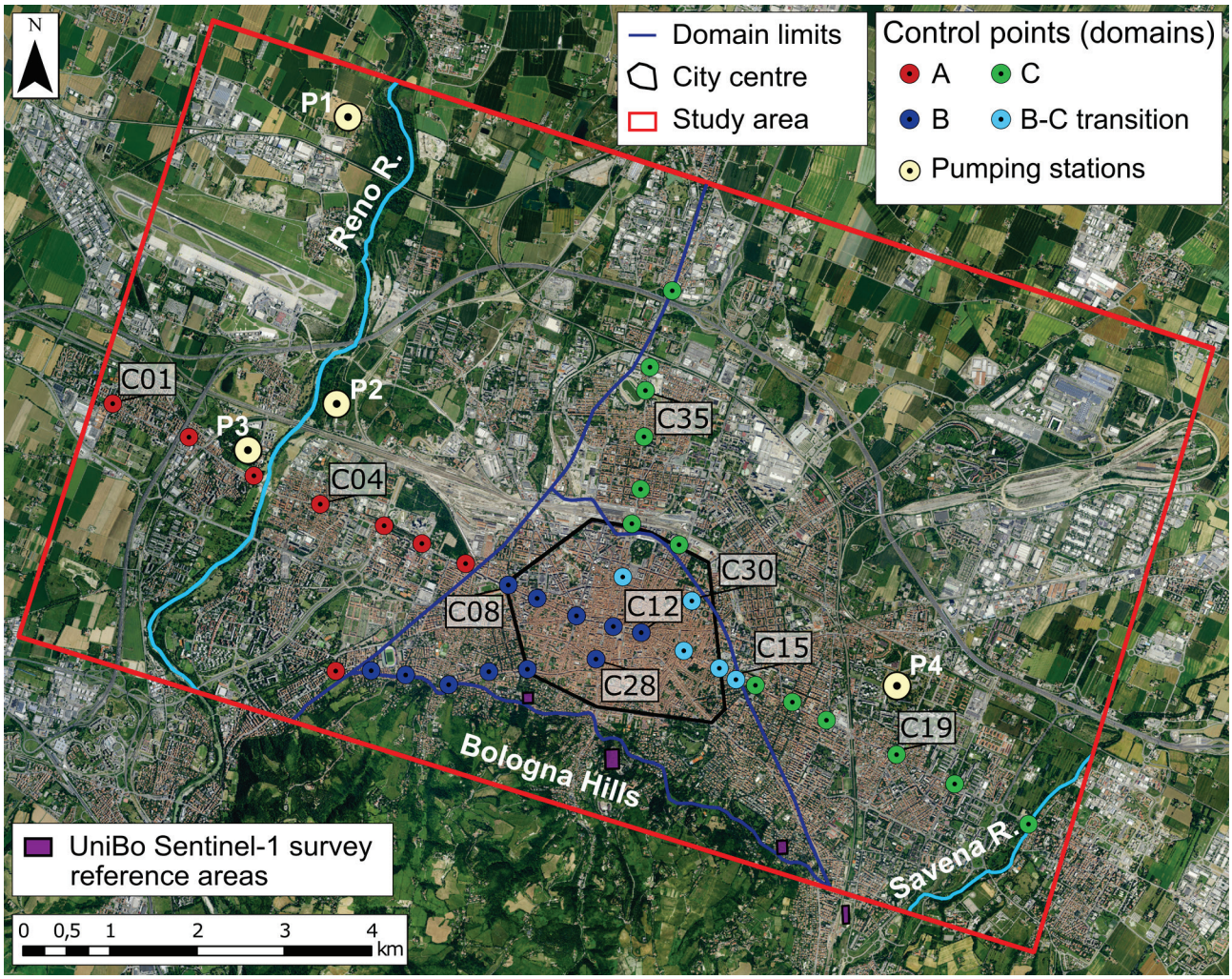

Fig. 3.6 Location of the 37 control points (C_p) in which the long-term subsidence evolution is reconstructed. The colour of the circles varies according to the respective geological domains. The centroids of the four main water pumping stations (*P1-P4*) are displayed as light yellow circles. The purple squares highlight the stable reference areas considered in the Sentinel-1 InSAR survey performed by the University of Bologna (UniBo) spin-off *"Fragile"*.

Over the period considered, the multi-annual pumping trend, and hence that of the groundwater level, have undergone strong variations that can be summarised into a few consecutive stages. The records from the three main pumping stations (*P1 – P3*), built upon the Reno River stacked gravel deposits, exhibit a similar trend that can be split into four phases, in which the groundwater level curves strictly follow pumping trend fluctuations (Fig. 3.7a-c).

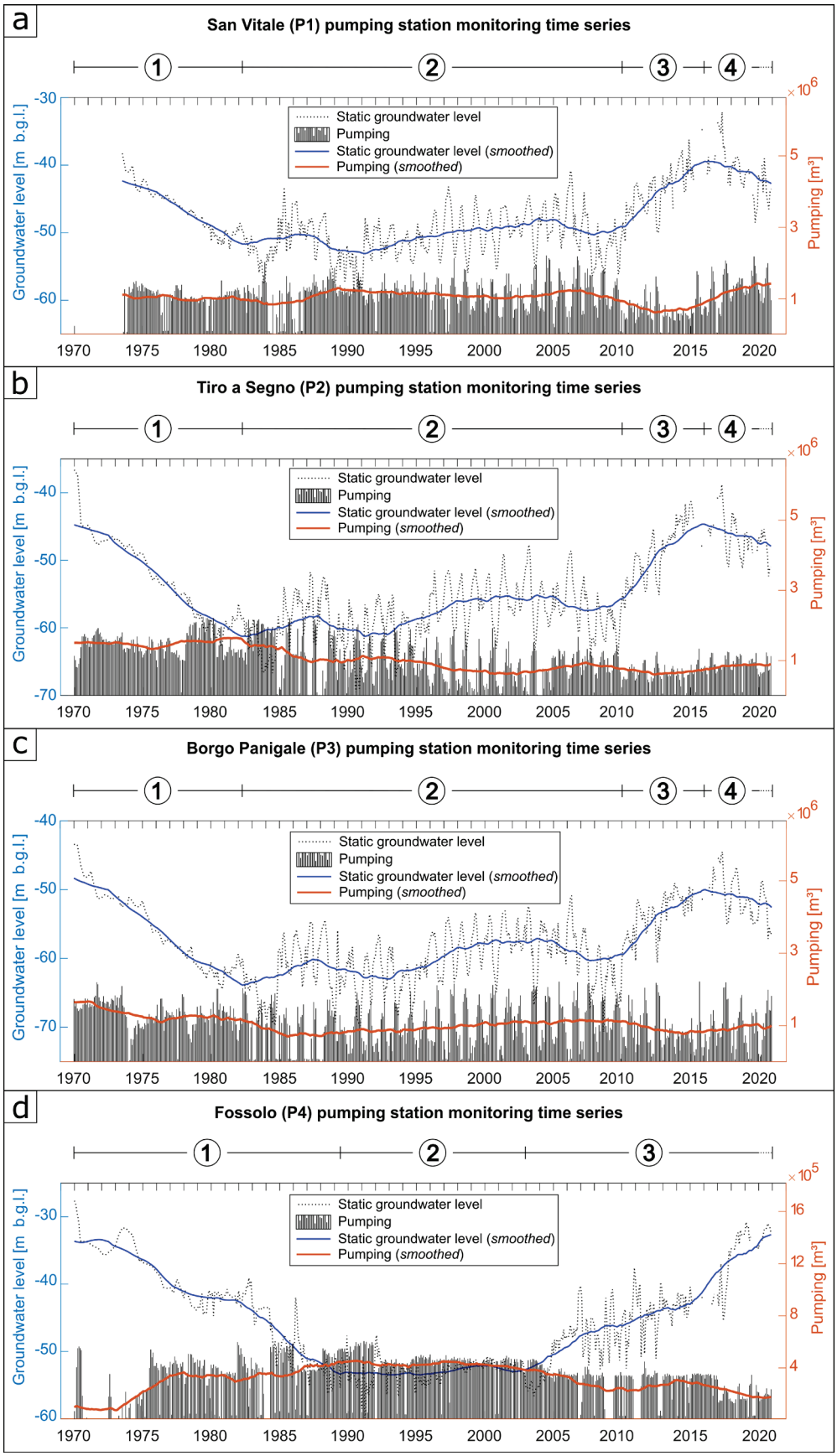

Fig. 3.7 Water pumping stations monitoring records comparison. The figures display the original and the smoothed groundwater level and pumping time series of each pumping station, as well as the subdivision of the long-term trends into 4 (a-c) and 3 (d) phases for *P1-P3* and *P4* stations, respectively.

The first stage (*Stage 1* in Fig. 3.7a-b-c), between 1970 and 1982, is distinguished by a steep groundwater level drawdown linked to the opening of the main pumping stations and high withdrawal rates. Then, starting from 1982, thanks to the introduction of regional groundwater management regulations, the piezometric drawdown ceased and the groundwater level stabilised, experiencing a mild and gradual rise in the following two decades (*Stage 2*). Since 2010, concurrently with the increasing usage of superficial waters, the monitoring records highlight a significant groundwater level rise, reaching values similar to the ones measured in the early pumping stages (*Stage 3*). Lastly, starting from 2016, the groundwater level began decreasing in response to higher pumping rates, which were increased to overcome the lack of precipitations of recent years (*Stage 4*). The described trend is not fully recognisable in the monitoring records of the *P4* station (Fig. 3.7d), which is located upon the Savena alluvial fan and is characterised by an order of magnitude lower pumping rates. The *P4* curves can be divided into three consecutive stages: drawdown (1), stabilisation (2) and rise (3) of the groundwater level, respectively, between 1970 – 1989, 1989 – 2003 and 2003 – 2020. Additionally, the third stage is characterised by a steeper groundwater level rise in recent years, approximately after 2016, reaching values similar to the initial levels as a result of a strong reduction in the pumping rates.

The ground subsidence, evaluated at the different control points (C_p) in terms of cumulative displacement (Fig. 3.8a) and displacement rate (Fig. 3.8b), closely follows the pumping trends. The cumulative displacement curves exhibit their steepest slopes during the first pumping phase, with the highest subsidence rate values of about 100-110 mm/year recorded in Domain C points located north of the city centre. In the second phase, the intensity of the subsidence process gradually decreases, resulting in progressively gentler slopes in the cumulative sinking curves, with maximum displacement rates of around 40 mm/year observed in the same area. During the third stage, the groundwater level rise coincides with a further decrease in subsidence, reflected by nearly flat slopes in the displacement curves of all control points and uniform rates of approximately 3-5 mm/year. Lastly, the fourth phase exhibits a subsidence upsurge, characterised by higher gradients and maximum rates of about 20 mm/year. Other than the general agreement with the pumping rates evolution, the continuous time series reported in Fig. 3.8a,b, also highlight distinct subsidence trends in the three different domains of the study area, explored along the two main topographic levelling lines. Along the first levelling line, which crosses the study area transversally with a NW-SE orientation (Fig. 3.6), a similar evolution trend can be recognised among the time series of the points in Domain A. These curves, represented in Fig. 3.8a by the *C01* and *C04*, follow the described general trend with gradients that clearly vary during the different groundwater pumping phases and display a reconstructed cumulative displacement ranging from 750 to 1300 mm between 1970 and 2020. Moving eastward, the sharp geological and morphological transition between Domains A and B described in section 3.4 seems to be reflected by a significant difference in subsidence evolution trends. Here, Domain B curves, depicted in Fig. 3.8a by the *C08* and *C12*, systematically exhibit sensibly gentler slopes and lower cumulative displacement values ranging from 300 to 650 mm. These curves also display consistently lower gradients during the fourth pumping stage than the previously described Domain A. Further east the control points belong to Domain C. The corresponding curves, highlighted in Fig. 3.8a by the *C19*, exhibit subsidence values that are visibly lower compared to Domain A ones, but slightly higher than in Domain B, ranging from 450 to 760 mm.

The other levelling line which crosses the study area N-S can be divided into two segments. The first one is located between the Apennine foothills and the southern portion of the city centre and includes control points mainly from Domain B, (Fig. 3.6). The corresponding time series, exemplified by the *C28* in Fig. 3.8a, exhibit a trend similar to that observed in Domain B points on the other levelling line, but with even gentler and more uniform gradients, and lower cumulative displacements ranging from 90 to 225 mm. Along the second segment, which continues further north in Domain C, the control point *C35* (Fig. 3.8a), depicts an abrupt increase in ground sinking. The time series systematically display significantly higher gradients and cumulative displacements values, ranging from 1700 to 2300 mm.

The analysis of the reconstructed time series also suggests the presence of a peculiar transition zone between Domain B and C, encompassing the control points near the northern and eastern sectors of the city centre

perimeter (Fig. 3.6). The corresponding cumulative displacement time series, shown in Fig. 3.8a as dashed curves *C15* and *C30*, display an intermediate behaviour that will be separately addressed and discussed in sub-section 3.7.1.

The displacement rate curves displayed in Fig. 3.8b support the previous remarks. Specifically, Domain B curves are distinguished by the lowest velocity values and limited subsidence rate fluctuations over the observation period, particularly in the region close to the Apennine foothills. In contrast, the ground sinking velocity measured in the adjacent Domains A and C, particularly during the first two and the last pumping stages, is systematically higher, indicating a sharp behaviour change towards the western and northeastern directions from the city centre. However, the evolution trend reconstructed in the southwestern portion of Domain C, represented by the *C19* time series in Fig. 3.8b, results to be similar to Domain B curves, with lower velocity values and gentler gradients.

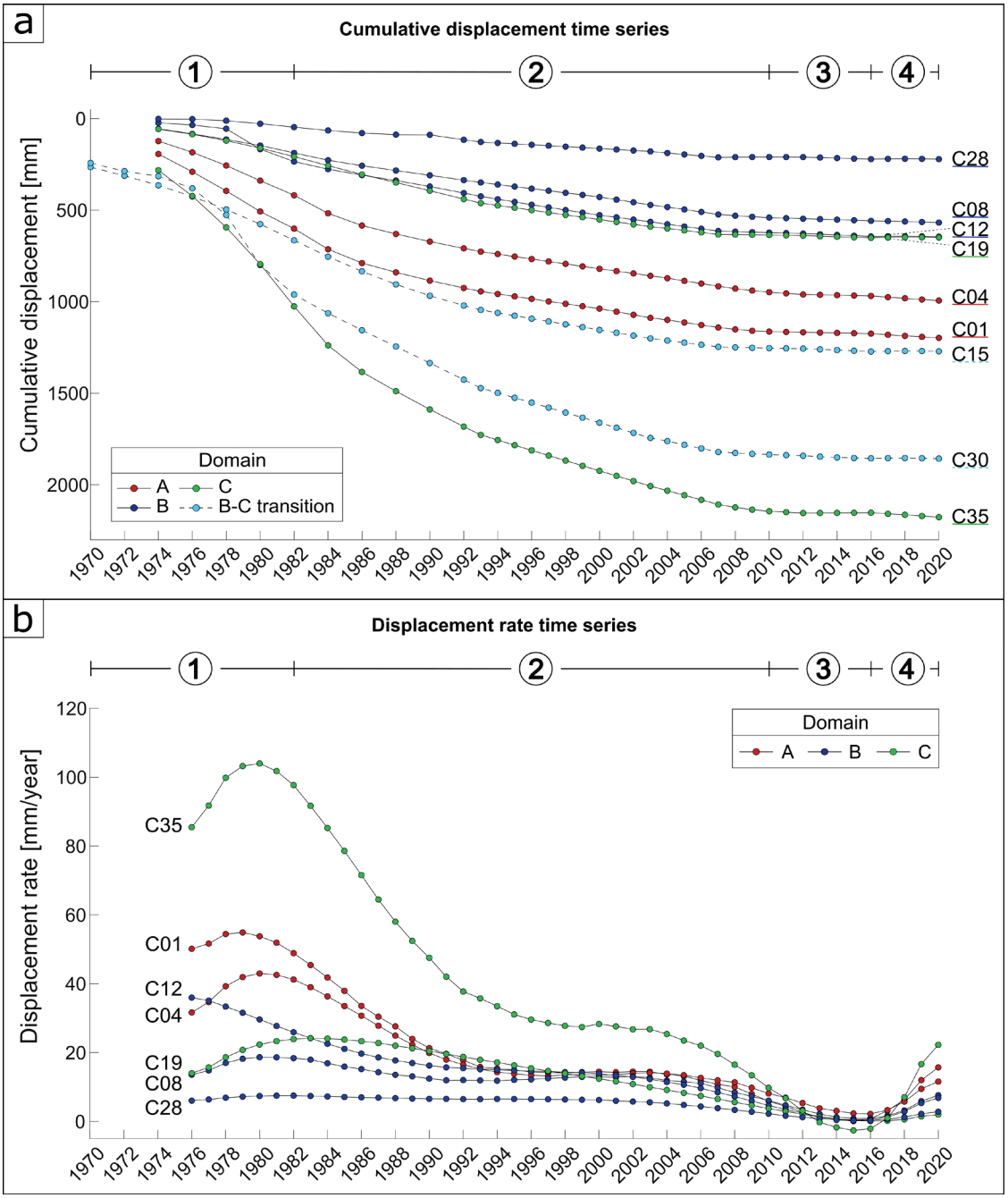

Fig. 3.8 Long-term cumulative ground displacements (a) and displacement rate (b) time series comparison. The reconstructed time series are also compared with the four evolution phases identified in the long-term trends of the *P1-P3* water pumping stations monitoring records.

3.6.1.2 Subsidence maps

Figure 3.9 shows the cumulative displacement raster, which integrates *D1* and *D3* data and displays the long-term spatial distribution of the subsidence process between 1900 and 2020. The map highlights an overall increase in documented ground deformations from the Apennine foothills to the northern portions of the study area. However, distinct trends can be observed both between and within the three geological domains. In Domain A, areas near the Reno River exhibit lower cumulative ground displacement values that gradually increase northeastward along the river's course, with a mild gradient that becomes steeper in its distal portion. The recorded ground sinking also increases laterally, moving from the Reno River towards Domain C. As highlighted by the displacement time series results (Fig. 3.8a), Domain B exhibits the lowest cumulative sinking values within the study area. These values abruptly increase north and northeast towards Domain C, with a high gradient transition zone that crosses the city centre with a NW-SE orientation, as shown by the cumulative displacement contours in Figure 3.9. Conversely, Domain C displays a gradual subsidence increase towards the north and northwest, moving from the apex to the distal portions of the Savena alluvial fan, reaching the highest values at the north of the city centre. Again, the transition between Domain B and the other domains is sharp and marked by significant changes in the subsidence distribution. In contrast, the transition between Domains A and C, which occurs in the northern portion of the study area, does not correspond to any abrupt change in the ground deformation pattern.

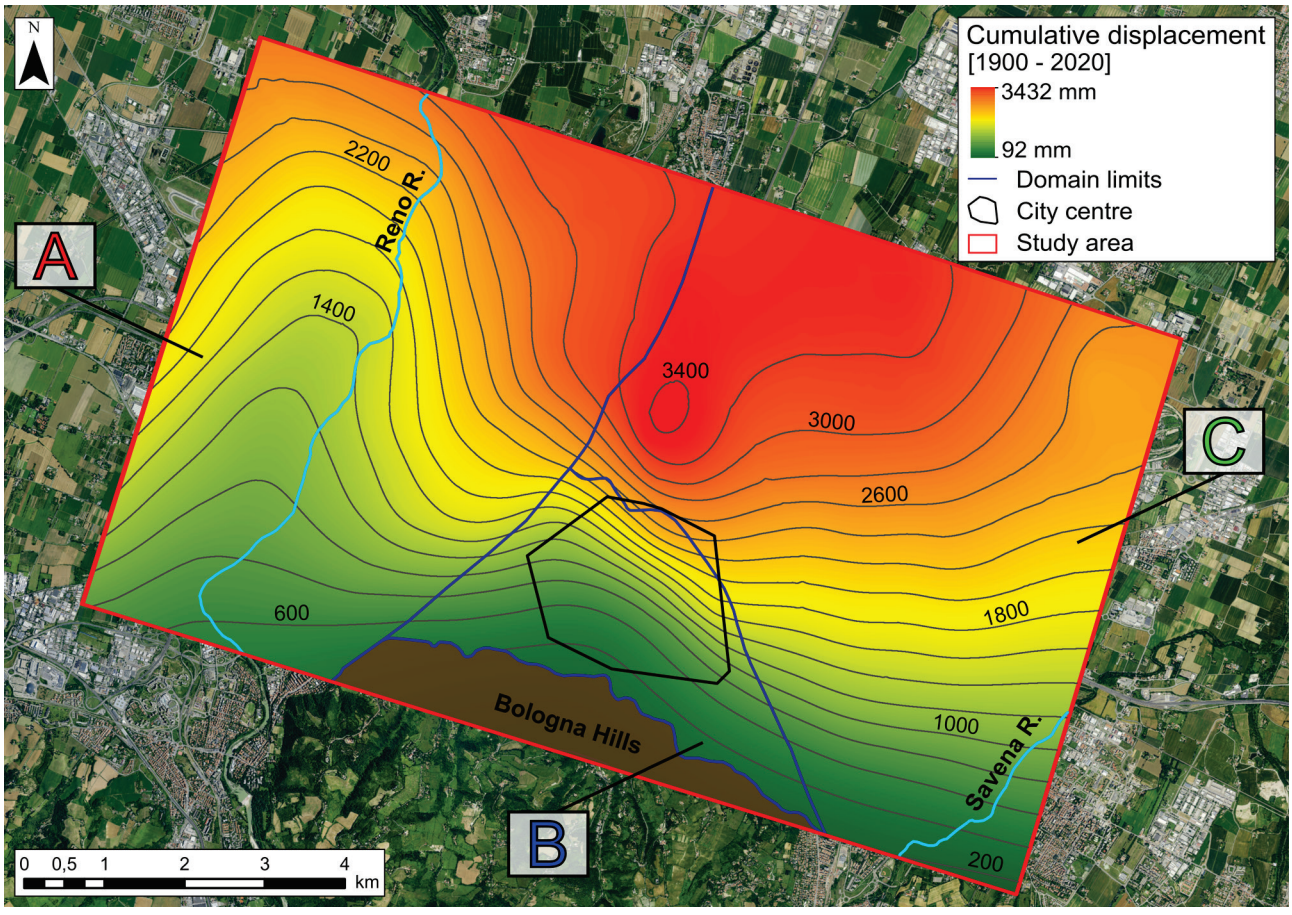

Fig. 3.9 Cumulative ground displacement map illustrating the long-term spatial distribution of the subsidence in the study area between 1900 and 2020.

Four maps illustrating the spatial distribution of subsidence rates during the different pumping stages are displayed in Figure 3.10. The map representing the first stage (Fig. 3.10a), which corresponds to the most intense pumping phase and the most pronounced groundwater level drawdown, exhibits the highest subsidence rates of the entire monitoring period. The map shows a steep increase in subsidence rates northwards, reaching approximately values of 100 mm/year north of the city centre, consistently with the ones highlighted by the curves in Fig. 3.8b. The overall trend observed in the different domains aligns with that depicted in the cumulative displacement raster (Fig. 3.9). Domain A, and especially Domain C, exhibit a gradual subsidence rate increase moving from proximal to more distal regions of the Reno River and the Savena alluvial fan, respectively. In contrast, Domain B displays an abrupt increment in the northern portion of the city centre. During the second phase (Fig. 3.10b), as pumping rates decrease and the groundwater level stabilises, the intensity of the subsidence process globally lessens in the study area, emphasising the described ground deformation distribution patterns between and within the domains. The third stage (Fig. 3.10c), depicts a more uniform subsidence rates distribution in the entire study area, with a significant reduction in ground sinking velocity values between 0 and 5 mm/year, concurrent with a marked rise in the groundwater level records. Only two areas, respectively in the northeastern sector of Domain A and in the northern portion of Domain C are characterised by slightly higher values. Lastly, the fourth phase (Fig. 3.10d) shows a clear divergence in the distribution of displacement rates, consistent with the observed recent trends in the reconstructed subsidence time series. The map highlights an upturn in the subsidence rates in the northern portion of Domain A, between the Reno River course and Domain C, with maximum values reaching approximately 15 mm/year. This upturn coincides with an increase in pumping rates and a groundwater level drawdown. On the other hand, Domain B and C are generally characterised by lower ground sinking velocity values, similar to the ones observed during the previous phase. These values, especially in Domain C, are consistent with the further drop in pumping rates and a steeper rise in the groundwater level measured at the *P4* station.

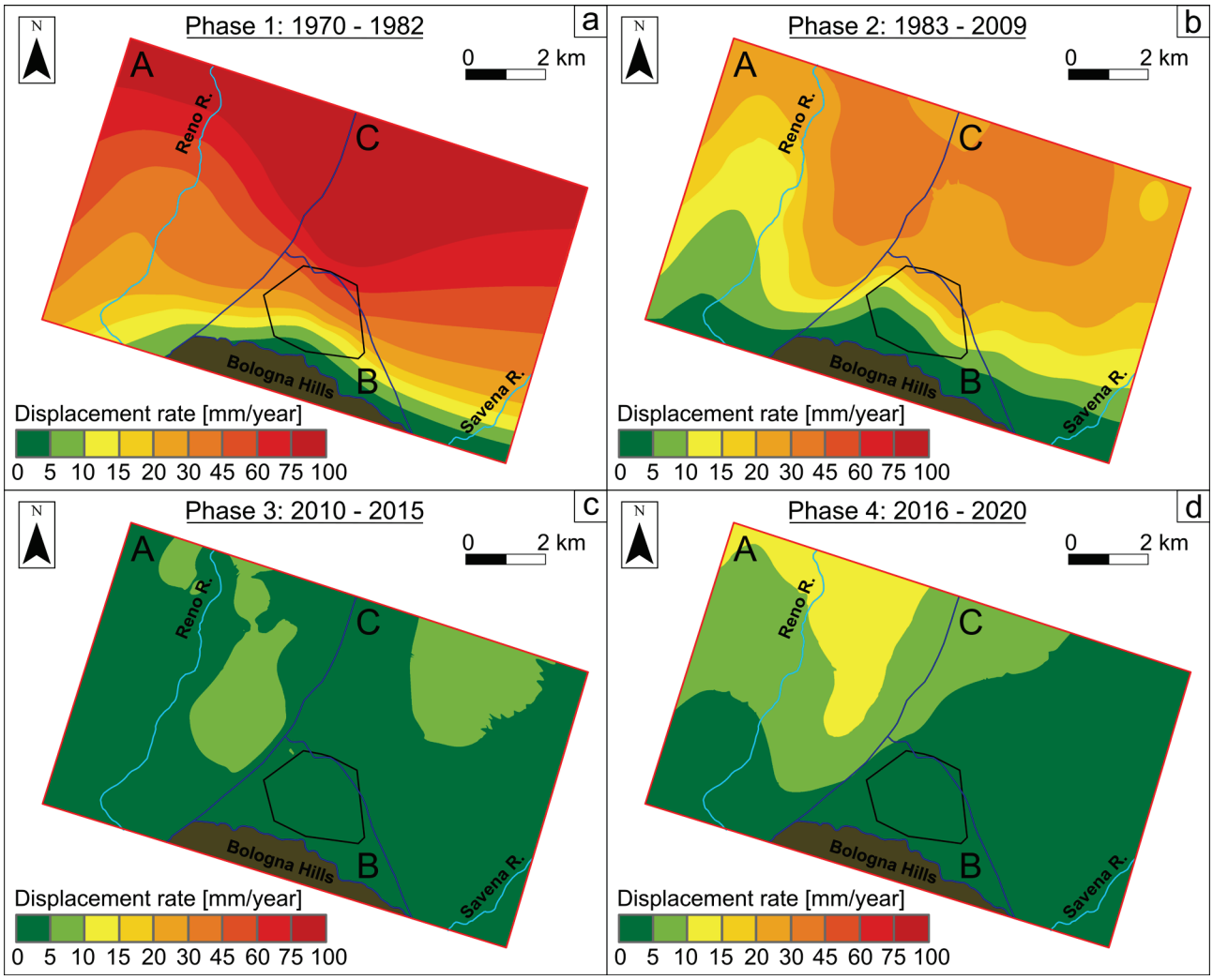

Fig. 3.10 Mean displacement rate distribution maps relative to the four subsidence evolution phases defined on the long-term groundwater level and pumping time series trends of the *P1-P3* water pumping stations.

3.6.1.3 Groundwater map

The available groundwater monitoring archives (Table 3.2) present considerable heterogeneity in terms of temporal and spatial resolution of the recorded data. As a result, a comprehensive temporal and spatial reconstruction of groundwater levels in the study area was not feasible.

The map reported in Fig. 3.11 displays the average groundwater level depth computed between 1995 - 2005, which represents a relatively stable period in both groundwater level and pumping rates records of the major water pumping stations. This period is a subset of the previously described pumping *Stage 2* (Fig. 3.7a-c). As expected, the highest groundwater depths are generally observed near the four pumping stations (*P1-P4*) and in other regions distinguished by the presence of deep wells, such as the southern portion of Domain A, in the proximal portion of the Reno River deposits, and towards Domain B boundary. The groundwater level is deep also in the northern sector of Domain C, in the distal portion of the Savena alluvial fan. The groundwater depth measured at pumping stations along the Reno River is 49.5, 55 and 56 m below the ground level (b.g.l.) for the *P1*, *P2* and *P3* stations, respectively. In Domain C, the groundwater level at the *P4* pumping is equal to 53 m b.g.l. The observed groundwater level distribution is consistent with the subdivision of the study area into three domains, highlighting significantly higher levels in Domain B and sharp transitions towards the other two. The boundary between Domains A and B, in particular, is marked by a steep gradient, with groundwater

depths rapidly increasing from values between 0 and 15 m in the city centre to depths greater than 60 m in the eastern portion of Domain A within a few hundreds of metres distance. Interestingly, the qualitative comparison between the groundwater level depth distribution (Fig. 3.11) and the described cumulative displacement and subsidence velocity distribution maps (Fig. 3.9-3.10) reveals that the maximum pumping rates do not always match the recorded subsidence peaks. In fact, pumping occurs in deep wells on coarse-grained gravelly deposits, whereas maximum subsidence values are generally found in areas with a higher occurrence of fine-grained bodies. In Domain A, for instance, while the highest pumping occurs in the southern portion and along the course of the Reno River, the greater ground deformations take place in the northeastern sector. Similarly, in the apical portion of the Savena alluvial fan, pumping rates are relatively high while displacements are low, but in distal portions located in the northern region of Domain C (Fig. 3.10b), the pumping rates are associated with higher deformations. Conversely, in Domain B high groundwater levels and low settlement values are observed. Despite its proximity to the water pumping station and the presence of a thick sequence of clay deposits, significant subsidence would have been expected, but this is not observed. These observations highlight the complex relationship among geological setting, pumping activities, and subsidence process, which will be addressed and further explored in a future numerical modelling analysis.

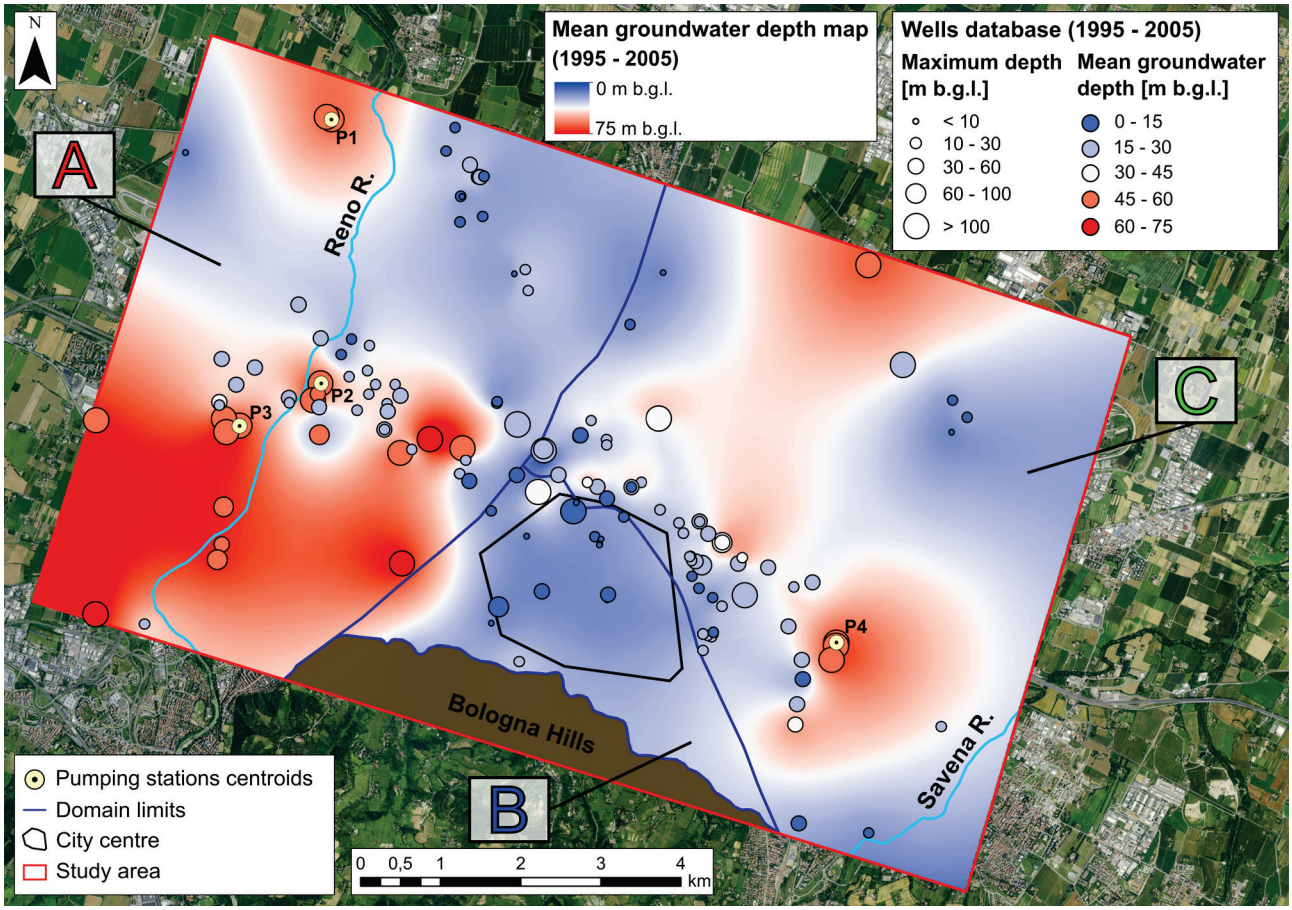

Fig. 3.11 Mean groundwater depth distribution map for the 1995-2005 time interval. The location of the wells is displayed by a series of circles whose size and colour depend on their maximum depth and the computed average groundwater level, respectively. Note that differences in the well depths can introduce a certain inhomogeneity in the data. However, appropriate categorisation of the wells was implemented to account for eventual measurements of a shallower perched water table in the shorter ones (see sub-section 3.5.3). The location of the four water pumping stations is marked by light yellow circles.

3.6.2 Recent subsidence evolution

3.6.2.1 Time series (2008 – 2020)

The short-term subsidence time series covering the 2008 – 2020 time interval were derived from the last three available InSAR surveys. The first two regard the 2006 – 2011 Radarsat-1 and the 2011 – 2016 Radarsat-2 and Cosmo-SkyMed data, which were processed by regional authorities (ARPAE) in collaboration with TRE Altamira and the Department of Civil, Chemical, Environmental, and Materials Engineering (DICAM) of the University of Bologna (UniBo). The most recent survey was specifically conducted for this study and processed by the UniBo *spin-off* "*Fragile*" from the free 2015-2020 Sentinel-1 data. These surveys, all in ascending geometries, have progressively higher PS density within the study area, as reported in Table 3.1, resulting in an increasing spatial resolution.

Four key control points were selected to summarise the recent trend of ground subsidence in the study area. Figure 3.12 shows the subsidence time series for control point *C01*, located in Domain A (Fig. 3.6), along with their comparison with the groundwater level and pumping data. Similar plots for the other three control points (*C12*, *C19*, and *C35)* are shown in Supplementary Materials. The plot in Figure 3.12a displays the monthly average of cumulative ground displacement data obtained from the PS time series within the *C01* interrogation circle, along with their corresponding standard deviation values. As can be seen, the number of original PS monitoring curves (shown in light grey) increases with time, reflecting the progressively higher spatial resolution of the satellite acquisitions. Additionally, a significant reduction in the noise of the extracted PS time series can be observed, resulting in lower standard deviation values around the average curve.

Consistently with the last part of the corresponding long-term curve described in the previous section (Fig. 3.8a), the overall cumulative ground displacement exhibits a steep initial portion followed by a gentler slope after 2010, and a subsequent increase after 2017, resulting in a total sinking value of 45 mm over the considered period. Similarly, the long-term displacement rate curve, represented by the dashed line in Fig. 3.12b, shows an initial drop in subsidence velocity, declining from around 15-20 mm/year to 0-5 mm/year by 2010. The displacement rates remained quite low in the following years, with a gradual increase reaching values higher than 5 mm/year since 2017. The observed trends are consistent with the overall evolution of the groundwater level and pumping time series from the main water pumping stations on the Reno River deposits, represented by the *P3* curves in Fig. 3.12c. Specifically, the curves highlight a sudden increase in the groundwater level after 2010, followed by a gradual rise and then a drop in 2017, induced by an increase of groundwater pumping in the last years.

The short-term trends in both the cumulative displacement (Fig. 3.12a) and subsidence rate (Fig. 3.12b) curves are consistent with the pumping and consequent fluctuations in the groundwater level (Fig. 3.12c). These seasonal trends are characterised by peaks in pumping during the summer, resulting in a decrease in groundwater levels and a corresponding upsurge in subsidence, and vice versa during the winter.

Similar remarks result for the time series generated at the other control points, indicating the consistency of the overall trend between the detailed and long-term subsidence time series, as well as the good correlation between the fluctuations of the pumping and subsidence curves. This is further highlighted in the ensemble charts presented in Fig. 3.13 and individually, in Fig. 3.20-3.22 provided in the Supplementary Materials for *C12*, *C19* and *C35* curves.

The displacement curves demonstrate generally consistent trends within each domain. From 2010 onwards, the time series in the study area exhibit similar patterns, with comparable displacement rate values typically ranging between 0 and 5 mm/year. These trends are accompanied by consistent short-term fluctuations. Notably, a significant divergence becomes apparent around 2016: Domain A and the distal part of Domain C indicate an increase in subsidence rate, while the city centre (Domain B) and the apical portion of the Savena alluvial fan (proximal part of Domain C) display a relatively constant trend with lower values and less pronounced short-term fluctuations. This behaviour aligns with the recent water extraction policy, characterised by increased pumping in stations *P1-P3* and a substantial recovery in *P4*.

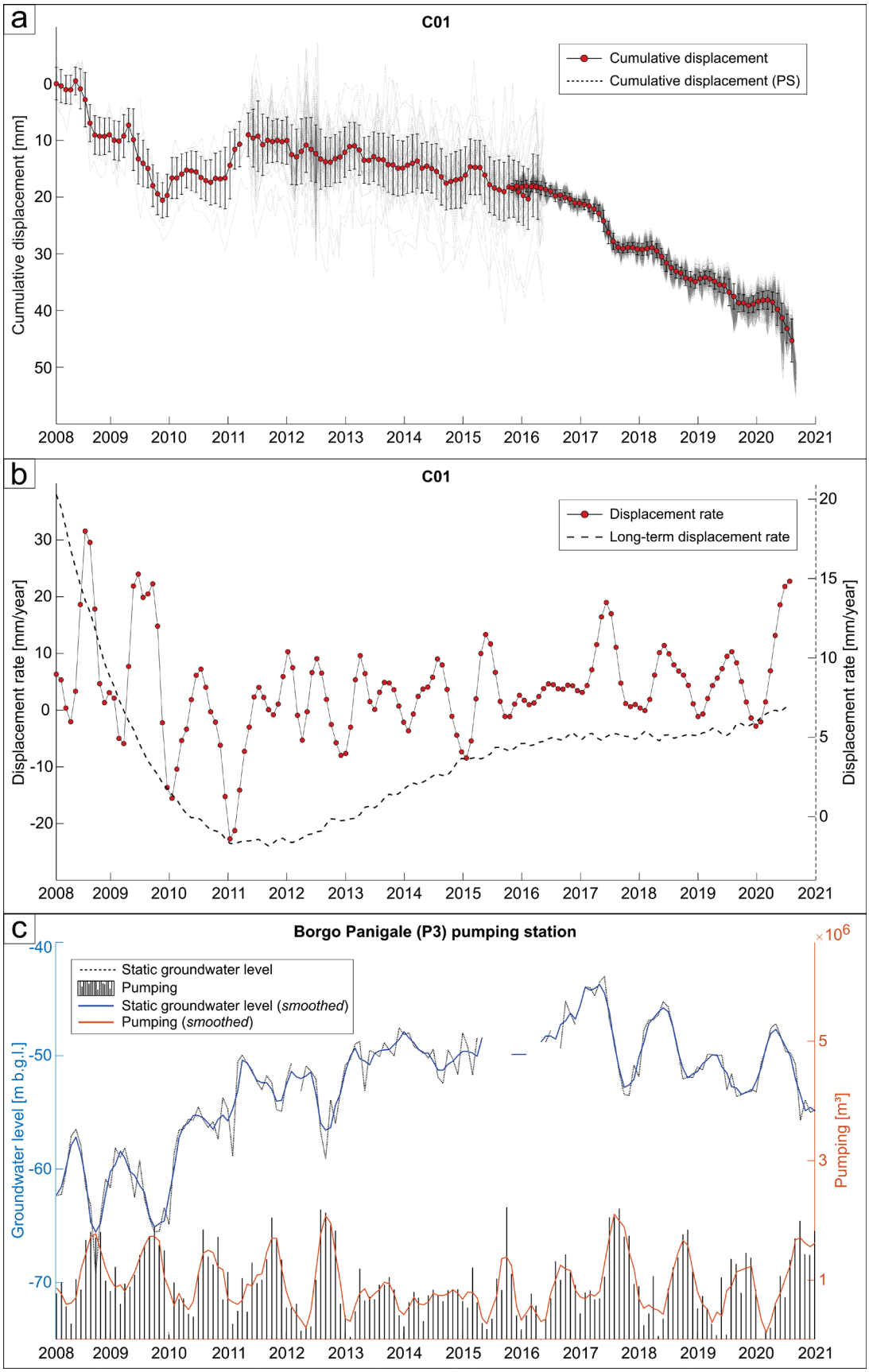

Fig. 3.12 Detailed short-term cumulative displacement (a) and displacement rate (b) time series, illustrating the recent subsidence process evolution in the *C01* control point in Domain A. The long-term displacement rate trend is also displayed as a dashed line (b). The detailed pumping and groundwater level time series from the closest major pumping station (*P3*) are included for comparison (c).

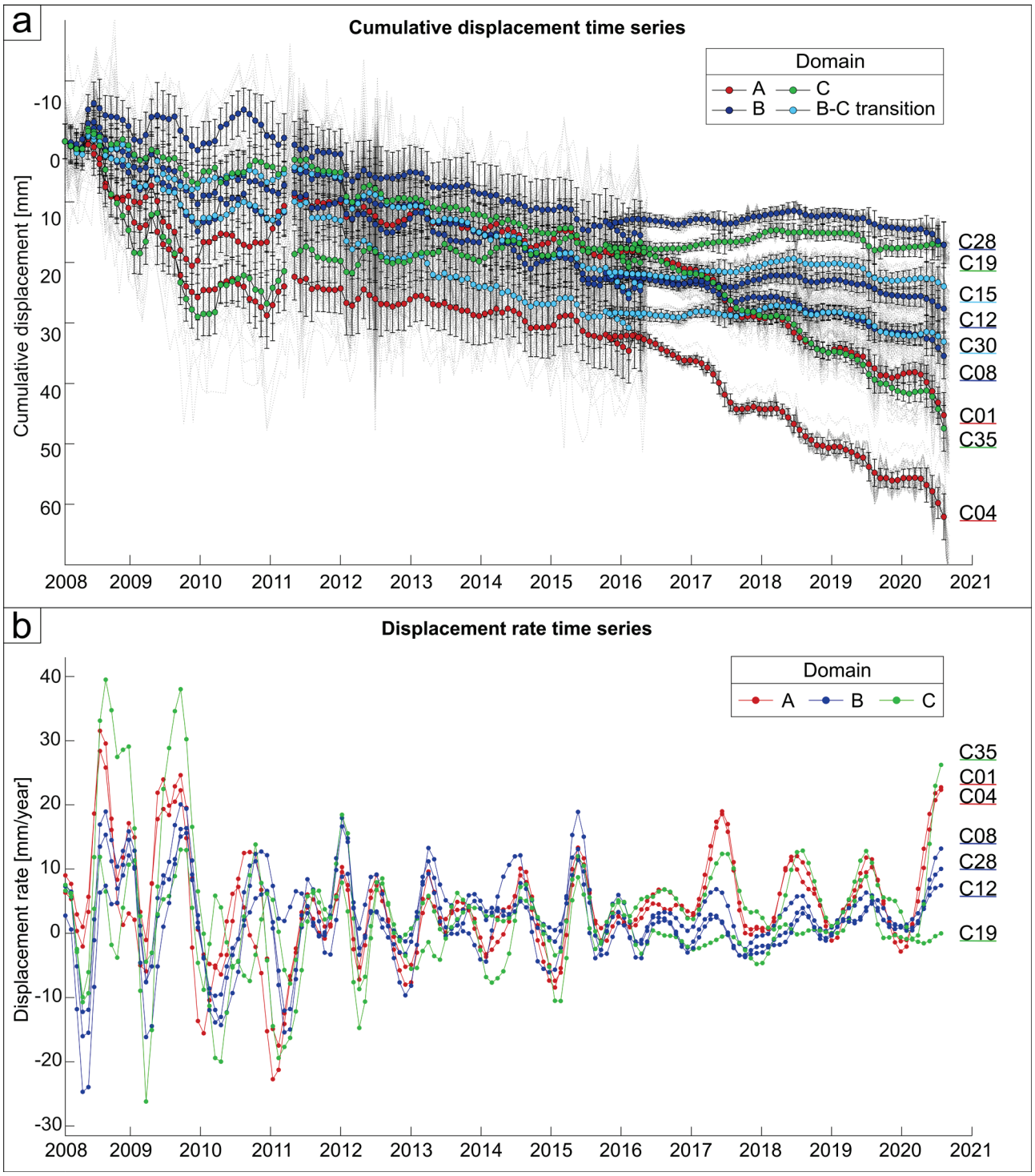

Fig. 3.13 Detailed short-term cumulative displacement (a) and displacement rate (b) time series comparison.

3.6.2.2 Comparison with EGMS data

The most recent satellite monitoring data reveals a notable subsidence increase in a significant portion of the study area, particularly in the distal portion of the Reno River deposits and laterally towards Domain C (Fig. 3.10d). This upsurge is also evident in the data provided by the *European Ground Motion Service* (*EGMS,* Costantini et al. 2021; Crosetto et al. 2021). These data, being freely available and consistently updated, could serve as a valuable tool for monitoring the future evolution of ground deformation. The availability of a detailed site-specific InSAR survey enables the evaluation of the *EGMS* data accuracy, which is generated on a broader scale and without a specific purpose like the University of Bologna survey.
Figure 3.14 compares the displacement time series obtained from the 2015 – 2020 Sentinel-1 InSAR data processed by the University of Bologna spin-off, "*Fragile*", and the corresponding *EGMS* ones, evaluated at the same points. The calibrated ascending geometry dataset "*Level 2b*" (Costantini et al. 2021; Crosetto et al. 2021) relative to the satellite orbit n° 117 was selected among the available *EGMS* datasets to match the characteristics of the UniBo survey and enable a meaningful comparison. The displayed *EGMS* curves were obtained by considering the same control points (C_p) and interrogation circles used for the UniBo time series (see sub-section 3.5.2.1) and extracting the corresponding average displacement trends from the enclosed PS data.

The comparison of the two sets of curves reveals a systematic divergence, with the *EGMS* time series consistently overestimating the cumulative ground displacements shown by the UniBo ones, with maximum differences of approximately 10-12 mm over the observation period. Despite the different subsidence values, the two sets of curves exhibit similar evolution trends in the control points located in Domain A and in the distal portions of Domain C, which are represented by the *C01* and *C35* time series, respectively. In these points, both UniBo and *EGMS* curves reveal steeper slopes after 2017, indicating higher displacement rates, consistent with the recent pumping increase described in the previous section (Fig. 3.12c). On the other hand, after an initial good correlation, since 2017 the two sets of time series exhibit a remarkable divergence in Domain B and the more proximal portions of Domain C, represented by *C12* and *C19*. Specifically, as described in the previous section, the UniBo curves indicate a substantial reduction in subsidence values in these portions of the study area that is consistent with the recent groundwater extractions decrease from the *P4* station in Domain C. Conversely, the *EGMS* curves do not seem to detect any lessening in the ground deformation process and exhibit a contrasting trend, with higher slopes after 2017 that would rather indicate a subsidence upsurge.

These discrepancies likely stem from the utilisation of different reference areas in the two satellite products. In fact, when the EGMS time series are recalculated using the same reference area employed for the UniBo survey (indicated in Fig. 3.6), a significantly improved agreement is observed. Figure 3.14 demonstrates that the corrected time series align well with those obtained through the UniBo analysis, exhibiting maximum differences of approximately 3-4 mm. Moreover, they exhibit a similar temporal trend that concurs with the groundwater records.

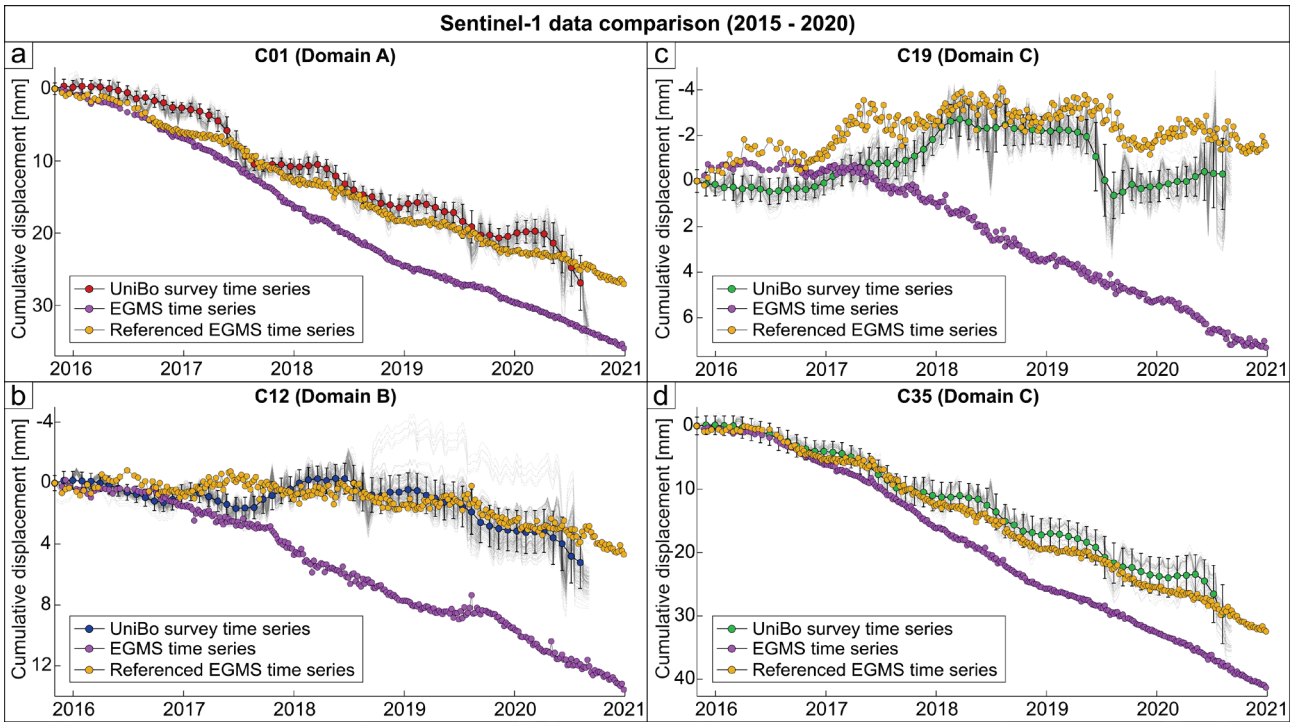

Fig. 3.14 Comparison of UniBo and *EGMS* Sentinel-1 displacement time series corresponding to four key points of the study area over the 2015-2020 period. The yellow curves represent the *EGMS* time series recalculated considering the same stable reference areas as the UniBo curves.

3.7 Discussion

3.7.1 Comparison between subsidence pattern and 3D geology

The analyses reveal a consistent correlation between the reconstructed long-term ground deformation field and the 3D geological model of the study area. As previously mentioned, the geological model is the result of a completely independent stratigraphic analysis, where the existing deposits were categorised in terms of *lithofacies*. This classification guided the correlations in both two and three dimensions, leading to the reconstruction of the depositional architecture of the study area subsurface, as described in Giacomelli et al. (in review). The comparison with the long-term subsidence deformation field is presented in Fig. 3.15, where the essential elements of the geological model have been highlighted and summarised. As can be seen, the southern parts of Domains A and C exhibit relatively low cumulative subsidence. In Domain A, this can be attributed to the presence of densely stacked coarse-grained bodies that were deposited in the proximal section of the Reno River. These coarse-grained bodies are represented by the amalgamated gravel deposits shown in the figure. Moving downstream, the subsidence values gradually increase, with a steeper gradient observed in the distal and lateral regions of the Reno River alluvial deposits. These areas are characterized by a higher proportion of fine-grained deposits, which are more compressible in nature. Similar remarks apply for Domain C, where the greater dispersion of the coarse-grained gravel deposits within the Savena River alluvial fan results in a more gradual and homogeneous increase in recorded sinking towards more distal areas. Domain B, which encompasses the location of the historical city, also exhibits relatively low cumulative subsidence. This domain is distinguished by the presence of thick and rather continuous sequences (about 100 m) of overconsolidated clayey deposits, defined by the occurrence of several orders of paleosols (see section 3.4). Further analyses based on Cone Penetration Test (CPT) data classify these deposits as "*Stiff*" to "*Very Stiff*" as reported in Giacomelli et al. (in review). In the geological model, the boundary between Domain B and the other two was defined as sharp. Differently, subsidence data suggest that this limit, particularly towards

Domain C, may be more gradual. The ground deformation field reveals, in fact, the existence of a transition zone that crosses the northern portion of the city centre, with a buffer region approximately 400 to 700 m wide (Fig. 3.15). This area exhibits an intermediate behaviour between the low subsidence experienced in the southern sector of Domain B, closer to the Apennine front, and the large deformations documented at the north of the city centre in Domain C (Fig.3.8). This behaviour may be ascribed to an heteropic transition with the more recent and compressible deposits found in the distal and lateral portions of the Savena alluvial fan. The northwestern sector of Domain C, extending towards Domain A, exhibits the most significant ground displacements, reaching maximum values of about 3.4 m between 1900 to 2020, recorded approximately 1.5 km north of the city centre. This region, in fact, aligns with the occurrence of fine-grained prevailing distal deposits of the Savena alluvial fan, characterised by higher compressibility.

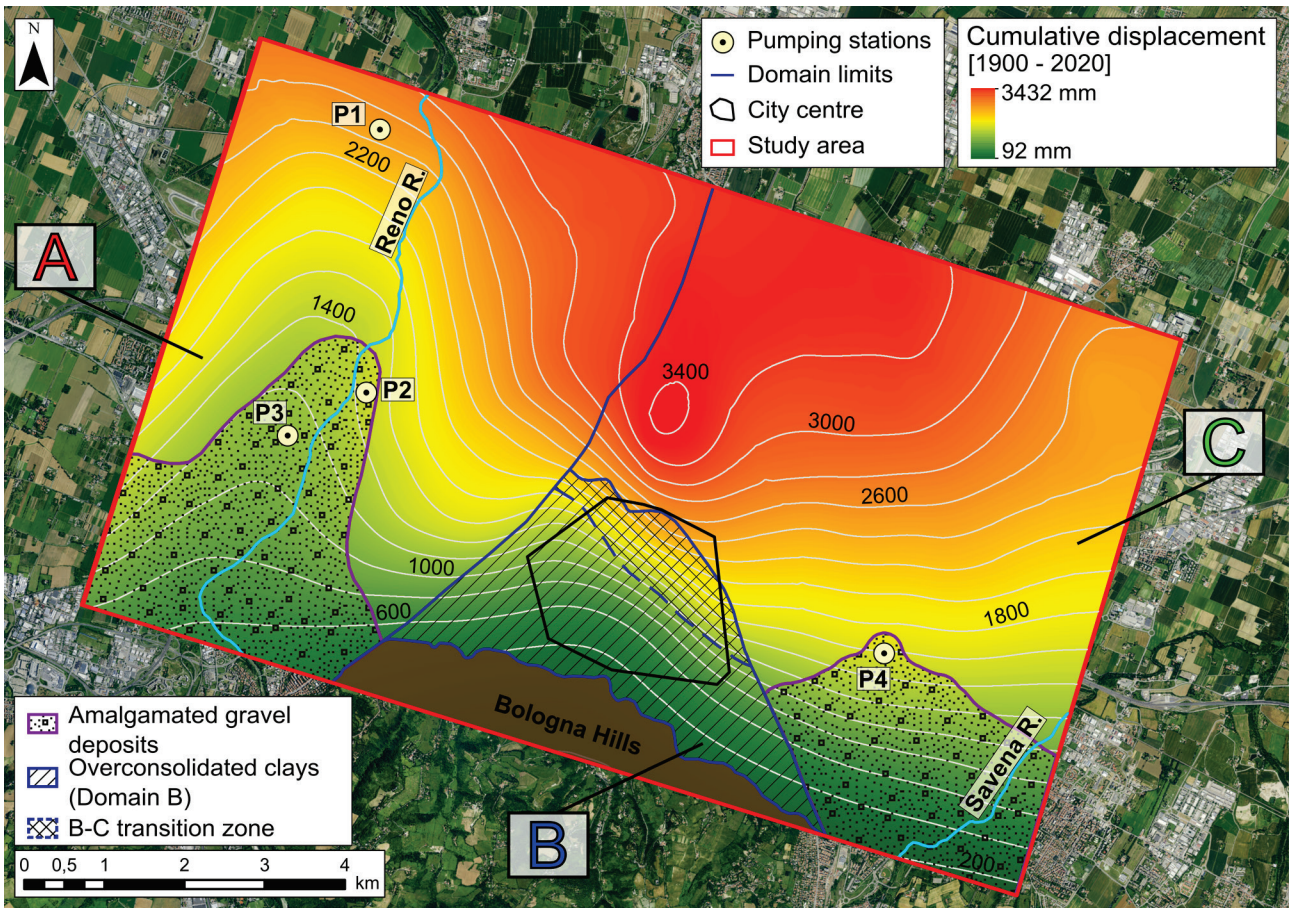

Fig. 3.15 Comparison between the long-term subsidence distribution (1900 – 2020) with the primary elements of the 3D geological model. The purple lines represent the envelope of the amalgamated gravel deposits found in the proximal portions of the Reno River and the Savena alluvial fan in Domains A and C, respectively. Within Domain B, characterised by thick sequences of stiff overconsolidated clays, a transition zone towards Domain C exhibiting intermediate behaviour is highlighted by a dashed line and crosshatch pattern, based on the analysis of subsidence data.

3.7.2 Impact of subsidence on structures

The generated cumulative sinking and displacement rate maps clearly highlight regions within the study area distinguished by steep subsidence gradients. These regions are typically more hazardous compared to others with overall higher deformations but milder gradients. Figure 3.16a displays the subsidence gradient computed from the long-term cumulative displacement raster (1900 – 2020), serving as a subsidence hazard map. The subsidence gradient values have been classified and compared to the theoretical angular distortion limits for

generic framed buildings and structures. In particular, the critical value of 0.002 has been identified as the maximum tolerable angular distortion threshold (Skempton & MacDonald 1956; Bjerrum 1963; Tomlinson 2001) typically recommended to prevent damage to urban infrastructure (Torres et al. 2020).

As previously mentioned, the steepest gradients are observed in the northern portion of the city centre, as displayed in detail in Fig.3.16b. Bologna's city centre is densely populated and home to numerous buildings of relevant historical and cultural significance. Although the calculated gradient never exceeds the identified critical threshold, damages have been reported on several buildings within the high-gradient zone of the city centre since the late 1970s (Modoni et al. 2013). One notable example is St. James Church, highlighted by the purple circle in Fig.3.16b, which has experienced relevant structural damages that have been monitored and studied over the years (Alessi 1985, Pieri & Russo 1985, Modoni et al. 2013). The analysis revealed that the damages sustained by the church were the result of a pronounced differential settlement process that aligns with the documented steep subsidence gradient.

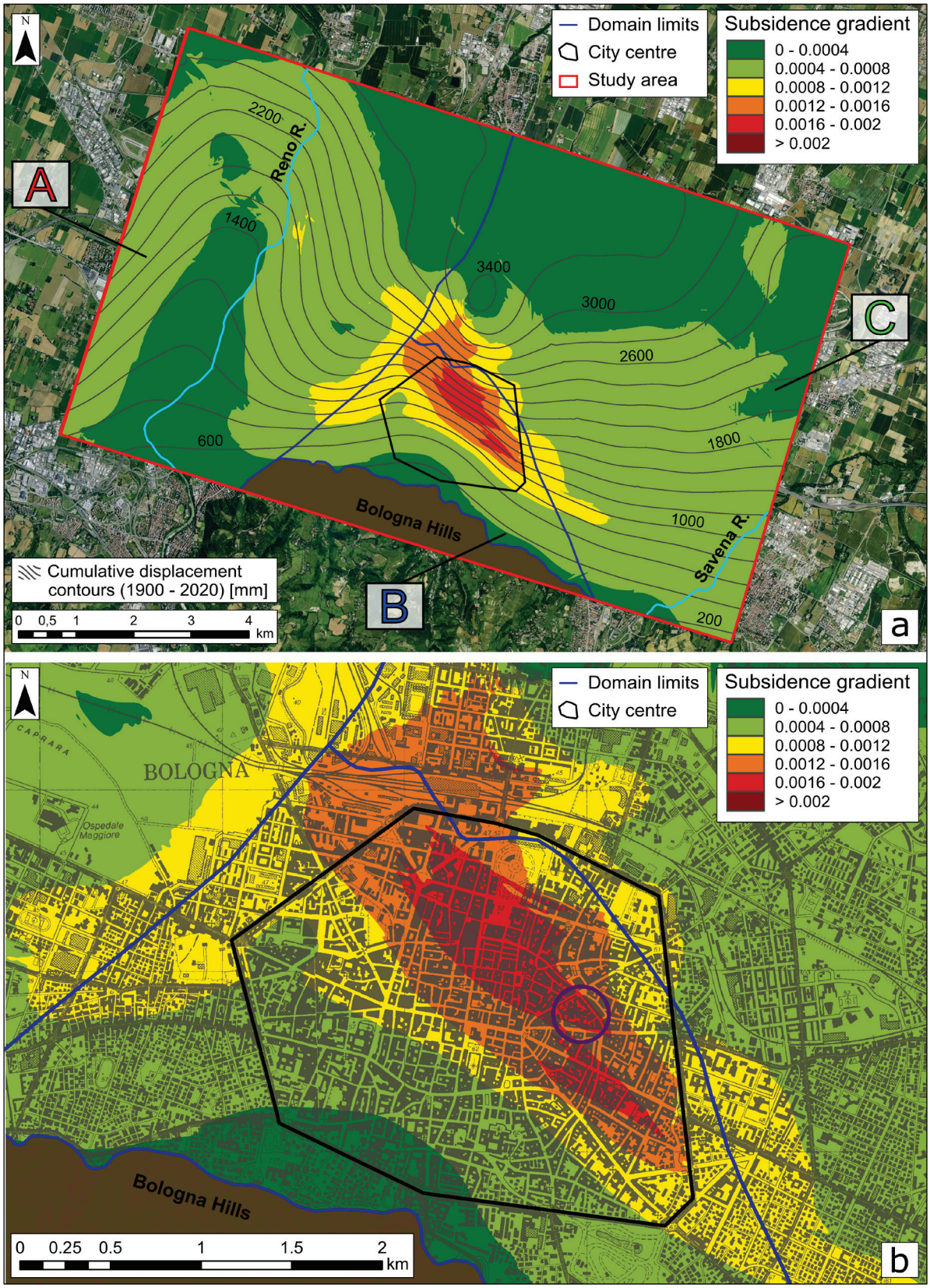

Fig. 3.16 (a) Subsidence gradient derived from the 1900 - 2020 cumulative displacement raster, serving as a hazard map. The subsidence gradient is classified with respect to theoretical angular distortion thresholds for generic framed buildings and structures. (b) Detailed view of the subsidence gradient within the historical city centre. The purple circle highlights St. James Church, which has experienced structural damages since the late 1970s due to differential settlement resulting from the ongoing subsidence process (Alessi, 1985, Pieri & Russo, 1985, Modoni et al., 2013).

3.8 Conclusions

In this study, we integrate topographic levelling and satellite interferometry monitoring data to reconstruct the long-term spatiotemporal evolution and achieve a comprehensive understanding of the subsidence process that has impacted the city of Bologna since the 1960s.

Based on the research findings, the following conclusions can be drawn.

1) The methodology employed successfully integrates ground-based and remotely sensed ground displacement data, enabling the generation of cumulative sinking time series and maps that depict the long-term temporal evolution and overall spatial distribution of the subsidence process, respectively.

2) The generated continuous cumulative displacement and subsidence rate curves exhibit a clear correlation with the pluriannual trends of groundwater level and pumping from the main pumping stations within the study area. The qualitative comparison reveals four distinct stages in the evolution of the pumping and subsidence processes, including a peak phase (1970 – 1982), a subsequent lessening (1983 – 2009), a stabilisation (2010 – 2016) and an upsurge (2017 – 2020) observed across a significant portion of the study area.

3) The produced cumulative sinking map spanning 1900 – 2020, aligns with the main features of the 3D geological model of the study area and its subdivision into three distinct depositional domains. This agreement underscores the significant influence of the peculiar geological setting of each domain on the long-term subsidence distribution. In particular, the proximal portion of Domains A and C, characterised by the amalgamated gravel deposits of the Reno River and the Savena alluvial fan, exhibit relatively low displacements that gradually increase downstream towards distal areas. Conversely, the occurrence of stiff overconsolidated clays in the subsurface of Domain B results in low subsidence values that abruptly increase towards the boundaries with the adjacent domains.

4) The detailed displacement and displacement rate time series generated for the period 2008-2020, reveal a rapid and consistent response of the subsidence process to pumping and groundwater level changes, including seasonal short-term trends, recorded at the main pumping stations.

5) The detailed cumulative displacement time series and subsidence rate maps show a subsidence upsurge in recent years consistently with the EGMS data, which frame the urban area of Bologna as one of the foremost ground deformation signals across Europe.

6) The reconstruction of the long-term subsidence deformation field allowed the development of a subsidence hazard map for the study area, where the calculated subsidence gradient is compared with the theoretical angular distortion limits for generic framed buildings and structures. The resulting map reveals a pronounced gradient zone traversing the city centre, which aligns with the area within the city centre where the historic buildings have been affected the most.

The present work provides a foundation for developing a numerical analysis of land subsidence in the city of Bologna, with the final aim of predicting future subsidence trends on the basis of anticipated groundwater pumping changes. Currently, a preliminary phase of a 3D coupled numerical modelling analysis of the ongoing subsidence is underway.

Acknowledgements

This study was supported by the research grant URGENT - Urban Geology and Geohazards: Engineering geology for safer, resilieNt and smart ciTies funded by the Italian Government (Progetti di Ricerca di Rilevante Interesse Nazionale, PRIN2017, Prot. 2017HPJLPW).

3.9 Supplementary Material

3.9.1 Long-term cumulative ground displacement time series (1970 – 2020)

This section presents the continuous cumulative ground displacement time series developed through the methodology described in section 3.5.2.1 for all the considered control points (Fig. 3.6), categorised by geological domain.

Domain A

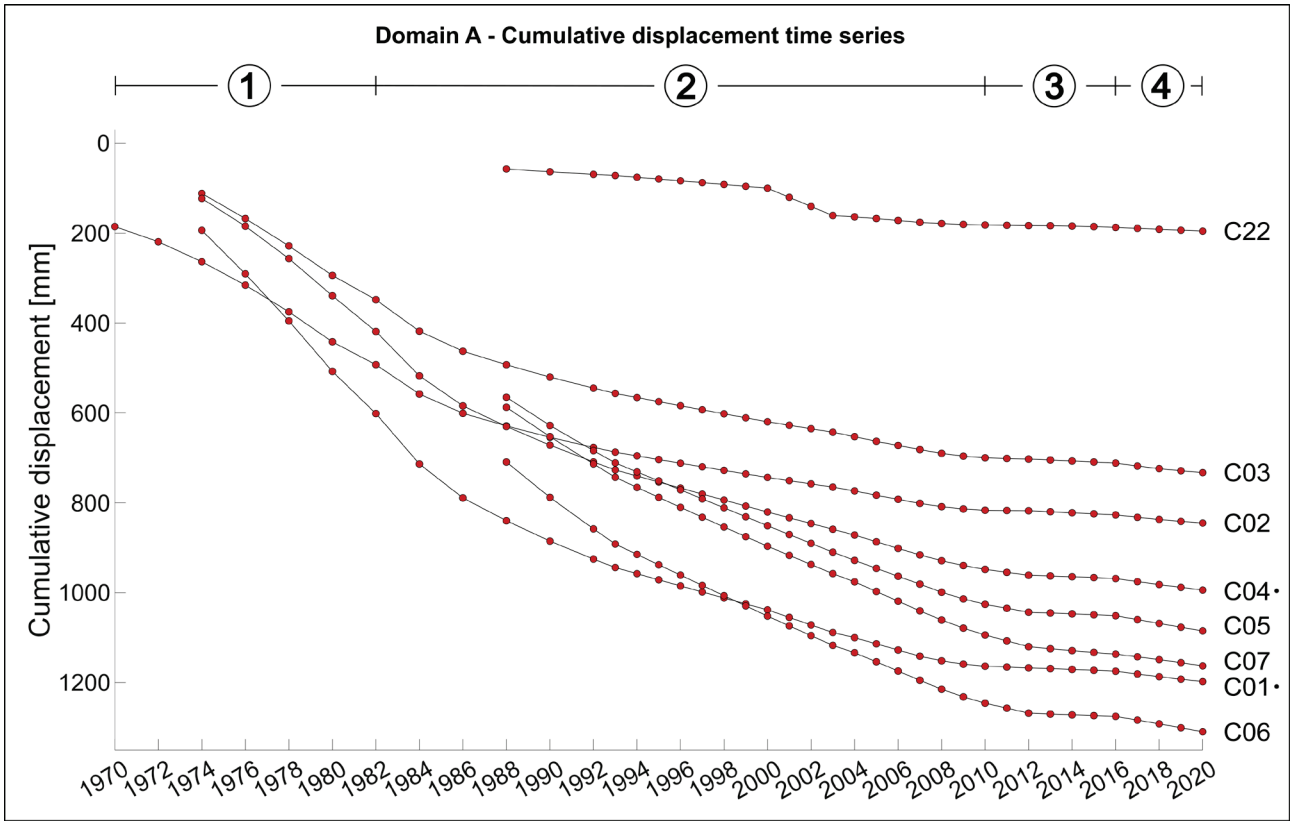

Fig. 3.17 Comparison of long-term cumulative ground displacement time series in Domain A. The reconstructed time series are also compared with the four evolution phases identified in the long-term trends of the *P1-P3* water pumping stations monitoring records. The black dots highlight the time series displayed and described in sub-section 3.6.1.1.

Domain B

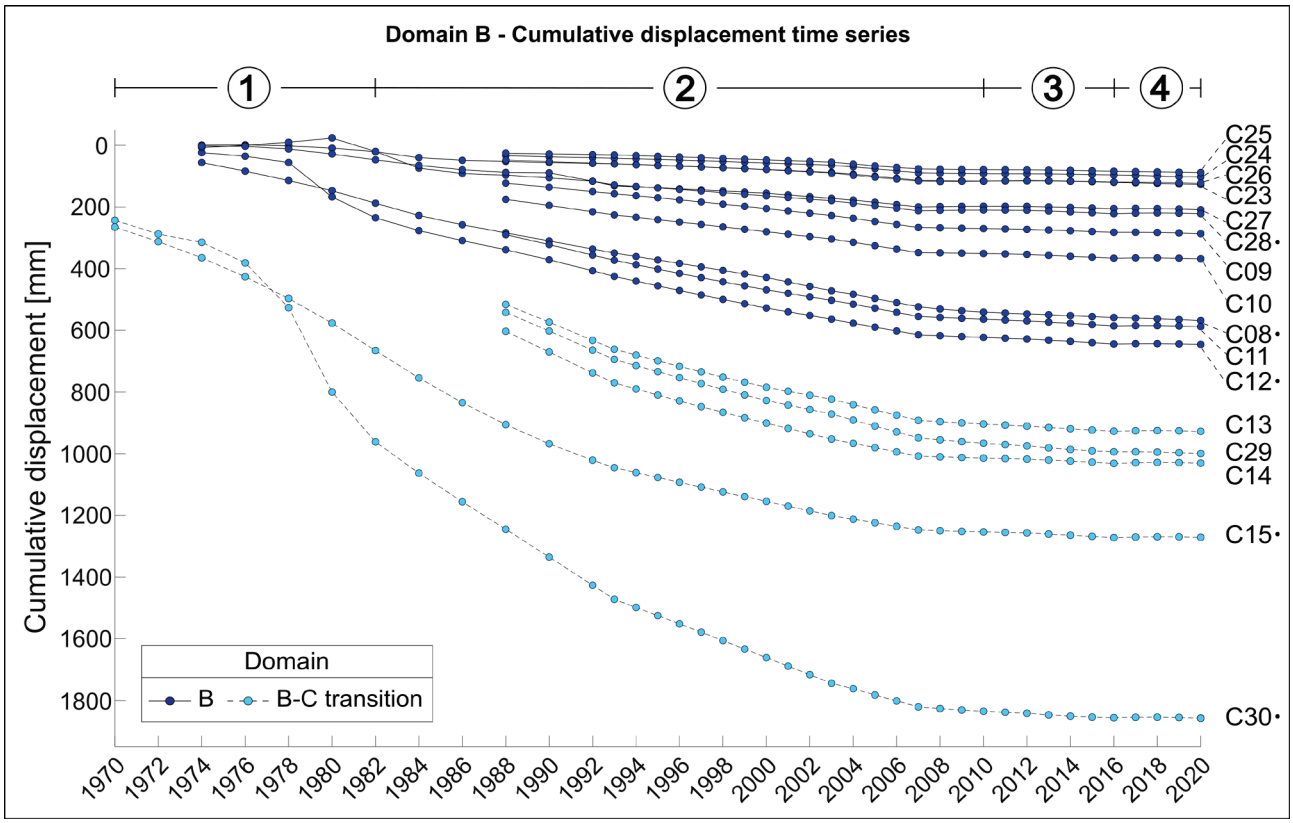

Fig. 3.18 Comparison of long-term cumulative ground displacement time series in Domain B. The curves representing the transition zone at the boundary between Domains B and C are displayed in light blue with a dashed line. The reconstructed time series are also compared with the four evolution phases identified in the long-term trends of the *P1-P3* water pumping stations monitoring records. The black dots highlight the time series displayed and described in sub-section 3.6.1.1.

Domain C

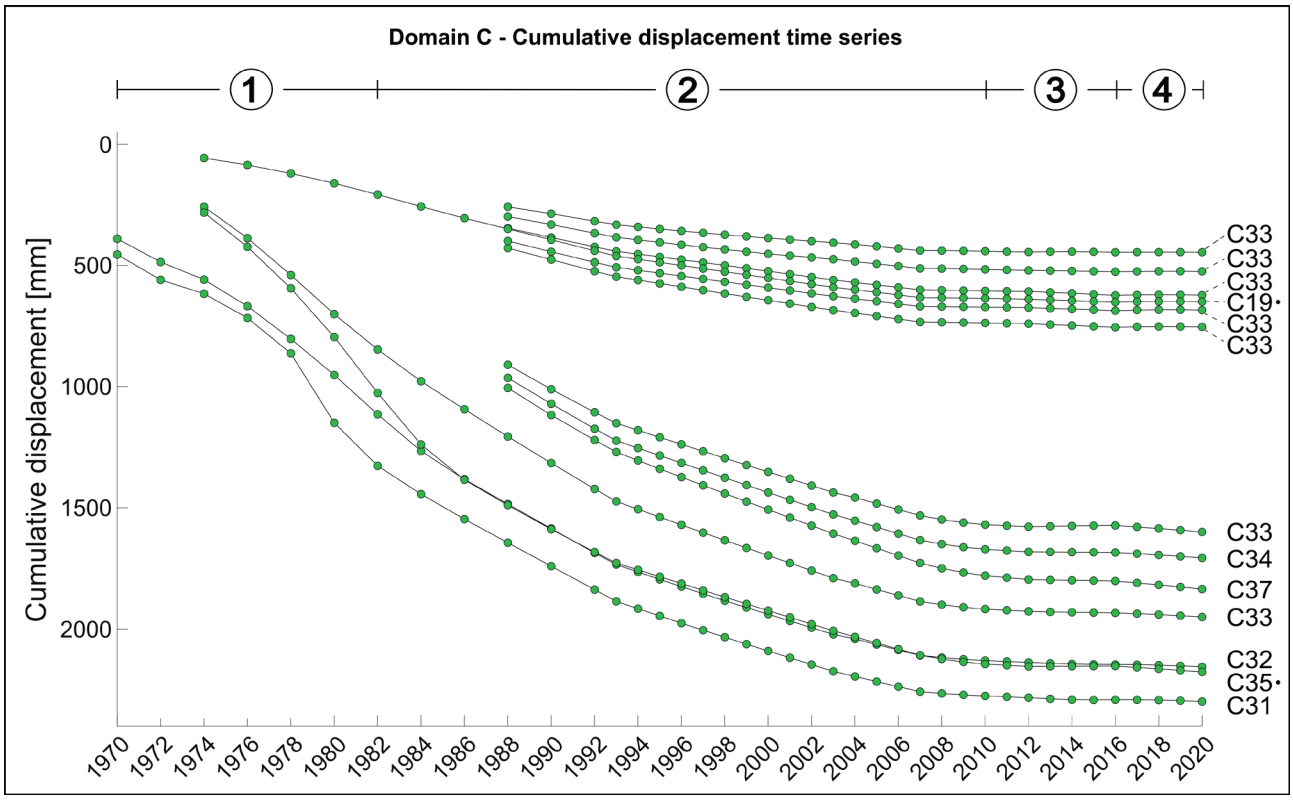

Fig. 3.19 Comparison of long-term cumulative ground displacement time series in Domain C. The reconstructed time series are also compared with the four evolution phases identified in the long-term trends of the *P1-P3* water pumping stations monitoring records. The black dots highlight the time series displayed and described in sub-section 3.6.1.1.

3.9.2 Recent subsidence and groundwater withdrawals time series comparison (2008 – 2020)

This section provides in full the detailed cumulative displacement and displacement rate time series generated for the time interval 2008 – 2020 at three key control points in the study area (one in Domain B and two in Domain C), which were briefly mentioned in section 3.6.2.1. These subsidence time series, generated through the processing chain described in section 3.5.1.1, are qualitatively compared with the recent groundwater level and pumping evolution, extracted as described in section 3.5.3.

C12 – Domain B

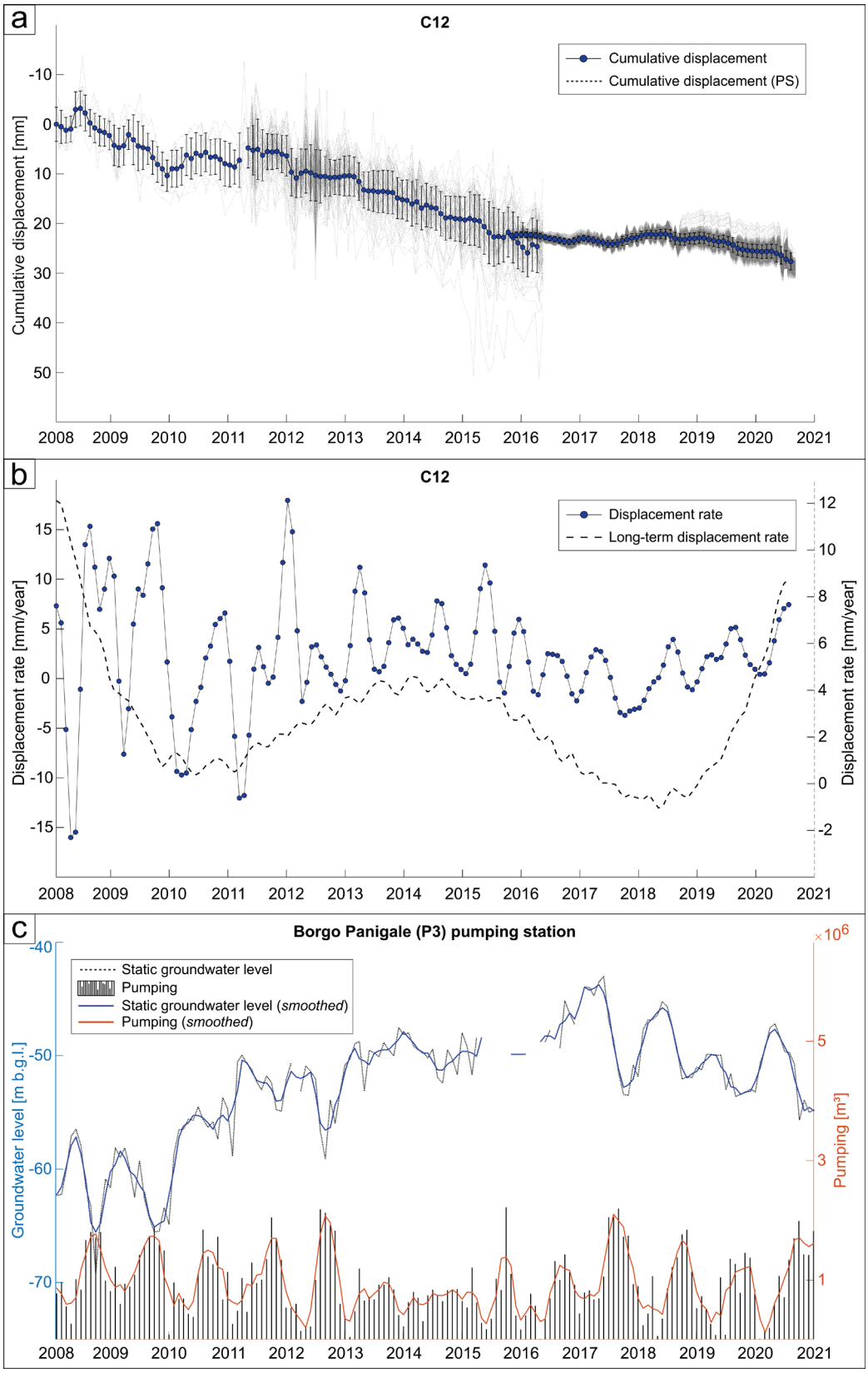

Fig. 3.20 Detailed short-term cumulative displacement (a) and displacement rate (b) time series, illustrating the recent subsidence process evolution in the *C12* control point of Domain B. The long-term displacement rate trend is also displayed as a dashed line (b). The detailed pumping and groundwater level time series from the closest major pumping station (*P3*) are included for comparison (c).

C19 – Domain C

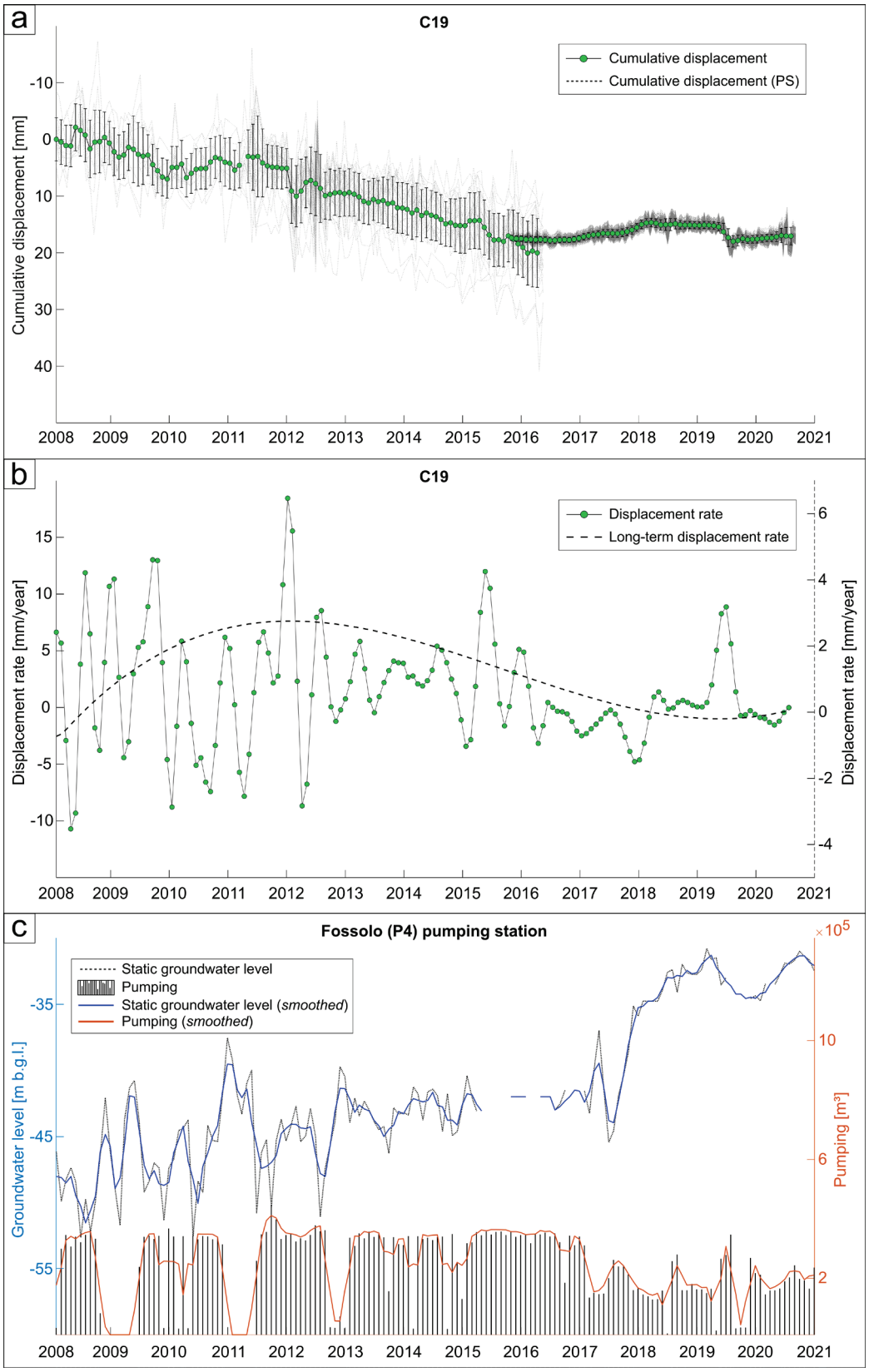

Fig. 3.21 Detailed short-term cumulative displacement (a) and displacement rate (b) time series, illustrating the recent subsidence process evolution in the *C19* control point of Domain C. The long-term displacement rate trend is also displayed as a dashed line (b). The detailed pumping and groundwater level time series from the closest major pumping station (*P4*) are included for comparison (c).

C35 – Domain C

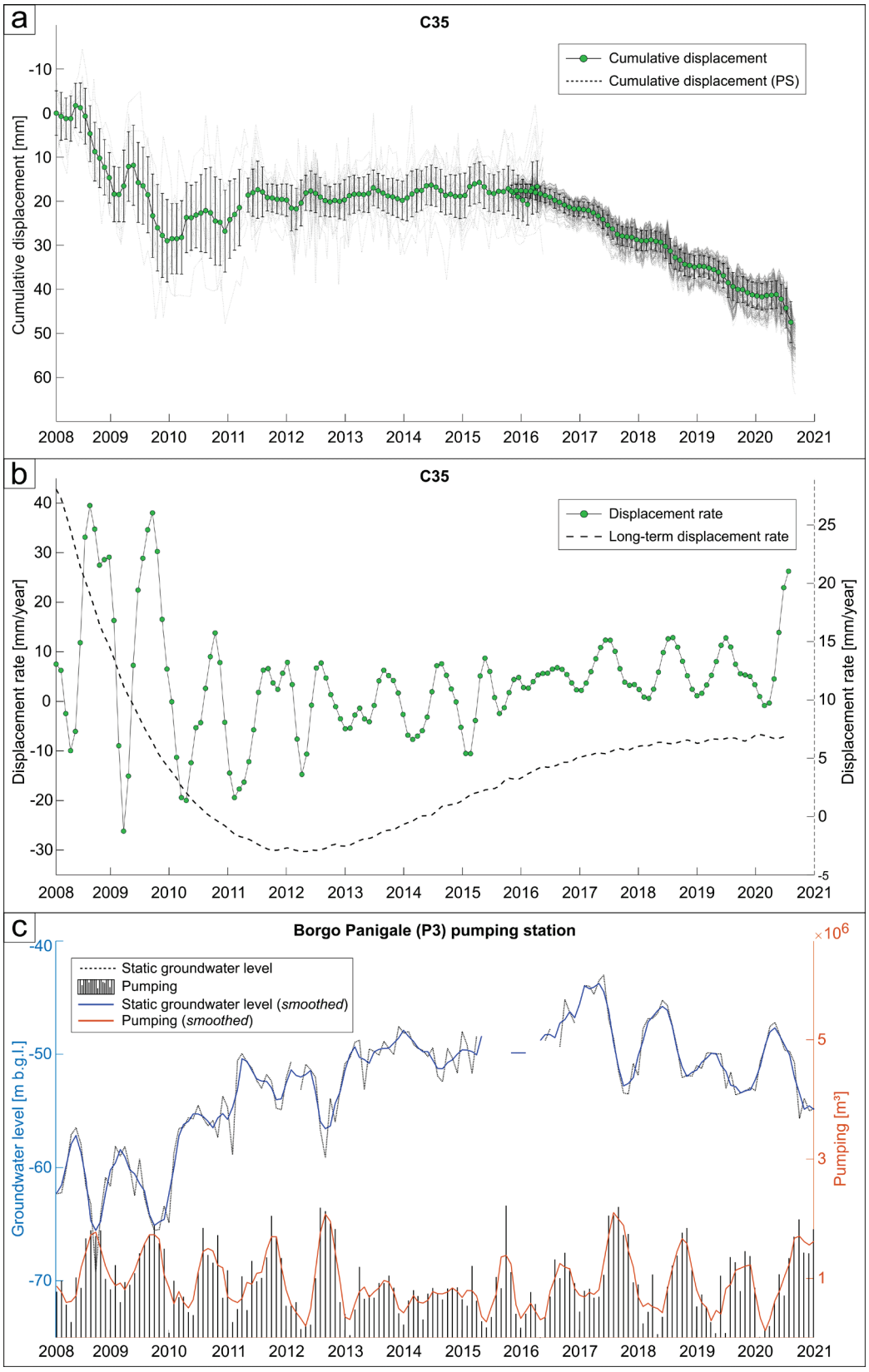

Fig. 3.22 Detailed short-term cumulative displacement (a) and displacement rate (b) time series, illustrating the recent subsidence process evolution in the *C35* control point of Domain C. The long-term displacement rate trend is also displayed as a dashed line (b). The detailed pumping and groundwater level time series from the closest major pumping station (*P3*) are included for comparison (c).

3.10 References

Alessi R, 1985. La subsidenza nel centro storico della città di Bologna. Il grado di dissesto dei fabbricati nella zona di via Zamboni. Inarcos, 456, 16-24, Bologna.

Amorosi A, Farina M, Severi P, Preti D, Caporale L, Di Dio G, 1996. Genetically related alluvial deposits cross active fault zones: an example of alluvial fan-terrace correlation from the upper Quaternary of the southern Po Basin, Italy. Sediment. Geol., 10'2, 275-295.

Amorosi A, Caporale L, Farina M, Preti D, Severi P, 1997. Late Quaternary sedimentation at the southern margin of the Po Basin (Northern Italy). Geologia Insubrica 2, 149-159.

Amorosi A, Bruno L, Rossi V, Severi P, Hajdas I, 2014. Paleosol architecture of a late Quaternary basin-margin sequence and its implications for high-resolution, nonmarine sequence stratigraphy. Glob. Planet. Chang. 112, 12-25.

Argnani A, Barbacini G, Bernini M, Camurri F, Ghielmi M, Papani P, Rizzini F, Rogledi S, Torelli L, 2003. Gravity tectonics driven by Quaternary uplift in the Northern Apennines: insights from the La Spezia-Reggio Emilia geo-transect. In Uplift and Erosion; Driving Processes and Resulting Landforms; Dynamic Relations Between Crustal and Surficial Processes, Bartolini C, Piccini L, Catto NR (eds). Quatern. Int., 13–26.

ARPAE (Agenzia Prevenzione Ambientale Energia Emilia-Romagna), 2008. Analisi preliminare degli effetti dei prelievi di acque sotterranee sulla evoluzione recente del fenomeno della subsidenza in Emilia-Romagna, Bologna, 2008.

ARPAE (Agenzia Prevenzione Ambientale Energia Emilia-Romagna), 2018. Rilievo della subsidenza nella pianura emiliano-romagnola - seconda fase, Bologna, 2018.

Attard G, Winiarski T, Rossier Y, Eisenlohr L, 2016. Revue: Impact des structures du sous-sol sur les écoulements des eaux souterraines en milieu urbain. Hydrogeology Journal 24, 5–19. doi:10.1007/s10040-015-1317-3.

Bagheri-Gavkosh M, Hosseini SM, Ataie-Ashtiani B, Sohani Y, Ebrahimian H, Morovat F, Ashrafi S, 2021. Land subsidence: A global challenge. Science of the Total Environment 778. doi:10.1016/j.scitotenv.2021.146193.

Bergonzoni A, Elmi C, 1985. La geologia dell'area bolognese in relazione al fenomeno della subsidenza, Inarcos, 456, 2-7, Bologna.

Bitelli G, Bonsignore F, Pellegrino I, Vittuari L, 2015. Evolution of the techniques for subsidence monitoring at regional scale: the case of Emilia-Romagna region (Italy), Proc. IAHS, 372, 315–32, https://doi.org/10.5194/piahs-372-315-2015.

Bitelli G, Roncari G, Tini MA, Vittuari L, 2018. High-precision topographical methodology for determining height differences when crossing impassable areas, Measurement, 118, 147-155, ISSN 0263-2241, https://doi.org/10.1016/j.measurement.2018.01.013.

Bitelli G, Bonsignore F, Del Conte S, Franci F, Lambertini A, Novali F, Severi P, Vittuari L, 2020. Updating the subsidence map of Emilia-Romagna region (Italy) by integration of SAR interferometry and GNSS time series: the 2011–2016 period, Proc. IAHS, 382, 39–44, https://doi.org/10.5194/piahs-382-39-2020.

Bjerrum L, 1963. Discussion, Proc. European Conference on Soil Mechanic and Foundation Engineering, Wiesbaden, Germany, vol. III, p. 135.

Brighenti G, Borgia GC, Mesini E, 1995. Chapter 5 Subsidence studies in Italy, Editor(s): Chilingarian G.V., Donaldson E.C., Yen T.F., Developments in Petroleum Science, Elsevier, Volume 41, 1995, Pages 215-283, ISSN 0376-7361, ISBN 9780444818201, https://doi.org/10.1016/S0376-7361(06)80052-X.

Bruno L, Amorosi A, Curina R, Severi P, Bitelli R, 2013. Human–landscape interactions in the Bologna area (northern Italy) during the mid–late Holocene, with focus on the Roman period. Holocene, 23, 1560 – 1571.

Bruno L, Marchi M, Bertolini I, Gottardi G, Amorosi A, 2020. Climate control on stacked paleosols in the Pleistocene of the Po Basin (northern Italy). J. Quaternary Sci, 35, 559-571, https://doi.org/10.1002/jqs.3199.

Carminati E, Di Donato G, 1999. Separating natural and anthropogenic vertical movements in fast subsiding areas: the Po plain (N Italy) case. Geophys. Res. Lett., 26, 2291-2294.

Carminati E, Martinelli G, 2002. Subsidence rates in the Po Plain, northern Italy: the relative impact of natural and anthropogenic causation. Engineering Geology, 66, 241-255.

Castellarin A, Eva C, Giglia G, Vai GB, Rabbi E, Pini GA, Crestana G, 1985. Analisi strutturale del fronte Appenninico Padano. Giorn. Geol. 47, 47-75.

Chaussard E, Amelung F, Abidin H, Hong SH, 2013. Sinking cities in Indonesia: ALOS PALSAR detects rapid subsidence due to groundwater and gas extraction. Remote Sensing of Environment, 128, 150–161.

Costantini M, Minati F, Trillo F, Ferretti A, Novali F, Passera E, Dehls J, Larsen Y, Marinkovic P, Eineder M, Brcic R, Siegmund R, Kotzerke P, Probeck M, Kenyeres A, Proietti S, Solari L, Andresen HS, 2021. European Ground Motion Service (EGMS), IEEE International Geoscience and Remote Sensing Symposium IGARSS, Brussels, Belgium, 2021, pp. 3293-3296, doi: 10.1109/IGARSS47720.2021.9553562.

Crosetto M, Solari L, Balasis-Levinsen J, Bateson L, Casagli N, Frei M, Oyen A, Moldestad DA, Mróz M, 2021. Deformation Monitoring at European Scale: The Copernicus Ground Motion Service, The International Archives of the Photogrammetry, Remote Sensing and Spatial Information Sciences, XLIII-B3-2021, 141-146. doi: 10.5194/isprs-archives-XLIII-B3-2021-141-2021.

De Caro M, Crosta GB, Previati A, 1985. Modelling the interference of underground structures with groundwater flow and remedial solutions in Milan, Engineering Geology, 272, 105652. 0013-7952, https://doi.org/10.1016/j.enggeo.2020.105652.

Dehghani M, Valadan Zoej MJ, Entezam I, Mansourian A, Saatchi S, 2009. InSAR monitoring of progressive land subsidence in Neyshabour, Northeast Iran. Geophys J Int 178:47–56.

Farolfi G, Del Soldato M, Bianchini S, Casagli N, 2019. A procedure to use GNSS data to calibrate satellite PSI data for the study of subsidence: an example from the north-western Adriatic coast (Italy), European Journal of Remote Sensing, 52:sup4, 54-63, DOI: 10.1080/22797254.2019.1663710.

Fernández-Torres E, Cabral-Cano E, Solano-Rojas D, Havazli E, Salazar-Tlaczani L, 2020. Land Subsidence risk maps and InSAR based angular distortion structural vulnerability assessment: an example in Mexico City, Proceedings of the International Association of Hydrological Sciences, 382, 583-587. doi: 10.5194/piahs-382-583-2020.

Ferretti A, Prati C, Rocca F, 2001. Permanent Scatterers in SAR Interferometry. IEEE Trans. IEEE Transactions on Geoscience and Remote Sensing, 39, 8–20. doi:10.1109/36.898661.

Foster S, 2022. The key role for groundwater in urban water-supply security. Journal of Water and Climate Change, 13 (10), 3566–3577. doi: https://doi.org/10.2166/wcc.2022.174.

Galloway DL, Burbey TJ, 2011. Regional land subsidence accompanying groundwater extraction. Hydrogeology Journal 19(8): 1459-1486. Galloway, D.L., Burbey, T. J., 2011. Review: Regional land subsidence accompanying groundwater extraction, Hydrogeology J., 19(8), 1459-1486.

Giacomelli S, Zuccarini A, Amorosi A, Bruno L, Di Paola G., Martini A, Severi P, Berti M, 2023. 3D geological modelling of the Bologna urban area (Italy), Engineering Geology, 324, 107242, ISSN 0013-7952. https://doi.org/10.1016/j.enggeo.2023.107242.

Hakim WL, Achmad AR, Eom J, Lee CW, 2020. Land subsidence measurement in Jakarta coastal area using time series interferometry with Sentinel-1 SAR data. In: Jung, H.-S.; Lee, S.; Ryu, J.-H., and Cui, T. (eds.), Advances in Geospatial Research of Coastal Environments. Journal of Coastal Research, Special Issue No. 102, pp. 75-81. Coconut Creek (Florida), ISSN 0749-0208.

He H, Xiao J, He J, Wei B, Ma X, Huang F, Cai X, Zhou Y, Bi J, Zhao Y, Wang C, Wei J, 2023. Three-Dimensional Geological Modeling of the Shallow Subsurface and Its Application: A Case Study in Tongzhou District, Beijing, China. Applied Sciences, 13, 1932. https://doi.org/10.3390/app13031932.

Herrera-García G, Ezquerro P, Tomás R, Béjar-Pizarro M, López-Vinielles J, Rossi M, Mateos RM, Carreón-Freyre D, Lambert J, Teatini P, Cabral-Cano E, Erkens G, Galloway D, Hung W, Kakar N, Sneed M, Tosi L, Wang H, Ye S, 2021. Mapping the global threat of land subsidence. Science, 371, 34-36 (2021). DOI:10.1126/science.abb8549.

Luberti GM, Prestininzi A, Esposito C, 2015. Development of a geological model useful for the study of the natural hazards in urban environments: An example from the eastern sector of Rome (Italy). Italian Journal of Engineering Geology and Environment 15, 41–62. doi:10.4408/IJEGE.2015-02.O-04.

Mahmoudpour M, Khamehchiyan M, Nikudel MR, Ghassemi MR, 2016. Numerical simulation and prediction of regional land subsidence caused by groundwater exploitation in the southwest plain of Tehran, Iran. Engineering Geology 201, 6–28. doi:10.1016/j.enggeo.2015.12.004.

Miall AD, 1985. Architectural-element analysis: A new method of facies analysis applied to fluvial deposits, Earth-Science Reviews, 22, Issue 4, 261-308. https://doi.org/10.1016/0012-8252(85)90001-7.

Modoni G, Darini G, Spacagna RL, Saroli M, Russo G, Croce P, 2013. Spatial analysis of land subsidence induced by groundwater withdrawal. Engineering Geology. 167. 59–71. 10.1016/j.enggeo.2013.10.014.

Ng AH, Ge L, Li X, 2015. Assessments of land subsidence in the Gippsland Basin of Australia using ALOS PALSAR data, Remote Sensing of Environment, 159, 86-101. ISSN 0034-4257, https://doi.org/10.1016/j.rse.2014.12.003.

Ori GG; 1993: Continental depositional systems of the Quaternary of the Po Plain (northern Italy). Sediment. Geol., 83, 1-14, doi: 10.1016/S0037-0738(10)80001-6.

Pieri L, Russo P, 1980. Abbassamento del suolo della zona di Bologna: considerazioni sulle probabili cause e sulla metodologia per lo studio del fenomeno. Collana di orientamenti geomorfologici ed agronomico-forestali. Pitagora Editrice, Bologna, 1980.

Pieri L, Russo P, 1985. Situazione attuale delle ricerche sull'abbassamento del suolo nel territorio bolognese. Inarcos, 456, 11-15, Bologna.

Ricci Lucchi F, 1986. Oligocene to Recent foreland basins of Northern Apennines. In Foreland Basins, Allen, Homewood P (eds). International Association of Sedimentologists, Special Publications, 105-139.

Savitzky A, Golay MJE, 1964. Smoothing and Differentiation of Data by Simplified Least Squares Procedures. Analytical Chemistry 1964 36 (8), 1627-1639. DOI: 10.1021/ac60214a047

Sclater JG, Christie PAF, 1980. Continental stretching: an explanation of the post-mid-Cretaceous subsidence of the central North Sea basin. J. Geophys. Res. 85, 3711– 3739.

Severi P, 2021. Soil uplift in the Emilia-Romagna plain (Italy) by satellite radar interferometry. 527-542. 10.4430/bgta0349.

Skempton AW, MacDonald DH, 1956. Allowable settlement of buildings, Proc. Inst. Civ. Engrs., Part III, 5, 727–768.

Stramondo S, Saroli M, Tolomei C, Moro M, Doumaz F, Pesci A, Loddo F, Baldi P, Boschi E, 2007. Surface movements in Bologna (Po Plain — Italy) detected by multitemporal DInSAR. Remote Sensing of Environment. 110. 304-316. 10.1016/j.rse.2007.02.023.

Tomlinson MJ, 2001. Foundation Design and Construction, Pearson Education (US).

Vanicek E, Krakiwsky P, 1982. Geodesy: the concepts, North-Holland Publishing Co., Netherlands, 1982.

Vázquez-Suñé E, Sánchez-Vila X, Carrera J, 2005. Introductory review of specific factors influencing urban groundwater, an emerging branch of hydrogeology, with reference to Barcelona, Spain. Hydrogeol J 13, 522–533. https://doi.org/10.1007/s10040-004-0360-2.

Velasco V, Cabello P, Vázquez-Suñé E, López-Blanco M, Ramos E, Tubau I, 2012. A sequence stratigraphic based geological model in the urbanized area of the Quaternary Besòs delta (NW Mediterranean coast, Spain). Geologica Acta, 10, 373-393.

Viel G, Sangiorgi S, Zaccanti G, 2005. L'acqua dei bolognesi. Il Geologo dell'Emilia-Romagna, 21, 7-32.

Yousefi R, Talebbeydokhti N, 2021. Subsidence monitoring by integration of time series analysis from different SAR images and impact assessment of stress and aquitard thickness on subsidence in Tehran, Iran. Environmental Earth Sciences 80. doi:10.1007/s12665-021-09714-3.

Zhang L, Lu Z, Ding X, Jung HS, Feng G, Lee CW, 2012. Mapping ground surface deformation using temporarily coherent point SAR interferometry: Application to Los Angeles Basin. Remote Sensing of Environment, 117, 429–439.

Zhang Y, Huang H, Liu Y, Liu Y, 2018. Self-weight consolidation and compaction of sediment in the Yellow River Delta, China. Physical Geography, 39(1), 84–98. https://doi.org/10.1080/02723646.2017.1347420.

Zhao Q, Ma G, Wang Q, Yang T, Liu M, Gao W, Falabella F, Mastro P, Pepe A, 2019. Generation of long-term InSAR ground displacement time-series through a novel multi-sensor data merging technique: The case study of the Shanghai coastal area, ISPRS Journal of Photogrammetry and Remote Sensing, 154, 10-27. ISSN 0924-2716, https://doi.org/10.1016/j.isprsjprs.2019.05.005.

Chapter 4 – One-dimensional analysis of the observed subsidence

4.1 Preface

The analyses detailed in the previous chapters highlighted the long-term evolution of the subsidence process and its relationship with the geological setting of the Bologna urban area's subsurface. The present chapter aims to examine the described relationship from a geotechnical perspective, considering the mechanical properties of the existing deposits and piezometric data, through one-dimensional subsidence calculations.

This work involved the analysis of the Cone Penetration Tests (CPT) included in the geognostic surveys archive provided by the Geologic, Soil, and Seismic Survey of the Emilia-Romagna Region. The digitisation of original CPT charts, lithological classification and mechanical characterisation of the existing deposits were performed in parallel with the development of the 3D geological model during the first year of this PhD project. Conversely, the one-dimensional subsidence analysis was performed during the third year of this PhD, bringing together the various datasets obtained thus far, and detailed in the previous sections, encompassing stratigraphic and piezometric data, long-term subsidence distribution, and the mechanical characteristics of the involved soils.

The analyses summarised and presented in this chapter constitute the foundation for a forthcoming paper, integrating and concluding the analyses conducted during the course of this PhD project.

4.2 Methodology

4.2.1 Input stratigraphies

The one-dimensional calculation of cumulative ground displacement at representative locations within the study area requires as fundamental input data, the vertical stratigraphic profiles of the selected observation points. These profiles may be derived through two distinct methods. In the first approach, the vertical sequences of coarse-grained and fine-grained intervals are directly extracted from the previously developed 3D geological model (section 2.6.7). These intervals are determined by the intersections between the volumes of the sedimentary bodies illustrated in Fig. 2.16 and the reference verticals. The extracted sequences are subsequently discretised and divided into 5-meter-thick layers to facilitate and standardise the subsidence calculation. Conversely, in the second approach, the input stratigraphic sequences are represented as a proportion of compressible fine-grained and coarse-grained soils. This ratio can be computed and expressed as the downhole percentage of fine-grained intervals for each survey considered in the stratigraphic analysis (section 2.5.4) or as the average value within a buffer region encompassing the surveys around the reference verticals. The fine-grained soil percentage was derived for every borehole through the following procedure. For each survey, the vertical lithofacies sequence obtained previously (section 2.5.5) was systematically reclassified into three main categories, based on the prevalence of fine-grained (*L1*) and coarse-grained bodies (*L2*) or the presence of unknown or anthropogenic deposits (*L3*), as outlined in Table 4.1. After excluding the unknown intervals (*L3*), the downhole fine-grained soil percentage was computed for each survey over the cumulative thickness of *L1* and *L2* deposits, rather than the entire borehole length.

Code	Lithofacies	Reclassification
A/S	Anthropogenic/Soil	*Unknown (L3)*
PC/ DC	Proximal alluvial fan channel/ Distal alluvial fan channel	*Coarse-grained prevalence (L2)*
Ch	Fluvial channel	*Coarse-grained prevalence (L2)*
ChA/Dv	Channel abandonment/ Deactivation	*Coarse-grained prevalence (L2)*
Lv	Levee	*Coarse-grained prevalence (L2)*
Cr	Crevasse	*Coarse-grained prevalence (L2)*
O	Floodplain with overbank	*Fine-grained prevalence (L1)*
WF	Well-drained floodplain	*Fine-grained prevalence (L1)*
PF	Poorly-drained floodplain	*Fine-grained prevalence (L1)*

Table 4.1 Reclassification of the previously defined lithofacies intervals into *unknown* (*L3*), *coarse-grained* (*L2*) and *fine-grained prevalent* (*L1*) intervals. The description of the reported lithofacies is fully detailed in Table 2.1.

This last approach offers the advantage of accounting for the eventual occurrence of thin and isolated coarse-grained deposits that due to their limited extent or the inability to perform stratigraphic correlations may not have been included in the final 3D geological model (section 2.6.7). Conversely, the former approach provides reliable vertical stratigraphies resulting from detailed two and three-dimensional stratigraphic analyses and correlations, that are not limited to the immediate borehole proximities and the respective maximum depths. Therefore, the soil stratigraphies extracted directly from the geological model were ultimately employed for the one-dimensional subsidence calculations.

4.2.2 Mechanical characterisation

As previously described, the 3D geological model primarily comprises two units: fine-grained and coarse-grained deposits. Evaluating the mechanical properties of the latter, due to the frequently high gravel fraction, is often challenging and requires specific in situ tests (e.g. plate load tests), that are not available in the considered RER database. Consequently, the parametrisation of the existing fine-grained and coarse-grained soils was performed separately, as illustrated in the following sections.

4.2.2.1 Fine-grained deposits

4.2.2.1.1 Available data

In view of the mechanical characterisation of the subsurface fine-grained deposits in the urban area of Bologna, the available in situ geotechnical survey data were extracted from the open-access RER geognostic archive. The RER database provided 589 Cone Penetration Test (CPT) surveys, as reported in Figure 4.1a. These surveys predominantly encompass mechanical cone tests (CPTm, 534), as well as 46 electrical cone (CPTe) and 9 piezocone (CPTu) tests. The overall data density averages around 7 points per km², although the available surveys exhibit an uneven distribution across the study area. Higher density clusters are observed along the railway, main roads, and in proximity to densely populated or urbanised sectors. The maximum investigation depth achieved by the surveys also displays significant heterogeneity. As depicted in Figure 4.1b, only about 12% of the surveys reach or exceed a depth of 20 meters, while the majority explore depths ranging from 10 to 14 meters below the ground level. The considered archive covers CPT surveys conducted approximately between 1970 and 2013 by diverse agencies, employing varying equipment and data processing software, leading to heterogeneous outputs. Within the RER database, the CPT available data consist of scanned charts capturing instrumentation readings acquired during each survey. While these charts may vary in representation across different surveys, they consistently portray profiles of the measured *cone resistance* (q_c) and the local *unit sleeve friction resistance* (f_s) with depth. These parameters, both expressed in kPa, are respectively defined as follows:

$$q_c = \frac{Q_c}{A_c} \quad [4.1]$$

and

$$f_s = \frac{Q_s}{A_s} \quad [4.2]$$

where:

- Q_c = axial force acting on the cone [N]
- A_c = area of the base of the penetration cone [m²]
- Q_s = friction force acting on the sleeve [N]
- A_s = lateral surface of the sleeve [m²].

While these charts represent mechanical and electrical CPT outputs, CPTu surveys' data include a third graph that illustrates the variation with depth of the pore pressure (u_2), measured in a porous filter behind the cone and also expressed in kPa.

The existing charts were then appropriately digitised to convert the available visual representations of q_c, f_s and eventually u_2 depth profiles into the corresponding numerical values measured in situ. This operation was executed through an original Matlab script that employs a graphical interface, that enables the manual retracing of curves point by point, yielding the corresponding downhole values for the considered parameter (Fig. 4.2). This procedure not only provides usable numerical data for determining the mechanical parameters of the deposits but also facilitates input data homogenisation, as it organises the data into a consistent set of tables.

During this operation, the selection of CPTs to be digitised involved prioritising surveys deeper than 15 m, and those located in areas with limited stratigraphic data coverage. Instances arose where the digitisation procedure could not be applied due to partially complete or illegible input charts, resulting in the exclusion of corresponding tests. This process ultimately led to the digitisation of 143 CPTs, including 113 CPTm, 21 CPTe and 9 CPTu surveys, as displayed in Figure 4.1a.

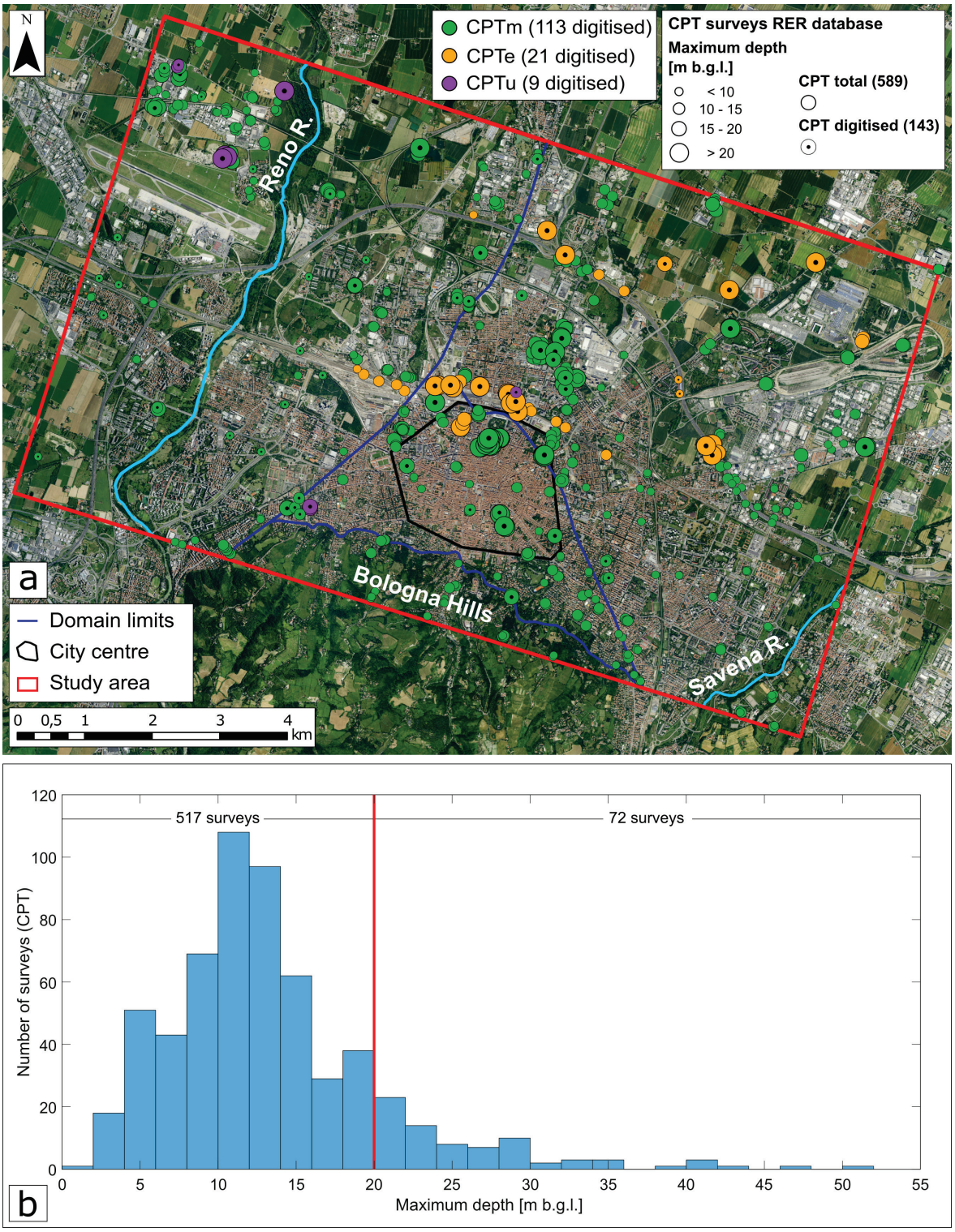

Fig. 4.1 (a) Spatial distribution of the CPT surveys extracted from the RER database in the study area. Coloured circles indicate survey type, while their width reflects the maximum exploration depth. Digitized CPTs are marked by black dots at circle centres. (b) Histogram illustrating the frequency distribution of available CPT survey maximum depths. The red line distinguishes surveys shallower and deeper than 20 m. Bin widths correspond to 2 m intervals.

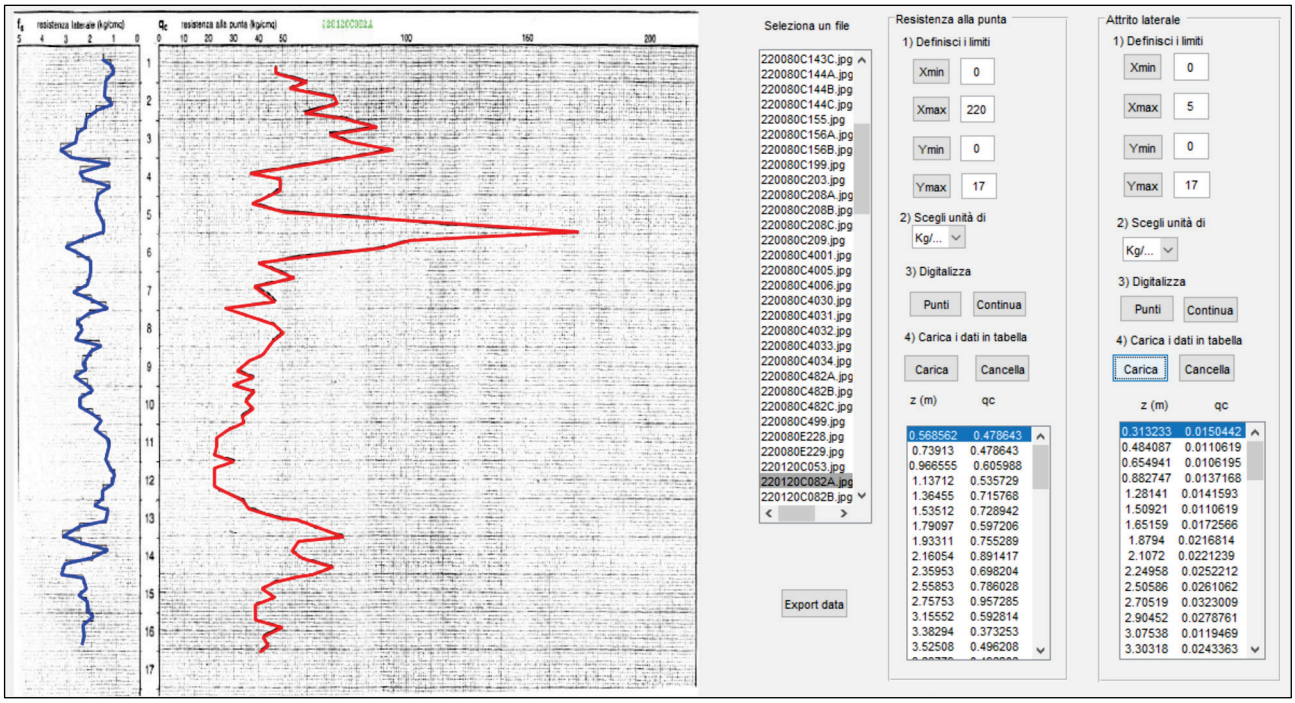

Fig. 4.2 Example of the digitisation procedure through the graphical interface integrated into the developed Matlab script. Starting from the original scanned charts, the retraced q_c (red) and f_s (blue) profiles are converted into their corresponding numerical values reported in the bottom-right corner.

4.2.2.1.2 Lithological classification

The obtained downhole numerical values of q_c, f_s and u_2, in the case of CPTu surveys, have been employed to perform a lithological categorisation of the encountered subsurface deposits following established literature classification methods, allowing the transposition of the input numerical data into a vertical sequence of lithology intervals.

In relation to mechanical CPTs, the classification approach introduced by Schmertmann (1978) and depicted in Figure 4.3 has been utilised. The presented classification chart is partitioned into distinct zones, each representing specific soil categories based on their anticipated in situ mechanical responses. Progressing from the lower-right corner to the left side of the chart, five main lithological fields are identified, encompassing organic clays, inorganic clays, silty clays, sandy silts, and sands. The allocation of the examined deposit to one of these categories is based on its q_c and friction ratio (R_f) values, which are respectively plotted on the graph's y and x axes using logarithmic and natural scales. R_f, typically expressed as a percentage, can be defined as follows:

$$R_f = 100 \frac{f_s}{q_c} \qquad [4.3]$$

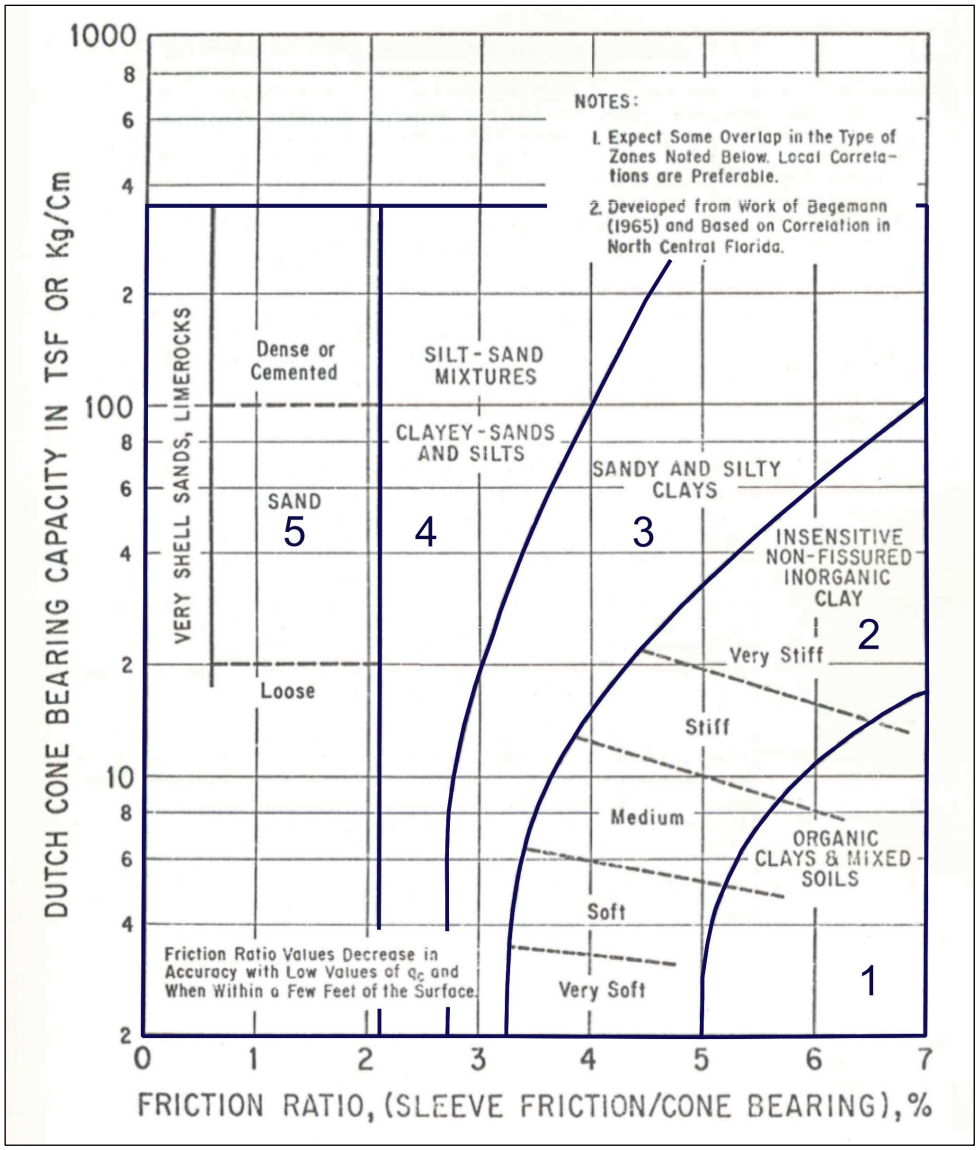

Fig. 4.3 Soil classification chart for mechanical CPT surveys (Schmertmann 1978, modified).

As regards both electrical cone and piezocone surveys, the classification criterion introduced by Robertson et al. (1986) was followed. As displayed in Figure 4.4, this approach relies on the attribution of *soil behaviour type* (*SBT*) categories, based on the typical in situ mechanical response of the deposits rather than their grain size distribution or plasticity (Robertson 2010). Within the presented chart, subdivided into 12 *SBT* regions, similar to the Schmertmann (1978) classification (Fig. 4.3), the x-axis encompasses R_f expressed as a percentage. Conversely, the y-axis portrays the *corrected cone resistance* (q_t), presented on a logarithmic scale. q_t represents the measured cone resistance (q_c) value that has been corrected for the different ambient pore water pressure action exerted on distinct portions of the cone as the penetration occurs, known as *unequal area effect* (Cestari 1990). This effect, primarily contingent on the internal geometry of the cone and the in situ pore pressure during the penetration, influences the total stress determined from the cone, leading to potential differences between cone resistance measurements and their actual value (Lunne et al 1997). In systems where the geometry of the cone is known, and the pore water pressure can be measured, such as in piezocone CPT surveys, q_t can be defined as:

$$q_t = q_c + u_2\left(1 - \frac{A_n}{A_c}\right) = q_c + u_2(1 - a) \qquad [4.4]$$

where:

- An = cross-sectional area of the load cell [m²], where u_2 does not act (Cestari 1990)
- a = cone area ratio, specified by the cone constructor, and typically designed to be as close to the unity as possible to minimise deviations between q_c and q_t.

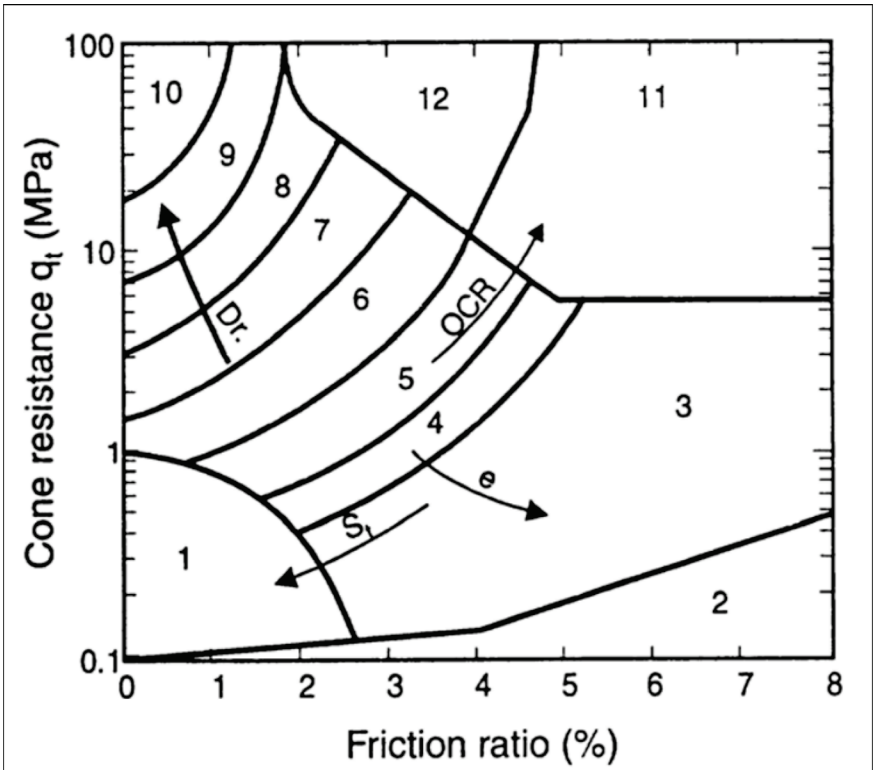

Zone	Soil Behaviour Type
1	Sensitive fine-grained
2	Organic material
3	Clay
4	Silty clay to clay
5	Clayey silt to silty clay
6	Sandy silt to clayey silt
7	Silty sand to sandy silt
8	Sand to silty sand
9	Sand
10	Gravelly sand to sand
11	Very stiff fine-grained*
12	Sand to clayey sand*

*Overconsolidated or cemented

Fig. 4.4 Robertson et al (1986) soil classification chart for electrical and piezocone CPT surveys (Robertson 2010).

As described in Lunne et al. (1997) and Robertson (2010), the chart displayed in Figure 4.4, presented in terms of q_t, can be employed for CPTe surveys as well, using the uncorrected cone resistance q_c instead, as u_2 is not measurable and the unequal area effect is not discernible. The assumption $q_c = q_t$ is generally reasonable, as their deviation is typically small. Nonetheless, discrepancies may arise in correspondence of soft clayey soils,

occupying the lower portions of the chart, where the cone resistance is relatively low (q_c < 1 MPa) and the generated penetration pore pressures (u_2) may be large.

The lithological classification of the digitised CPTs was performed employing two original Matlab scripts which include graphical interfaces allowing the manual categorisation of the encountered deposits based on the described Schmertmann (1978) and Robertson et al. (1986) criteria, as illustrated in Figure 4.5 and Figure 4.6, respectively. The digitised downhole numerical values of q_c, f_s and u_2, were homogenised and regularly resampled at 5 cm intervals, ensuring that they correspond to the same depths. For a selected CPT survey, as displayed in Figure 4.5 and Figure 4.6, the resampled profiles of q_c and f_s are displayed in sector A of the developed graphical interfaces as red and blue curves, respectively. The graph in sector B is a downhole representation of the adopted classification chart reported in sector D. The black solid line represents the downhole lithology or *SBT* category determined for each depth value. The resulting *SBT* profile reveals downhole lithology variations, highlighting both q_c and f_s reciprocal fluctuations. To refine and validate the recognised upper and lower limits of different soil intervals, indicated by abrupt shifts in mechanical behaviour, the classic representation of the classification chart in sector D is employed. Once these limits are defined, the corresponding SBT category is marked for every depth value within the selected interval using a black dot on the classification chart. The percentage of points within each field is quantified, facilitating the lithological attribution of the considered interval. Subsequently, the upper and lower limits, alongside the corresponding lithological classification, are recorded in the blank fields of sector C, progressively reconstructing the downhole lithostratigraphy, as visually represented by a log on the left. Ultimately, the complete stratigraphies obtained for each CPT survey are compiled into a homogeneous set of tables.

The described procedure is equally applicable to both interfaces, with the only distinction being the classification method employed. Additionally, in the case of thin deposits or interbedded layers, a vertical resolution threshold of 20 cm was adopted. This cut-off value aligns with the vertical resolution of CPTm surveys.

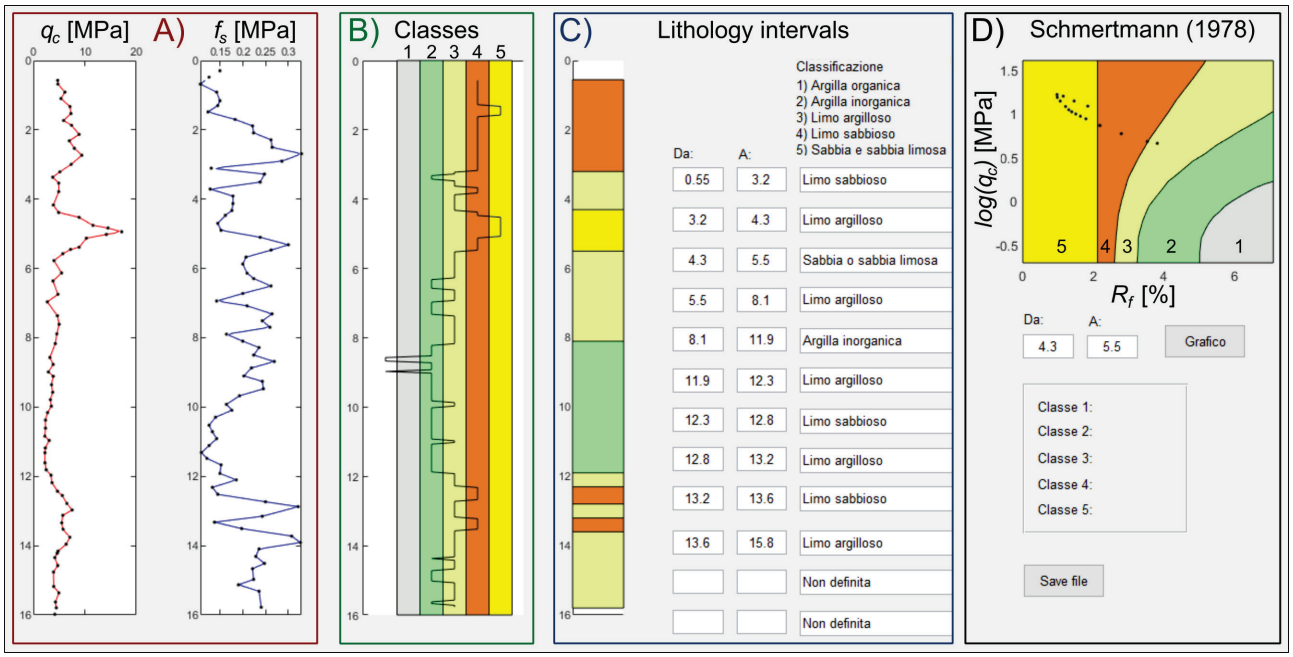

Fig. 4.5 Example of the lithological classification procedure through the graphical interface integrated into the developed Matlab script, employing the Schmertmann (1978) approach for CPTm surveys.

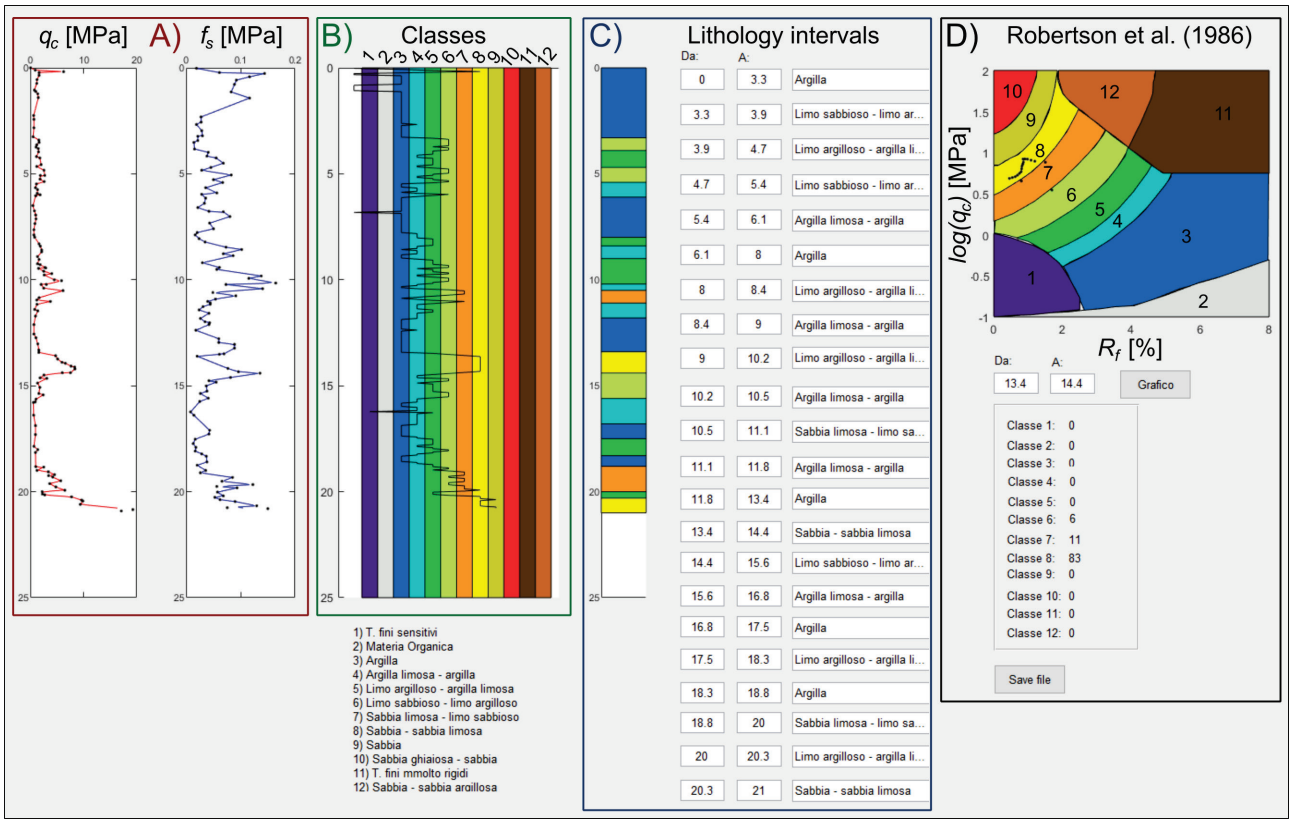

Fig. 4.6 Example of the lithological classification procedure through the graphical interface integrated into the developed Matlab script, employing the Robertson et al. (1986) approach for CPTe and CPTu surveys.

4.2.2.1.3 Fine-grained intervals parametrisation

The attribution of appropriate mechanical parameter values to the obtained downhole sequence of lithological intervals for each digitised CPT survey was performed through an original Matlab script. Firstly, the identified intervals were grouped and classified into two primary categories aligning with their anticipated overall mechanical behaviour: fine-grained and coarse-grained soils. This distinction is graphically presented in Table 4.2, where fine-grained soils are represented by the blue fields corresponding to the 1-5 and 11 and the 1-3 classes of Robertson et al. (1986) and Schmertmann (1978) classification methods, respectively. The remaining categories, highlighted in orange, are classified as coarse-grained soils.

In parallel, the identified lithological intervals were provided with a suitable estimate of the corresponding soil unit weight (γ), relying on their *SBT* classification, as indicated in Lunne et al. (1997) for the 12 classes specified in the Robertson et al. (1986) classification (Table 4.2). The table also outlines the approximate γ values considered for the 5 Schmertmann (1978) categories.

SBT zone (Robertson et al. 1986)	Corresponding soil zone in Schmertmann (1978)	Approximate soil unit weight (γ) [kN/m³]
1	–	17.5
2	–	12.5
3	1 – 2	17.5
4	3	18
5		18
6	–	18
7	4	18.5
8	5	19
9	–	19.5
10	–	20
11	–	20.5
12	–	19

Table 4.2 Estimate of soil unit weights (γ) based on *SBT* category (Lunne et al. 1997, modified). The lithology classes are grouped into two primary categories: fine-grained and coarse-grained intervals, highlighted in blue and orange, respectively.

The adopted Robertson et al. (1986) classification chart can be also expressed in terms of normalised dimensionless corrected cone resistance Q_t and friction ratio F_r expressed as:

$$Q_t = \frac{q_t - \sigma_{v0}}{\sigma'_{v0}} \quad [4.5]$$

and:

$$F_r = \frac{f_s}{q_t - \sigma_{v0}} 100 \quad [4.6]$$

where:

- σ_{v0} = in situ total vertical stress [kPa]
- σ'_{v0} = in situ effective vertical stress [kPa].

The resulting normalised soil behaviour type (*SBTn*) chart introduced by Robertson (1990) and updated by Robertson (2010), is presented in Figure 4.7. This approach offers the advantage of mitigating the eventual misclassification of soils, accounting for the potential increment of cone resistance (q_c or q_t) and sleeve friction (f_s) values with increasing overburden stress and depth. Nonetheless, Robertson et al. (1986) classification method, as detailed above, was employed instead of the more recent one due to the absence of prior knowledge regarding the unit weight (γ) of the existing soils, which is essential to calculate the in situ natural stress state and perform the normalisation of cone parameters. As displayed in Figure 4.7, alongside the *SBTn* regions the chart highlights the Soil Behaviour Type Index (I_c) values, which correspond to the radius of a series of concentric circles approximating the boundaries between each SBTn zone (Robertson & Cabal 2015). I_c values and profiles variations provide numerical representation of downhole lithological variations and can be used to evaluate the mechanical response of the existing deposits. I_c derives from the normalised cone parameters and can be expressed as follows:

$$I_c = \sqrt{(3.47 - logQ_{tn})^2 + (1.22 + logF_r)^2} \quad [4.7]$$

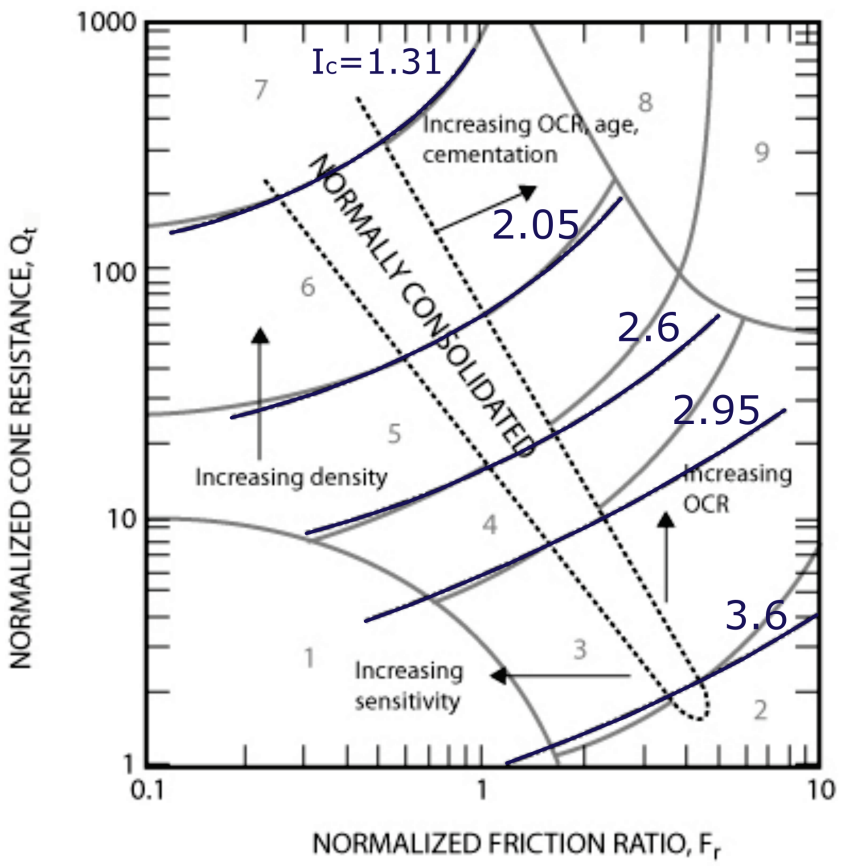

Zone	Normalised Soil Behaviour Type	I_c
1	Sensitive fine-grained	N/A
2	Organic soils - clay	>3.6
3	Clays - silty clay to clay	2.95-3.6
4	Silt mixtures - clayey silt to silty clay	2.6-2.95
5	Sand mixtures - silty sand to sandy silt	2.05-2.6
6	Sands - clean sands to silty sands	1.31-2.05
7	Gravelly sand to dense sand	<1.31
8	Very stiff sand to clayey sand*	N/A
9	Very stiff fine-grained*	N/A

*Heavily overconsolidated or cemented

Fig. 4.7 Robertson et al (1990) normalised CPT Soil Behaviour Type (*SBTn*) chart, updated by Robertson (2010). The chart also presents the Soil Behaviour Type Index (I_c) values and curves approximating the limits between *SBTn* regions (Robertson & Cabal 2015, modified).

Q_{tn} in the previous equation represents the normalised corrected cone resistance considering an appropriate stress exponent n, which depends on the *SBTn* category, and thus on I_c, and is determined through an iterative procedure. Q_{tn} can be expressed as:

$$Q_{tn} = \frac{q_t - \sigma_{v0}}{p_a}\left(\frac{p_a}{\sigma'_{v0}}\right)^n \quad [4.8]$$

where:

$$n = 0.381 I_c + 0.05\frac{\sigma'_{v0}}{p_a} - 0.15 \quad [4.9]$$

in which p_a is the atmospheric pressure measured in kPa.

The suitable value of the stress exponent (n) is achieved when its difference between two successive iterations (Δn) is equal to or less than a convergence threshold of 0.01.

The mechanical characterisation of the identified fine-grained intervals was performed considering well-established empirical relationships outlined in recent reference publications: Robertson (2009), Mayne (2014) and Robertson & Cabal (2015). The values of the main mechanical parameters were first computed for each pair of cone resistance and sleeve friction measurements, uniformly resampled every 5 cm, and subsequently averaged to derive single representative values encompassing the entire soil interval in question.

Shear strength characteristics

In fine-grained deposits, as the penetration of the cone occurs under undrained conditions, the undrained shear strength or cohesion (S_u) can be determined as follows:

$$S_u = \frac{q_t - \sigma_{v0}}{N_{kt}} \qquad [4.10]$$

Here, the term N_{kt} denotes a dimensionless empirical cone factor typically varying between 10 to 18, with an average value of 14 that can be applied when prior information about the investigated deposits is unavailable (Robertson & Cabal 2015).

Deformation characteristics

As regards the deformability parameters of the investigated fine-grained deposits, the monodimensional constrained modulus (E_m) also referred to as oedometric modulus (see section 1.2.2) was considered. E_m from the digitised CPT surveys has been determined employing two different approaches relying on the use of the uncorrected cone resistance (q_c) and the normalised cone resistance (Q_{tn}), respectively. The first method can be expressed through the following equation (Lunne et al. 1997):

$$E_m = \alpha_m q_c \qquad [4.11]$$

where α_m is a coefficient that assumes different values based on the type of soil under investigation, as reported in Table 4.3.

Soil type	q_c [MPa]	α_m
Clays – low plasticity	< 0.7	3 – 8
	0.7 – 2	2 – 5
	> 2	1 – 2.5
Silts – low plasticity	< 2	3 – 6
	> 2	1 – 2
Clays and silts – high plasticity	< 2	2 – 6

Table 4.3 Coefficient α_m values in equation [4.16] for estimating the constrained modulus (E_m) based on soil type and uncorrected cone resistance qc, applied to fine-grained intervals (Sanglerat 1972; Mitchell & Gardner 1975).

For the present analyses, the constrained modulus (E_m) for fine-grained intervals was determined considering the recommended values for low-plasticity clays, using the average α_m value within the suggested interval based on the measured cone resistance (q_c).

As regards the alternative approach adopted, based on Q_{tn} and I_c, the constrained modulus can be expressed as:

$$E_m = \alpha_m(q_t + \sigma_{v0}) \quad [4.12]$$

Here, for $I_c > 2.2$:

- $\alpha_m = Q_{tn}$ when $Q_{tn} < 14$
- $\alpha_m = 14$ when $Q_{tn} > 14$.

Conversely, for $I_c < 2.2$:

- $\alpha_m = 0.03\left[10^{(0.55I_c+1.68)}\right]$, as reported in Robertson (2009).

4.2.2.1 Coarse-grained deposits

Differently from the fine-grained deposits, due to the inability of Cone Penetration Tests to provide significant data for coarse-grained intervals distinguished by a substantial gravel fraction, the mechanical properties of these soils were investigated through a back analysis. Specifically, the constrained modulus E_m was back-calibrated considering a reference vertical sequence of amalgamated gravelly bodies located in the proximal portions of the Reno River deposits (Fig. 4.14). The reference E_m value for the selected gravel deposits' thickness was determined using the same equations employed to calculate the settlement of each soil layer [4.13] and the corresponding cumulative subsidence [4.14]. In particular, the value of E_m, kept constant for all the soil layers, was adjusted to identify the one that produced a computed ground displacement value closest to the measured one, obtained from the cumulative subsidence map displayed in Figure 3.9 at the same location. Subsequently, this back-calibrated value of E_m was assigned to all the coarse-grained bodies within the geological model. However, it must be noted that the determined E_m, represents a black-box parameter that allows considering and estimating the compressibility of coarse-grained deposits that would otherwise remain uncharacterised.

4.2.3 Groundwater

Another critical parameter for subsidence calculation is groundwater level, whose variations over time due to groundwater extractions represent the main driver of the observed ground deformation. The initial groundwater level for all the reference verticals was assumed to be at the ground level (0 m b.g.l.). On the other hand, to determine the final groundwater level, which represents the condition after the considered pumping phase and is responsible for the final effective stress (σ'_v) distribution, the mean groundwater depth map (Fig. 3.11) and values computed over the time interval 1995 – 2005 (section 3.6.1.3) were considered. Specifically, the final groundwater level attributed to each reference vertical coincides with the one measured in the nearest deep wells.

While this methodology applies to the reference verticals located in Domain A and C, the scenario in Domain B is different. Firstly, the computed mean groundwater depth map spanning 1995 – 2005, consistently indicates low drawdown values with the groundwater table remaining approximately at the ground level. Furthermore, field data from the University of Bologna archive, collected during a similar time frame around the mid-1990s, reveal a pore pressure distribution (u_f) that significantly diverges from the natural hydrostatic profile (u_i), as illustrated in Figure 4.8.

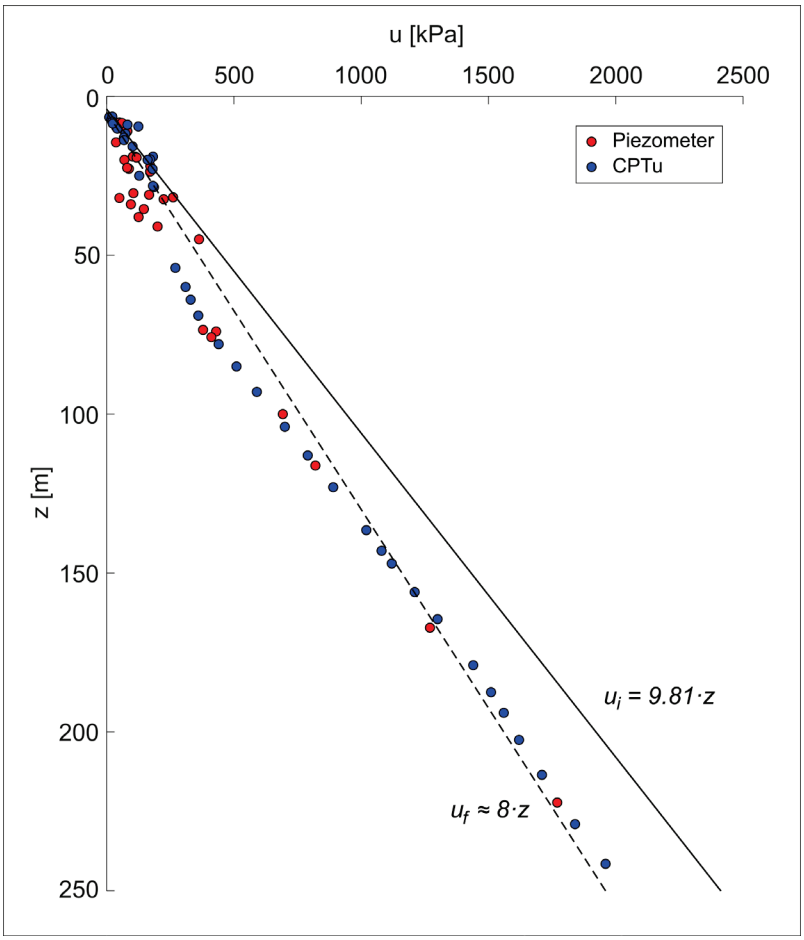

Fig. 4.8 Pore pressure distribution field data recorded during the mid-1990s in the city centre of Bologna encompassing piezometer measurements (red dots) and CPTu surveys (blue dots). The black solid line displays the natural hydrostatic profile (u_i), whereas the black dashed line approximates the observed pore pressure distribution (u_f).

These field data indicate the occurrence and effect of the downward component of a seepage flow in the subsurface stiff clayey deposits of Domain B, induced by pumping in the adjacent coarse-grained deposit sequences of the Reno River and the Savena River alluvial fan apex. As a consequence, for the reference verticals within Domain B, the final groundwater level and pore pressure values were determined assuming a null drawdown and a distribution with depth that aligns with the equation of the dashed line in Figure 4.8.

4.2.4 One-dimensional subsidence calculation

After establishing the calculation reference verticals, discretised in 5-meter intervals, and incorporating the respective derived mechanical properties, along with defining the groundwater level and pore pressure variations, the settlement (ΔH) of each layer was computed through the following equation, obtained inverting [1.11]:

$$\Delta H = \frac{H_0 \Delta \sigma'_v}{E_m} \qquad [4.13]$$

where:

- H_0 = initial thickness of each layer (equal to 5 m)
- $\Delta \sigma'_v$ = effective stress increase [kPa] measured in each layer, resulting from the imposed groundwater level and pore pressure distribution variations
- E_m = constrained modulus of each layer [kPa].

The cumulative ground displacement (S_{tot}) is then obtained by the sum of the settlement computed in the various layers:

$$S_{tot} = \sum_{i=z_0}^{z_f} \Delta H_i \qquad [4.14]$$

in which the index i denotes the *i-th* soil layer comprised between the minimum (z_0) and maximum (z_f) depths of the reference calculation vertical considered.

However, as highlighted by the frequency distribution presented in Figure 4.1b, CPT data primarily explores the shallowest portions of the geological model and the reference verticals, with survey depths rarely exceeding 30 meters. Consequently, the derived mechanical parameters only reflect the characteristics of the shallowest deposits. To obtain representative computed subsidence values, it is essential to understand and define the specific trend of the soil deformability parameters with depth. For instance, the values of the constrained modulus (E_m) are highly dependent on the stress state in which they are determined (Craig 1974; Lancellotta 1987). In the absence of deep field surveys and data, estimating the profiles of the deformation moduli with depth requires the adoption of empirical literature relationships. In this regard, the following equation, proposed by Janbu (1967) was considered to derive E_m depth profiles:

$$E_m = m p_a \left(\frac{\sigma'_v}{p_a}\right)^{1-\beta} \qquad [4.15]$$

where:

- m = modulus number (dimensionless)
- p_a = atmospheric pressure ≈ 100 kPa
- β = stress exponent, which describes the relationship between the soils' void ratio (e), and its associated properties, with effective stress (σ'_v), and, consequently, depth.

For instance, values of β can be schematised based on the expected behaviour of different soil types, as illustrated in Table 4.4.

Soil type	β
OC clays and rocks	1
NC silts and sands	0.5
NC clays, silts and silty or clayey sands	0

Table 4.4 Coefficient β values in equation [4.15] based on soil type (Janbu 1967; Di Buò 2020).

The extremes of the β variation range represent two opposite end members in which E_m either increases linearly [4.16] or remains constant with depth [4.17], corresponding to the theoretical behaviour of NC and OC clays, respectively (Fig. 4.9):

$$E_m = m\sigma'_v \qquad (\text{for } \beta = 0) \qquad [4.16]$$

and:

$$E_m = E_{m0} = m p_a \qquad (\text{for } \beta = 1) \qquad [4.17]$$

where E_{m0} is the constrained modulus measured in shallowest deposits ($z \approx 0$) and the modulus number (m) can be derived and defined as:

$$m = \frac{E_{m0}}{p_a} \qquad [4.18]$$

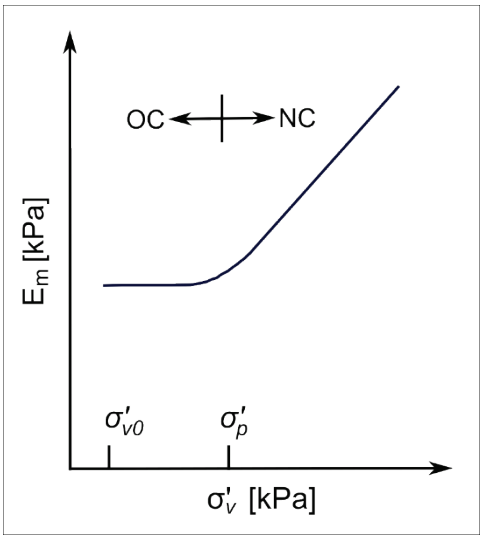

Fig. 4.9 Theoretical constrained modulus (*Em*) variation with effective stress for overconsolidated (OC) and normally consolidated (NC) clays (Janbu 1967, modified).

Since the actual E_m trend with depth is unknown, the one-dimensional subsidence along each reference vertical has been computed considering different combinations of E_{m0}, derived from CPT data, and β (ranging from 0 to 1), to determine which parameter sets produced a closer match to the observed subsidence. The quality of this alignment was then evaluated by calculating the *root mean squared error* (*RMSE*) between the computed and observed ground displacements at the corresponding reference points. While different combinations and depth profiles were explored for the constrained modulus of the fine-grained deposits, for coarse-grained soils, the unique black-box value, back-calibrated over the entire thickness of amalgamated gravels at the considered reference vertical (section 4.2.2.1), was systematically employed.

4.3 Results

4.3.1 Fine-grained to coarse-grained soil percentage distribution

The determination of the downhole percentage of fine-grained and coarse-grained soils within the various stratigraphic surveys, performed as outlined in the previous section, provides a detailed and quantitative representation of the primary lithostratigraphic pattern variations summarised in the 3D geological model. Figure 4.10a illustrates the distribution of the downhole fine-grained interval percentage across each survey considered for the stratigraphic analysis in the study area. This distribution is compared with the long-term cumulative ground displacement map spanning 1900 – 2020, described in section 3.6.1.2. Domains A and C exhibit an overall limited fine-grained soil fraction that gradually increases towards more distal and lateral portions of the Reno River deposits and the Savena River alluvial fan, consistently with the recorded subsidence values, as discussed in section 3.7.1. As highlighted in the figure, the fine-grained soil percentage has been analysed primarily focusing on two neighbouring regions distinguished by notably different long-term subsidence patterns, separated by a marked transition. These areas coincide with Domain B, distinguished by low cumulative displacements, and the region immediately north of the city centre, referred to as the "Navile area", where the highest deformations have been documented. Histograms reported in Figure 4.10b, based on stratigraphic data of 118 continuous cores and wells in Domain B, and 174 in the Navile area, reveal significantly distinct fine-grained percentage distributions in these two regions. Domain B subsoil appears predominantly constituted of fine-grained deposits, with over 40% of the considered surveys displaying a fine-grained percentage comprised between 90% and 100%. In contrast, the Navile area exhibits a sensibly greater variability, with fine-grained content typically ranging from 30% to 90%, and an average value of approximately 58%.

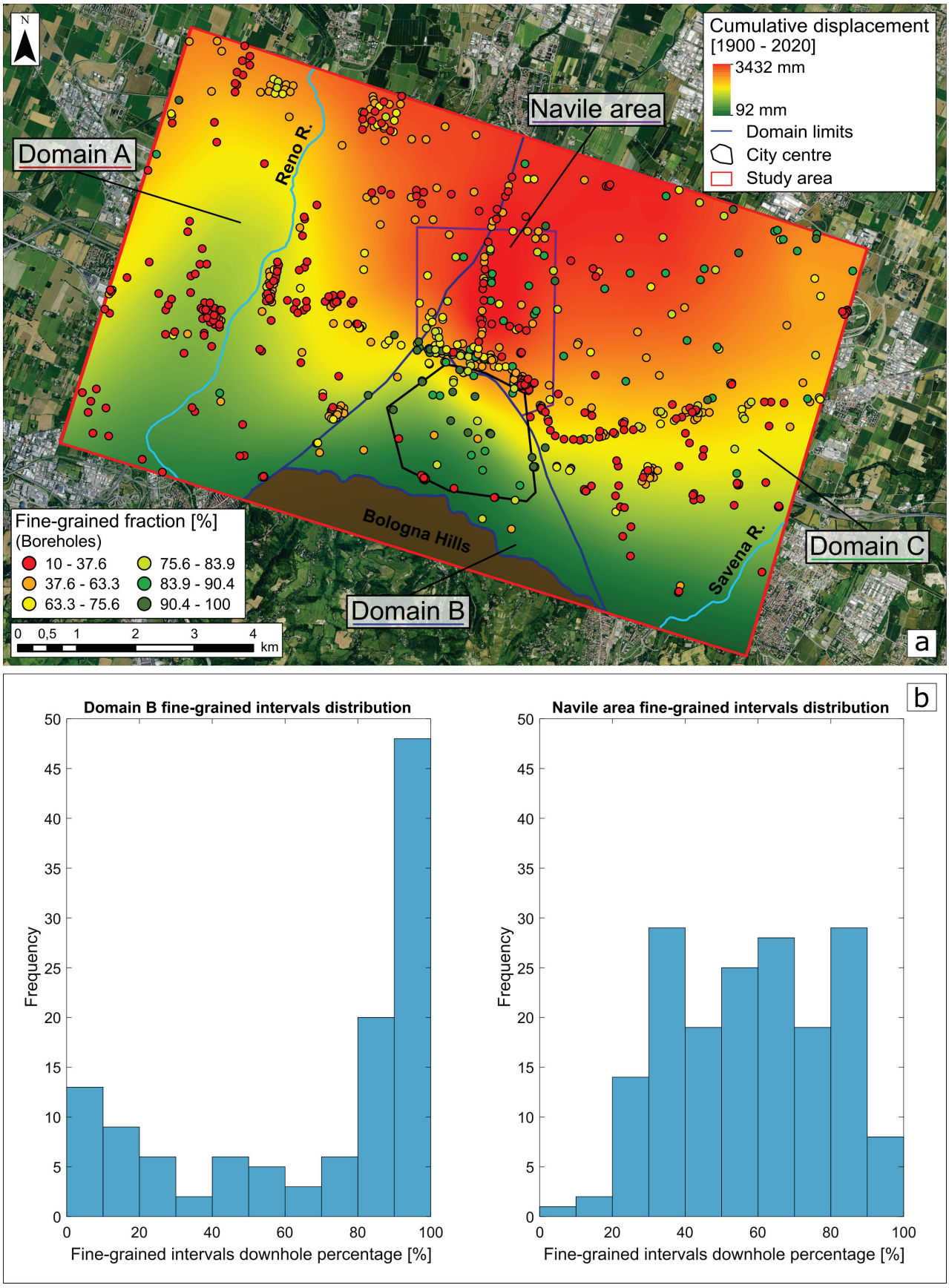

Fig. 4.10 Downhole fine-grained interval percentage distribution across the stratigraphic surveys within the study area, compared with the long-term subsidence distribution map covering the 1900 – 2020 period (a). Histograms illustrating the frequency distribution of downhole fine-grained soil percentages among Domain B (left) and Navile area (right) surveys (b).

4.3.2 Parametrisation of fine-grained soils

The characterisation of the fine-grained intervals was performed from the digitised CPT surveys employing the methodology and the empirical equations detailed in section 4.2.2.1. Similarly to the analysis of fine-grained soils percentage distribution displayed in Figure 4.10, the examination of the mechanical properties of fine-grained soils mainly focused on the same two regions: Domain B and the Navile area. These sectors of the study area are in fact distinguished by the presence of the deepest surveys, due to the lower occurrence of shallow and extensive gravel deposits compared to the areas along the Reno River course in Domain A and the apex of the Savena River alluvial fan in Domain C.

Figure 4.11 provides an overview of the investigation into the shear strength characteristics of the fine-grained intervals within these two regions. In alignment with section 2.7.3, Figures 4.11a and 4.11b present a comparison of the undrained shear strength (S_u) profiles derived from the 31 and 35 CPTs digitised in Domain B and the Navile area, respectively. Both charts reveal similar mean S_u trends, exhibiting relatively high values approximately varying from 100 to 230 kPa, falling within the "Stiff" and "Very Stiff" ranges of the soil consistency classification introduced by Terzaghi & Peck (1967). Furthermore, these high S_u values do not display a significant increase with depth and consequently with the in situ effective stress (σ'_{v0}), deviating consistently from the theoretical profile expected for normally consolidated soils expressed by the equation introduced by Mesri (1975):

$$S_u = 0.22\sigma'_{vo} \qquad [4.19]$$

The direct quantitative comparison of the mean S_u values computed at corresponding depths from Domain B and the Navile area CPTs, as illustrated in Figure 4.11c, consistently reveals similar values clustering around the identity line.

Similarly, Figures 4.12 and 4.13 offer a summary of the analysis concerning the deformability characteristics of the investigated fine-grained soils, focusing on the determination of the Constrained modulus (E_m) employing the empirical relationships proposed by Robertson (2009) and by Sanglerat (1972) and Mitchell & Gardner (1985), respectively. The E_m depth profiles displayed in (a) and (b) charts of both figures reveal similar E_m trends between Domain B and the Navile area. The reported E_m mean profiles consistently exhibit approximately constant values with depth, ranging approximately around 20 to 30 MPa and 4 to 6 MPa in Figure 4.12 and 4.13, respectively. The observed constant trends with depth suggest the presence of overconsolidated soils (Fig. 4.9), aligning with S_u data (Fig. 4.11). The quantitative comparison of E_m values computed in Domain B and the Navile area at corresponding depths, is presented for both calculation methods in Figure 4.12c and 4.13c. In both cases, this comparison highlights a significant correspondence between the compared sets of values, systematically falling along the identity line in the charts.

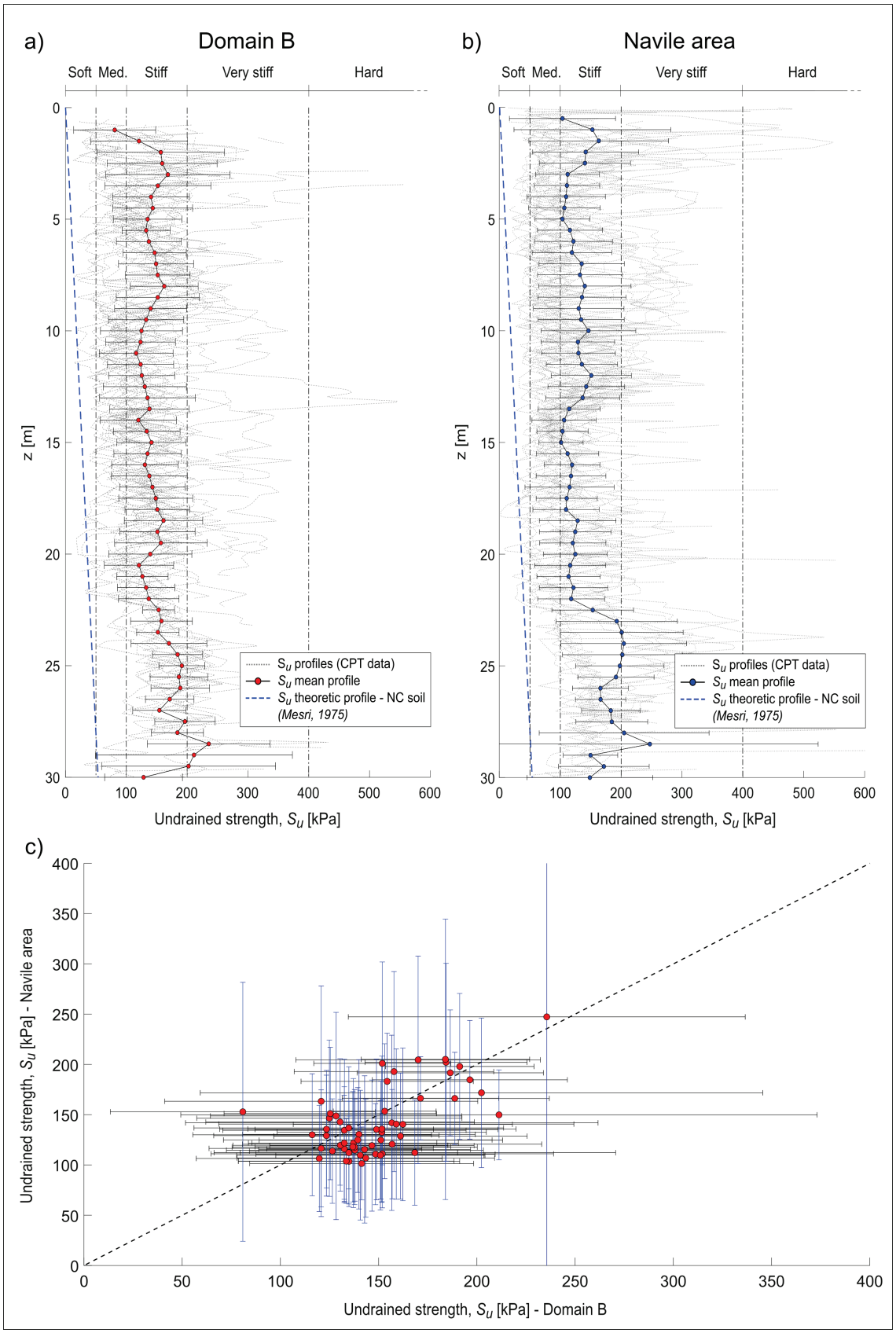

Fig. 4.11 Undrained shear strength (S_u) profiles comparison in Domain B (a) and the Navile area (b) derived from CPT data. The mean S_u profiles along with the corresponding standard deviation values are compared with the typical consistency values chart for fine-grained soils developed by Terzaghi & Peck (1967) and the theoretical trend for normally consolidated (NC) soils proposed by Mesri (1975). A Direct comparison of mean S_u values at corresponding depths in both regions is shown in (c), with black and blue error bars referring to Domain B and the Navile area data, respectively.

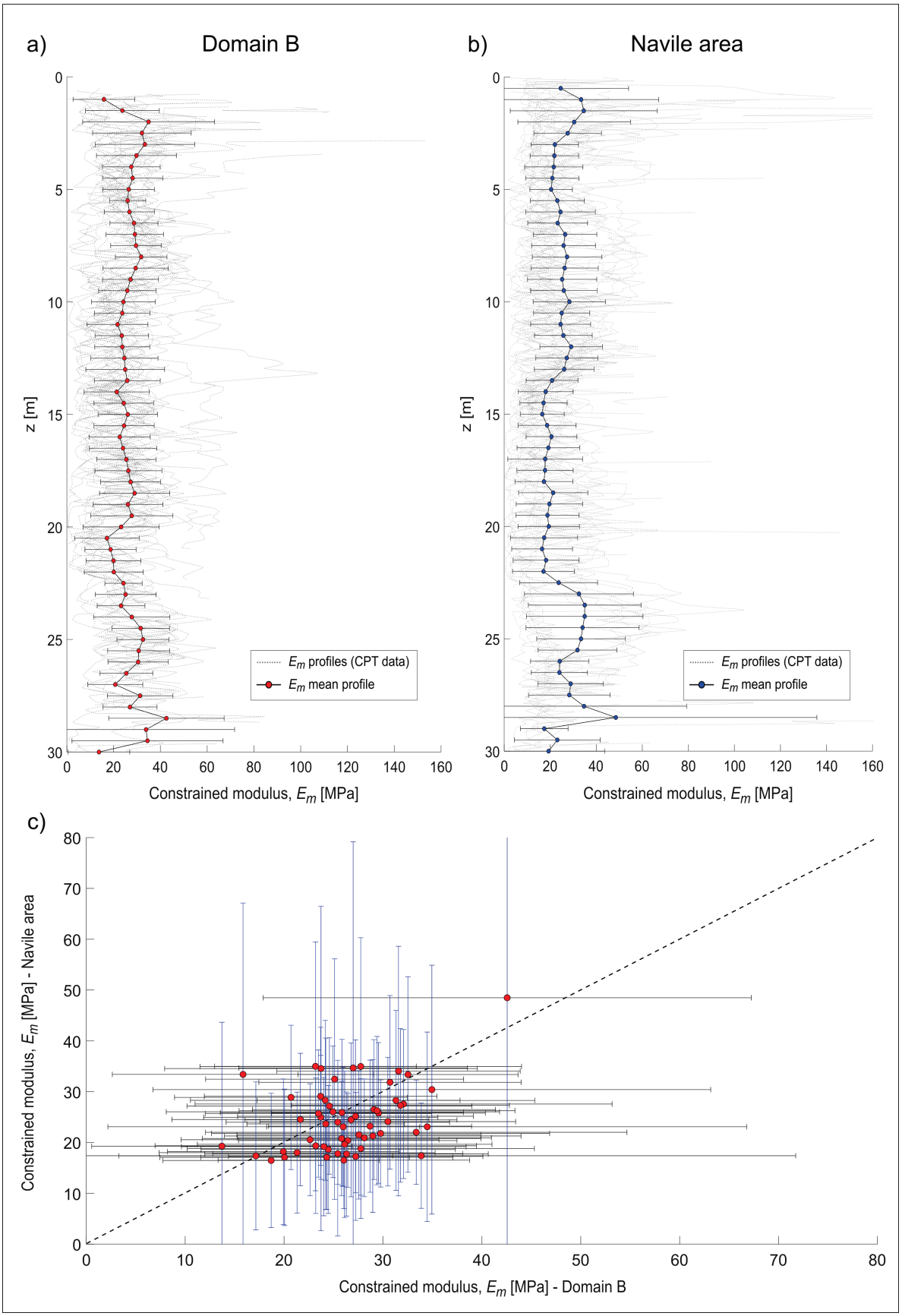

Fig. 4.12 Constrained modulus (E_m) profiles comparison in Domain B (a) and the Navile area (b) derived from CPT data employing the empirical equations proposed by Robertson (2009), described in section 4.2.2.1.3. A direct comparison of mean E_m values at corresponding depths in both regions is shown in (c), with black and blue error bars referring to Domain B and the Navile area data, respectively.

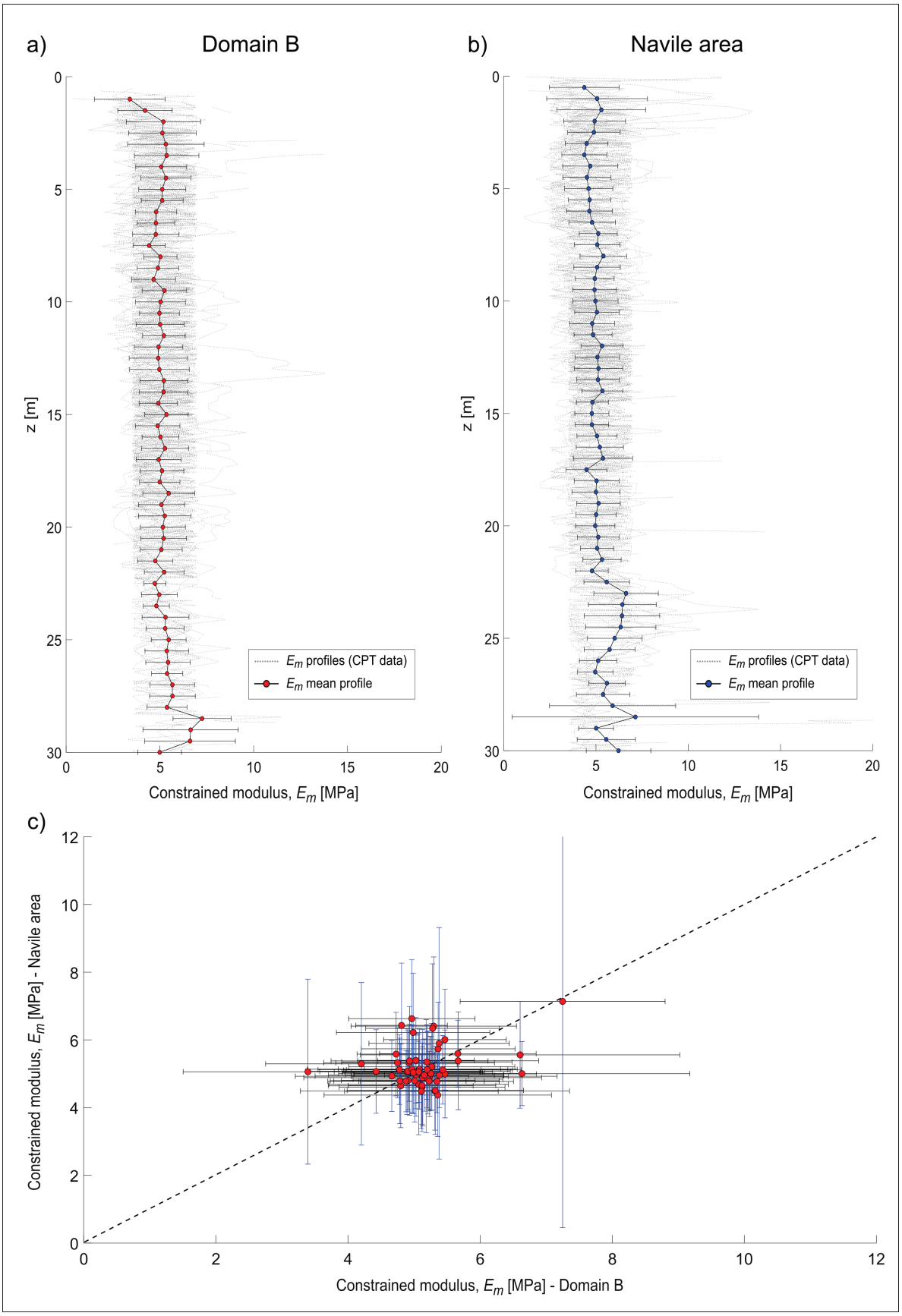

Fig. 4.13 Constrained modulus (E_m) profiles comparison in Domain B (a) and the Navile area (b) derived from CPT data employing the empirical equations proposed by Sanglerat (1972) and Mitchell & Gardner (1975), described in section 4.2.2.1.3. A direct comparison of mean E_m values at corresponding depths in both regions is shown in (c), with black and blue error bars referring to Domain B and the Navile area data, respectively.

4.3.3 One-dimensional subsidence calculation

The one-dimensional subsidence calculation has been performed as outlined in section 4.2.4. Cumulative ground displacements were computed at ten representative reference verticals within the study area (Fig.4.14), whose details, concerning the total sediment thickness, the percentage of fine-grained intervals, and the final groundwater level and pore pressure distribution, are summarised in Table 4.5. The considered reference verticals include the E_m calibration point for coarse-grained deposits (A0) and other four verticals located along the course of the Reno River (A1-A4), in Domain A. Two verticals are located in the historical city centre within Domain B (B1-B2), while the remaining three are positioned in Domain C, in progressively more distal and lateral portions of the Savena River alluvial fan (C1-C3).

Table 4.5 also reports the values of the mechanical parameters equally attributed to all the involved fine-grained and coarse-grained deposits, primarily concerning their unit weight (γ) and constrained modulus (E_m). Specifically, the range of input values considered for the constrained modulus (E_{m0}) for fine-grained deposits, which extends from 5 to 25 MPa, corresponds to the average values determined from CPT data employing the two alternative methods discussed in section 4.2.2.1.

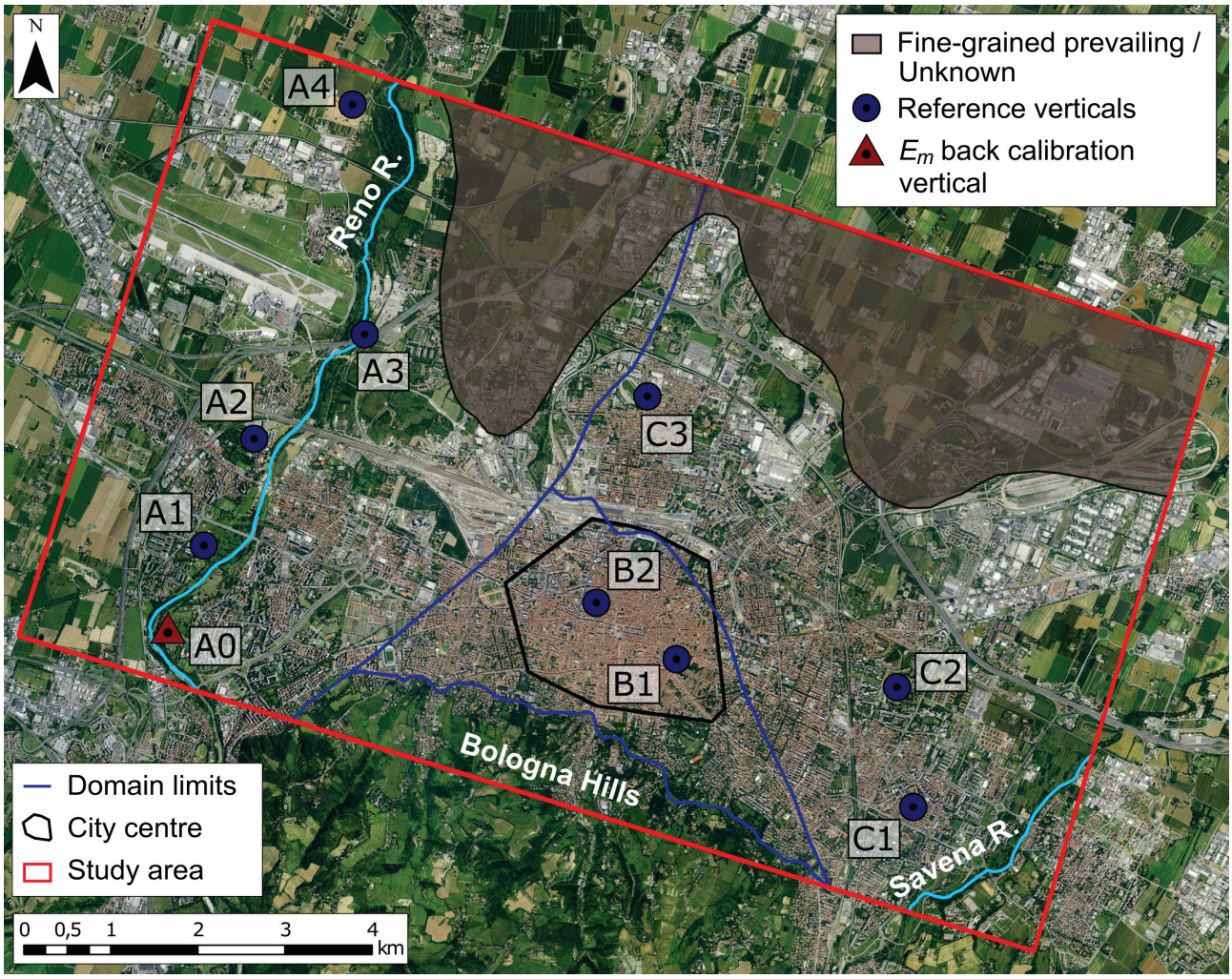

Fig. 4.14 Locations of the reference verticals considered for one-dimensional subsidence calculations (blue dots). The red triangle marks the calibration point of the constrained modulus (E_m) for coarse-grained soils. The greyed-out area represents the regions of the 3D geological model indicated as *unknown* or *fine-grained prevailing*, where correlations were not conducted due to limited stratigraphic data coverage (section 2.6.7).

ID	Total thickness [m]	Fine-grained thickness [m]	Fine-grained percentage [%]	Final groundwater depth [m b.g.l.]
A0	170	0	0	55
A1	235	0	0	55
A2	310	80	25.8	50
A3	355	135	38	50
A4	415	200	48.2	45
B1	190	190	100	(*)
B2	180	180	100	(*)
C1	100	0	0	50
C2	210	105	50	50
C3	310	275	88.7	35
γ (fine-grained) [kN/m³]	**γ (coarse-grained) [kN/m³]**	**E_{m0} (fine-grained) [MPa]**	**E_m (coarse-grained) [MPa]**	**β**
18	20	5 – 25	114	0 – 1

(*) Seepage flow, non-hydrostatic pore pressure distribution: $u_f = 8 \cdot z$.

Table 4.5 Overview of the reference verticals characteristics and soil mechanical parameters considered for one-dimensional subsidence calculations. The reference verticals are colour-coded by their respective geological domains (Domain A: red, Domain B: blue, Domain C: green).

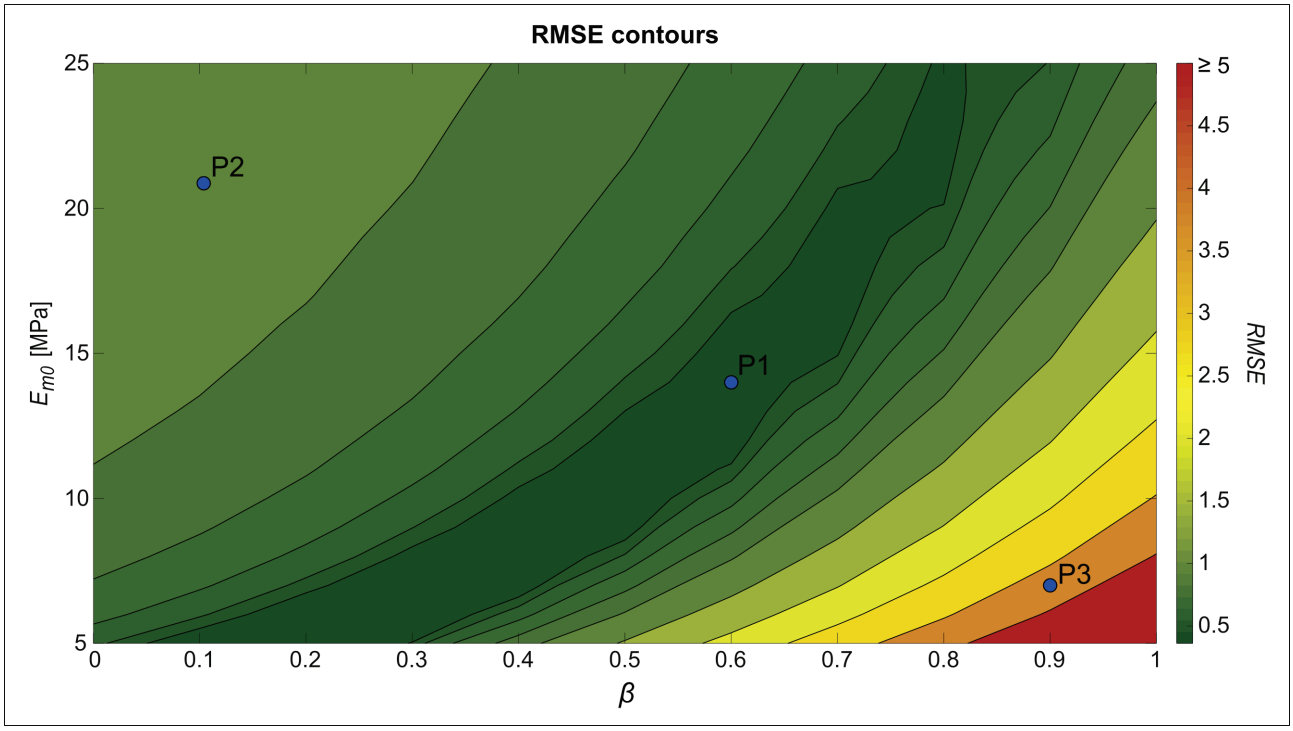

Fig. 4.15 Root mean squared error (RMSE) contours calculated between measured and computed subsidence values at the reference verticals over the considered range of β and input constrained modulus (E_{m0}) values for fine-grained soils. The blue dots mark three different scenarios (P1 – P3) illustrated in detail in Figures 4.16 – 4.18, respectively.

Figure 4.15 illustrates the root mean squared errors (RMSE) contours calculated by comparing the measured and computed subsidence along each reference vertical, for each combination of β and E_{m0}. The lowest RMSE values (RMSE $\leq$ 0.5), are visibly aligned in a narrow band that covers the entire spectrum of E_{m0}, mainly encompassing β values approximately ranging from 0.2 to 0.8. This area defines the specific combinations of β and E_{m0}, and consequently, the E_{m0} depth profiles that minimise the disparity between measured and computed subsidence, providing insight into the actual material behaviour. Moving away from this central band, the RMSE sharply rises towards the top-left and bottom-right corners of the chart. These regions are respectively characterised by decreasing β and increasing E_{m0}, and vice versa. Below are presented three computed subsidence scenarios based on the E_m depth profiles derived from the combination of input data, highlighted by the blue dots in Fig 4.15. These scenarios represent the three regions described earlier: P1, located in the central band of low RMSE values; and P2 and P3, situated in the top-left and bottom-right corners, respectively.

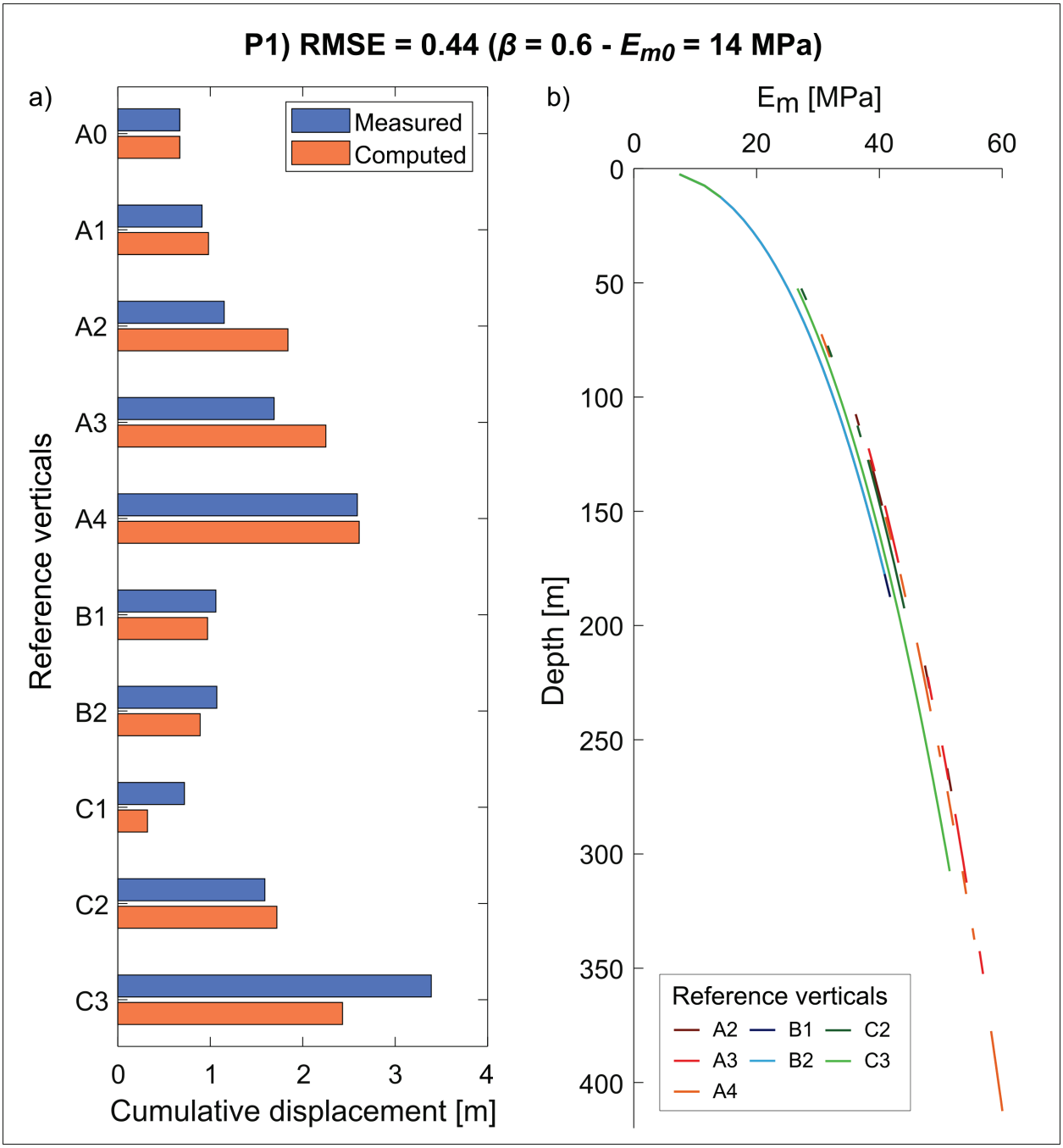

Fig. 4.16 Bar chart comparing the measured and computed cumulative displacements at reference verticals (a), based on the E_m depth profiles for fine-grained soils derived using the considered combination (P1) of β and E_{m0} (b).

The P1 point represents an illustrative combination of β and E_{m0} that results in a good correspondence between measured and computed subsidence (RMSE < 0.5), as displayed in Figure 4.16a. The bar chart presented highlights an overall good agreement in Domain A between calculated and measured values, particularly at reference verticals A1 and A4, constituted by amalgamated gravel deposits and alternating thick coarse-grained and fine-grained intervals, respectively. The cumulative subsidence computed in A1, however, is not influenced by the selected combination of β and E_{m0} but depends on the back-calibrated constrained modulus value for coarse-grained soils, determined at the nearby point A0. Conversely, at verticals A2 and A3 cumulative displacements are overestimated, with the most significant differences reaching approximately 70 cm at A2. In contrast, reference verticals in Domain B, consistently exhibit a strong correspondence between calculated and observed subsidence, with maximum differences on the order of 10 cm at B2. As regards Domain C, at reference vertical C1, which consists entirely of coarse-grained soils, ground displacement is underestimated, with a difference of approximately 40 cm. On the other hand, C2 displays a good alignment between observed and computed values. However, subsidence is visibly underestimated at C3, with discrepancies on the order of 90 cm.

The chart reported in Figure 4.16b provides a comparison of the E_m depth profiles determined at every reference vertical distinguished by the occurrence of fine-grained intervals, based on the considered β and E_{m0} input values. These curves reveal a relatively gradual and moderate non-linear increase of the constrained modulus with depth reaching maximum values of approximately 60 MPa at 415 m b.g.l. at the A4 vertical.

Similar remarks consistently apply also to the cumulative displacements computed for other combinations of β and E_{m0} that fall within the RMSE = 0.5 contour, displayed in Figure 4.19a. Detailed subsidence comparison bar charts and E_m depth profiles corresponding to these combinations are fully provided in section 4.5 (Fig. 4.20 – 25).

The P2 point in Figure 4.15 represents a different scenario characterised by higher RMSE values. As can be seen from the corresponding chart in Figure 4.17b, the combination of high E_{m0} and low β values yields constrained modulus trends marked by a rapid and pronounced increase with depth. These profiles exhibit peak values around 550 MPa, measured at 415 m b.g.l. at the A4 vertical, in sharp contrast to the 60 MPa observed in the optimal scenario (P1). These trends result in a consistent and significative underestimation of measured displacements at the reference verticals containing fine-grained soils, with differences frequently exceeding 1 m and a maximum discrepancy of approximately 2.8 m recorded at the C3 vertical (Fig. 4.17a).

Conversely, the point labelled as P3 in Figure 4.15, frames an opposing scenario, distinguished by high RMSE values as well. The corresponding chart in Figure 4.18b illustrates the corresponding constrained modulus profiles for each reference vertical obtained by considering high β and low E_{m0} input values. The resulting curves depict a subtle increase in E_m with depth, revealing maximum values of around 10 MPa at 415m b.g.l., measured at the reference vertical A4, compared to the 60 MPa obtained at the same depth when using optimal parameters sets as in the P1 scenario. Consequently, the computed subsidence at the same locations, excluding the verticals entirely constituted of gravel deposits, systematically and vastly overestimates the actual measured displacements by several meters, with peak differences of approximately 7 m at A4 and C3.

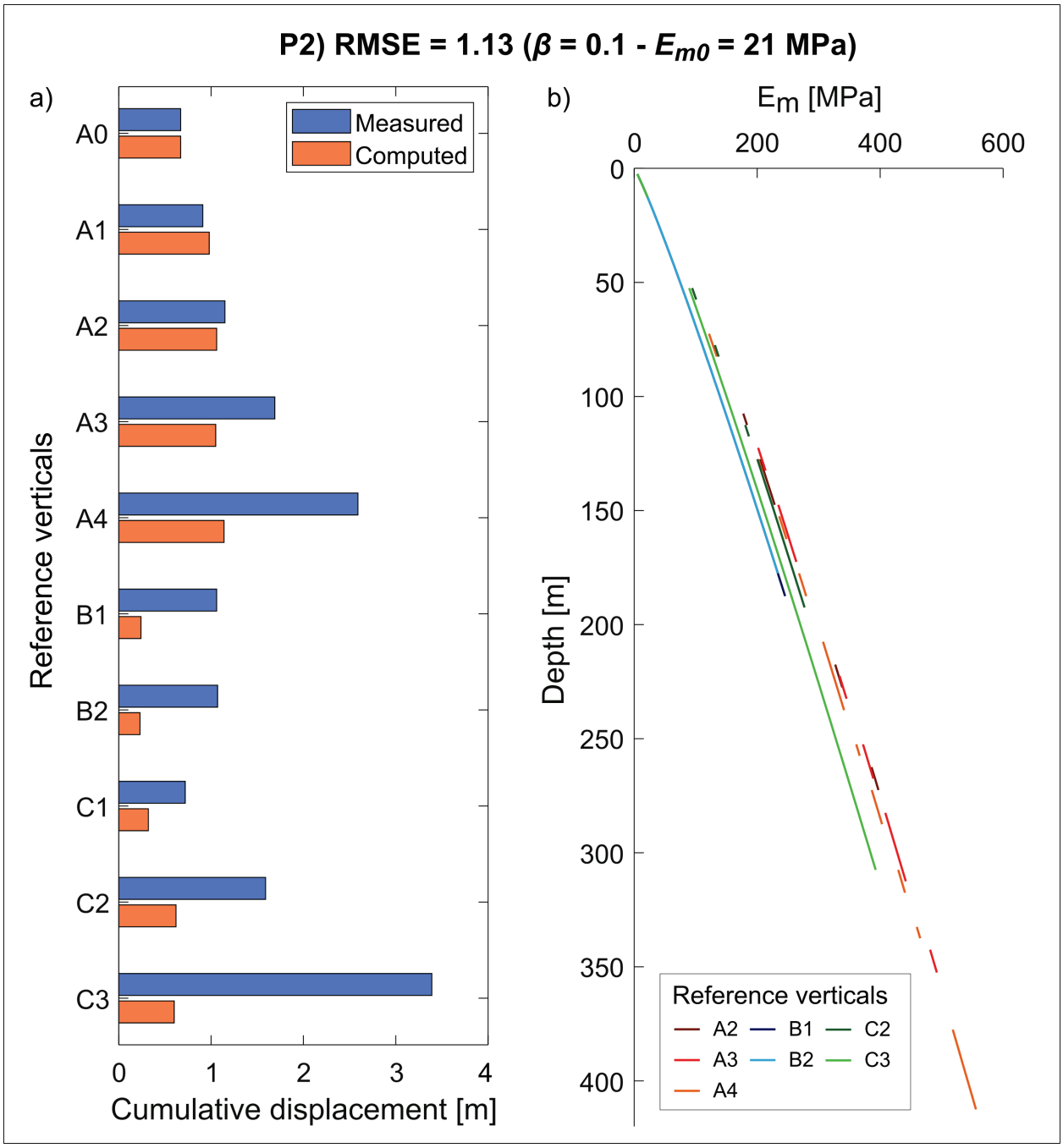

Fig. 4.17 Bar chart comparing the measured and computed cumulative displacements at reference verticals (a), based on the E_m depth profiles for fine-grained soils derived using the considered combination (P2) of β and E_{m0} (b).

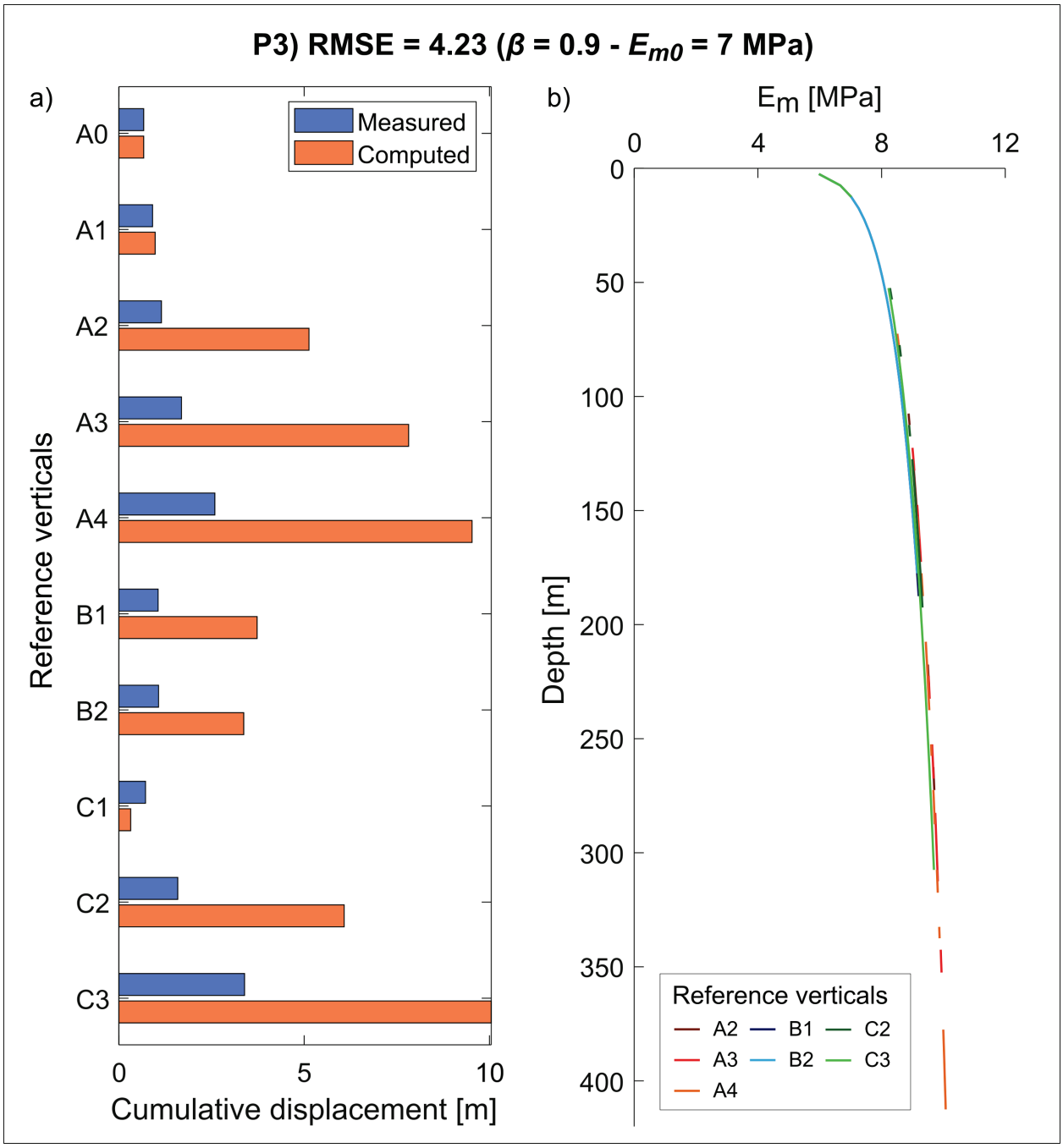

Fig. 4.18 Bar chart comparing the measured and computed cumulative displacements at reference verticals (a), based on the E_m depth profiles for fine-grained soils derived using the considered combination (P3) of β and E_{m0} (b).

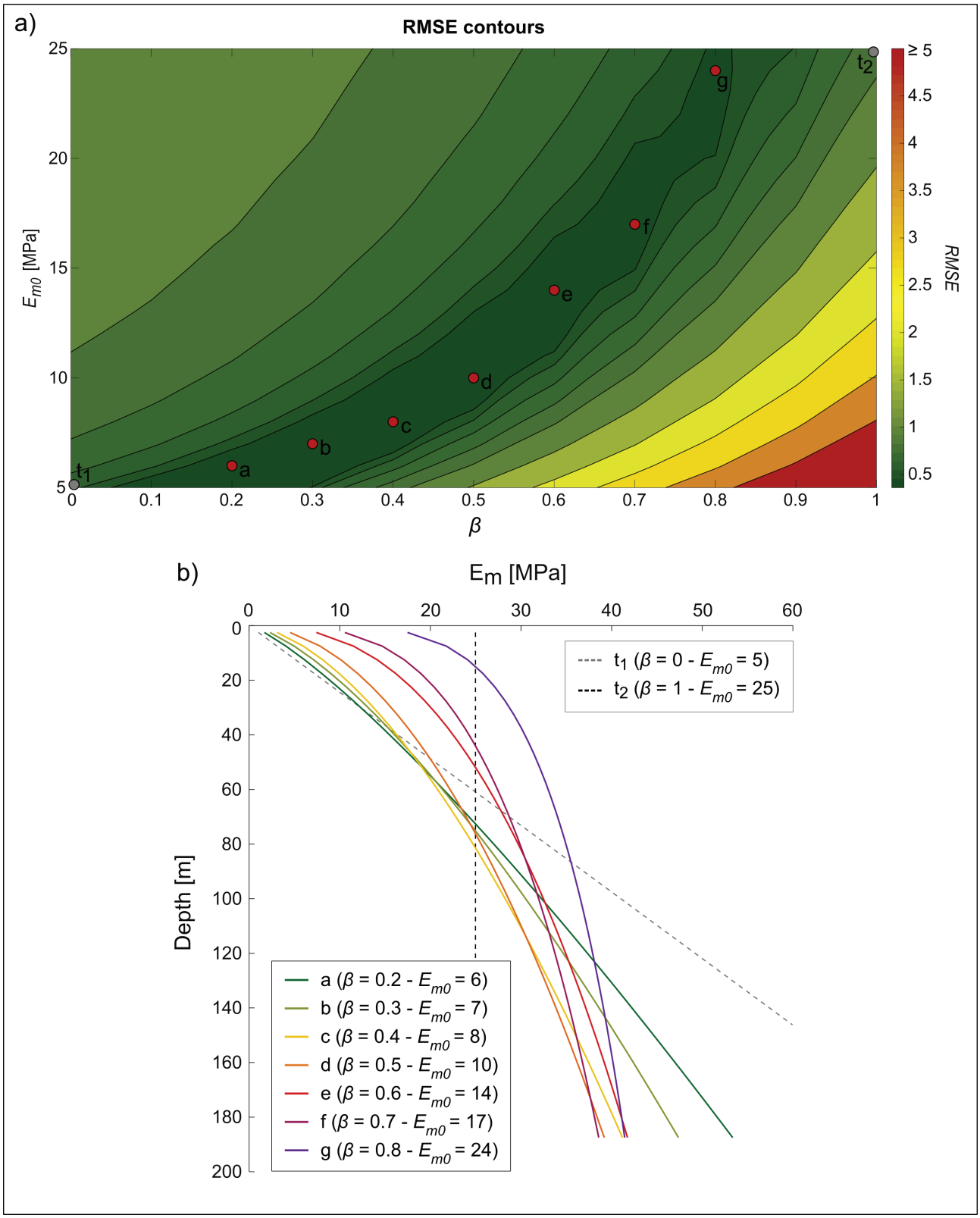

Fig. 4.19 Root mean squared error (RMSE) contours calculated between measured and computed subsidence values at the reference verticals over the considered range of β and input constrained modulus (E_{m0}) values for fine-grained soils (a). Red dots mark seven different optimal β and E_{m0} combinations falling within the RMSE = 0.5 contour, while grey dots represent the two closest theoretical combinations for NC (t_1) and OC (t_2) soils. Corresponding E_m depth profiles are displayed and compared in chart (b), considering the B1 reference vertical input stratigraphy (Table 4.5).

Figure 4.19 chart presents a comparison of various E_m depth profiles corresponding to the seven optimal combinations of β and E_{m0} that fall within the RMSE = 0.5 contour, highlighted in Figure 4.19a. These combinations, labelled from *a* to *g*, progressively consider higher β and E_{m0} values, ranging from 0.2 to 0.8 and between 6 and 24 MPa, respectively. The resulting E_m trends are depicted in Figure 14.9b for the B1 reference vertical input stratigraphy, schematised in Table 4.5. The obtained curves display more pronounced curvatures as β increases, coupled with a diminishing E_m increase with depth. Despite the wide spectrum of considered input E_{m0}, the derived constrained modulus profiles, evaluated at a 190 m b.g.l depth, exhibit overall similar values, ranging approximately from 39 to 53 MPa. Notably, curves corresponding to scenarios *c* to *g* tend to converge, yielding E_m values between 39 and 42 MPa at the same depth of 190 m. Furthermore, the derived E_m profiles were compared to two curves representing the nearest combinations, in terms of RMSE, that describe the theoretical trends of NC (t_1) and OC (t_2) soils. These trends correspond to the scenarios marked by the grey dots in Figure 4.19a: t_1 assumes an E_{m0} equal to 5 MPa, increasing linearly with depth (β = 0); t_2 represents the diametrically opposing case with E_{m0} of 25 MPa, which remains constant with depth (β = 1). This comparison reveals a systematic divergence between the optimal E_m profiles and the nearest theoretical trends for NC and OC soils. Specifically, the constrained modulus values obtained at a depth of 190 m are equal to 77 and 25 MPa, for the t_1 and *t2* curves, respectively, showing a significant difference from the optimal values range evaluated at the same depth.

4.4 Discussion and conclusive remarks

The analyses performed, aimed at calculating the one-dimensional cumulative ground displacement at specific reference verticals across the study area, revealed and enabled the analysis of some fundamental aspects of the ongoing subsidence in Bologna.

The distribution of the downhole percentage of fine-grained soils computed in each borehole considered for the construction of the 3D geological model, when compared with the long-term cumulative subsidence map, reveals notable differences in the neighbouring regions of Domain B and the Navile area. While the former consistently exhibits low subsidence values and a high percentage of fine-grained soils, the latter displays the strongest ground deformations and a significantly different fine-grained deposit proportion distribution, with consistently lower values. These discrepancies may primarily be attributed to three factors, including the mechanical properties and the thickness of the compressible soils and the final groundwater, and hence pore pressure distribution. The analysis of the mechanical properties of the fine-grained deposits in the same two areas highlighted a consistent correspondence between the derived shear strength and deformability characteristics, to the extent that they were treated as a uniform material in the analyses. Due to the inability to consider eventual differences in the mechanical properties below the available CPTs investigation depth, the final groundwater table distribution was then addressed. The scenario considered in the one-dimensional analyses, involves the occurrence of a seepage flow in Domain B towards the adjacent domains, exhibiting a downward component which results in a non-hydrostatic final pore pressure distribution beneath the city centre. This scenario, in which ground displacements in Domain B would result from a pore pressure decrease rather than an actual groundwater level drawdown, consistently yielded accurate correspondence between the calculated and measured subsidence. In addition to this scenario, two alternative final groundwater table conditions were evaluated in Domain B. Firstly, similarly to the points outside Domain B, the mean groundwater depth measured between 1995 and 2005 in the nearest deep wells (section 4.2.3) was assigned to the reference verticals within the city centre. In such a scenario, marked by a final groundwater depth of 5 m b.g.l. and a hydrostatic pore pressure distribution, a consistent and substantial underestimation of the measured subsidence was observed, with discrepancies reaching 0.5 m. Conversely, the other scenario assumes a final groundwater depth of 35 m b.g.l., equivalent to the value assigned at C3 reference vertical (Table 4.5), representative of the Navile area. This condition also allows an evaluation of whether the cumulative

subsidence variation between Domain B and the Navile area could be attributed to the differing thickness of compressible deposits, which in the Navile area is nearly 100 m greater. In this scenario, the assumption of a final groundwater table drawdown of 35 m and a hydrostatic pore pressure distribution leads to a systematic and considerable overestimation of the measured subsidence, with maximum discrepancies on the order of 1 m. This would indicate the final groundwater distribution as the predominant factor in the observed differences and the consideration of a non-hydrostatic pore pressure distribution resulting from the downward component of a seepage flow in Domain B, in alignment with field data, as the most reasonable scenario.

The analysis of different profiles of the constrained modulus (E_m) for fine-grained soils highlights that the optimal configurations, which provide the best correspondence between calculated and measured cumulative subsidence for the same final groundwater distribution, systematically exhibit a non-linear trend with depth. These optimal E_m profiles tend to converge towards similar values with increasing depth, consistently deviating from the theoretical trend anticipated for normally consolidated soils. This observation aligns with the analysis of the mechanical characteristics that, at least for the shallower portion investigated, indicates the presence of overconsolidated deposits. The optimal E_m profiles also diverge from the expected constant trend for overconsolidated soils, instead displaying a progressive increase with depth, suggesting a concurrent gradual decrease in void ratio (e).

In the perspective of future 3D numerical modelling or predictive analyses, some fundamental aspects require further investigation and consideration. Firstly, the final groundwater level and, consequently, pore pressure distribution, which emerges as a critical factor influencing the observed cumulative ground displacements, and hence, their modelling. Additionally, the present analyses underscore the need to consider deformations moduli exhibiting depth-dependent increases, and characterise the coarse-grained gravelly to sandy deposits, through specific in situ tests (i.e., plate load tests and geophysical surveys), as their deformation properties have been here solely estimated through a local back calibration approach.

4.5 Supplementary Material

This sections presents the bar charts comparing the computed and measured subsidence at the various reference verticals, as well as the corresponding E_m depth profiles for each optimal E_{m0} and β combination highlighted in Figure 4.19 in section 4.3.3, labelled from *a* to *g*. The charts for point *e* are reported in Figure 4.16, labelled as *P1*.

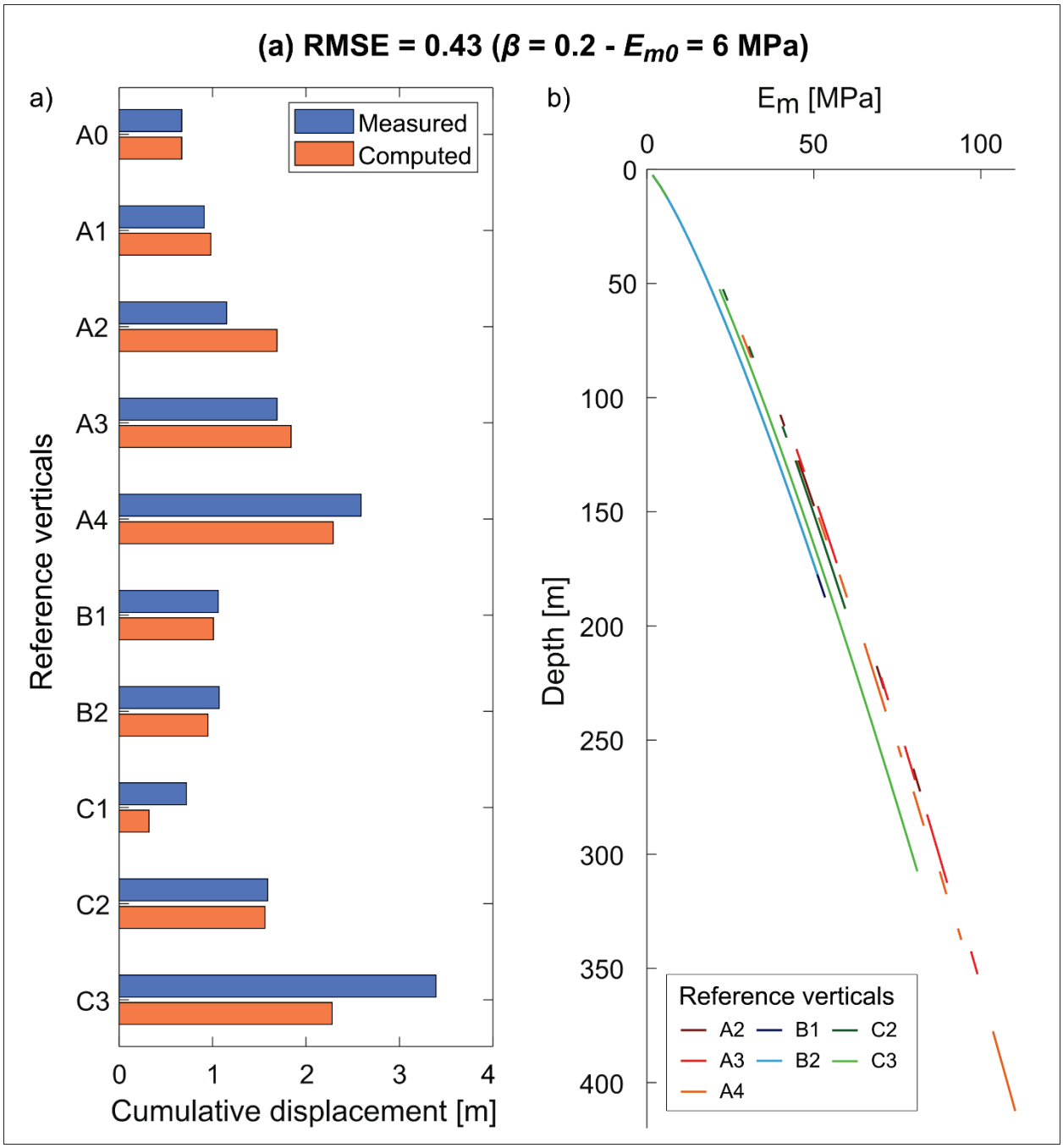

Fig. 4.20 Bar chart comparing the measured and computed cumulative displacements at reference verticals (a), based on the E_m depth profiles for fine-grained soils derived using the considered combination (Point *a* in Figure 4.19a) of β and E_{m0} (b).

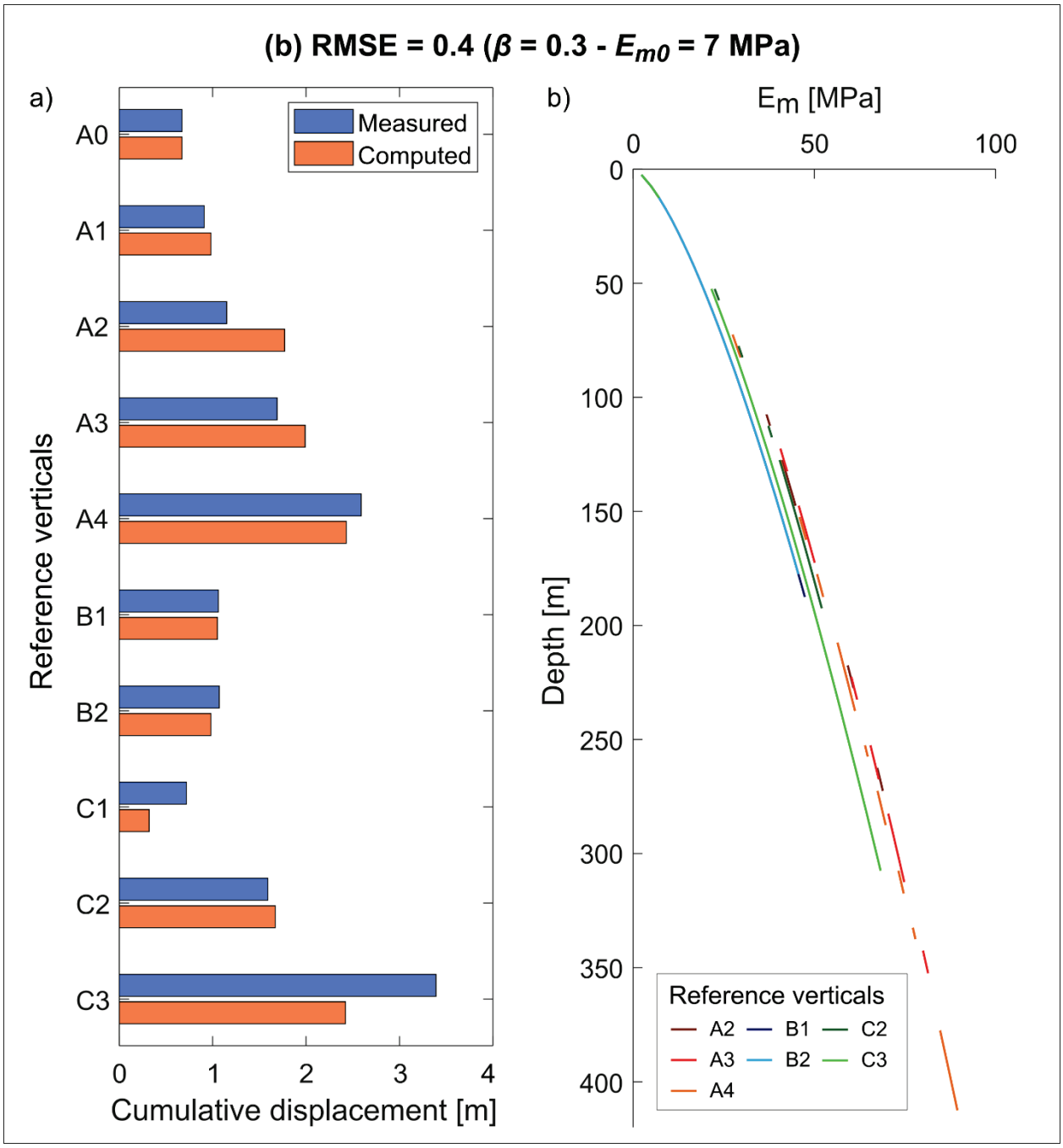

Fig. 4.21 Bar chart comparing the measured and computed cumulative displacements at reference verticals (a), based on the E_m depth profiles for fine-grained soils derived using the considered combination (Point *b* in Figure 4.19a) of β and E_{m0} (b).

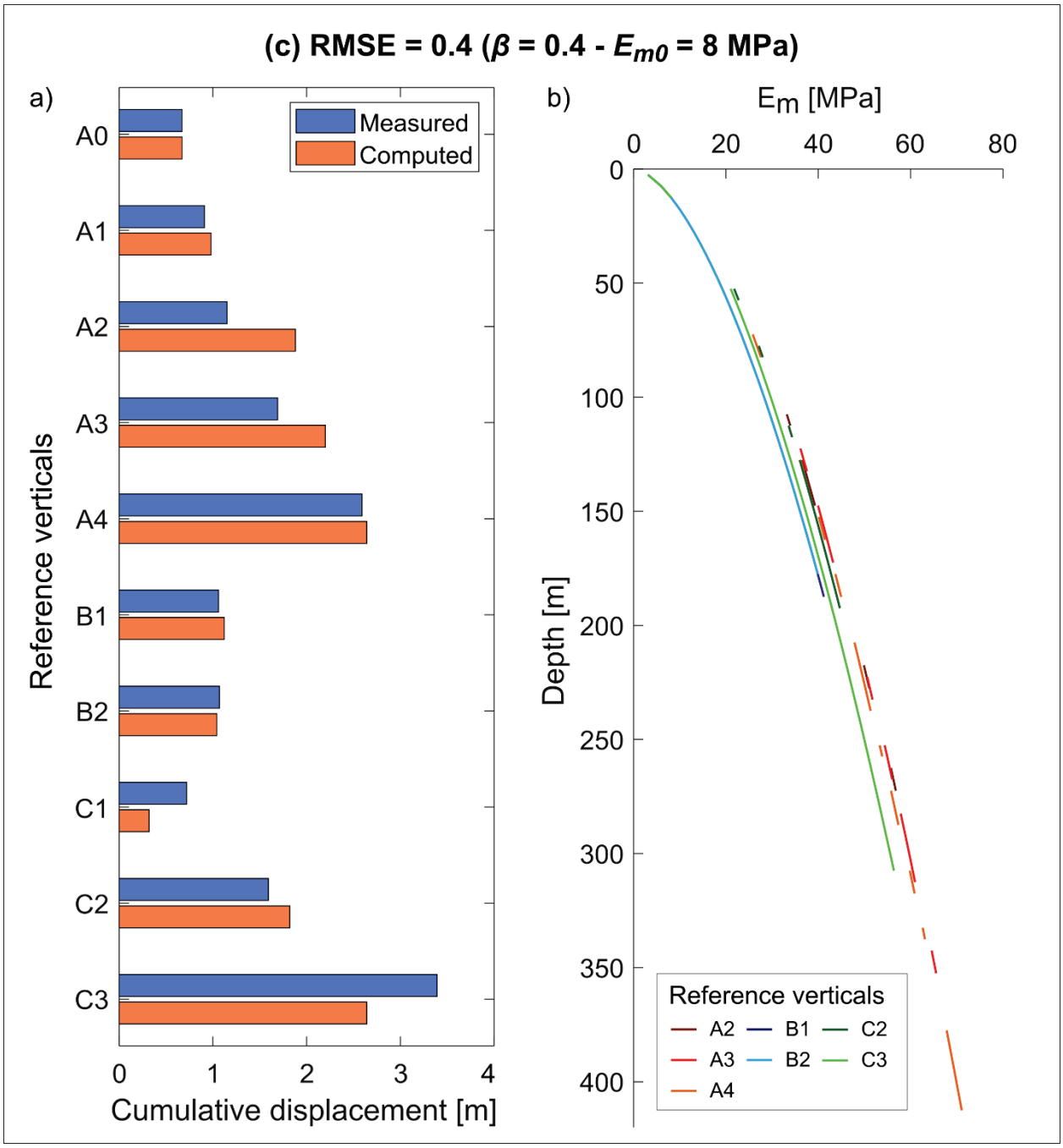

Fig. 4.22 Bar chart comparing the measured and computed cumulative displacements at reference verticals (a), based on the E_m depth profiles for fine-grained soils derived using the considered combination (Point *c* in Figure 4.19a) of β and E_{m0} (b).

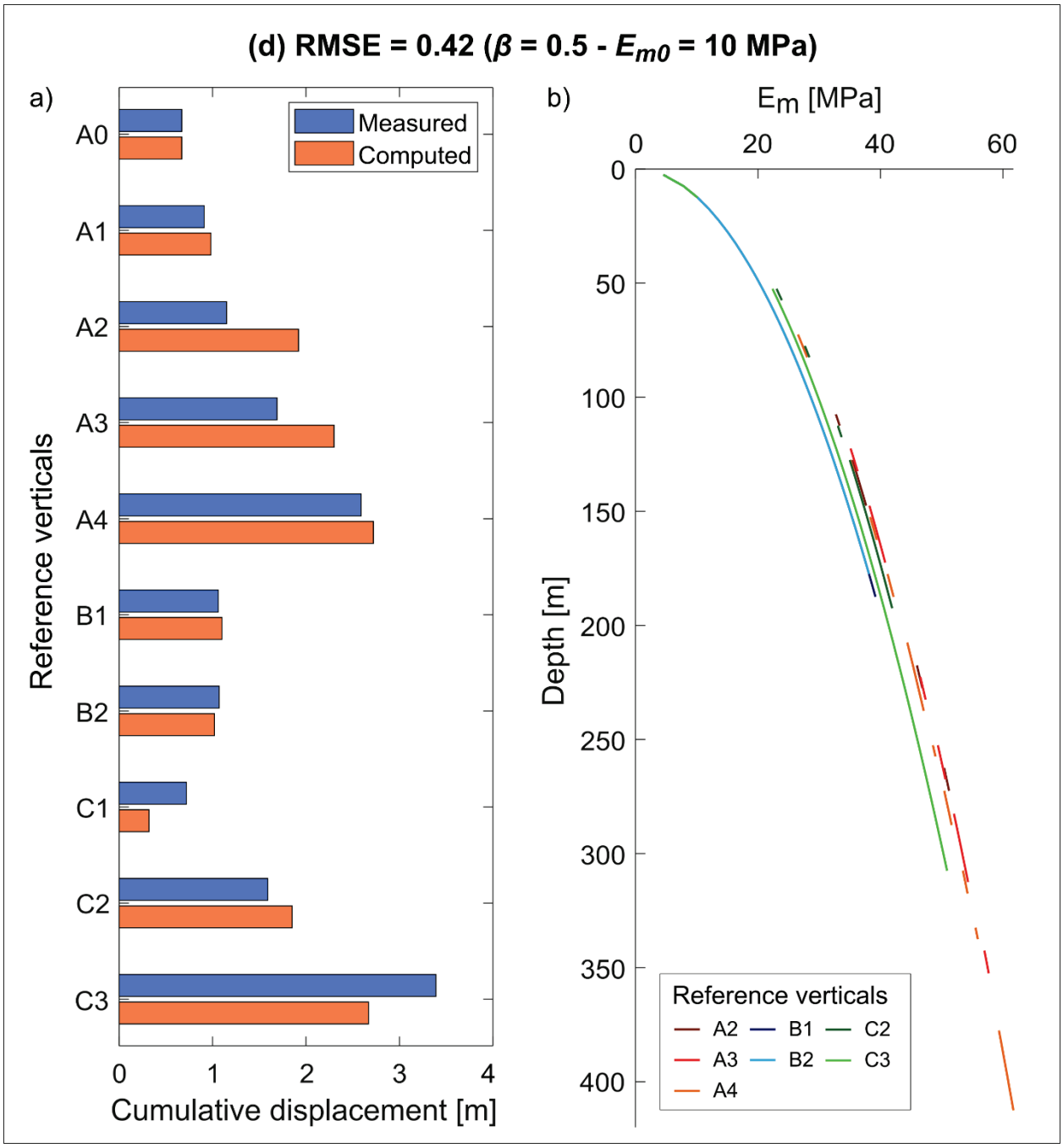

Fig. 4.23 Bar chart comparing the measured and computed cumulative displacements at reference verticals (a), based on the E_m depth profiles for fine-grained soils derived using the considered combination (Point *d* in Figure 4.19a) of β and E_{m0} (b).

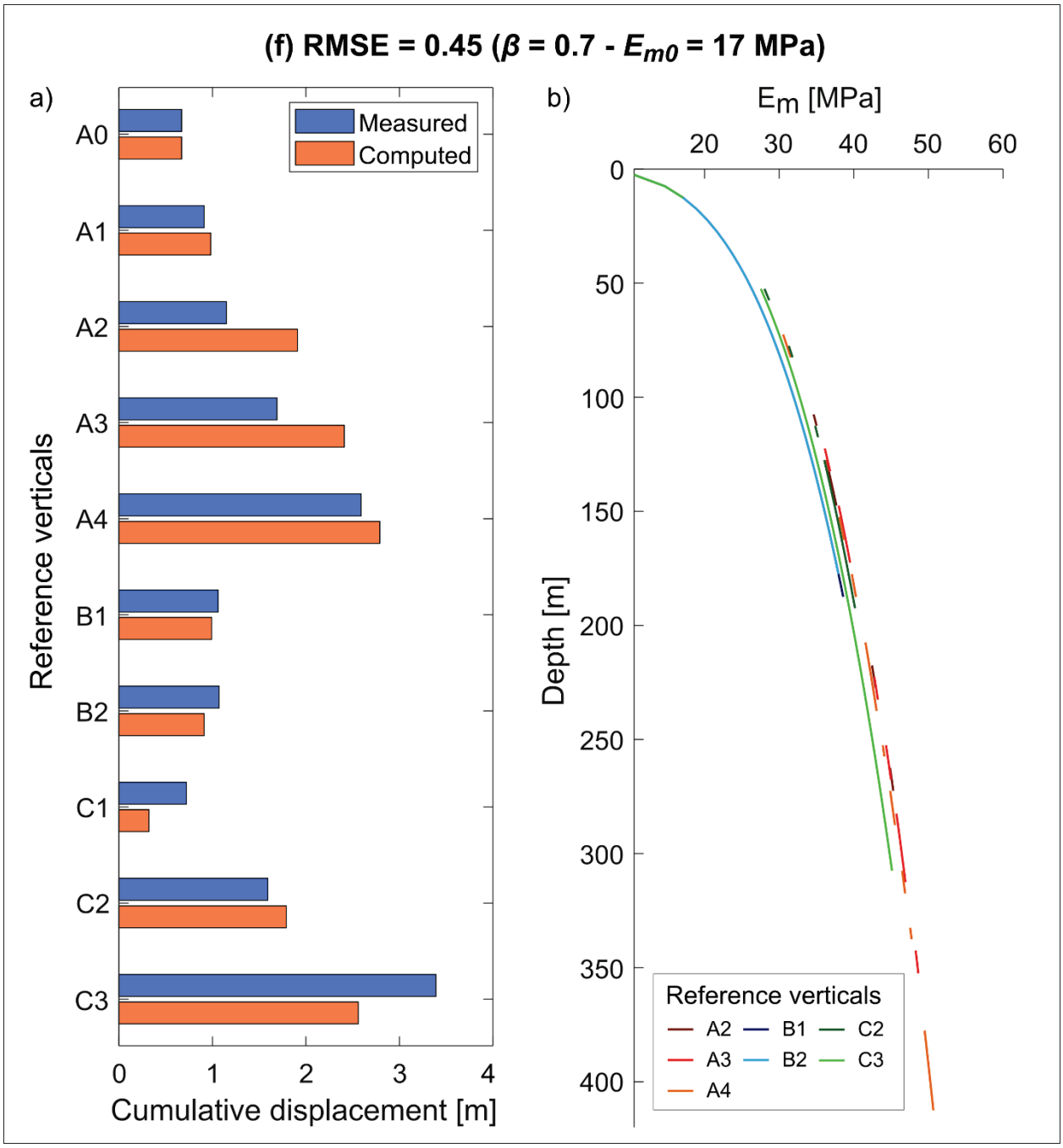

Fig. 4.24 Bar chart comparing the measured and computed cumulative displacements at reference verticals (a), based on the E_m depth profiles for fine-grained soils derived using the considered combination (Point *f* in Figure 4.19a) of β and E_{m0} (b).

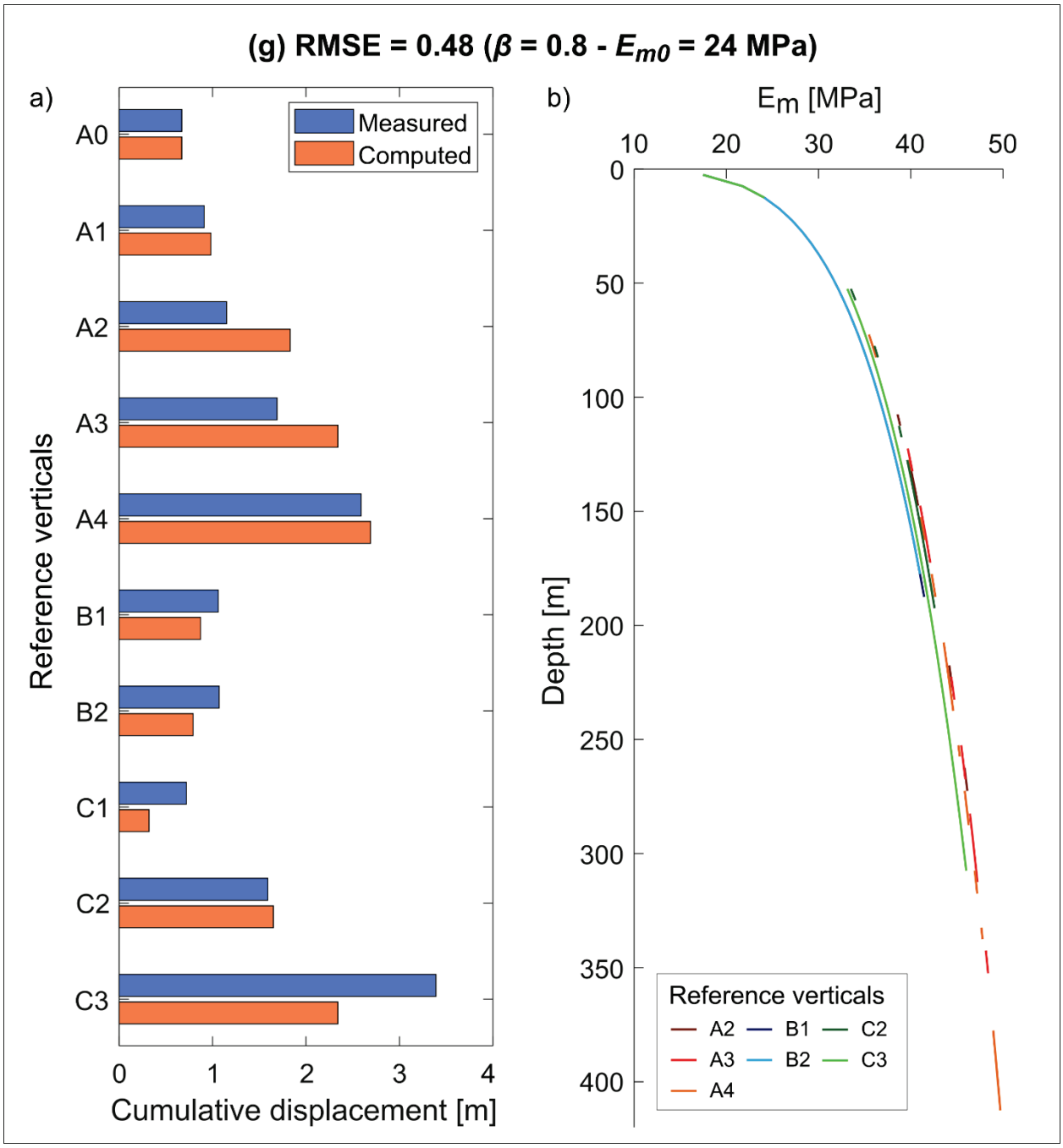

Fig. 4.25 Bar chart comparing the measured and computed cumulative displacements at reference verticals (a), based on the E_m depth profiles for fine-grained soils derived using the considered combination (Point *g* in Figure 4.19a) of β and E_{m0} (b).

4.6 References

Cestari F, 1990. Prove geotecniche in sito, Ed. Geo-Graph s.n.c. Segrate, Milano.

Craig RF, 1974. Craig's Soil Mechanics (7th edition), CRC Press, London. https://doi.org/10.4324/9780203494103.

Di Buò B, 2020. Evaluation of the Preconsolidation Stress and Deformation Characteristics of Finnish Clays based on Piezocone Testing, [Doctoral dissertation, Tampere University], ISBN: 978-952-03-1468-2. http://urn.fi/URN:ISBN:978-952-03-1468-2.

Janbu N, 1967. Settlement calculations based on the tangent modulus concept, Soil Mechanics and Foundation Engineering, University of Trondheim, Norwegian Institute of Technology, pp. 57.

Kulhawy FH, Mayne PW, 1990. Estimating Soil Properties for Foundation Design, EPRI Report EL-6800, Electric Power Research Institute, Palo Alto, pp. 306.

Lancellotta R, 1983. Analisi di Affidabilità in Ingegneria Geotecnica, Atti Istituto Scienza Costruzioni, 625, Politecnico di Torino.

Lancellotta R, 1987. Geotecnica, Zanichelli, Bologna, p.1-531, ISBN 88-08-04362-2.

Lunne T, Robertson PK, Powell JJM, 1997. Cone penetration testing in geotechnical practice, Blackie Academic, EF Spon/Taylor & Francis Publ., New York, 1997, pp. 312.

Mayne PW, 2014. Interpretation of geotechnical parameters from seismic piezocone tests. Proceedings, 3rd International Symposium on Cone Penetration Testing (CPT'14, Las Vegas), ISSMGE Technical Committee TC 102, Edited by P.K. Robertson and K.I. Cabal, c 47-73.

Mesri G, 1975. New design procedure for stability of soft clays. Discussion, J. of the Geotech. Eng. Div., ASCE, 101(4), 409-412.

Mitchell, J.K. and Gardner; W.S., 1975. "In Situ Measurement of Volume Change Characteristics," State-of-the-Art Report, Proceedings of the Conference on In-Situ Measurement of Soil Properties, Specialty Conf. of the Geotechnical Div., North Carolina State University, Raleigh, Vol. II, 279-345.

Robertson PK, 1990. Soil classification using the cone penetration test, Canadian Geotechnical Journal 27(1), 151-158.

Robertson PK, 2009. Interpretation of cone penetration tests – a unified approach. Canadian Geotechnical Journal 49(11), 1337-1355.

Robertson PK, 2010. Soil Behaviour Type from the CPT: An Update, 2nd International Symposium on Cone Penetration Testing, Huntington Beach, Vol. 2, 575-583.

Robertson PK, Campanella RG, 1983. Interpretation of cone penetration tests – Part I (sand). Canadian Geotechnical Journal, 20(4), 718-733.

Robertson PK, Campanella RG, Gillespie D, Greig J, 1986. Use of Piezometer Cone data. In-Situ'86 Use of In-situ testing in Geotechnical Engineering, GSP 6, ASCE, Reston, VA, Specialty Publication, SM 92, pp 1263-1280.

Robertson PK, Cabal KL, 2015. Guide to Cone Penetration Testing for Geotechnical Engineering, Gregg drilling, 6th edition.

Sanglerat G, 1972. The penetration and soil exploration, Development in geotechnical engineering, Elsevier Scientific Publishing, New York, 52-80.

Schmertmann JH, 1978. Guidelines for Cone Penetration Test, Performance and Design, Report No. FHWA-TS-78-209, U.S. Department of Transportation, Washington, D.C., pp. 145.

Terzaghi K, Peck RB, 1967. Soil mechanics in engineering practice, John Wiley, New York, NY, USA, p. 729.

Chapter 5 – General conclusions

This PhD research focussed on the comprehensive analysis of the severe subsidence process that has been affecting the city of Bologna (Italy) since the early 1960s, due to excessive groundwater withdrawals. This ground deformation process reached its peak at the turn of the 1970s and 1980s, with subsidence rates exceeding 10 cm/year, resulting in manifest damage to structures and infrastructures. Subsequently, the application of regional policies to rationalise groundwater resource extractions led to a gradual and substantial reduction in these displacement rates over the following decades. Nevertheless, recent monitoring data indicate a resurgence of ground deformation with visibly higher rates, attributable to increased pumping to compensate for reduced precipitations, exposing the criticality of the potential impact of climate change on the ongoing subsidence.

The analyses performed during the course of this PhD project allowed the investigation and yielded answers to three main research questions.

Question 1 – *What is the 3D depositional architecture of the subsurface in the urban area of Bologna and can it be reconstructed through a stratigraphic approach based on lithofacies?*

In order to answer this question and establish a robust foundation for subsequent analyses of the ongoing subsidence process, a comprehensive multidisciplinary approach was defined and adopted. This articulated approach encompassed topographical and morphological analyses, the examination of urban hydrography, and the execution of HVSR (Horizontal to Vertical Spectral Ratio) geophysical surveys, supporting and complementing the primary stratigraphic analyses, based on the lithofacies criterion.
The convergence and the integration of surface and subsurface data analyses within this multidisciplinary framework, enabled the definition of three geological domains within the study area, that despite the common alluvial origin consistently exhibit distinct morphological features and depositional stacking patterns. The west portion of the city (Domain A) lies over massive, heavily stacked thick gravel deposits that gradually filled the subsiding alluvial valley of the Reno River, expressed on the surface by an overall flat morphology. Conversely, the central region (Domain B), encompassing the historical city centre, consists of an interfluve area, topographically elevated with respect to its surroundings. This region is dominated by extensive and homogenous sequences of fine-grained stiff soils that remained essentially unaffected by the main rivers' dynamics. Lastly, the eastern sector (Domain C) coincides with the Savena River alluvial fan, displaying a gentle convex-up surface morphology. In the subsurface, this area is distinguished by gravel-dominated proximal deposits that progressively grade to fine-grained prevailing ones towards more distal and lateral regions.
These three distinct depositional domains guided the development of the 3D geological model of the Bologna urban area's subsurface. The overall bounding volume was partitioned into three independent sub-volumes, each representing a different geological domain. The internal characterisation of these sub-volumes involved transposing the 2D stratigraphic correlations, performed on a dense grid of vertical cross-sections, into the three dimensions, gradually reconstructing the 3D geometry and extent of the main sedimentary bodies. In such a complex alluvial setting, no automatic algorithm proved to be suitable for reliably interpolating stratigraphic data.
The lithofacies criterion emerged as an effective approach for reconstructing the urban subsurface in Bologna where the main complexities arise from the extent of urbanisation, limiting the access to potential outcrops, and the intricate alluvial context where conventional concepts of superposition and lateral continuity of strata are frequently challenged. Stratigraphic correlations guided by lithofacies on diversely and appropriately oriented cross-sections provided a reliable representation of the sediment bodies and their geometry, overcoming the limitations of lithology-based correlation criteria commonly employed in engineering geology.

The analyses also revealed that the main difficulty of this approach is represented by the identification of depositional facies relying uniquely on the available log descriptions, considering the thickness, textural characteristics and vertical downhole position of the deposits. Lithological descriptions can in fact be subjective, meagre, and occasionally poorly informative, making the reinterpretation of borehole data in terms of lithofacies a time-consuming process, which requires specific sedimentological expertise.

Question 2 – *What is the long-term spatiotemporal evolution of the subsidence process in Bologna, and how is it influenced by groundwater pumping trends and the local geological setting?*

To address this question, and achieve a comprehensive understanding of the ongoing subsidence process in Bologna, a methodology was developed to integrate ground-based and remotely sensed ground displacement monitoring data. The implemented processing chain effectively enables the generation of cumulative subsidence time series and maps, describing the long-term temporal evolution and overall spatial distribution of the ground deformation process, respectively.
The reconstructed cumulative ground displacement time series and the corresponding subsidence rate curves display a significant correlation with the multi-year evolution trends in groundwater level and pumping recorded at the main pumping stations within the study area. The qualitative comparison of these sets of curves, spanning from 1970 to 2020, consistently indicates four distinct evolution phases in both subsidence and pumping processes. These successive stages include an initial peak phase (1970 - 1982), followed by a gradual reduction between 1983 and 2009, a subsequent stabilisation from 2010 to 2016, and, lastly, a notable resurgence observed across a substantial portion of the study area (2017 – 2020).
Detailed displacement and displacement rate time series were concurrently generated with the long-term ones, to investigate the recent subsidence evolution with higher temporal resolution. These curves highlight a rapid and consistent reaction of the subsidence process to pumping and, consequently, groundwater level short-term fluctuations, reaching the scale of seasonal oscillations. The observation of this pronounced alignment across all the observation points within the study area suggests a generally high equivalent permeability of the aquifer system in question.
Moreover, the cumulative ground displacement map reconstructed for the period ranging from 1900 to 2020 aligns visibly with the primary stratigraphic features and variations in depositional stacking patterns summarised in the developed 3D geological model of the study area and its partition into distinct domains. This agreement is also discernible in the long-term time series which display consistent differences in cumulative displacements or subsidence rates reconstructed at the various observation points across the study area. These correspondences underscore the influence of the peculiar geological setting of each depositional domain on the reconstructed long-term ground deformation field. Specifically, the proximal portions of Domains A and C, corresponding to the amalgamated gravel deposits of the Reno River and the Savena alluvial fan, respectively, exhibit rather low subsidence values that progressively increase downstream towards more distal and lateral regions. In contrast, Domain B, distinguished by extensive and continuous sequences of stiff overconsolidated clayey deposits, displays low cumulative displacement values that sharply increase approaching the boundaries with the two adjacent domains.
Lastly, the reconstruction of the long-term ground deformation field enabled the generation of a subsidence hazard map, where the computed subsidence gradient and the theoretical angular distortion thresholds for generic framed buildings and structures are compared. The resulting map identifies a high-gradient region that corresponds to the area of the city centre where historical buildings have predominantly suffered manifest damage.

Question 3 – *How can the observed relationships between geological setting and subsidence evolution be interpreted from a geotechnical perspective, considering the mechanical characteristics of the deposits and piezometric data?*

To answer this thematic question, a series of one-dimensional subsidence analyses were performed along fixed reference verticals within the study area, representative of the distinct geological domains and the primary depositional stacking pattern variations, summarised in the 3D model. These 1D calculations involved the integration of various datasets resulting from the exploration of the previous research questions, encompassing stratigraphic and piezometric data, as well as the reconstructed long-term cumulative subsidence. Additionally, the analysis of the available CPT surveys provided the mechanical parameters for shallower fine-grained soils up to a maximum depth of approximately 30 m. As subsidence calculation requires the knowledge of the entire depth profiles of the mechanical parameters, focusing on the constrained modulus (E_m), theoretical trends were considered after Janbu (1967). Given a fixed input stratigraphy and final groundwater level distribution, various 1D subsidence calculations were performed considering different E_m depth profiles. These analyses enabled the assessment of which configurations yielded better correspondences in terms of root mean squared error (RMSE) between measured and computed displacements across the reference verticals, providing insight into the actual material behaviour. The optimal E_m profiles obtained exhibit a systematic deviation from theoretical trends of normally consolidated (NC) soils, aligning with CPT data which indicate the occurrence of overconsolidated (OC) deposits, at least within the shallower portion investigated. Furthermore, these optimal trends also diverge from the constant profiles expected for OC soils, indicating a gradual E_m increase and void ratio (e) reduction with depth.
The analyses conducted frame the groundwater level and, consequently, the pore pressure distribution as critical parameters. Specifically, considering a non-hydrostatic pore pressure distribution beneath the city centre, resulting from the downward component of a seepage flow occurring in Domain B, emerges as the most reasonable and representative scenario, aligning with field data from piezometers and CPTu surveys.
For the purposes of any future 3D numerical modelling or predictive analyses, in addition to accurately defining the final groundwater level distribution and representative E_m depth profiles for fine-grained soils, it is crucial to comprehensively characterise coarse-grained deposits, whose E_m value, in this study, was solely estimated through a local back calibration procedure.

A methodological approach such as the one employed and detailed in this work allows the reconstruction of the various aspects characterising subsidence in urban areas and enables the assessment of their relationships and interactions, even within complex stratigraphic and hydrogeological environments.

5.1 References

Janbu N, 1967. Settlement calculations based on the tangent modulus concept, Soil Mechanics and Foundation Engineering, University of Trondheim, Norwegian Institute of Technology, pp. 57.

General references

Abidin HZ, Andreas H, Gumilar I, Sidiq T, Gamal M, 2015. Environmental Impacts of Land Subsidence in Urban Areas of Indonesia, in: Proceedings of the FIG Working Week 2015, TS 3– Positioning and Measurement, Sofia, Bulgaria, Paper no. 7568, 17–21 May 2015.

Akkaya İ, & Özvan A, 2019. Site characterization in the Van settlement (Eastern Turkey) using surface waves and HVSR microtremor methods. J. Appl. Geophys., 160, 157-170.

Alessi R, 1985. La subsidenza nel centro storico della città di Bologna. Il grado di dissesto dei fabbricati nella zona di via Zamboni. Inarcos, 456, 16-24, Bologna.

Aljammaz A, Sultan M, Izadi M, Abotalib AZ, Elhebiry MS, Emil MK, Abdelmohsen K, Saleh M, Becker R, 2021. Land Subsidence Induced by Rapid Urbanization in Arid Environments: A Remote Sensing-Based Investigation. Remote Sensing, 13, 1109. https:// doi.org/10.3390/rs13061109.

Allen JRL, 1963. The classification of cross-stratified units with notes on their origin. Sedimentology, 2, 93-114.

Amorosi A, Farina M, Severi P, Preti D, Caporale L, Di Dio G, 1996. Genetically related alluvial deposits across active fault zones: an example of alluvial fan-terrace correlation from the upper Quaternary of the southern Po Basin, Italy, Sedimentary Geology, 102, 275-295. ISSN 0037-0738. https://doi.org/10.1016/0037-0738(95)00074-7.

Amorosi A, Caporale L, Farina M, Preti D, Severi P, 1997. Late Quaternary sedimentation at the southern margin of the Po Basin (Northern Italy). Geologia Insubrica 2, 149-159.

Amorosi A, Pavesi M, Ricci Lucchi M, Sarti G, Piccin A, 2008. Climatic signature of cyclic fluvial architecture from the Quaternary of the central Po Plain, Italy. Sediment. Geol. 209, 58–68.

Amorosi A, Bruno L, Rossi V, Severi P, Hajdas I, 2014. Paleosol architecture of a late Quaternary basin-margin sequence and its implications for high-resolution, nonmarine sequence stratigraphy. Glob. Planet. Chang. 112, 12-25.

Amorosi A, Bruno L, Cleveland DM, Morelli A, Hong W, 2017. Paleosols and associated channel-belt sand bodies from a continuously subsiding late Quaternary system (Po Basin, Italy): new insights into continental sequence stratigraphy. Geol. Soc. Am. Bull, 129, 449–463.

Argnani A, Barbacini G, Bernini M, Camurri F, Ghielmi M, Papani P, Rizzini F, Rogledi S, Torelli L, 2003. Gravity tectonics driven by Quaternary uplift in the Northern Apennines: insights from the La Spezia-Reggio Emilia geo-transect. In Uplift and Erosion; Driving Processes and Resulting Landforms; Dynamic Relations Between Crustal and Surficial Processes, Bartolini C, Piccini L, Catto NR (eds). Quatern. Int., 13–26.

ARPAE (Agenzia Prevenzione Ambientale Energia Emilia-Romagna), 2008. Analisi preliminare degli effetti dei prelievi di acque sotterranee sulla evoluzione recente del fenomeno della subsidenza in Emilia-Romagna, Bologna, 2008.

ARPAE (Agenzia Prevenzione Ambientale Energia Emilia-Romagna), 2012. Rilievo della subsidenza nella pianura emiliano-romagnola - seconda fase, Bologna, 2018.

ARPAE (Agenzia Prevenzione Ambientale Energia Emilia-Romagna), 2018. Rilievo della subsidenza nella pianura emiliano-romagnola - seconda fase, Bologna, 2018.

Attard G, Winiarski T, Rossier Y, Eisenlohr L, 2016. Revue: Impact des structures du sous-sol sur les écoulements des eaux souterraines en milieu urbain. Hydrogeology Journal 24, 5–19. doi:10.1007/s10040-015-1317-3.

Bagheri-Gavkosh M, Hosseini SM, Ataie-Ashtiani B, Sohani Y, Ebrahimian H, Morovat F, Ashrafi S, 2021. Land subsidence: A global challenge. Science of the Total Environment 778. doi:10.1016/j.scitotenv.2021.146193.

Barbarella M, Pieri L, Russo P, 1990. Studio dell'abbassamento del suolo nel territorio bolognese mediante livellazioni ripetute: Analisi dei movimenti e considerazioni statistiche. Inarcos, 506, 1-19.

Barends FBJ, Brouwer FJJ, Schroder FH, 1995. Land subsidence: natural causes; measuring techniques; the Groningen Gasfields. IAHS Publ 234, IAHS, Wallingford, UK, pp. 409.

Battaglia M, Pagli C, Meuti S, 2021. The 2008–2010 Subsidence of Dallol Volcano on the Spreading Erta Ale Ridge: InSAR Observations and Source Models. Remote Sensing 2021, 13, 1991. https://doi.org/10.3390/rs13101991.

Bawden GW, Thatcher W, Stein RS, Hudnut KW, Peltzer G, 2001. Tectonic contraction across Los Angeles after removal of groundwater pumping effects, Nature, 412, 812–815.

Bergonzoni A, Elmi C, 1985. La geologia dell'area bolognese in relazione al fenomeno della subsidenza, Inarcos, 456, 2-7, Bologna.

Bitelli G, Bonsignore F, Del Conte S, Novali F, Pellegrino I, Vittuari L, 2014. Integrated use of advanced InSAR and GPS data for subsidence monitoring. In: Lollino G, Manconi A, Guzzetti F, Culshaw M, Bobrowsky PT and Luino F (eds), Engineering Geology for Society and Territory, Springer, Berlin, Germany, Vol. 5, pp. 147-150, doi: 10.1007/978-3-319-09048-1_29.

Bitelli G, Bonsignore F, Pellegrino I, Vittuari L, 2015. Evolution of the techniques for subsidence monitoring at regional scale: the case of Emilia-Romagna region (Italy), Proc. IAHS, 372, 315–32, https://doi.org/10.5194/piahs-372-315-2015.

Bitelli G, Roncari G, Tini MA, Vittuari L, 2018. High-precision topographical methodology for determining height differences when crossing impassable areas, Measurement, 118, 147-155, ISSN 0263-2241, https://doi.org/10.1016/j.measurement.2018.01.013.

Bitelli G, Bonsignore F, Del Conte S, Franci F, Lambertini A, Novali F, Severi P, Vittuari L, 2020. Updating the subsidence map of Emilia-Romagna region (Italy) by integration of SAR interferometry and GNSS time series: the 2011–2016 period, Proc. IAHS, 382, 39–44, https://doi.org/10.5194/piahs-382-39-2020.

Borchers JW, 1998. Land subsidence case studies and current research. Proceedings of the Dr. J.F. Poland Symposium, Association of Engineering Geologists, Star Publishing, Belmont, California.

Bjerrum L, 1963. Discussion, Proc. European Conference on Soil Mechanic and Foundation Engineering, Wiesbaden, Germany, vol. III, p. 135.

Bräuner G, 1973. Subsidence due to underground mining (in Two Parts): 1. Theory and Practices in Predicting Surface Deformation, US Department of the Interior, Bureau of Mines, Denver.

Bridge JS, Jalfin GA, Georgieff SM, 2000. Geometry, Lithofacies, and Spatial Distribution of Cretaceous Fluvial Sandstone Bodies, San Jorge Basin, Argentina: Outcrop Analog for the Hydrocarbon-Bearing Chubut Group. J. Sed. Res., 70 (2): 341–359. https://doi.org/10.1306/2DC40915-0E47-11D7-8643000102C1865D.

Brighenti G, Borgia GC, Mesini E, 1995. Chapter 5 Subsidence studies in Italy, Editor(s): Chilingarian G.V., Donaldson E.C., Yen T.F., Developments in Petroleum Science, Elsevier, Volume 41, 1995, Pages 215-283, ISSN 0376-7361, ISBN 9780444818201, https://doi.org/10.1016/S0376-7361(06)80052-X.

Bruno L, Amorosi A, Curina R, Severi P, Bitelli R, 2013. Human–landscape interactions in the Bologna area (northern Italy) during the mid–late Holocene, with focus on the Roman period. Holocene, 23, 1560 – 1571.

Bruno L, Amorosi A, Severi P, Bartolomei P, 2015. High-frequency depositional cycles within the late Quaternary alluvial succession of Reno River (northern Italy). Ital. J. Geosci., 134(2), 339–354. https://doi.org/10.3301/IJG.2014.4

Bruno L, Campo B, Costagli B, Stouthamer E, Teatini P, Zoccarato C, Amorosi A, 2020. Factors controlling natural subsidence in the Po Plain, Proceedings of IAHS, 382, 285–290. https://doi.org/10.5194/piahs-382-285-2020.

Bruno L, Marchi M, Bertolini I, Gottardi G, Amorosi A, 2020. Climate control on stacked paleosols in the Pleistocene of the Po Basin (northern Italy). J. Quaternary Sci, 35, 559–571.https://doi.org/10.1002/jqs.3199.

Burbey TJ, 2020. Extensometer forensics: what can the data really tell us?, Hydrogeology Journal, 28 (2), 637–655. https://doi.org/10.1007/s10040-019-02060-6.

Carminati E, Di Donato G, 1999. Separating natural and anthropogenic vertical movements in fast subsiding areas: the Po plain (N Italy) case. Geophys. Res. Lett., 26, 2291-2294.

Carminati E, Martinelli G, 2002. Subsidence rates in the Po Plain, northern Italy: the relative impact of natural and anthropogenic causation. Engineering Geology, 66, 241-255.

Casagrande A, 1936. The Determination of the Pre-Consolidation Load and its Practical Significance, Proceedings of the 1st International Conference on Soil Mechanics, Harvard University Cambridge, Mass., 3, D-34, p. 60-64.

Castellarin A, Eva C, Giglia G, Vai GB, Rabbi E, Pini GA, Crestana G, 1985. Analisi strutturale del fronte Appenninico Padano. Giorn. Geol. 47, 47-75.

Castellaro S, & Mulargia F, 2009. Vs30 estimates using constrained H/V measurements. Bull. Seismol. Soc. Am., 99:761–773.

Catuneanu O, 2006. Principles of Sequence Stratigraphy, Elsevier, Amsterdam, 375 pp.

Cestari F, 1990. Prove geotecniche in sito, Ed. Geo-Graph s.n.c. Segrate, Milano.

Chang YL, Tsai TL, Yang JC, 2019. Flood hazard mitigation in land subsidence prone coastal areas by optimal groundwater pumping, Journal of Flood Risk Management, 12(2). https://doi.org/10.1111/jfr3.12517.

Chapman DM, 1984. The edge of the sea, In M. Schwartz (Ed.), Beaches and coastal Geology. Springer US.

Charpentier A, James M, Ali H, 2022. Predicting drought and subsidence risks in France, Natural Hazards and Earth System Sciences, 22, 2401–2418. https://doi.org/10.5194/nhess-22-2401-2022.

Chaussard E, Amelung F, Abidin H, Hong SH, 2013. Sinking cities in Indonesia: ALOS PALSAR detects rapid subsidence due to groundwater and gas extraction. Remote Sensing of Environment, 128, 150–161.

Chaussard E, Havazli E, Fattahi H, Cabral-Cano E, Solano-Rojas D, 2021. Over a century of sinking in Mexico City: No hope for significant elevation and storage capacity recovery. Journal of Geophysical Research: Solid Earth, 126, e2020JB020648. https://doi.org/10.1029/2020JB020648.

Chiesa A, 1742. Carta topografica di tutta la pianura del Bolognese, scala in miglia italiane.

Choobbasti AJ, Rezaei S, Farrokhzad F, 2013. Evaluation of site response characteristics using microtremors. Gradevinar, 65: 731–741.

Cooper AH, 1988. Subsidence resulting from the dissolution of Permian gypsum in the Ripon area; its relevance to mining and water abstraction, Published in Bell FG, Culshaw MG, Cripps JC, Lovell MA (eds), 1988. Engineering Geology of Underground Movements, Geological Society Engineering Geology Special Publication No. 5, pp. 387-390.

Costantini M, Minati F, Trillo F, Ferretti A, Novali F, Passera E, Dehls J, Larsen Y, Marinkovic P, Eineder M, Brcic R, Siegmund R, Kotzerke P, Probeck M, Kenyeres A, Proietti S, Solari L, Andresen HS, 2021. European Ground Motion Service (EGMS), IEEE International Geoscience and Remote Sensing Symposium IGARSS, Brussels, Belgium, 2021, pp. 3293-3296, doi: 10.1109/IGARSS47720.2021.9553562.

Craig RF, 1974. Craig's Soil Mechanics (7th edition), CRC Press, London. https://doi.org/10.4324/9780203494103.

Cremonini S, 1980. Evoluzione morfologica della pianura bolognese tra Reno e Idice. Tesi di laurea, Università di Bologna, inedita.

Cremonini S, 1992. Il torrente Savena oltre i limiti dell'analisi storica. Un esempio di "archeologia fluviale". Atti e Memorie della Deputazione di Storia Patria per le province di Romagna, 12:159-205.

Crosetto M, Solari L, Balasis-Levinsen J, Bateson L, Casagli N, Frei M, Oyen A, Moldestad DA, Mróz M, 2021. Deformation Monitoring at European Scale: The Copernicus Ground Motion Service, The International Archives of the Photogrammetry, Remote Sensing and Spatial Information Sciences, XLIII-B3-2021, 141-146. doi: 10.5194/isprs-archives-XLIII-B3-2021-141-2021.

Culshaw MG, & Price SJ, 2012. The contribution of urban geology to the development, regeneration and conservation of cities. The 2010 Hans Cloos lecture. Bull. Eng. Geol. Environ, Volume 70, No 3, pp 333-376. doi 10.1007/s10064-011-0377-4.

Das BM, 1983. Advanced soil mechanics, Hemisphere Publishing Corporation and McGraw-Hill, New York, p.1-511, ISBN 0-07-015416-3.

De Caro M, Crosta GB, Previati A, 1985. Modelling the interference of underground structures with groundwater flow and remedial solutions in Milan, Engineering Geology, 272, 105652. 0013-7952, https://doi.org/10.1016/j.enggeo.2020.105652.

Dehghani M, Valadan Zoej MJ, Entezam I, Mansourian A, Saatchi S, 2009. InSAR monitoring of progressive land subsidence in Neyshabour, Northeast Iran. Geophys J Int 178:47–56.

Di Buò B, 2020. Evaluation of the Preconsolidation Stress and Deformation Characteristics of Finnish Clays based on Piezocone Testing, [Doctoral dissertation, Tampere University], ISBN: 978-952-03-1468-2. http://urn.fi/URN:ISBN:978-952-03-1468-2.

Domenico PA, Schwartz FW, 1990. Physical and Chemical Hydrogeology, John Wiley & Sons, New York, p. 824.

Doornhof D, Kristiansen TG, Nagel NB, Pattillo PD, Sayers C, 2006. Compaction and Subsidence. Oilfield Review, Autum, 50-67.

El May M, Dlala M, Chenini I, 2010. Urban geological mapping: Geotechnical data analysis for rational development planning. Eng. Geol., 116 (1-2), 129-138, https://doi.org/10.1016/j.enggeo.2010.08.002

Elmi C, Bergonzoni A, Massa T, Montaletti V, 1984. Il territorio di pianura del Comune di Bologna: aspetti geologici e geotecnici. Giornale di Geologia, Rivista di Geologia Sedimentaria e Geologia Marina, 46, n. 2. ISSN 0017-0291.

Erkens G, Bucx T, Dam R, de Lange G, Lambert J, 2015. Sinking coastal cities, Proceedings of IAHS, 372, 189-198, https://doi.org/10.5194/piahs-372-189-2015.

Farolfi G, Del Soldato M, Bianchini S, Casagli N, 2019. A procedure to use GNSS data to calibrate satellite PSI data for the study of subsidence: an example from the north-western Adriatic coast (Italy), European Journal of Remote Sensing, 52:sup4, 54-63, DOI: 10.1080/22797254.2019.1663710.

Fernández-Torres E, Cabral-Cano E, Solano-Rojas D, Havazli E, Salazar-Tlaczani L, 2020. Land Subsidence risk maps and InSAR based angular distortion structural vulnerability assessment: an example in Mexico City, Proceedings of the International Association of Hydrological Sciences, 382, 583-587. doi: 10.5194/piahs-382-583-2020.

Ferretti A, Prati C, Rocca F, 2001. Permanent Scatterers in SAR Interferometry. IEEE Trans. IEEE Transactions on Geoscience and Remote Sensing, 39, 8–20. doi:10.1109/36.898661.

Fileccia A, 2015. Some simple procedures for the calculation of the influence radius and well head protection areas (theoretical approach and a field case for a water table aquifer in an alluvial plain), Italian Journal of Groundwater (2015). DOI 10.7343/AS-117-15-0144.

Fletcher WD, Smith CB, 2020. Chapter 1 – Introduction, Eds: Fletcher WD, Smith CB, Reaching Net Zero, Elsevier, p.1-8. ISBN 9780128233665, https://doi.org/10.1016/B978-0-12-823366-5.00001-4.

Fordyce FM, Campbell SDG, 2017. The Geosciences in Europe's Urban Sustainability: Lessons from Glasgow and Beyond (CUSP). Earth and Environmental Science Transactions of the Royal Society of Edinburgh Special Issue, 108 (2–3).

Foster S, 2022. The key role for groundwater in urban water-supply security. Journal of Water and Climate Change, 13 (10), 3566–3577. doi: https://doi.org/10.2166/wcc.2022.174.

Foster SSD, Morris BL, Chilton PJ, 1999. Groundwater in urban development: a review of linkages and concerns. IAHS-AISH publication, 259, 3-12.

Franceschetti G, Migliaccio M, Riccio D, Schirinzi G, 1992. SARAS: a synthetic aperture radar (SAR) raw signal simulator, in IEEE Transactions on Geoscience and Remote Sensing, 30(1), p. 110-123, doi: 10.1109/36.124221.

Gabriel AK, Goldstein RM, Zebker HA, 1989. Mapping small elevation changes over large areas: Differential radar interferometry, J. Geophys. Res., 94(B7), 9183–9191, doi:10.1029/JB094iB07p09183.

Galloway DL, Jones D, Ingebritsen SE, 1999. Land subsidence in the United States, U.S. Geological Survey, Circular 1182, 185 pp., doi: 10.3133/cir1182.

Galloway DL, Burbey TJ, 2011. Regional land subsidence accompanying groundwater extraction. Hydrogeology Journal 19(8): 1459-1486. Galloway, D.L., Burbey, T. J., 2011. Review: Regional land subsidence accompanying groundwater extraction, Hydrogeology J., 19(8), 1459-1486.

Gambolati G, Teatini P, Ferronato M, 2005. Anthropogenic Land Subsidence, Encyclopedia of Hydrological Sciences. John Wiley & Sons, Ltd. doi:10.1002/0470848944.hsa164b.

Gambolati G, Teatini P, 2015. Geomechanics of subsurface water withdrawal and injection, Water Resources Research, 51(6), 3922-3955. https://doi.org/10.1002/2014WR016841.

Gambolati G, Teatini P, 2021. Land Subsidence and its Mitigation, Guelph, Ontario, Canada, pp. 92, ISBN: 978-1-77470-001-3, https://gw-project.org/books/land-subsidence-and-its-mitigation.

Gehrels R, Garrett E, 2021. Chapter 11 - Rising sea levels as an indicator of global change, Ed(s): Letcher TM, Climate Change (Third Edition), Elsevier, p.205-217. ISBN 9780128215753, https://doi.org/10.1016/B978-0-12-821575-3.00011-6.

Geological Map of Italy 1:50.000 by the Geological Survey of Italy-ISPRA –Sheets: 220 Casalecchio di Reno-221 Bologna and Geological notes.

Giacomelli S, Zuccarini A, Amorosi A, Bruno L, Di Paola G., Martini A, Severi P, Berti M, 2023. 3D geological modelling of the Bologna urban area (Italy), Engineering Geology, 324, 107242, ISSN 0013-7952. https://doi.org/10.1016/j.enggeo.2023.107242.

Giomi I, Francisca FM, 2022. Numerical Modeling of the Oedometrical Behavior of Collapsible Loess, Geotechnical and Geological Engineering, 40(5), 2501-2512. https://doi.org/10.1007/s10706-021-02042-0.

Guo H, Hao A, Li W, Zang X, Wang Y, Zhu J, Wang L, Chen Y, 2022. Land subsidence and its affecting factors in Cangzhou, North China Plain, Front. Environ. Sci. 10:1053362. doi: 10.3389/fenvs.2022.1053362.

Gunderson K, Pazzaglia FJ, Picotti V, Anastasio DA, Kodama KP, Rittenour T, Frankel KF, Ponza A, Berti C, Negri A, Sabbatini A, 2014. Unraveling tectonic and climatic controls on synorogenic growth strata (Northern Appennines, Italy). Geol. Soc. Am. Bull., 126, 3/4: 532-552.

Gurjar BR, Ojha CSP, Surampalli RY, Walvekar PP, Tyagi V, 2013. Greenhouse Gas Emissions and Climate Change: An Overview, in: Climate Change Modeling, Mitigation, and Adaptation (Chapter 2), 9-25, American Society of Civil Engineers, USA. doi: 10.1061/9780784412718.ch02.

Guzy A, Malinowska AAA, 2020. Assessment of the Impact of the Spatial Extent of Land Subsidence and Aquifer System Drainage Induced by Underground Mining. Sustainability, 12, 7871.

Guzy A, Witkowski WT, 2021. Land subsidence estimation for aquifer drainage induced by underground mining. Energies 14. doi:10.3390/en14154658.

Haghshenas Haghighi M, Motagh M, 2021. Land subsidence hazard in Iran revealed by country-scale analysis of Sentinel-1 InSAR, Int. Arch. Photogramm. Remote Sens. Spatial Inf. Sci., XLIII-B3-2021, 155–161, https://doi.org/10.5194/isprs-archives-XLIII-B3-2021-155-2021.

Hakim WL, Achmad AR, Eom J, Lee CW, 2020. Land subsidence measurement in Jakarta coastal area using time series interferometry with Sentinel-1 SAR data. In: Jung, H.-S.; Lee, S.; Ryu, J.-H., and Cui, T. (eds.), Advances in Geospatial Research of Coastal Environments. Journal of Coastal Research, Special Issue No. 102, pp. 75-81. Coconut Creek (Florida), ISSN 0749-0208.

Hamlyn J, Wright T, Walters R, Pagli C, Sansosti E, Casu F, Pepe S, Edmonds M, McCormick Kilbride B, Keir D, Neuberg J, Oppenheimer C, 2018. What causes subsidence following the 2011 eruption at Nabro (Eritrea)?, Prog Earth Planet Sci 5, 31. https://doi.org/10.1186/s40645-018-0186-5.

Hammett KM, Katz BG, McPherson BF, Patiño E, Schiffer DM, Wedderburn L, Yobbi DK, 2001. Science Plan U.S. Geological Survey Florida District. 37, Open-File Report 01-180, Tallahassee, Florida.

Harnischmacher S, Zepp H, 2010. Bergbaubedingte Höhenänderungen im Ruhrgebiet – Eine Analyse auf Basis digitalisierter historischer Karten, zfv:386–397.

Harrison AM, Plim JFM, Harrison M, Jones LD, Culshaw MG, 2012. The relationship between shrink–swell occurrence and climate in south-east England, Proceedings of the Geologists' Association, 123(4), p.556-575. ISSN 0016-7878, https://doi.org/10.1016/j.pgeola.2012.05.002.

He H, He J, Xiao JZ, Zhou YX, Liu Y, Li C, 2020. 3D geological modeling and engineering properties of shallow superficial deposits: a case study in Beijing, China. Tunn Undergr Sp Tech.;100:103390, https://doi.org/10.1016/j.tust.2020.103390.

He H, Xiao J, He J, Wei B, Ma X, Huang F, Cai X, Zhou Y, Bi J, Zhao Y, Wang C, Wei J, 2023. Three-Dimensional Geological Modeling of the Shallow Subsurface and Its Application: A Case Study in Tongzhou District, Beijing, China. Applied Sciences, 13, 1932. https://doi.org/10.3390/app13031932.

Hemmerle H, Ferguson G, Blum P, Bayer P, 2022. The evolution of the geothermal potential of a subsurface urban heat island. Environ. Res. Lett., 17 (8).

Herrera-García G, Ezquerro P, Tomás R, Béjar-Pizarro M, López-Vinielles J, Rossi M, Mateos RM, Carreón-Freyre D, Lambert J, Teatini P, Cabral-Cano E, Erkens G, Galloway D, Hung W, Kakar N, Sneed M, Tosi L, Wang H, Ye S, 2021. Mapping the global threat of land subsidence. Science, 371, 34-36 (2021). DOI:10.1126/science.abb8549.

Holtz RD, Kovacs WD, 1981. An Introduction to Geotechnical Engineering. Prentice-Hall Inc., New Jersey.

Holzer TL, 1984. Man-Induced Land Subsidence, Reviews in Engineering Geology, vol. VI, Geological Society of America, Boulder, CO, 221.

Hooimeijer FL, Maring L, 2018. The significance of the subsurface in urban renewal. Journal of Urbanism: International Research on Placemaking and Urban Sustainability, 11:3, 303-328, DOI: 10.1080/17549175.2017.1422532.

Hu RL, Yue ZQ, Wang LC, Wang SJ, 2004. Review on current status and challenging issues of land subsidence in China, Engineering Geology, 76, 65-77, ISSN 0013-7952. https://doi.org/10.1016/j.enggeo.2004.06.006.

Huggenberger P, Epting J, 2011. Urban Geology. Process-Oriented Concepts for Adaptive and Integrated Resource Management. Springer, Basel, https://doi.org/10.1007/978-3-0348-0185-0.

Jalota SK, Vashisht BB, Sharma S, Kaur S, 2018. Chapter 4 - Climate Change and Groundwater, Eds. Jalota SK, Vashisht BB, Sharma S, Kaur S, Understanding Climate Change Impacts on Crop Productivity and Water Balance, Academic Press, 2018, 149-181, ISBN 9780128095201, https://doi.org/10.1016/B978-0-12-809520-1.00004-5.

Janbu N, 1967. Settlement calculations based on the tangent modulus concept, Soil Mechanics and Foundation Engineering, University of Trondheim, Norwegian Institute of Technology, pp. 57.

Janbu N, Bjerrum L, Kjaernsli B, 1956. Soil Mechanics Applied to some Engineering Problems, Norwegian Geotechnical Institute Publication, 16, Oslo, Norway.

Jiang L, Lin H, Cheng S, 2011. Monitoring and assessing reclamation settlement in coastal areas with advanced InSAR techniques: Macao city (China) case study, International Journal of Remote Sensing, 32(13), 3565-3588. DOI:10.1080/01431161003752448.

Knappett J, Craig RF, 2019. Craig's Soil Mechanics (9th edition), CRC Press, London. https://doi.org/10.1201/9781351052740.

Kok S, Costa AL, 2021. Framework for economic cost assessment of land subsidence, Natural Hazards, 106, 1931–1949. https://doi.org/10.1007/s11069-021-04520-3.

Kokkala A, Marinos V, 2022. An engineering geological database for managing, planning and protecting intelligent cities: The case of Thessaloniki city in Northern Greece. Eng. Geol., 301, https://doi.org/10.1016/j.enggeo.2022.106617.

Lancellotta R, 1983. Analisi di Affidabilità in Ingegneria Geotecnica, Atti Istituto Scienza Costruzioni, 625, Politecnico di Torino.

Lancellotta R, 1987. Geotecnica, Zanichelli, Bologna, p.1-531, ISBN 88-08-04362-2.

Laouafa F, Guo J, Quintard M, 2021. Underground Rock Dissolution and Geomechanical Issues. Rock Mech Rock Eng 54, 3423–3445. https://doi.org/10.1007/s00603-020-02320-y.

Laouafa F, Guo J, Quintard M, 2023. Modelling and applications of dissolution of rocks in geoengineering. J. Zhejiang Univ. Sci. A 24, 20–36. https://doi.org/10.1631/jzus.A2200169.

Lapenna V, Chambers J, Shi B, Lienhart W, Zhu H, 2020. Frontiers and applications of geological engineering and geophysical monitoring technologies in urban areas. Eng. Geol., Special Issue, 268, https://doi.org/10.1016/j.enggeo.2020.105508.

Leeper R, Rhodes B, Kirby M, Scharer K, Carlin J, Hemphill-Haley E, Avnaim-Katav S, MacDonald G, Starratt S, Aranda A, 2017. Evidence for coseismic subsidence events in a southern California coastal saltmarsh. Sci Rep 7, 44615. https://doi.org/10.1038/srep44615.

Li G, Zhao C, Wang B, Liu X, Chen H, 2022. Land Subsidence Monitoring and Dynamic Prediction of Reclaimed Islands with Multi-Temporal InSAR Techniques in Xiamen and Zhangzhou Cities, China. Remote Sensing, 14(12), 2930. https://doi.org/10.3390/rs14122930.

Li P, Gu J, Liu Y, Li Y, 2022. The study of soft soil seismic subsidence based on the 3D OpenSees model. Geoenviron Disasters 9, 10. https://doi.org/10.1186/s40677-022-00212-7.

Lixin Y, Jie W, Chuanqing S, Guo J, Yanxiang J, Liu B, 2010. Land subsidence disaster survey and its economic loss assessment in Tianjin, China, Natural Hazards Review, 11(1), 35-41. https://doi.org/10.1061/(ASCE)1527-6988(2010)11:1(35).

Lu Z, Masterlark T, Power J, Dzurisin D, Wicks C, 2002. Subsidence at Kiska volcano, western Aleutians, detected by satellite radar interferometry. Geophysical research letters, 29(18). http://dx.doi.org/10.1029/2002GL014948 (2-1-2-4).

Luberti GM, Prestininzi A, Esposito C, 2015. Development of a geological model useful for the study of the natural hazards in urban environments: An example from the eastern sector of Rome (Italy). Italian Journal of Engineering Geology and Environment 15, 41–62. doi:10.4408/IJEGE.2015-02.O-04.

Lunne T, Robertson PK, Powell JJM, 1997. Cone penetration testing in geotechnical practice, Blackie Academic, EF Spon/Taylor & Francis Publ., New York, 1997, pp. 312.

Lyu HM, Shen SL, Zhou A, Yang J, 2020. Risk assessment of mega-city infrastructures related to land subsidence using improved trapezoidal FAHP. Science of The Total Environment, 717, 135310. ISSN 0048-9697, doi: 10.1016/j.scitotenv.2019.135310.

Ma T, Du Y, Ma R, Xiao C, Liu Y, 2018. Review: Water–rock interactions and related eco-environmental effects in typical land subsidence zones of China, Hydrogeology Journal, 26, 1339–1349. https://doi.org/10.1007/s10040-017-1708-8.

Maaß AL, Schüttrumpf H, 2018. Long-term effects of mining-induced subsidence on the trapping efficiency of floodplains. Anthropocene 24, 1–13. doi:10.1016/j.ancene.2018.10.001.

Mahmoudpour M, Khamehchiyan M, Nikudel MR, Ghassemi MR, 2016. Numerical simulation and prediction of regional land subsidence caused by groundwater exploitation in the southwest plain of Tehran, Iran. Engineering Geology 201, 6–28. doi:10.1016/j.enggeo.2015.12.004.

Marker BR 2013. Land Subsidence. In: Bobrowsky, P.T. (eds) Encyclopedia of Natural Hazards. Encyclopedia of Earth Sciences Series. Springer, Dordrecht. https://doi.org/10.1007/978-1-4020-4399-4_208.

Martelli L, Bonini M, Calabrese L, Corti G, Ercolessi G, Molinari FC, Piccardi L, Pondrelli S, Sani F, Severi P, 2017. Seismotectonic map of the Emilia-Romagna Region and surrounding areas, Scale 1:250,000, nd edn. D.R.E.AM, Firenze.

Martorana R, Capizzi P, Avellone G, D'Alessandro A, Siragusa R, Luzio D, 2017. Assessment of a geological model by surface wave analyses, J. Geophys. Eng., 14, 1, 159–172. https://doi.org/10.1088/1742-2140/14/1/159.

Mathers S, Burke H, Terrington R, Thor S, Dearden R, Williamson J, Ford J, 2014. A geological model of London and the Thames Valley, southeast England. Proceedings of the Geologists' Association, 125(4): 373-382.

Mayne PW, 2014. Interpretation of geotechnical parameters from seismic piezocone tests. Proceedings, 3rd International Symposium on Cone Penetration Testing (CPT'14, Las Vegas), ISSMGE Technical Committee TC 102, Edited by P.K. Robertson and K.I. Cabal, c 47-73.

Meade RH, 1968. Compaction of sediments underlying areas of land subsidence in central California, Geological Survey Professional Paper, 497 (D), 10.3133/pp497D.

Mendoza M, Romo M, 1989. Behavior of building foundations in Mexico City during the 1985 Earthquake: second stage. In: Proc., Lessons Learned from the 1985 Mexico Earthquake, pp 66–70.

Mesri G, 1975. New design procedure for stability of soft clays. Discussion, J. of the Geotech. Eng. Div., ASCE, 101(4), 409-412.

Miall AD, 1977. A review of the braided river depositional environment. Earth Sci. Rev., 13 (1), 1-62.

Miall AD, 1978. Lithofacies types and vertical profile models in braided river deposits: a summary Canadian Society of Petroleum Geologists, 52 (5), 597-604.

Miall AD, 1985. Architectural-element analysis: A new method of facies analysis applied to fluvial deposits, Earth-Science Reviews, 22, Issue 4, 261-308. https://doi.org/10.1016/0012-8252(85)90001-7.

Miall AD, 1996. The geology of fluvial deposits: sedimentary facies, basin analysis and petroleum geology. Berlin, Springer International, 582 p. https://doi.org/10.1007/978-3-662-03237-4.

Miall AD, 2016. Stratigraphy: A Modern Synthesis. Switzerland, Springer International, 454 p.

Mitchell, J.K. and Gardner; W.S., 1975. "In Situ Measurement of Volume Change Characteristics," State-of-the-Art Report, Proceedings of the Conference on In-Situ Measurement of Soil Properties, Specialty Conf. of the Geotechnical Div., North Carolina State University, Raleigh, Vol. II, 279-345.

Modoni G, Darini G, Spacagna RL, Saroli M, Russo G, Croce P, 2013. Spatial analysis of land subsidence induced by groundwater withdrawal. Engineering Geology. 167. 59–71. 10.1016/j.enggeo.2013.10.014.

Moisidi M, Vallianatos F, Kershaw S, Collins P, 2015. Seismic site characterization of the Kastelli (Kissamos) basin in northwest Crete (Greece): assessments using ambient noise recordings. Bull. Earthq. Eng., 13, 725–753.

Nakamura Y, 1989. A method for dynamic characteristics estimation of subsurface using microtremor on the ground surface. Q. Rep. Railw. Tech. Res. Inst. 30:25–33.

Nelson FE, Anisimov OA, Shiklomanov NI, 2001. Subsidence risk from thawing permafrost, Nature 410 (6831), 889–890. https://doi.org/10.1038/35073746.

Ng AH, Ge L, Li X, 2015. Assessments of land subsidence in the Gippsland Basin of Australia using ALOS PALSAR data, Remote Sensing of Environment, 159, 86-101. ISSN 0034-4257, https://doi.org/10.1016/j.rse.2014.12.003.

NotesISPRA (Istituto Superiore per la Protezione e la Ricerca Ambientale), 20232009. Geological Map of Italy 1:50000: Sheet 220 "Casalecchio di Reno", Sheet 221 "Bologna", and Geological Notes. https://www.isprambiente.gov.it/Media/carg/220_CASALECCHIO_DI_RENO/Foglio.html; https://www.isprambiente.gov.it/Media/carg/220_CASALECCHIO_SOTTO/Foglio.html; https://www.isprambiente.gov.it/Media/carg/221_BOLOGNA/Foglio.html; https://www.isprambiente.gov.it/Media/carg/221_BOLOGNA_SOTTO/Foglio.html.

Ori GG, 1982. Braided to meandering channel patterns in humid-region alluvial fan deposits, River Reno, Po Plain (northern Italy). Sediment. Geol. 31, 231–248.

Ori GG; 1993: Continental depositional systems of the Quaternary of the Po Plain (northern Italy). Sediment. Geol., 83, 1-14, doi: 10.1016/S0037-0738(10)80001-6.

Picotti V, Ponza A, Pazzaglia FJ, 2009. Topographic expression of active faults in the foothills of the Northern Apennines. Tectonophysics, 474, 285–294.

Pieri L, Russo P, 1980. Abbassamento del suolo della zona di Bologna: considerazioni sulle probabili cause e sulla metodologia per lo studio del fenomeno. Collana di orientamenti geomorfologici ed agronomico-forestali. Pitagora Editrice, Bologna, 1980.

Pieri M, Groppi G, 1981. Subsurface geological structure of the Po Plain, Italy. P.F. Geodin. Publ., 414. C.N.R., Roma 1–23.

Pieri L, Russo P, 1985. Situazione attuale delle ricerche sull'abbassamento del suolo nel territorio bolognese. Inarcos, 456, 11-15, Bologna.

Pirazzoli PA, 1996. Sea level changes, The Last 20000 Years, Wiley, Chichester, 211.

Poland JF, Yamamoto S, et al., 1984. Field measurement of deformation, Guidebook to studies of land subsidence due to groundwater withdrawal, Poland JF, ed., United Nations Educational Scientific and Cultural Organization (UNESCO), Paris, 17–35.

Posamentier HW, Allen GP, 1999. Siliciclastic sequence stratigraphy— concepts and applications. Concepts in sedimentology and paleontology, SEPM Society for Sedimentary Geology, Tulsa, 7, 210 p. https://doi.org/10.2110/csp.99.07.

Price SJ, Ford JR, Campbell SDG, Jefferson I, 2016. Urban Futures: the sustainable management of the ground beneath cities. In: Developments in Engineering Geology (Eggers et al., eds.), https://doi.org/10.1144/EGSP27.2.

Rahimi MR, Mohammadi SD, Taleb Beydokhti A, 2022. Laboratory simulation of gypsum rock dissolution at different pressures, water-flow velocities and pH ranges, Quarterly Journal of Engineering Geology and Hydrogeology, 56(1), doi: https://doi.org/10.1144/qjegh2021-120.

Raspini F, Caleca F, Del Soldato M, Festa D, Confuorto P, Bianchini S, 2022. Review of satellite radar interferometry for subsidence analysis, Earth-Science Reviews, doi:10.1016/j.earscirev.2022.104239.

RER & ENI-AGIP, 1998. Riserve idriche sotterranee della Regione Emilia-Romagna. Bologna. A cura di G.M: DI Dio. S.EL.CA, Firenze, 120 pp.

Ricci Lucchi F, 1986. Oligocene to Recent foreland basins of Northern Apennines. In Foreland Basins, Allen, Homewood P (eds). International Association of Sedimentologists, Special Publications, 105-139.

Riley FS, 1984. Developments in borehole extensometry, Proceedings of the 3rd International. Symposium on Land Subsidence, International Association of Hydro-logical Sciences, London, 169–186.

Robertson PK, 1990. Soil classification using the cone penetration test, Canadian Geotechnical Journal 27(1), 151-158.

Robertson PK, 2009. Interpretation of cone penetration tests – a unified approach. Canadian Geotechnical Journal 49(11), 1337-1355.

Robertson PK, 2010. Soil Behaviour Type from the CPT: An Update, 2nd International Symposium on Cone Penetration Testing, Huntington Beach, Vol. 2, 575-583.

Robertson PK, Campanella RG, 1983. Interpretation of cone penetration tests – Part I (sand). Canadian Geotechnical Journal, 20(4), 718-733.

Robertson PK, Campanella RG, Gillespie D, Greig J, 1986. Use of Piezometer Cone data. In-Situ'86 Use of In-situ testing in Geotechnical Engineering, GSP 6, ASCE, Reston, VA, Specialty Publication, SM 92, pp 1263-1280.

Robertson PK, Cabal KL, 2015. Guide to Cone Penetration Testing for Geotechnical Engineering, Gregg drilling, 6th edition.

Roque D, Fonseca AM, Henriques MJ, Falcão AP, 2014. A First Approach for Displacement Analysis in Lisbon Downtown Using PS-InSAR, Procedia Technology, 16, 288-293. https://doi.org/10.1016/j.protcy.2014.10.094.

Salvany JM, Aguirre J, 2020. The Neogene and Quaternary deposits of the Barcelona city through the high-speed train line. Geologica Acta, 18. DOI: 10.1344/GeologicaActa2020.18.10.

Sanglerat G, 1972. The penetration and soil exploration, Development in geotechnical engineering, Elsevier Scientific Publishing, New York, 52-80.

Savitzky A, Golay MJE, 1964. Smoothing and Differentiation of Data by Simplified Least Squares Procedures. Analytical Chemistry 1964 36 (8), 1627-1639. DOI: 10.1021/ac60214a047.

Schmertmann JH, 1970. Static cone to compute static settlement over sand. JSMF Div. ASCE, Vol.96 (3), 1011–1043.

Schmertmann JH, 1978. Guidelines for Cone Penetration Test, Performance and Design, Report No. FHWA-TS-78-209, U.S. Department of Transportation, Washington, D.C., pp. 145.

Sclater JG, Christie PAF, 1980. Continental stretching: an explanation of the post-mid-Cretaceous subsidence of the central North Sea basin. J. Geophys. Res. 85, 3711– 3739.

Scott RF, 1963. Principles of Soil Mechanics, Addison-Wesley Publishing Co., Boston.

Seed RB, 1990. Preliminary report on the principal geotechnical aspects of the October 17, 1989, Loma Prieta Earthquake Report No. UCB/EERC-90/05.

Seequent, 2019. User Manual for Leapfrog Works version 3.0.

Sengupta D, Choi YR, Tian B, Brown S, Meadows M, Hackney CR, Banerjee A, Li Y, Chen R, Zhou Y, 2023. Mapping 21st century global coastal land reclamation, Earth's Future, 11(2), e2022EF002927. https://doi.org/10.1029/2022EF002927.

SESAME, 2004. Guidelines for the implementation of the H/V spectral ratio technique on ambient vibrations measurements, processing, and interpretation. In: SESAME European Research Project Wp12 – Deliverable d23.12, European Commission – Research General Directorate, Project No. EVG1-CT-2000-00026, http://sesame.geopsy.org/Papers/HV_User_Guidelines.pdf Accessed 21 Jun 2022.

Severi P, 2021. Soil uplift in the Emilia-Romagna plain (Italy) by satellite radar interferometry. 527-542. 10.4430/bgta0349.

Skempton AW, MacDonald DH, 1956. Allowable settlement of buildings, Proc. Inst. Civ. Engrs., Part III, 5, 727–768.

Stafleu J, Maljers D, Gunnink JL, Busschers FS, 2011. 3D modelling of the shallow subsurface of Zeeland, the Netherlands, Netherlands. J. Geosc., 16(1), 5647. https://doi.org/10.5242/iamg.2011.0076.

Stauber JL, Chariton A, Apte S, 2016. Global Change, in: Marine Ecotoxicology: Current Knowledge and Future Issues, Elsevier, p. 273–313. doi:10.1016/B978-0-12-803371-5.00010-2.

Stramondo S, Saroli M, Tolomei C, Moro M, Doumaz F, Pesci A, Loddo F, Baldi P, Boschi E, 2007. Surface movements in Bologna (Po Plain — Italy) detected by multitemporal DInSAR. Remote Sensing of Environment. 110. 304-316. 10.1016/j.rse.2007.02.023.

Sweet WV, Hamlington BD, Kopp RE, Weaver CP, Barnard PL, Bekaert D, Brooks W, Craghan M, Dusek G, Frederikse T, Garner G, Genz AS, Krasting JP, Larour E, Marcy D, Marra JJ, Obeysekera J, Osler M, Pendleton M, Roman D, Schmied L, Veatch W, White KD, Zuzak C, 2022. Global and Regional Sea Level Rise Scenarios for the United States: Updated Mean Projections and Extreme Water Level Probabilities Along U.S. Coastlines, NOAA Technical Report NOS 01, National Oceanic and Atmospheric Administration, National Ocean Service, Silver Spring, Maryland, MD, pp. 111. https://oceanservice.noaa.gov/hazards/sealevelrise/noaa-nostechrpt01-global-regional-SLR-scenarios-US.pdf.

Szelag S, Weber U, 1993. Bergsenkung. In: Wiggering, H. (Ed.), Steinkohlebergbau: Steinkohle als Grundstoff. Energieträger und Umweltfaktor, Ernst & Sohn, Essen.

Taylor DW, 1948. Fundamentals of Soil Mechanics, John Wiley and Sons, New York.

Terzaghi K, 1925. Erdbaumechanik auf Bodenphysikalisher Grundlage, Deuticke, Vienna.

Terzaghi K, 1943. Theoretical soil mechanic. Wiley, New York.

Terzaghi K, Peck RB, 1967. Soil mechanics in engineering practice, John Wiley, New York, NY, USA, p. 729.

Thierry P, Prunier-Leparmentier A, Lembezat C, Vanoudheusden E, Vernoux J, 2009. 3D geological modelling at urban scale and mapping of ground movement susceptibility from gypsum dissolution: The Paris example (France). Eng. Geol., 105 (1–2), https://doi.org/10.1016/j.enggeo.2008.12.010.

Tomlinson MJ, 2001. Foundation Design and Construction, Pearson Education (US).

United Nations, 2004. World Economic and Social Survey, UN, New York.

Vail PR, Mitchum Jr RM, Thompson III S, 1977. Seismic Stratigraphy and Global Changes of Sea Level, Part 4: Global Cycles of Relative Changes of Sea Level. In: Payton C.E. (Ed.). Seismic Stratigraphy — Applications to Hydrocarbon Exploration. AAPG Memoir, 26, 83-97.

Van Wagoner JC, Mitchum RM, Campion KM, Rahmanian VD, 1990. Siliciclastic Sequence Stratigraphy in Well Logs, Cores, and Outcrops: Concepts for High-Resolution Correlation of Time and Facies. Mem. Am. Assoc. Pet. Geol. Memoir, 55 p. https://doi.org/10.1306/Mth7510 Van Wagoner J.C.

Vanicek E, Krakiwsky P, 1982. Geodesy: the concepts, North-Holland Publishing Co., Netherlands, 1982.

Vázquez-Suñé E, Sánchez-Vila X, Carrera J, 2005. Introductory review of specific factors influencing urban groundwater, an emerging branch of hydrogeology, with reference to Barcelona, Spain. Hydrogeol J 13, 522–533. https://doi.org/10.1007/s10040-004-0360-2.

Velasco V, Cabello P, Vázquez-Suñé E, López-Blanco M, Ramos E, Tubau I, 2012. A sequence stratigraphic based geological model in the urbanized area of the Quaternary Besòs delta (NW Mediterranean coast, Spain). Geologica Acta, 10, 373-393.

Viel G, Sangiorgi S, Zaccanti G, 2005. L'acqua dei bolognesi. Il Geologo dell'Emilia-Romagna, 21, 7-32.

Vittuari L, Tini MA, Sarti P, Serantoni E, Borghi A, Negusini M, Guillaume S, 2016. A comparative study of the applied methods for estimating deflection of the vertical in terrestrial geodetic measurements, Sensors (Switzerland), 16. http://dx.doi. org/10.3390/s16040565.

Volchko Y, Norrman J, Ericsson LO, Nilsson KL, Markstedt A, Öberg M, Mossmark F, Bobylev N, Tengborg P, 2020. Subsurface planning: Towards a common understanding of the subsurface as a multifunctional resource. Land Use Policy, 90, 104316, https://doi.org/10.1016/j.landusepol.2019.104316.

Von der Tann L, Sterling RL, Zhou Y, Metje N, 2019. Systems approaches to urban underground space planning and management – A review. Underground Space 5(2), DOI: 10.1016/j.undsp.2019.03.003.

Wang G, Yu J, Kearns TJ, Ortega J, 2014. Assessing the Accuracy of Long-Term Subsidence Derived from Borehole Extensometer Data Using GPS Observations: Case Study in Houston, Texas, Journal of Surveying Engineering, 140 (3), doi:10.1061/(ASCE)SU.1943-5428.0000133.

Wang X, Yuan Y, Hu C, Mei Y, 2021. Research on the Geostatic Stress Field Procedure under Complex Conditions, Advances in Civil Engineering, https://doi.org/10.1155/2021/6674369.

Whittaker BN, Reddish DJ, 1989. Subsidence: Occurrence, Prediction, and Control; Elsevier: Amsterdam, The Netherlands.

Wood HO, 1908. Distribution of apparent intensity in San Francisco. The California Earthquake of April, 18(1906), pp 220–227.

Wornardt WW, 1993. Application Of Sequence Stratigraphy To Hydrocarbon Exploration. Paper presented at the Offshore Technology Conference, Houston, Texas, May 1993. doi: https://doi.org/10.4043/7084-MS.

Yang M, Yang T, Zhang L, Lin J, Qin X, Liao M, 2018. Spatio-Temporal Characterization of a Reclamation Settlement in the Shanghai Coastal Area with Time Series Analyses of X-, C-, and L-Band SAR Datasets, Remote Sensing, 10(2), 329. https://doi.org/10.3390/rs10020329.

Yousefi R, Talebbeydokhti N, 2021. Subsidence monitoring by integration of time series analysis from different SAR images and impact assessment of stress and aquitard thickness on subsidence in Tehran, Iran. Environmental Earth Sciences 80. doi:10.1007/s12665-021-09714-3.

Zeitoun DG, Wakshal E, 2013. Land Subsidence Analysis in Urban Areas - The Bangkok Metropolitan Area Case Study, Springer Dordrech. https://doi.org/10.1007/978-94-007-5506-2.

Zhai Y, Cao X, Jiang Y, Sun K, Hu L, Teng Y, Wang J, Li J, 2021. Further Discussion on the Influence Radius of a Pumping Well: A Parameter with Little Scientific and Practical Significance That Can Easily Be Misleading. Water. 13(15):2050. https://doi.org/10.3390/w13152050.

Zhang L, Lu Z, Ding X, Jung HS, Feng G, Lee CW, 2012. Mapping ground surface deformation using temporarily coherent point SAR interferometry: Application to Los Angeles Basin. Remote Sensing of Environment, 117, 429–439.

Zhang Y, Huang H, Liu Y, Liu Y, 2018. Self-weight consolidation and compaction of sediment in the Yellow River Delta, China. Physical Geography, 39(1), 84–98. https://doi.org/10.1080/02723646.2017.1347420.

Zhao Q, Ma G, Wang Q, Yang T, Liu M, Gao W, Falabella F, Mastro P, Pepe A, 2019. Generation of long-term InSAR ground displacement time-series through a novel multi-sensor data merging technique: The case study of the Shanghai coastal area, ISPRS Journal of Photogrammetry and Remote Sensing, 154, 10-27. ISSN 0924-2716, https://doi.org/10.1016/j.isprsjprs.2019.05.005.